On the Measurement of High-Energetic Neutrinos with the IceCube Neutrino Telescope and with Acoustic Detection Methods

Von der Fakultät für Mathematik, Informatik und Naturwissenschaften der RWTH Aachen University zur Erlangung des akademischen Grades eines Doktors der Naturwissenschaften genehmigte Dissertation

vorgelegt von

Diplom-Physiker Matthias Schunck

aus Berlin

Berichter:

Universitätsprofessor Herr Prof. Dr.rer.nat Christopher Wiebusch
Universitätsprofessor Herr Prof. Dr.rer.nat Thomas Hebbeker

Tag der mündlichen Prüfung: 7. 10. 2011

Contents

1 Introduction **1**

2 Astroparticle physics **3**
2.1 High-Energy Cosmic Rays . . . 3
2.1.1 Observation . . . 3
2.1.2 Cosmic-Ray Acceleration . . . 4
2.1.3 Candidates for Cosmic-Ray Acceleration . . . 6
2.1.4 The GZK Effect . . . 8
2.2 High-Energy Neutrinos . . . 9
2.2.1 Production Mechanism . . . 9
2.2.2 Neutrinos from Cosmic-Ray Sources . . . 10
2.2.3 Cosmogenic (GZK) Neutrinos . . . 11
2.2.4 Top-Down Scenarios . . . 13
2.2.5 Current Limits on the Neutrino Flux . . . 13
2.3 The Atmospheric Background . . . 15

3 Detection of Neutrinos at the South Pole **17**
3.1 The Ice at the South Pole . . . 17
3.2 Neutrino Interactions in Ice . . . 19
3.2.1 Inelastic Neutrino Collisions . . . 19
3.2.2 Lepton Signatures . . . 20
3.2.3 Cascades . . . 23
3.3 Optical Neutrino Detection . . . 25
3.3.1 Cherenkov Effect . . . 25
3.3.2 Optical Ice Properties . . . 26
3.4 Acoustic Neutrino Detection . . . 28
3.4.1 The Thermo-Acoustic Model . . . 28
3.4.2 Acoustic Ice Properties . . . 32
3.5 Radio Neutrino Detection . . . 38
3.6 High-Energy-Neutrino Detectors . . . 39

4 The IceCube Neutrino Observatory **42**
4.1 The Detector . . . 42
4.2 Data Processing . . . 45
4.2.1 Data Acquisition (DAQ) . . . 45
4.2.2 Standard Processing . . . 46
4.3 Simulation . . . 47
4.4 Event Reconstruction . . . 48
4.4.1 Maximum-Likelihood Method . . . 49
4.4.2 Muon Track Reconstruction . . . 50
4.4.3 Muon Energy Reconstruction . . . 51

5 The South-Pole Acoustic Test Setup (SPATS) **55**
5.1 Setup . . . 55
5.1.1 In-ice Components . . . 55
5.1.2 On-ice Components . . . 58
5.1.3 Pinger . . . 59
5.1.4 Acoustic Data Taking . . . 60
5.2 Recent Results of SPATS . . . 61
5.2.1 Attenuation Length . . . 61
5.2.2 Ambient Noise . . . 61
5.2.3 Sound Speed . . . 62
5.2.4 Shear Waves . . . 63
5.2.5 Transients . . . 63

6 Acoustic Attenuation Length **65**
6.1 Attenuation . . . 65
6.2 Pinger Data Sample . . . 67
6.2.1 Pinger Depth Measurement . . . 71
6.3 Frequency Domain Pinger Analysis . . . 73
6.3.1 Data Selection . . . 73
6.3.2 Pulse Extraction . . . 74
6.3.3 Fourier Spectra and Noise Subtraction . . . 77
6.3.4 Effective Amplitude . . . 79
6.3.5 Attenuation Fit . . . 81
6.3.6 Error Estimation . . . 82
6.4 Results . . . 89
6.4.1 Single-Channel Fit . . . 89
6.4.2 Multi-Channel (Global) Fit . . . 93
6.4.3 Depth Dependence . . . 94
6.4.4 Frequency Dependence . . . 95
6.5 SPATS Attenuation Analysis . . . 97
6.5.1 Pinger Time Domain Energy Analysis . . . 97
6.5.2 Inter-String Analysis . . . 97

6.5.3 Transients 98
6.6 Comparison of Results 99

7 Top-Down Reconstruction of Muon Energies 102
7.1 The Top-Down Concept 102
7.2 Implementation 103
7.2.1 Monte-Carlo Database 103
7.2.2 Event Comparison 106
7.2.3 Observables 107
7.2.4 Likelihood Definition 108
7.3 Monte-Carlo Data Study 111
7.3.1 Data Sample 111
7.3.2 Quality Selection 113
7.3.3 Results 115
7.4 Future Developments 128

8 Summary & Outlook 130

A Thermo-acoustic effect in solids 134

Danksagung 149

List of Figures

2.1 All-particle cosmic ray spectrum 4
2.2 The Hillas criterion 5
2.3 Observation of cutoff in cosmic ray spectrum 8
2.4 GZK neutrino flux for different nuclei 12
2.5 Observational limits on the diffuse flux 13
2.6 Observational limits in the EHE range 14
2.7 Observational limits on the acoustic and radio neutrino detection 15

3.1 Phase diagram of water 18
3.2 Density and temperature profiles at South Pole 19
3.3 Neutrino cross section 20
3.4 Muon energy loss 21
3.5 Optical absorption and scattering coefficients 26
3.6 Bi-polar pressure pulse 29
3.7 Acoustic wave trajectories 33
3.8 Acoustic absorptivity and effective scattering 35
3.9 Energy ratio of P and S wave at medium boundary 37

4.1 The IceCube detector 43
4.2 IceCube string distances 44
4.3 Digital Optical Module 45
4.4 Visualization of track and cascade in detector 48
4.5 Track reconstruction 50
4.6 Correlation: NChannel and MMCdEdX with muon energy 51

5.1 Schematic of the SPATS array 56
5.2 Position of the SPATS array within IceCube 57
5.3 SPATS sensor types 58
5.4 Schematic view of the pinger 59
5.5 SPATS ambient noise evolution 62
5.6 SPATS sound speed measurement 63

5.7 Transient vertex reconstruction 64

6.1 SPATS pinger waveform and spectrum versus distance 66
6.2 Layout of all pinger measurements 67
6.3 Vertical pinger measurement 68
6.4 Horizontal pinger measurement 69
6.5 Pinger depth versus time 72
6.6 Depth correction factor 73
6.7 Full SPATS waveform from pinger 2008/09 74
6.8 Example pinger pulse seen by SPATS 75
6.9 Example noise during pinger measurements 76
6.10 Spectral shapes of SPATS channels 77
6.11 Spectrum versus pinger distance 78
6.12 Example noise-subtraction 79
6.13 Correlation signal waveform and noise energies 80
6.14 Correlation signal waveform and noise energies 81
6.15 Deviation of the effective amplitude in one waveform 82
6.16 Error versus distance 83
6.17 Error estimate: pinger distance and transmission 84
6.18 Uncertainty of effective amplitude 87
6.19 Effective amplitude versus distance 89
6.20 Effective amplitude versus distance 90
6.21 Example attenuation length fits 91
6.22 Attenuation versus SPATS channel 92
6.23 Histogram attenuation coefficients 92
6.24 Global attenuation fit on all channels 93
6.25 Depth dependence of attenuation coefficient 94
6.26 Dependence of attenuation on frequency bounds 95
6.27 Example pinger spectrum 2009/10 96
6.28 Summary attenuation analyses 100

7.1 TopDown principle: Monte-Carlo database 103
7.2 TopDown principle: event reconstruction 106
7.3 Distribution of Capp position and direction 112
7.4 Distribution of COG position 113
7.5 Angular resolution before and after quality selection 114
7.6 Single likelihood landscape examples 116
7.7 Correlation of reconstructed with MC dE/dX 117
7.8 Reconstruction resolution of single likelihoods 118
7.9 Top-Down reconstruction resolution versus database parameters 121
7.10 Top-Down reconstruction in dependence of the geometrical constraints 122
7.11 Top-Down dE/dX reconstruction resolution 123
7.12 Top-Down energy reconstruction resolution 124

7.13 Energy resolution versus muon energy 126
7.14 Energy resolution versus neutrino energy 126
7.15 Top-Down reconstructed muon dE/dX spectra 127
7.16 Top-Down reconstructed muon energy spectra 127

List of Tables

2.1 Expected event rates for GZK neutrinos in IceCube 12

3.1 Comparison of optical properties in ice and water 27
3.2 Grüneisen coefficients 32
3.3 Relaxation times for energy loss of acoustic waves 36

4.1 IceCube construction phases 44

5.1 Distances and depth of SPATS sensors 58

6.1 Azimuthal spread of pinger samples 71
6.2 Horizontal pinger distances 71
6.3 Final well depth after drilling 85
6.4 Pinger data systematic effects 88
6.5 Acoustic attenuation: depth dependence 94
6.6 Summary attenuation analysis 101
6.7 Summary systematic effects in attenuation analysis 101

7.1 Database parameters 106
7.2 List of Top-Down likelihoods 111
7.3 Number of events in data sample 113
7.4 List of quality selection 115
7.5 Results of single likelihood reconstruction 118
7.6 Product likelihoods, Mean 119
7.7 Product likelihoods, standard deviation 120
7.8 Product of likelihoods 120

1 Introduction

Astroparticle physics (or particle astrophysics) is an interdisciplinary field of physics at the intersection of particle physics, astronomy and cosmology. Its primary goal is the detection of extra-terrestrial elementary particles and their relation to astrophysical phenomena as well as to investigate the structure and nature of matter in the Universe. Historically, astroparticle physics has been established by the first discovery of cosmic rays by Victor Hess in 1912. Since then, cosmic rays have been subject to extensive research and many experiments have measured their energy spectrum and composition. From these measurements it is known that the composition of the cosmic rays reaching Earth is dominated by protons and light nuclei, with a contribution of gamma rays, neutrinos and heavier nuclei. The energy spectrum of the cosmic-ray flux has been measured over a large range, with individual particle energies up to 10^{20} eV. The flux decreases rapidly with energy, reaching about one cosmic ray per square kilometer and century at the highest energies. Up to today, neither the astronomical objects nor the exact mechanisms that are able to accelerate cosmic rays to such high energies have been identified. This is mainly because charged cosmic rays are deflected in the intergalactic magnetic fields and therefore do not directly point back toward their source.

In contrast, neutrinos are considered as ideal cosmic messengers for two reasons. They have no electric charge and hence are not deflected by electromagnetic fields. Secondly, they only interact through the weak interaction and because of their small interaction cross sections, they rarely interact with matter and can travel unobstructed over large cosmic distances. Up to now the only confirmed astrophysical neutrinos besides solar neutrinos were observed from the supernova SN1987A, with energies below 100 MeV.

Various models predict that the sources of cosmic rays are also sources of high-energetic neutrinos, with energies above 1 TeV and beyond. In these models, matter or photon fields in the vicinity of the sources act as a beam dump for accelerated cosmic rays, resulting in an astrophysical neutrino flux that depends on the cosmic-ray acceleration mechanism and the physical conditions at the source. Furthermore, a cosmogenic neutrino flux is predicted from the interaction of the highest-energy cosmic rays with the cosmic microwave background. The detection of these neutrinos would allow to identify the sources of cosmic rays and would help to understand the physical processes taking place in these sources as well as during the propagation of cosmic rays in the universe.

However, the detection of these neutrinos is challenging. One of the advantages of neutrinos as messenger particles – their low interaction probability – also constitutes the main experimental challenge for their detection. In addition, the predicted flux of astrophysical

neutrinos is very small and is steeply falling with energy. Therefore, in order to accumulate sufficient numbers of detected neutrinos within reasonable time, large detector volumes are required. The recently completed IceCube detector is the largest neutrino detector built to date, with an instrumented volume of about $1\,\mathrm{km}^3$. It uses the Antarctic ice at the South Pole as detector medium, measuring the Cherenkov light from charged particles created in neutrino interactions. The primary goals of IceCube are to detect point sources of astrophysical neutrinos and to measure the energy spectrum of the diffuse neutrino flux from unresolved sources. In IceCube, astrophysical neutrinos are principally indistinguishable from the background of neutrinos produced in the Earth's atmosphere, except for their different energy spectrum and angular distribution. Hence, the challenge for the measurement of the diffuse neutrino flux is to search for a small excess of neutrinos at the high-energy tail of the observed energy spectrum, which requires a good energy resolution.

In order to efficiently probe the astrophysical neutrino flux at the highest energies, the IceCube detector is not large enough. Above $10^{17}\,\mathrm{eV}$, the expected rate of detected neutrinos is less than $1\,\mathrm{event/km^3/yr}$ and a detection volume of the order of $10 - 100\,\mathrm{km}^3$ is desirable. However, scaling up the existing design of IceCube by two orders of magnitude is prohibitive in cost. Instead, new detector designs are currently investigated, including alternative detection methods such as the acoustic and the radio detection methods. The acoustic method is based on the thermo-acoustic effect, whereby a neutrino-induced cascade causes local heating of the medium, resulting in an outgoing pressure wave. The acoustic neutrino detection is in an early phase of development and various experimental setups exist, using either ice or water as detector medium. Before an acoustic detector can be built into the ice at the South Pole, the corresponding ice properties have to be known, namely the acoustic attenuation length, the sound speed and refraction, the ambient noise level and the rate of transient events. In order to determine these properties, the South-Pole Acoustic Test Setup (SPATS) has been built at South Pole. SPATS is operating successfully since January 2007 and it was possible to measure or to constrain all acoustic ice properties.

This thesis is structured as follows. In chapter 2, a short overview is given of the current observations and potential sources of high-energy cosmic rays. The production mechanism of high-energetic astrophysical neutrinos, their expected fluxes as well as the current observational limits on their detection are described. In chapter 3, the Antarctic ice as detector medium for the detection of neutrinos is discussed. The different detection methods are described, with a focus on the optical and the acoustic detection method. The IceCube detector and the SPATS array are presented in chapters 4 and 5, respectively.

The acoustic attenuation length has been determined from in-situ measurements with SPATS, using a retrievable transmitter (pinger). The data analysis and the comparison with theoretical predictions are presented in chapter 6.

Finally, a new muon energy reconstruction method based on the Top-Down principle has been developed for the IceCube software framework. The implementation of the method and a proof-of-concept study using Monte-Carlo data are presented in chapter 7.

2 Astroparticle physics

Abstract

Astrophysical neutrinos, i.e. neutrinos with an extraterrestrial origin, are predicted to originate from various cosmic objects as well as being produced through the GZK effect. This is closely connected to the acceleration and propagation of cosmic rays. The sources and the mechanisms by which cosmic rays are accelerated to the highest energies is still under debate. In this chapter an overview of the current observations and potential sources of high-energy cosmic rays is given. A possible production mechanism and the expected fluxes of astrophysical neutrinos are discussed. An overview of the current observational limits is given.

2.1 High-Energy Cosmic Rays

2.1.1 Observation

The atmosphere of the Earth is continuously hit by an extraterrestrial flux of elementary particles, mostly protons and heavier nuclei. These particles are also called *primary* cosmic rays, in contrast to the particles that are created in air showers when primary cosmic rays hit the Earth's atmosphere, also called *secondary* cosmic rays. The primary cosmic-ray spectrum has been measured over many orders of magnitude up to an energy of $10^{20}\,\mathrm{eV}$. For instance, in 1963, a cosmic ray with an energy of $10^{20}\,\mathrm{eV}$ was detected by the Volcane Ranch Array [2]. Cosmic rays with energies above $10^{18}\,\mathrm{eV}$ are referred to as ultra-high-energy cosmic rays (UHECR), though there is no common nomenclature. Figure 2.1 shows the primary cosmic-ray spectrum, measured by various air shower experiments. For energies up to 100 TeV, direct measurements of the primary cosmic rays are possible, e.g. with balloon- or satellite-borne detectors. The flux is steeply falling with energy, and at higher energies only indirect measurements are feasible because of the small rates of detected particles. Such indirect measurements are done with large ground-based detector arrays that detect secondary particles produced in extensive air showers. The observed all-particle cosmic-ray spectrum follows a broken power law

$$\frac{\mathrm{d}N}{\mathrm{d}E} \propto E^{-\gamma}, \tag{2.1}$$

where the spectral index γ changes at certain energies, forming several features in the spectrum, see figure 2.1. At the so-called *knee* at about 4 PeV, the index steepens from about 2.7 to 3. A second knee is discussed for 400 PeV [3]. This change in the observed energy spectrum suggests that there are different kinds of sources of cosmic rays. The bulk of cosmic rays with energies below the knee is usually explained with Galactic sources, whereas the highest energies have

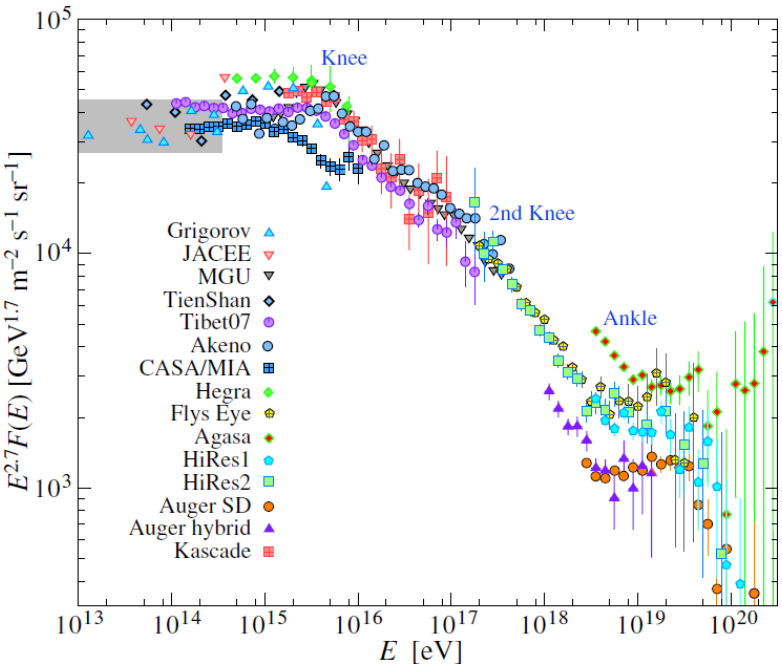

Figure 2.1: *The all-particle spectrum from various air shower measurements, image taken from [1]. The shaded area shows the range of the direct cosmic-ray spectrum measurements. See reference for a comprehensive overview on the individual experiments.*

to originate from extragalactic sources. The mechanism by which cosmic rays are believed to be accelerated is discussed in section 2.1.2.

The spectrum hardens again at the *ankle* at about 3 EeV, where the spectral index changes to about 2.7. For even larger energies, a suppression of the spectrum is observed, as predicted by Greisen, Zatsepin and Kuzmin, and hence is called GZK cutoff. Cosmic rays observed with these energies have to originate within 100 Mpc distance from Earth. The GZK cutoff discussed in more detail in section 2.1.4.

Recent observations by the Pierre Auger Observatory show evidence for an anisotropy in the cosmic-ray arrival directions at the highest energies above the GZK regime [4]. The anisotropy was found as a correlation of the measured events with the highest energy (69 events with $E > 57$ Eev) with a catalog of known astrophysical objects that are discussed as potential cosmic-ray sources. Moreover, no correlation with the Galactic plane was observed, which confirms that these events must have an extra-galactic origin.

2.1.2 Cosmic-Ray Acceleration

The scenarios that have been developed to describe cosmic-ray acceleration can be subdivided into two categories, namely the stochastic (diffuse) and the inductive (direct or one-shot) mechanism. A general discussion of these scenarios is given in [6].

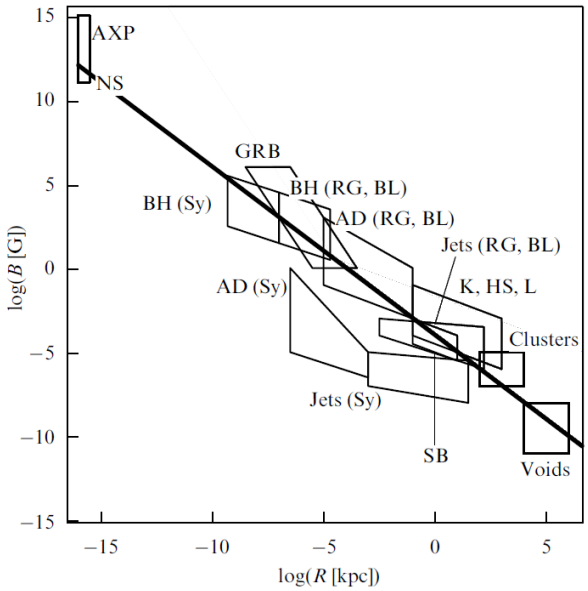

Figure 2.2: *The Hillas criterion on cosmic-ray acceleration in astrophysical sources for* 10^{20} eV *protons. The black line represents the lower limit allowed by the Hillas criterion. The boxes denote parameter regions for the various sources, namely neutron stars (NS), anomalous pulsars (AXP); super-massive central black holes (BH), jets and central region (AD) of AGN, from low-power Seyfert galaxies (Sy) to powerful radio galaxies (RG) and blazars (BL); knots, hot spots and lobes of AGN; starburst galaxies (SB); gamma-ray-bursts (GRB); galaxy clusters and intergalactic voids. Image adapted from [5], see text and reference for details.*

Stochastic Acceleration

In the stochastic mechanism, such as the 'Fermi acceleration' discussed below, cosmic rays are accelerated in small portions by a number of 'encounters' inside an acceleration region. This mechanism gives a consistent explanation for the observed power law spectrum. It is commonly explained by the diffusion of charged particles in turbulent magnetic fields that are carried along with moving plasma. In his original theory, Fermi [7] described acceleration in interstellar clouds. This model has later been modified to describe acceleration at supersonic shock fronts, [8, 9, references therein]. In both cases, the particles gain energy by elastic scatterings in time-dependent inhomogeneous magnetic fields in a plasma. A comprehensive treatment of this mechanism can be found in e.g. [10] In the case of the plasma clouds, the average fractional energy gain $\xi = \Delta E/E$ for a particle with energy E is proportional to the square of the cloud velocity v_c

$$\xi \propto \beta_c^2 = (v_c/c)^2, \tag{2.2}$$

and is therefore called second order Fermi acceleration. The acceleration at shock fronts is called first order Fermi acceleration, because in this case the average energy gain is linearly proportional to the velocity of the shock front and is therefore more efficient

$$\xi \propto \beta_s = (v_s/c). \tag{2.3}$$

An interstellar plasma cloud is expected to have a velocity small compared to the speed of light, $\beta_c \ll 1$, while for shocks much larger velocities are expected. Therefore, a charged particle will gain energy much faster in the first order acceleration.

To gain a high kinetic energy, a particle has to undergo numerous subsequent encounters, e.g. moving back and forth across the shock. At each encounter, there is a probability that the particle escapes and is lost to the acceleration. Calculations, e.g. in [10], performed for the first order mechanism and a mono-atomic gas yield a power law spectrum at the source

$$\frac{\mathrm{d}N}{\mathrm{d}E} \propto E^{-\gamma}, \quad \gamma = 2 + \delta \tag{2.4}$$

where δ is a small positive number. The spectral index γ depends on the particular conditions inside the acceleration region, e.g. the magnetic field configuration, velocity of the shock front, density of the medium, etc.

In order to explain the spectrum with an index $\gamma = 2.7$ observed at Earth, the propagation of the cosmic rays has to be considered. A steepening of the source spectrum is expected from an energy dependent diffusion of the cosmic rays in the galaxy, where cosmic rays with a higher energy have a larger probability to escape the galaxy. A common simple model to explain the steepening of the spectrum is the leaky box [11]. In this model, the cosmic rays propagate freely in a given volume, e.g. the Galaxy, while at the boundaries, the particles have an energy-dependent escape probability.

Inductive Acceleration

In an inductive mechanism, a charged particle is accelerated in a single acceleration process by an electric field and then leaves the acceleration region. This mechanism requires a strong, electric field which for instance can be found near rapidly rotating neutron stars. Compared to the stochastic mechanism, the direct mechanism can explain acceleration on much shorter time scales because the particles only 'interact' once with the accelerator. On the other hand, there is no natural explanation how the observed power law arises from this scenario. It is therefore assumed that the majority of cosmic rays are accelerated in a stochastic mechanism.

2.1.3 Candidates for Cosmic-Ray Acceleration

With increasing energy, it becomes more difficult to confine the cosmic rays in the acceleration region and to continue the accelerating process up to higher energies. This leads to a basic estimate of the maximum energy that can be acquired by a particle inside a given accelerator, called the Hillas criterion. When the gyromagnetic radius of a particle exceeds the size of the accelerator, it escapes and is not further accelerated. Considering first order Fermi acceleration, Hillas [6] derived the condition on the achievable energy E

$$\left(\frac{B}{\mathrm{G}}\right)\left(\frac{R}{\mathrm{pc}}\right) > \frac{0.2}{\beta Z}\left(\frac{E}{10^{20}\,\mathrm{eV}}\right) \tag{2.5}$$

for a particle with charge Z in an accelerator with size R and magnetic field B and the velocity $\beta = v/c$. The maximum energy is further constrained by energy losses from the interaction of

cosmic rays with particles or photons inside the acceleration region. The energy losses depend on the particular conditions in the accelerator, see [12] for a discussion. Figure 2.2 shows a so-called Hillas plot, which is a graphical representation of the Hillas criterion. For this, the typical magnetic field strength and size for a number of potential cosmic-ray sources are plotted with the limit given by equation 2.5. In the following sections, a brief overview is given on potential sources of cosmic-ray acceleration.

Super Nova Remnants

A supernova (SN) occurs at the end of the stellar evolution of massive stars, when the thermal energy released in the nuclear fusion does no longer balance the gravitational force. In type II supernovae the core of the star collapses, leaving a neutron star or a black hole. During the supernova explosion several solar masses of ionized material are ejected with supersonic speed, creating an expanding plasma shell, called supernova remnant (SNR). This leads to a shock wave propagating through the surrounding interstellar medium (ISM) whereby the associated magnetic fields are compressed and pile up in front of the supernova ejecta. The acceleration at these shock fronts is considered a promising mechanism for the acceleration of cosmic rays up to an energy of about 100 TeV [10]. It is believed that the majority of cosmic rays with energies just below the knee are from galactic SNR. Beyond that energy, SNR are not efficient and a different mechanism is required.

Active Galactic Nuclei

In many galaxies, the central core has a higher luminosity than the entire rest of the galaxy. These cores are called Active Galactic Nuclei (AGN), while the galaxy hosting an AGN is called active galaxy. AGNs are the most luminous non-transient sources of electromagnetic radiation in the universe with emissions over a large range of the electromagnetic spectrum. The appearance (and classification) of AGNs depends on the observation angle, e.g. whether the line of sight is obstructed by a surrounding torus of gas and dust. In [13], an overview is given of the classification and the different phenomena connected to AGNs (such as Seyfert galaxies, Blazars and Quasars). It is commonly assumed that the high luminosity is the result of mass accretion by a super-massive black hole in the center of the host galaxy. Because of the conservation of angular momentum, the inflowing mass forms an accretion disc. In some cases, highly collimated outflows of matter, called jets, are observed. In these jets, matter is ejected at relativistic speeds along the rotation axis of the disc into the surrounding medium. The resulting shock fronts at the jets are promising regions for the first order Fermi acceleration. The exact mechanism of these jets is not known, it is believed that they are produced by the rotating magnetic field of the accretion around the black hole [14].

Gamma Ray Bursts

Gamma Ray Bursts (GRB) are extremely luminous explosions causing the emission of large amounts of gamma rays. They are isotropically distributed over the sky and last typically for a few seconds, while the initial burst is followed by a longer afterglow with emissions at longer

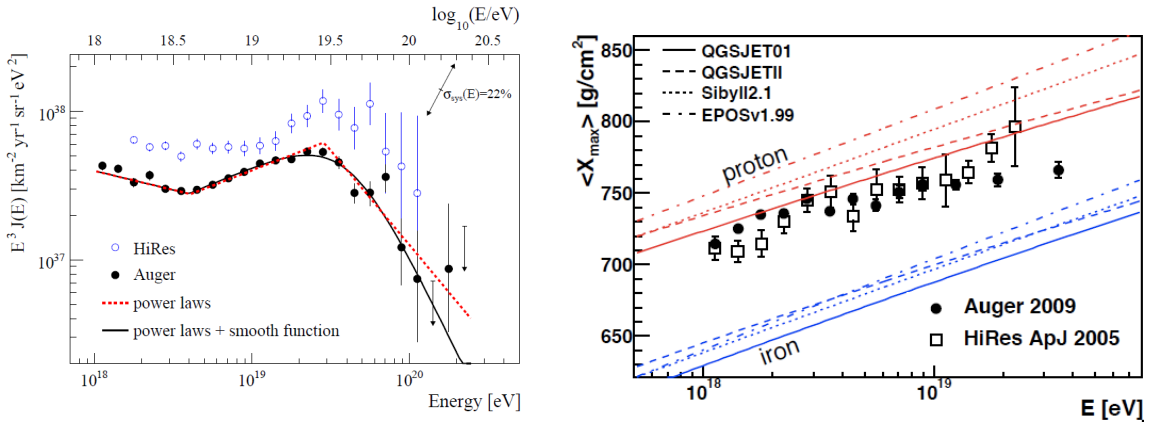

(a) (b)

Figure 2.3: *(a) The cosmic-ray energy spectrum at high energies determined by the Pierre Auger Observatory and the HiRes instrument, from [20]. The spectrum is multiplied with E^{-3} to accentuate the cutoff at high energies which was predicted from the GZK effect. (b) Measurement of the shower depth $X_{\max}$ in comparison with theoretical predictions from various particle interaction models, indicating a transition to a heavy composition at high energies for the Auger data [21].*

wavelengths. There are two subclasses, long ($\gtrsim 2\,\mathrm{s}$) and short-duration ($\lesssim 2\,\mathrm{s}$) GRBs. The exact mechanism of this phenomenon is still under debate. A common explanation for the long GRBs is a stellar collapse scenario where a rapidly rotating star collapses in a supernova explosion to form a neutron star or black hole [15], while the short GRBs are associated with the merger of binary star systems (double neutron stars or a neutron star and a black hole) [16]. The leading model for the observed electromagnetic emissions from long GRBs is the *fireball* model, see [17] for a review. Another scenario considers mass ejecta in the form of discrete "bullets", or "cannon-balls" ejected at relativistic velocities [18]. In both cases, an accretion disk is created after a stellar collapse around the newly formed compact object. When material falls onto the compact object, highly relativistic jets are emitted in opposite directions along the rotation axis. Because of the strong magnetic fields involved, GRBs are possible candidates for the acceleration of cosmic rays and are believed to accelerate cosmic rays up to an energy of $10^{20}\,\mathrm{eV}$ [19]. The observed gamma ray emission is explained by synchrotron radiation and/or inverse Compton scattering in the outflows.

2.1.4 The GZK Effect

In the highest-energy region, the cosmic-ray spectrum is expected to be suppressed by the GZK effect. Soon after the discovery of the Cosmic Microwave Background (CMB), Greisen [22] and Zatsepin and Kuzmin [23] independently predicted a cutoff in the cosmic-ray spectrum. This cutoff is due to the energy loss of cosmic rays by photo-pion production processes in the interaction with the CMB photons:

$$p + \gamma_{\mathrm{CMB}} \rightarrow \Delta^{+} \rightarrow \begin{cases} n + \pi^{+} \\ p + \pi^{0} \end{cases} .$$

This mechanism is significant for cosmic rays with energies above $\mathcal{O}(10^{19}\,\mathrm{eV})$. Therefore, the CMB is opaque for the highest cosmic-ray energies and their flux is attenuated with traveling distance.

If the cosmic-ray composition is dominated by heavy elements, their flux in the trans-GZK regime is expected to be reduced compared to a light composition of mainly protons. This is because if a heavy nucleus such as iron interacts with the CMB photons, it can photo-dissociate into lighter fragments. In this case, the energy of the primary cosmic ray is shared between multiple nucleons. Because these nucleons have a lower energy than the primary particle, the flux at the highest energies is reduced.

The recent observations from the HiRes [24] and Pierre Auger [20] observatories report a cutoff, see figure 2.3(a). However, the confirmation that the observed feature is truly the GZK effect also requires support from measurements of the elementary composition. The HiRes data is consistent with a proton-dominated composition, while the Auger data favors a transition towards a heavier composition, see figure 2.3(b). A possibility to discriminate between the heavy and the proton-dominated composition, is the detection of neutrinos that would be produced from the decay of the charged pions and neutrons in the proton-dominated scenario, see next section.

2.2 High-Energy Neutrinos

Neutrinos can be produced at the sources of cosmic-ray acceleration as well as during the propagation of cosmic rays. In this section, the production mechanism and possible neutrino sources are discussed and a short overview of sources of high-energy neutrinos is given. A wide range of models has been developed to elucidate the production of neutrinos in galactic and extra-galactic objects. These models are closely linked to the acceleration and interaction of cosmic rays and therefore the sources of cosmic rays are primary candidates for sources of neutrinos and vice versa. A cosmogenic neutrino flux is predicted from the GZK effect as well as from the decay of super-massive particles.

2.2.1 Production Mechanism

Neutrinos may be produced from the interaction of cosmic rays with interstellar matter or radiation. These processes involve the generation of secondary pions (and kaons) which subsequently decay and produce neutrinos. The most relevant channels for pion production are nucleon-nucleon scattering and the interaction of protons with the radiation field, called nucleon-meson and photo-meson production respectively

$$p + p(n) \;\rightarrow\; \begin{cases} p + p(n) + \pi^0 \\ p + n(p) + \pi^{\pm} \end{cases}$$

$$p + \gamma \rightarrow \Delta^+ \;\rightarrow\; \begin{cases} p + \pi^0 \\ n + \pi^+ \end{cases}$$

From these processes, the ratio of charged to neutral pions is 1 : 1. While the neutral pions decay into two photons, the charged pions and kaons decay dominantly into muons which in turn produce muon and electron neutrinos (and antineutrinos)

$$\begin{aligned} \pi^0 &\longrightarrow \gamma\gamma \\ \pi^+ &\longrightarrow \mu^+ + \nu_\mu, \quad \mu^+ \to e^+ + \nu_e + \bar{\nu}_\mu \\ \pi^- &\longrightarrow \mu^- + \bar{\nu}_\mu, \quad \mu^- \to e^- + \bar{\nu}_e + \nu_\mu. \end{aligned}$$

Hence, the resulting neutrino flavor ratio at the source is $\nu_e : \nu_\mu : \nu_\tau = 1 : 2 : 0$. Because of neutrino flavor oscillations, this ratio changes with the traveling distance. For a large distance, the expected ratio is $\nu_e : \nu_\mu : \nu_\tau = 1 : 1 : 1$.

The secondary neutrons produced in the cosmic-ray interaction decay, resulting in an additional contribution of electron neutrinos

$$n \longrightarrow \nu_e + p + e^-.$$

For all neutrinos produced at the acceleration site, the energy spectrum is not affected by the propagation effects on the cosmic rays and therefore follows the cosmic-ray source spectrum with an spectral index $\gamma = 2 + \delta \approx 2$.

2.2.2 Neutrinos from Cosmic-Ray Sources

The astrophysical objects that are thought to accelerate cosmic rays to high energies, are discussed in section 2.1.3. There are in principle two different acceleration scenarios, a purely leptonic scenario and a hadronic one. In the hadronic scenario, protons and heavier nuclei are accelerated to high energies. The protons then can interact with the surrounding matter or intense radiation fields at the source and produce pions which in turn lead to the production of neutrinos and gamma rays. Therefore, the sources of high-energetic protons are possible sources for neutrinos. In a purely leptonic scenario on the other hand, only electrons are accelerated. These electrons can emit gamma rays through Bremsstrahlung or inverse Compton scattering, but in this scenario no protons are accelerated and no neutrinos are produced.

In order to estimate the neutrino flux from astrophysical sources, one can use the measured cosmic-ray flux and estimate the matter and photon density at the source to calculate the neutrino production rate. Another method is to use the observed high-energy photon flux assuming that the photons are from π^0 decay and not produced in the leptonic scenario described above. Assuming that half of the produced pions are charged or neutral respectively, this leads to an estimate of the number of charged pions and thus to an estimate of the neutrino flux. In the following part of this section, a short overview on potential neutrino sources is given. The flux predictions from the various models are shown in figure 2.5 together with current observational limits.

The observed high-energy cosmic-ray flux implies a model-independent upper bound on the flux of high-energy neutrinos, known as the Waxman-Bahcall bound [25, 26]). It is calculated for astronomical sources that are, like GRBs or jets of AGN, “optically thin” to photo-meson

interactions of protons. Here, the pions produced in pp or pn collisions rather decay than interact and therefore produce neutrinos. The Waxman-Bahcall flux is calculated by requiring that the neutrino energy production rate in any source cannot exceed the cosmic-ray energy production rate derived from observations at highest energies. Assuming a generic cosmic-ray spectrum at the source with $\mathrm{d}N_{\mathrm{CR}}/\mathrm{d}E_{\mathrm{CR}} \propto E^{-2}$, as typically expected for Fermi acceleration, the Waxman-Bahcall bound for the differential neutrino energy spectrum is

$$E_\nu^2 \frac{\mathrm{d}N_\nu}{\mathrm{d}E_\nu} < \frac{t_H\, c\, \xi_Z}{16\pi} E_{\mathrm{CR}}^2 \frac{\mathrm{d}^2 N_{\mathrm{CR}}}{\mathrm{d}E_{\mathrm{CR}} \mathrm{d}t} = \begin{cases} 1.5 \\ 2.25 \end{cases} \times 10^{-8}\,\mathrm{GeV cm^{-2} s^{-1} sr^{-1}} \tag{2.6}$$

with the Hubble time t_H and a correction factor ξ_Z that accounts for the evolution of sources in dependence of the redshift, and the energy E and particle number N for cosmic rays and neutrinos. The lower and higher values are without and with source evolution, respectively.

The jets of AGN are potential candidates for the cosmic-ray acceleration and $p\gamma$ or $pp(n)$ interactions and the subsequent neutrino production from pions. In [27] Becker, Biermann and Rhode calculate a neutrino flux for the jets of FR-II radio galaxies. In these calculations, the observations in the radio band from these objects is used to normalize the flux, by assuming a relationship between the neutrino flux with the radio luminosity of the jets.

Mücke et al. [28] calculated a neutrino flux for BL-LACs, that are optically thin to photon-neutron interactions, assuming that protons are produced by the decay of escaping neutrons. In this model, a neutrino flux arises which is proportional to the observed cosmic-ray flux. For GRB, an average neutrino spectrum is calculated by Razzaque et al. [29], connecting the gamma-ray emission to the observed cosmic-ray flux.

In optically thick sources, the high-energetic γ from π^0 decay interact with the surrounding medium and cascade into lower energies. In this case, the observed diffuse extra-galactic gamma ray flux can be used to normalize the neutrino flux, assuming a hadronic scenario. This has been done e.g. by Mannheim [30] and Stecker [31], using the data collected by the Compton Gamma Ray Observatory.

2.2.3 Cosmogenic (GZK) Neutrinos

The GZK effect (section 2.1.4) for cosmic rays implies the existence of a guaranteed cosmogenic neutrino flux, as the energy of the ultra-high-energy cosmic rays is converted to neutrinos (and photons and hadrons) with lower energy. The existence of such neutrinos was first suggested in [33] and the detection of a cosmogenic (or GZK) neutrino flux is one of the main motivations for the search of high-energetic neutrinos. A calculation of the expected neutrino flux has been performed by various authors, for instance by Engel, Seckel and Stanev [34]. The calculated flux depends on the assumed cosmic ray injection spectrum and the cosmological source evolution. However, these calculations are based on a pure proton cosmic-ray composition. If a substantial fraction of the cosmic-ray primaries are heavy nuclei, the flux at high energies is reduced by photo-dissociation. In order to contribute to GZK neutrino production, the photo-disassociated remnants must exceed the GZK threshold. Therefore, the number of particles available for the GZK mechanism is lower than in the case for a pure proton composition, leading to a smaller contribution to the neutrino flux.

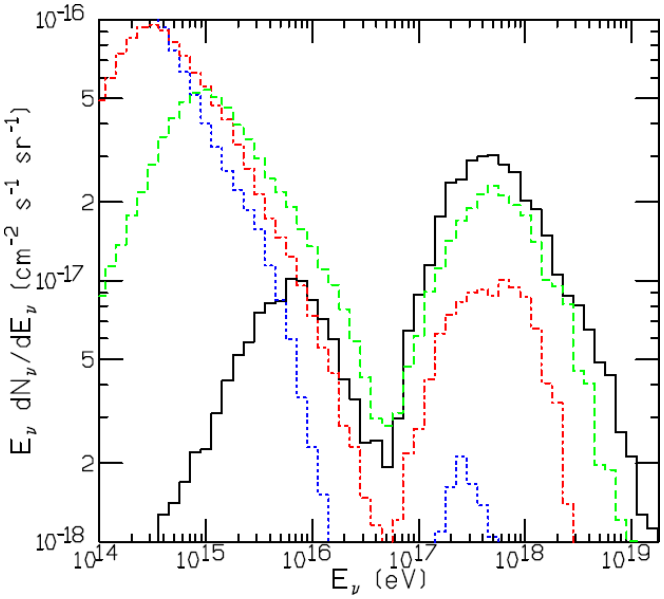

Figure 2.4: *The all-flavor neutrino spectrum produced in the interaction of cosmic rays with the Cosmic Microwave Background. Shown are the calculations for heavy nuclei helium (green, dashed), oxygen (red, dot-dashed) and iron (blue, dots) compared to the result for protons (black, solid line) [32]. For heavy nuclei, the flux is reduced at higher energies.*

The expected GZK neutrino flux has been calculated for various heavy nuclei e.g. by Hooper et al. [32]. In figure 2.4, the all-flavor GZK neutrino flux for different nuclei is shown. These calculations were performed assuming a pure proton, helium, oxygen or iron composition, respectively. While the high-energetic neutrino flux is suppressed for heavy nuclei, there is an additional contribution of $\bar{\nu}_e$ from decaying neutrons at lower energies. An estimate of the expected event rate of GZK neutrinos in the IceCube detector has been calculated in [32] and is shown in table 2.1. The predicted differential neutrino fluxes for a compilation various models are shown in figure 2.6.

Table 2.1: *The expected event rates of GZK neutrinos per year in IceCube. Shown are the results for protons and various heavy nuclei for two different detection thresholds for the neutrino-induced muons and for neutrino-induced cascades with threshold [32].*

nucleus	cascade $E > 1\,\mathrm{PeV}$	muon $E > 1\,\mathrm{PeV}$	muon $E > 10\,\mathrm{TeV}$
proton	0.57	0.72	1.16
helium	0.42	0.50	0.80
oxygen	0.19	0.23	0.73
iron	0.036	0.042	0.17

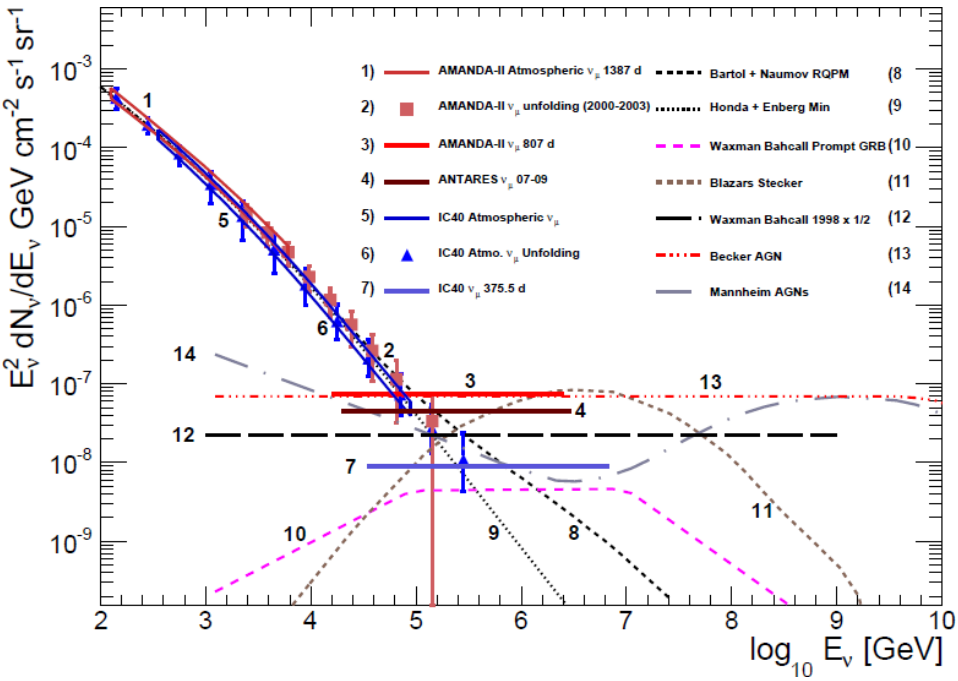

Figure 2.5: *Upper limits on the astrophysical muon-neutrino flux shown along with theoretical model predictions of muon neutrinos from various sources. Shown is the currently most stringent limit on the diffuse neutrino flux, set by IC40 [38]; see text and reference for details.*

2.2.4 Top-Down Scenarios

A high-energy neutrino flux is also predicted through the decay of super-massive elementary particles related to some grand unified theories (GUT). These particles could be released from topological defect relics which could have formed during spontaneous breaking of GUT symmetries in the early Universe. This scenario is called *Top-Down*, as it involves the decay of exotic super-massive particles into lighter ones, whereas in the *Bottom-Up* scenario particles are accelerated to higher energies. Calculations of the expected neutrino flux for different scenarios are discussed e.g. in [35].

Another possible source of neutrinos is the Z-burst model, as discussed in [36]. In this model, hypothetical high-energy neutrinos emitted by various sources interact with the cosmic background of relic neutrinos from the Big Bang and produce Z bosons. The Z boson decays in 69.9% of all cases into hadronic jets. The jets contain large numbers of pions which decay into neutrinos with lower energies, but also contain γ rays and nucleons. Hence, the Z-burst mechanism has been proposed as a possible explanation for the highest energy cosmic rays in the trans-GZK regime. Numerical calculations of the expected fluxes are presented in [37].

2.2.5 Current Limits on the Neutrino Flux

While the fluxes from individual point sources are possibly too small to be detected, the superposition of all astrophysical neutrinos from many sources may give rise to a detectable diffuse flux. On cosmic scales, this flux is isotropic, because of the uniform distribution of the

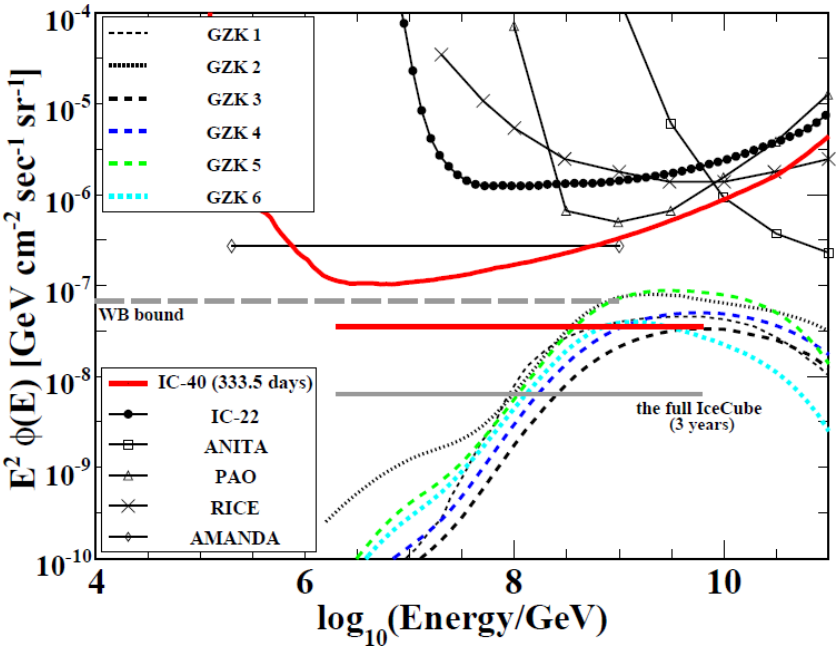

Figure 2.6: *The all flavor neutrino flux differential limit and the E^{-2} spectrum integrated limit from the IceCube-40 extremely-high-energy (EHE) analysis [39] (red solid lines) in comparison with the upper limits by the Pierre Auger Observatory (PAO), RICE, ANITA, Amanda and the previous result from Ice- Cube-22, alongside with the predicted fluxes from various GZK models, see reference for details. Also shown for reference are the estimated limit for three years of observation with the full* IceCube *detector and the Waxman-Bahcall bound with cosmological evolution.*

assumed sources in the universe.

The most recent experimental results of the astrophysical neutrino flux in the high-energy regime are shown in figures 2.5, 2.6 and 2.7 together with the various model predictions. So far, no astrophysical neutrinos in this energy range have been detected and limits on the diffuse fluxes have been calculated by various collaborations. The most stringent upper limit on an integral diffuse neutrino flux in the range of $10^4 - 10^7$ GeV has been set by the IceCube collaboration [38]. The data from a full year of data from the half-completed IceCube detector (IC40) showed no evidence for astrophysical neutrinos and are consistent with a background of atmospheric neutrinos. The calculated limit is shown in figure 2.5 alongside with various predicted flux models. The ANTARES [41] and the AMANDA [42] collaborations also published limits, which are less constraining than the limit set by IceCube.

The IceCube collaboration also reported an upper limit on the all-flavor neutrino flux for neutrinos with energies exceeding 10^7 GeV [43], using the data collected between April 2008 and May 2009 with IC40. This limit is already capable to constrain various cosmogenic neutrino flux models and a significant improvement is expected for the full IceCube detector, see figure 2.6. Upper limits in this energy range have also been presented by various experiments using the radio-Cherenkov method, namely RICE [44], ANITA [45], FORTE [46] and GLUE [47], see figures 2.6 and 2.7.

The Pierre Auger Observatory (PAO) and the HiRes detector are sensitive to upward-

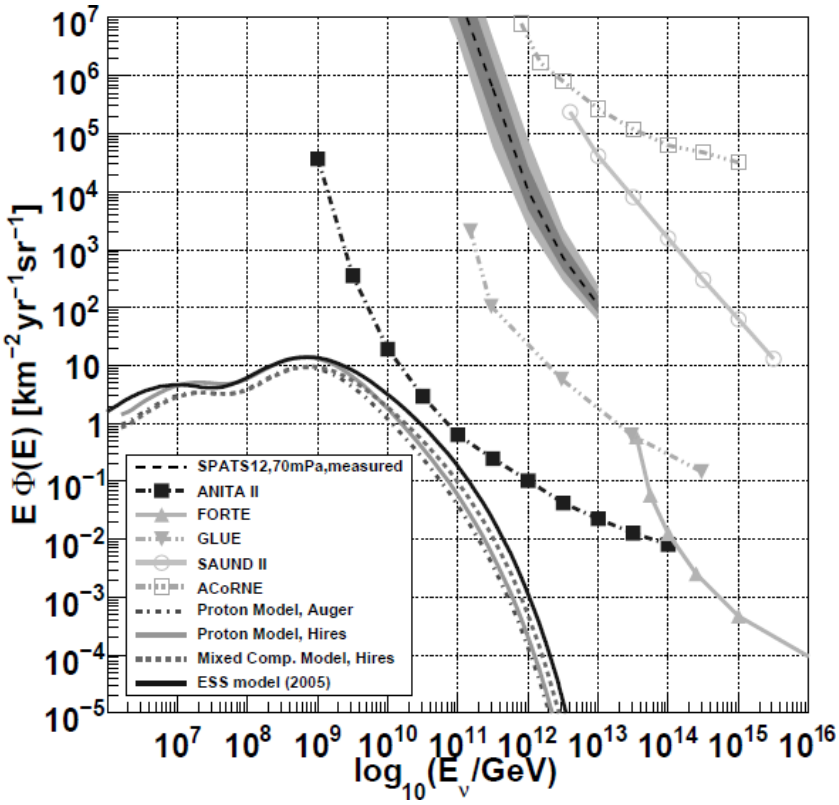

Figure 2.7: *Limits on the high-energy neutrino flux from various experiments that use either the radio (ANITA II, FORTE, GLUE) or the acoustic (SPATS, SAUND, ACoRNE) detection method [40] and section 3.6.*

going, Earth-skimming neutrinos in the EeV range. Neutrinos interacting in the Earth's crust produce particle showers that are detectable by these experiments after exiting the Earth into the atmosphere. No evidence for such neutrinos has been found and upper limits have been calculated by PAO [48] and HiRes [49] respectively, see figure 2.6. In the acoustic neutrino detection channel (section 3.4), the first upper limit has been set by the SAUND experiment [50]. The ACoRNE [51] and the SPATS [40] collaborations also have set limits for the acoustic method, see figure 2.7. However, the acoustic detection is still in an early phase of development and these limits are not competitive with the above limits.

2.3 The Atmospheric Background

Atmospheric Neutrinos

The interaction of cosmic rays in the Earth's atmosphere leads to extensive air showers. Similar to the production of astrophysical neutrinos, charged pions and kaons are generated, which subsequently decay into muons and neutrinos. For energies above $\sim 100\,\mathrm{TeV}$, also large numbers of charmed mesons should be produced. The neutrinos which are expected to arise from the decay of these charmed mesons are called *prompt* atmospheric neutrinos, whereas the neutrinos

from the pion and kaon decay are called *conventional* atmospheric neutrinos. The prompt and conventional contribution to the atmospheric flux have different energy spectra and angular dependence. These have been calculated in three-dimensional Monte-Carlo calculations by various authors, for instance by Honda et al. [52] or at the Bartol research institute [53].

The different energy spectra are explained by the different lifetimes of the involved mesons. Only when the mesons decay before they interact with the atmosphere, neutrinos are produced. The ratio of the interaction probability and the decay probability is proportional to the pion (kaon) energy. Hence, the resulting neutrino spectrum steepens from the primary particle spectrum by one power of energy. Moreover, the conventional spectrum has a characteristic angular dependency due to the different column densities for different zenith angles. Close to the horizon, the mesons travel a longer distance through the relatively sparse upper layers of the atmosphere. Hence, their interaction probability is smaller and they have a higher chance to decay and to produce neutrinos, resulting in an increased flux close to the horizon. In contrast, charmed mesons have a much shorter lifetime ($\mathcal{O}(10^{-13}\,\mathrm{s})$) compared to charged kaons or pions ($\mathcal{O}(10^{-8}\,\mathrm{s})$), so they mostly decay before interacting. Their spectrum follows that of the primary cosmic rays while their angular distribution is isotropic.

For the search of astrophysical neutrinos, the atmospheric neutrinos are an irreducible background and on detector level both are indistinguishable from each other, except for the different energy spectrum and angular distribution. On the other hand, atmospheric neutrinos themselves are of interest for a variety of studies. One prominent example is the search for flavor oscillations. The neutrinos arrive from different directions and therefore have a different traveling distance through the Earth, allowing to investigate flavor disappearance over a large baseline.

Atmospheric Muons

The muons produced in air showers have a mean live time of about $2\,\mu$s in their rest frame, which enables them to reach Earth's surface and also underground particle detectors. The atmospheric muon flux has been calculated in Monte-Carlo simulations, see e.g. [54]. For large zenith angles, most of the muons have stopped or decayed before reaching a detector, hence the muon flux decreases with zenith. Below the horizon, the Earth acts as a shield against air showers. Because of their large numbers they constitute a major background for neutrino detection. In neutrino detectors such as IceCube, this background can be significantly reduced by "looking downward", i.e. rejecting particle tracks that have a reconstructed arrival direction from above the horizon. The atmospheric muon flux has been measured with the IceCube detector for energies $E_\mu > \mathcal{O}(1\,\mathrm{TeV})$ [55], showing a good agreement with the theoretical expectation.

3
Detection of Neutrinos at the South Pole

Abstract

The polar ice sheet at the South Pole offers unique possibilities as a detector medium for a large-scale neutrino detector. After a general overview of the physical properties of the South Pole ice, the principles of various detection techniques are explained and discussed, with a focus on optical and acoustic detection. An overview of the currently operational high-energy neutrino detectors is given for each of the respective methods.

3.1 The Ice at the South Pole

There are eleven known crystalline phases of water. Most of these are limited to rather extreme environments (see figure 3.1 and [56, 62]). Almost all natural occurrences of ice on earth such as in snow or glaciers are in the ice-Ih phase, with smaller amounts of cubic or amorphous ice in the upper atmosphere. Ice-Ih has a hexagonal structure with a density of $0.9167\,\mathrm{g/cm^3}$ at $0\,^\circ\mathrm{C}$, which is slightly less dense than water at the same temperature. Large volumes of ice are usually poly-crystalline, as the natural growth from precipitation leads to a random orientation of mono-crystalls of different sizes.

The antarctic continent is almost completely covered with a huge ice sheet, with a maximum thickness of 4000 m and an average thickness of 1500 m. At the geographical South Pole, the ice is about 2800 m deep. Even though there is a continuous precipitation with an annual rate of 2.5 cm/year (which is rather low and qualifies Antarctica as a frozen desert), the ice sheet is not growing. Instead, the pressure on the deeper ice layers causes a plastic flow toward the coast with a speed of about 10 m/a.

The accumulating snow becomes increasingly dense with depth due to the pressure of the overlaying layers until the maximum density is reached at $\sim 200\,\mathrm{m}$, see figure 3.2(a). The upper part with lower density is called firn ice and still contains many air bubbles. With increasing depth, the snow is compactified as the snow crystals are fused by sintering (see e.g. [63]) and the gaseous inclusions are converted into solid air-hydrate clathrate crystals [64]. The ice below the firn is called bulk ice.

Evaluation of deep core drillings such as the one taken near Byrd station [58, 65] show that the mean air bubble diameter decreases monotonically from $\sim 1\,\mathrm{mm}$ near the surface to $\sim 0.1\,\mathrm{mm}$ at a depth of 1400 m with an average number density of $n_0 = \mathcal{O}(100\,\mathrm{cm^{-3}})$. The clathrate concentration in Antarctic ice has first been measured by [66], indicating that air bubbles and clathrate crystals coexist over a depth range of several hundred meters until all air bubbles are transformed at a depth around 1500 m.

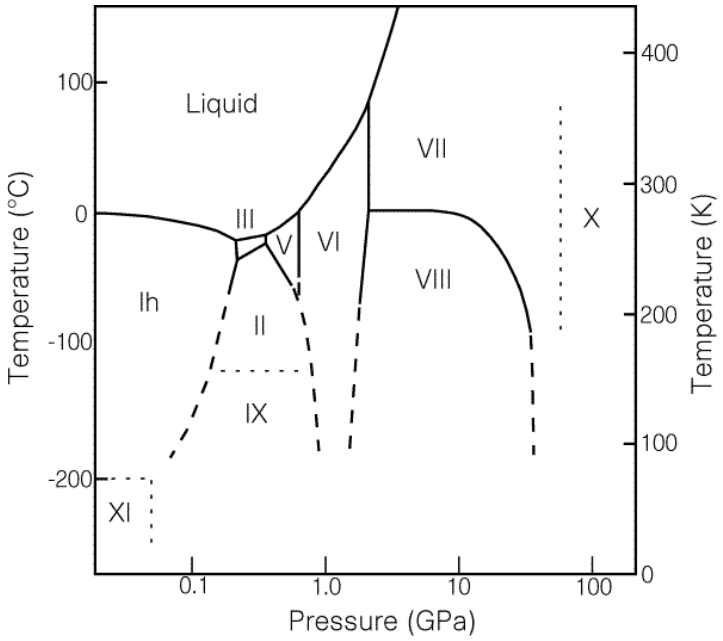

Figure 3.1: *Phase diagram of water, illustrating the different crystalline phases of water ice [56]. Ih is the form of most natural occurrences in snow and ice. In the deep ice at South Pole, the pressure is of the order of* 1 MPa *and the temperatures are from about* $-50\,^{\circ}$C *to* $-20\,^{\circ}$.

The surface temperature is about $-50\,^{\circ}$C during the southern winter, while the temperature increases steadily with depth due to the natural heat of the earth crust [60]. Figure 3.2(b) shows the temperature profile for the ice at the South Pole. Due to its low heat conductivity ($\sim 2 - 3\,\mathrm{Wm^{-1}K^{-1}}$), the bulk ice will only slowly react to climatic variations. Below $\sim 50\,$m, the ice is nearly unaffected by the short-term seasonal change of the surface temperature.

Due to the remoteness of the location and the extreme climate conditions, the number of anthropogenic and natural sources of radio, sound or light emissions is very low. Consequently the South Pole has become of interest for particle physics experiments, that require large detector volumes with a small environmental background.

In the following the use of South Pole ice as a detector medium for neutrino detection is discussed. In principle there are three different detecting channels, optical, acoustic and the radio detection, where each of these methods requires knowledge of the specific ice properties. The optical ice properties are discussed in section 3.3. The deep ice below the firn is relatively transparent with an optical absorption length of $\sim 100\,$m.

With the construction of various detectors, such as the IceCube detector, the optical neutrino detection channel has been established, this is discussed in section 3.3 and chapter 4. For both of the other two neutrino detection methods - radio and acoustic detection - there are currently ongoing feasibility and design studies including in-situ measurements of the ice properties. Section 5.2 summarizes the most recent results of the South Pole Acoustic Test Setup (SPATS) while the determination of the acoustic attenuation length is subject of chapter 6. Section 3.5 gives a brief overview of the radio detection channel.

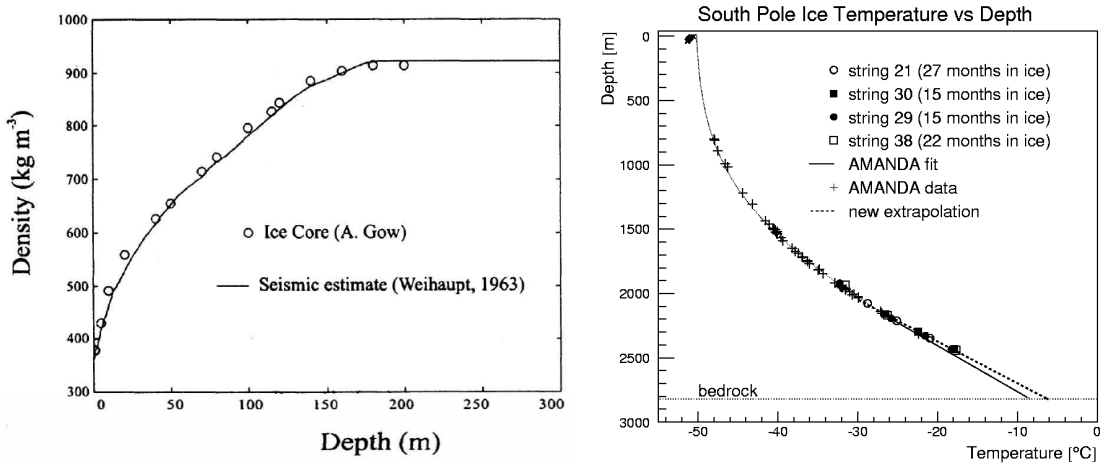

(a) (b)

Figure 3.2: *(a) Density profile of the antarctic ice, illustrating the transition from firn to bulk ice [57]. The graphic combines results from bore hole [58] and seismic measurements [59]. (b) Vertical temperature profile combining data from bore hole measurements of AMANDA (2001) and* IceCube *(2007) [60], [61].*

3.2 Neutrino Interactions in Ice

3.2.1 Inelastic Neutrino Collisions

Because of their small interaction cross sections, and small expected fluxes, a direct detection of high-energetic neutrinos is not feasible. Instead, they are detected by indirect methods where the products of rare neutrino interactions are observed. Neutrinos can interact with the nuclei of the target material via deep inelastic scattering (DIS), either by the neutral current (NC) or charged current (CC) weak interaction

$$\nu_l + N \xrightarrow{Z^0} \nu_l + X \quad (NC)$$
$$\nu_l + N \xrightarrow{W^\pm} l + X \quad (CC).$$

Here, l and ν_l are a lepton and a neutrino of the same flavor, N is the nucleus and X is the hadronic remnant after the interaction. The neutral and charged current interactions are intermediated by Z^0 and $W^\pm$ bosons, respectively. For energies above 10 GeV, the energy transfer to the nucleus is sufficient to disintegrate it. The cross section for both reactions is shown in figure 3.3(a). The hadronic fragments X also interact with the medium, producing a hadronic cascade. For a neutral current neutrino interaction, only this cascade is observed, whereas in the charged current interaction, a charged lepton of the same flavor is created. The lepton continues roughly with the initial neutrino direction and the average angular deviation is given by the approximation [68]

$$\Delta\psi_{\nu l} = \frac{0.7^\circ}{(E_\nu/TeV)^{0.7}}. \tag{3.1}$$

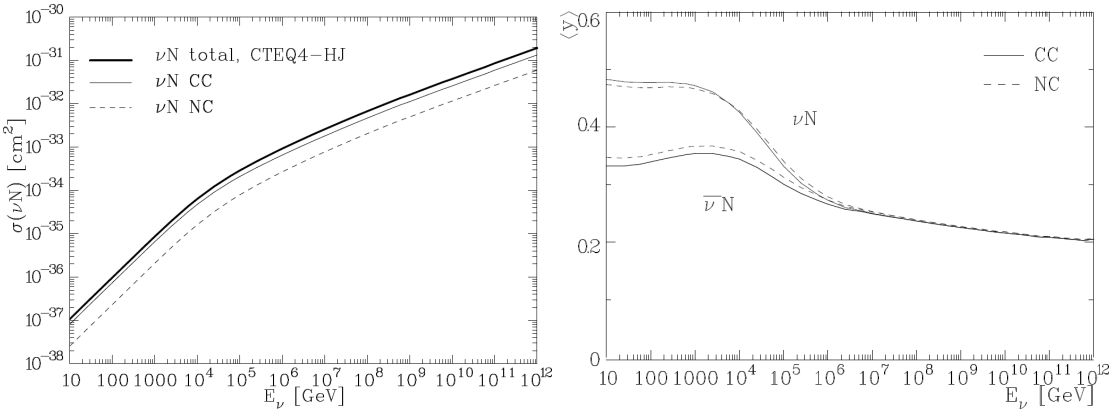

(a) (b)

Figure 3.3: *The cross sections (a) and the mean in-elasticity parameter $\langle y \rangle$ (b) for charged (CC) and neutral current (NC) neutrino-nucleon scattering at high neutrino energies [67].*

This means that there is an inherent uncertainty on the original neutrino direction in the measurement of the lepton direction. The deviation depends on the neutrino energy E_ν and due to the increased relativistic boost of the lepton the deviation is smaller at larger energies. The energy fraction that is transferred to the hadronic fragments is described by the in-elasticity parameter.

$$y = \frac{E_X}{E_\nu} = \frac{E_\nu - E_l}{E_\nu}. \tag{3.2}$$

In the EeV range, the mean in-elasticity is $\langle y \rangle \approx 0.2$, see figure 3.3(b). This means, that on average the lepton carries 80% of the primary neutrino energy.

3.2.2 Lepton Signatures

The leptons produced in the charged current neutrino interaction lose energy when they propagate through the detector medium. Due to different contributions to their energy losses, the three lepton flavors will produce distinguishable event topologies. In this section, the different energy loss mechanisms are discussed, with a focus on the energy loss of a muon.

Muon

The dominant processes, by which a high-energy muon loses energy are ionization, pair production, bremsstrahlung, and photo-nuclear interactions. The energy loss by ionization is due to numerous collisions with the atoms in the material with small energy depositions and is therefore called a continuous energy loss. The other three processes are called stochastic energy losses, since they occur randomly along the muon track and lead to large, fluctuating energy deposits. The different contributions to the muon energy loss are shown in figure 3.4 and are:

- **Ionization:** In matter, the muon loses energy by ionization and excitation of atoms in single collisions. The mean energy loss per unit length of a heavy particle with charge

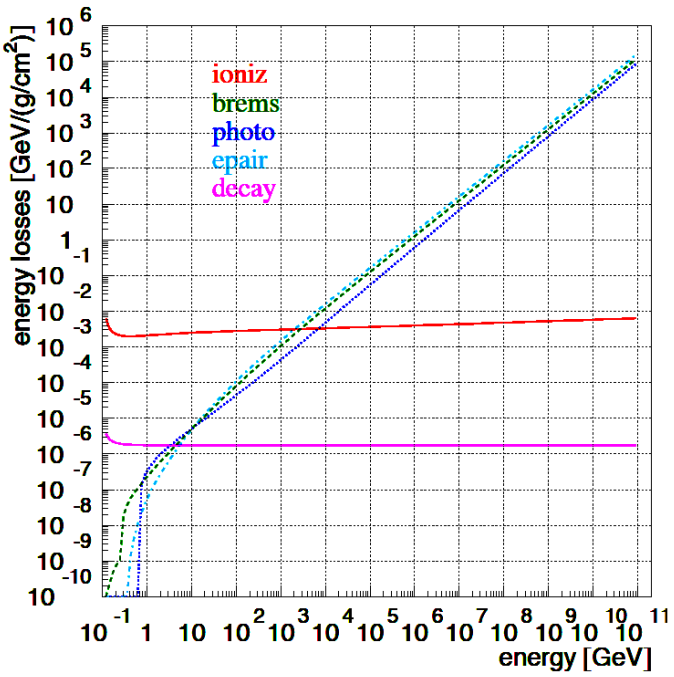

Figure 3.4: *The main contributions to the mean muon energy loss in ice as a function of the energy of the muon, calculated with a dedicated muon propagation simulation in ice, image adapted from [69].*

ze is described by the Bethe-Bloch-Formula [70]

$$-\left\langle \frac{dE}{dx} \right\rangle \propto \frac{\rho\, Z}{A} \frac{z^2}{\beta^2} \left[\frac{1}{2} \ln \left(\frac{2 m_e c^2 \beta^2 \gamma^2 T_{\max}}{I^2} \right) - \beta^2 - \frac{\delta}{2} \right] \tag{3.3}$$

with the density ρ, charge Z and mass number A of the medium, a density correction term δ, and the relativistic factors β and γ. $T_{\max}$ is the maximum kinetic energy which can be transferred to an electron in a single collision and I is the mean excitation energy of the target. The energy loss per collision is small and the ionization can be regarded as continuous along the track. However, the mean value given by equation 3.3 also includes the rare stochastic production of delta electrons with large energy deposits in single-collisions.

- **Pair production:** The electron pair production is the dominant muon energy loss mechanism above about 1 TeV, see figure 3.4. The minimum energy for this process is given by the rest masses of the created pair and is about 1 MeV for electron-positron pairs and about 210 MeV for muon pairs.

- **Bremsstrahlung:** A charged lepton which is deflected in the electric field of a nucleus, emits a bremsstrahlung photon. This is a stochastic process and the average energy loss is proportional to the lepton energy. As the energy loss is reverse proportional to the fourth power of the mass, muons lose less energy than electrons, with $(m_e/m_\mu)^4 \approx 5 \times 10^{-10}$.

- **Photo-nuclear reactions:** Here, a virtual photon transfers enough energy to a nucleus to disintegrate it. These interactions are rare compared to pair production, but lead to

a stochastic energy loss with large energy deposits.

The contributions of the different processes as a function of muon energy are shown in figure 3.4. The total muon mean energy loss is described by [70]

$$-\left\langle \frac{\mathrm{d}E_\mu}{\mathrm{d}x} \right\rangle = a + b\,E_\mu. \tag{3.4}$$

The coefficient a describes the energy loss by ionization whereas b summarizes the stochastic processes. For ice, both a and b are slowly varying with energy and the typical values are [69]

$$a \approx 0.26\,\mathrm{GeV/mwe} \tag{3.5}$$

$$b \approx 3.57 \times 10^{-4}\,\mathrm{mwe}^{-1}, \tag{3.6}$$

where mwe denotes meter water equivalents. The muon travels a certain distance until it is stopped or decays, the mean range x_0 of a muon with initial energy E_0 is given by solving equation 3.4:

$$x_0 \approx \frac{1}{b}\,\ln(1 + E_0/E_{\mu c}), \quad E_{\mu c} = \frac{a}{b} \approx 730\,\mathrm{GeV}, \tag{3.7}$$

where $E_{\mu c}$ is the critical energy, defined as the energy for which stochastic and ionization energy losses of the muon are equal. The energy as function of the traveling distance is

$$E(x) = E_0 \mathrm{e}^{-bx} - \frac{a}{b}\left(1 - \mathrm{e}^{-bx}\right), \tag{3.8}$$

with the energy E_0 at position $x = 0$, where x is the traveling distance in mwe. In ice, a muon with energy 1 TeV will on average travel about 2 km before it is stopped. Below the critical energy $E_{\mu c}$, the energy loss is almost independent of energy and dominated by ionization. Above the critical energy, the stochastic processes dominate the energy loss and the relationship between the energy loss per unit length becomes approximately linear with the muon energy. The stochastic processes produce electromagnetic cascades, or in the case of the photo-nuclear interactions hadronic cascades. Due to the high relativistic boost, the secondaries produced in these cascades are closely aligned to the muon track direction.

The energy loss from Cherenkov radiation is negligibly small compared to the described energy loss processes, see section 3.3.1. However, it is the basis for the optical detection of charged leptons in ice (section 3.3). The charged particles created in the secondary cascades also contribute to the light emission, enhancing the light yield of the muon track.

Electron and Tau

An electron initiates an electromagnetic cascade at the neutrino interaction vertex, see section 3.2.3. In IceCube, this cascade is inseparable from the initial hadronic cascade.

The energy loss of tau leptons is also described by equation 3.4, but with different coefficients (a, b). Taus are much heavier than muons ($m_\tau \approx 17 m_\mu$) and lose less energy per unit length. After an average lifetime in the rest frame of about 0.29 ps, the tau decays into a tau neutrino and a virtual W-boson which then decays either hadronically or leptonically, creating a second cascade. Both cascades produce Cherenkov light, leading to the characteristic

double-bang topology, which in principle allows a good identification of taus. However, only for high energies and if the ν interaction and the decay happen inside the detector, the two cascades can be separated - for a tau with energy of 1 PeV the distance is about 50 m. For smaller energies the two cascades overlap and become more and more indistinguishable.

3.2.3 Cascades

In this section, an overview is given on the development of electromagnetic and hadronic cascades inside a thick absorber. The development of the cascade and the energy deposition inside the medium are relevant for the acoustic and radio detection method.

Electromagnetic Cascades

An electromagnetic cascade is initiated when a high-energy electron (or photon) interacts with the target material. The electron loses energy predominantly by bremsstrahlung and the bremsstrahlung photons can in turn create e^+ e^- pairs by pair production. Both processes repeat, leading to a rapid growth of the particle number, in which the secondaries generate many electrons and photons at lower energy. The cascade eventually stops when the average particle energy falls below the critical energy E_C, at which the energy loss due to ionization is equal to the energy loss by bremsstrahlung.

Another characteristic parameter is the radiation length X_0, which is 7/9 of the mean free path for electron pair production by a high-energy photon. The radiation length has been calculated for various materials and tabulated in [71]. Typical values of the critical energy and the radiation length of an electron in ice are:

$$E_C \approx 92\,\mathrm{MeV}, \qquad X_0 = 36.08\,\mathrm{cm}. \tag{3.9}$$

Hadronic Cascades

A hadronic cascade is produced by high-energy hadrons, e.g. the hadronic fragments from the deep-inelastic neutrino interactions with a nuclear target. Similar to the electromagnetic cascades, the secondary particles also interact with the material thus producing a cascade. The cascade primarily consists of nucleons and pions. While the nucleons and the charged pions live long enough to re-interact, the neutral pions quickly decay into two photons ($\pi^0 \to 2\gamma$), initiating an electromagnetic sub-cascade. Therefore, hadronic cascades consist of a central hadronic core accompanied by electromagnetic contributions. The central core roughly maintains the direction of the initial neutrino as the average transverse momentum is small $\mathcal{O}(100\,\mathrm{MeV})$. The typical length scale of the longitudinal development of a hadronic cascade is described by the nuclear interaction length, which for water is roughly

$$\lambda_I \approx 35\,\mathrm{gcm}^{-2}\,A^{1/3} \approx 75\,\mathrm{cm}. \tag{3.10}$$

Cascade Development and Energy Deposition

In a homogeneous medium, the energy deposition by a cascade can be assumed to be axially symmetric around the initial neutrino direction. Therefore, the description of the cascade can

be split into a longitudinal and a lateral part. For electromagnetic cascades, the longitudinal part of the energy deposition can be parametrized with a Gamma distribution [70]

$$\frac{\mathrm{d}E}{\mathrm{d}t} = E_0\, b\, \frac{(bt)^{a-1}\ \mathrm{e}^{-bt}}{\Gamma(a)}, \quad t = X/X_0 \tag{3.11}$$

where X_0 is the radiation length, E_0 the initial energy and a and b are parameters that depend on E_0 and the medium. The profile has a steep rising edge and a slow decrease after the maximum, which is given by

$$X_{\max} = X_0\, \log_2\left(\frac{E_0}{E_C}\right). \tag{3.12}$$

It has to be noted, that equation 3.11 describes an average profile. For individual cascades, the energy loss strongly fluctuates because of stochastic energy transfer to the secondary particles.

The lateral distribution of the particles in the cascade is typically described in units of the Moliere radius R_M, which defines the radius of a cylinder containing on average 90 % of the deposited energy of the electromagnetic cascade [70]

$$R_M \approx X_0\, \frac{21\,\mathrm{MeV}}{E_C}, \tag{3.13}$$

with the critical energy defined in equation 3.9 For ice, the typical value is $R_M \approx 10\,\mathrm{cm}$. A commonly used parametrization for the lateral distribution of the cascade is the Nishimura-Kamata-Greisen (NKG) formula, which describes the electron density caused by a cascade [72]

$$\rho_e(r, s(X)) = C(s)\, \left(\frac{r}{R_M}\right)^{s-2}\, \left(1 + \frac{r}{R_M}\right)^{s-4.5} \tag{3.14}$$

where $s(X)$ is an age parameter that describes the longitudinal distance relative to the maximum $X_{\max}$. $C(s)$ is a factor that only depends on the age parameter.

For hadronic cascades, the treatment is more difficult, as a variety of different hadronic processes take place within the cascade. The $\pi^{\pm}$ produced in the cascade can decay into muons, while the π^0 quickly decay and initiate electromagnetic sub-cascades. These particles do not contribute to the further development of the hadronic core; instead in each secondary interaction a fraction of the cascade energy is converted into the electromagnetic part. If these processes occur early on, they strongly affect the later development of the cascade. As a result, the energy deposition and length of individual hadronic cascades show a large fluctuation.

At high energies of the order of 10 PeV, the LPM effect (Landau, Pomeranchuk, Migdal), reduces the cross section for pair production and bremsstrahlung, causing elongation for electromagnetic cascades (a review of the LPM effect is given in [73]). While the LPM effect is large for electromagnetic cascades, it also affects hadronic cascades through the sub-cascades produced via the decay of π^0. However, the π^0 are created with high multiplicity and their average energy is typically below the energy where the LPM effect is relevant. Hence, only a small fraction of the particles in a hadronic cascade is affected by the LPM effect.

The development of electromagnetic and hadronic cascades in ice and water and the application to neutrino detection has been investigated by various authors using Monte-Carlo

simulations. The Cherenkov light produced by cascades has been investigated e.g. by [74], this is discussed in section 3.3.1. Calculations including the LPM effect and the implications for radio and acoustic neutrino detection have been performed, e.g. by [75, 76] for the radio detection and [77–79] for the acoustic detection respectively. As a consequence of the LPM effect, the expected radio and acoustic signals from the electromagnetic cascades are significantly reduced, while this effect is less pronounced for hadronic cascades. It is seen that at energies above 10^{10} GeV, a hadronic cascade deposits most of its energy in a cylinder with size of the order of 10 cm diameter and 10 m length.

3.3 Optical Neutrino Detection

3.3.1 Cherenkov Effect

Cherenkov radiation is emitted when a charged particle travels through a dielectric medium at a speed $\beta = v/c_n$ greater than the phase velocity of light in that medium c_n. The charged particle causes polarization of the atoms along its path. When returning to the equilibrium state the atoms emit photons that coherently interfere to a light cone. The half opening angle of the Cherenkov light cone is determined by

$$\cos\theta_c = 1/(\beta n) \tag{3.15}$$

where n is the refraction index. The number of Cherenkov photons produced per unit path length by a particle with charge ze and per wavelength interval is given by the Frank-Tamm formula [70]

$$\frac{\mathrm{d}N}{\mathrm{d}x\mathrm{d}\lambda} = \frac{2\pi\alpha z^2}{\lambda^2}\left(1 - \frac{1}{\beta^2 n^2(\lambda)}\right), \tag{3.16}$$

with the fine structure constant α and the refractive index $n(\lambda)$.

For detection, the wavelength dependence of the instrumentation has to be considered. The photomultipliers (PMTs) of the IceCube detector (section 4) tubes are sensitive in the range of $300 - 600$ nm with a maximum efficiency at around 400 nm. For wavelengths smaller than 300 nm, the light is absorbed by the glass pressure spheres around the PMTs, whereas for large wavelengths the efficiency of the PMTs is very low. For Antarctic ice the refractive index for this wavelength range is $n \approx 1.32$ which results in about 250 photons that are emitted per centimeter or an energy loss of 850 eV/cm and an cone angle of $\theta_c \approx 41\,^\circ$. Therefore, the energy loss due to Cherenkov radiation can be neglected compared to the other energy loss processes described in 3.2.2. The charged lepton produced in a charged current neutrino interaction as well as all secondaries produced in cascades will emit Cherenkov light.

The total light yield from an electromagnetic or hadronic cascade is given by the sum of the contributions from all charged particles in the cascade. In [74], a parametrization for the total number of Cherenkov photons and their angular distribution was determined from simulations. The parametrization is given in terms of an effective track length, which is roughly proportional

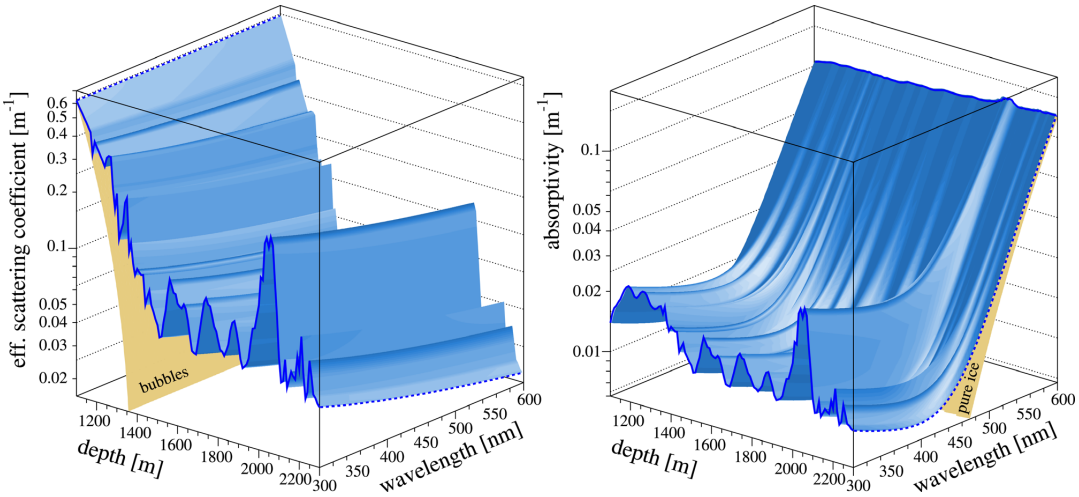

Figure 3.5: *The optical absorption and scattering coefficients as function of wavelength and depth [80].*

to the cascade energy E

$$l_{\text{eff}}(E)\,[\text{m}] = E\,[\text{GeV}] \cdot \begin{cases} 4.889\,\text{m/GeV} & \text{electromagnetic} \\ 4.076\,\text{m/GeV} & \text{hadronic} \end{cases} \tag{3.17}$$

Hadronic cascades have a smaller light yield, mostly because they contain large numbers of neutrons that do not contribute to Cherenkov light production. In addition, the energy threshold for Cherenkov radiation of charged hadrons is higher than for electrons. The total number of Cherenkov photons in a cascade is given by

$$N = l_{\text{eff}}(E) \times N_C \times \begin{cases} 0.894 & \text{electromagnetic} \\ 0.86 & \text{hadronic} \end{cases} \tag{3.18}$$

where N_C is obtained by the integral of the Frank-Tamm formula (equation 3.16) over the sensitivity range of the detector. The last term is a correction factor which has been introduced to account for non-relativistic tracks producing less Cherenkov photons with a different angular distribution [74].

3.3.2 Optical Ice Properties

Absorption

The absorption of optical and near UV photons is caused by electronic and molecular excitation processes of the medium and is described by the absorption length λ_a which denotes the geometrical distance from the source at which the light intensity has dropped by a factor e^{-1}. The absorptivity or absorption coefficient is given by $1/\lambda_a$. For the South Pole ice, the absorption by the pure ice itself and by impurities (as in the form of insoluble dust) has to be considered [80]. In the infrared and red regime, $\lambda > 500\,\text{nm}$, the absorption is dominated by different modes of molecular absorption of H_2O, with an exponential increase of the absorption

coefficient with wavelength. In the far-ultraviolet, $\lambda < 200\,\text{nm}$, the absorption increases for wavelengths shorter than the electronic band gap energy of ice. For the intermediate range $200 - 500\,\text{nm}$, the ice is expected to be very clear and the absorption to be dominated by impurities.

Scattering

In glacial ice, photons are scattered by various inhomogeneities such as air bubbles, dust grains, crystal point defects etc. The scattering of photons from (spherical) scattering centers of all sizes is described by the Mie scattering theory. The distribution of the scattering angle for any wavelength and scattering center sizes is described by the phase function. The mean free path between two scattering processes is given by the geometric scattering length λ_s. At each of these scatterings, the photon is scattered in a random direction, following the phase function. For anisotropic scattering, the phase function is peaked towards the forward direction and the mean of the cosine of the scattering angle θ_s is non-zero. For the South Pole ice, measurements show [68]

$$\langle \cos\theta_s \rangle \approx 0.94. \tag{3.19}$$

The phase function depends on the optical properties of the medium and the size distribution of the scattering centers. For natural media it is usually difficult to obtain the phase function from in-situ measurements. Instead, it is approximated with the Henyey-Greenstein parametrization [81], which approximates Mie scattering under the assumption that the scattering is forward peaked.

The effective scattering length λ_e takes into account that for an anisotropic scattering it takes several scattering processes before the direction of the photon is completely randomized

$$\lambda_e = \frac{\lambda_s}{1 - \langle \cos\theta_s \rangle}. \tag{3.20}$$

Measurements

Table 3.1: *Comparison of the absorption length λ_a and effective scattering length λ_e for ice and water (wavelength $300 - 600\,\text{nm}$, see text).*

material	ice	ocean water	fresh water
location	South Pole [80]	ANTARES [82]	Lake Baikal [83]
λ_a [m]	90 - 200	25-60	~ 20
λ_e [m]	10-50	122-265	~ 300

The optical properties of the South Pole ice have been measured in-situ with IceCube's precursor array, AMANDA (see chapter 4). The measurements were performed for several wavelengths between 300 nm and 600 nm, using the flasher LEDs installed in the optical modules as well as lasers embedded in AMANDA [80]. The absorption and scattering coefficients as functions of wavelength and depth are shown in figure 3.5, revealing a complex vertical

structure consisting of horizontal ice layers with varying optical properties. Each of these ice layers reflects the climatic situation in the atmosphere at the time the respective layer was formed, including varying amounts of minerals, acids, salt, organic material and ash from occasional volcanic eruptions. Similar structures have been observed in ice core measurements taken at various locations in Antarctica (e.g. [65, 84]), revealing information about the ice that was formed over a period of several 10,000 years. Therefore, such measurements are extremely useful for glaciologists and meteorologists, as they contain information on the climatic change over the history of Antarctica.

Down to a depth of 1400 m, the scattering is dominated by a large concentration of air bubbles. With increasing depth, the air bubbles are transformed to clathrate crystals with a refractive index in the optical range almost identical to that of the surrounding ice [66]. Hence, the scattering at the crystals is negligible and the scattering coefficient is dominated by dust inclusions. For the deep ice below 1400 m an absorption length of $90 - 200$ m is observed, whereas the effective scattering length is $10 - 50$ m. There are several distinct regions with an increased absorption and scattering coefficient. The highest dust concentration is found at a depth of about 2050 m, where the scattering coefficient is nearly a factor of four higher with respect to the neighboring ice layers.

Several measurements have been performed in deep ocean water at different locations, e.g by ANTARES [82] or NESTOR [85]. The absorption length determined by ANTARES for a depth of 2475 m increases from about 25 m for UV to 60 m for blue light (490 nm), while the effective scattering length increases from 112 m to 265 m. NESTOR found a similar absorption length, (55 ± 10) m at 490 nm. Measurements for fresh water have been performed in Lake Baikal [83]. The absorption length for wavelengths between 470 nm and 500 nm is about 20 m. The effective scattering length shows a strong seasonal variation due to different amounts of phytoplankton. A typical value is 300 m.

Table 3.1 summarizes the absorption and effective scattering lengths for the media of current Cherenkov telescopes. The light attenuation in both fresh and ocean water is dominated by the absorption length, while the effective scattering length is large. This is in contrast to the situation in ice, where the scattering length is comparably short.

3.4 Acoustic Neutrino Detection

3.4.1 The Thermo-Acoustic Model

The thermo-acoustic model states that an acoustic signal originates from the thermal expansion of a medium due to ionization energy loss from charged particles in hadronic or electromagnetic cascades. More specifically, the secondaries produced in an inelastic high-energy neutrino interaction will eventually dissipate most of the original neutrino energy as heat. The development of the cascade (and thus the energy deposition) occurs at the speed of light and therefore can be regarded as instantaneous compared to the typical time scales of the resulting thermal and acoustic energy dissipation. Therefore, the energy density ϵ deposited by the cascade is

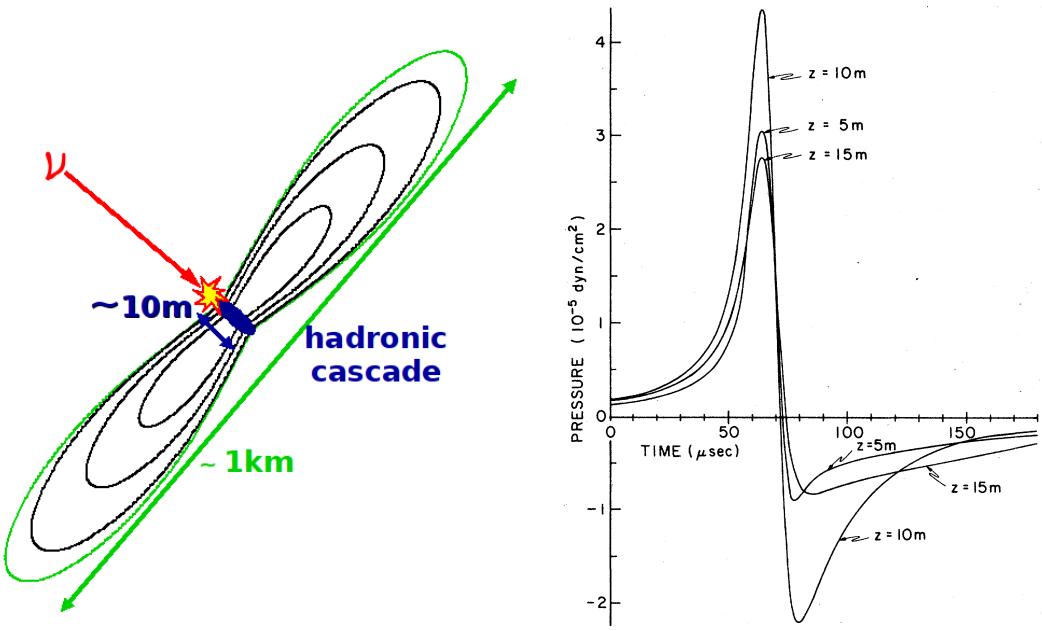

(a) (b)

Figure 3.6: *(a) Illustration of the thermo-acoustic effect for a neutrino-induced hadronic cascade, from [86]. The typical length of a high-energy cascade with* 10^{10} GeV *is about* 10 m*, resulting in a flat disc-shaped radiation pattern. (b) Calculated bi-polar pressure pulse arising from a* 10^{16} eV *cascade in sea water with a radial symmetric heat deposit. Pressure pulses are shown in different positions (z) in* 400 m *distance along the cascade axis, from [87].*

well-described by a δ-function in time

$$\frac{\partial \epsilon(\mathbf{r}, t)}{\partial t} = \epsilon(\mathbf{r})\delta(t). \tag{3.21}$$

In order to calculate the acoustic signal produced by a particle cascade, it is necessary to know the total deposited energy and the spatial distribution of this deposit. This distribution determines the frequency spectrum as well as the shape of the outgoing radiation pattern.

For a high-energy neutrino ($E \geq 10^{10}$ GeV) the cascade deposits the energy in a cylinder with size of the order of 10 cm diameter and 10 m length, [79, chapter 2]. The rapid heating causes a thermal expansion resulting in an outgoing acoustic wave. The outgoing acoustic radiation pattern is a wide, flat disk, perpendicular to the direction of the particle track, also called "acoustic pancake", illustrated in figure 3.6(a). This phenomenon is called thermo-acoustic effect and has first been described by Askaryan in 1957.

A comprehensive treatment of the effect was later developed by Askaryan and Learned [87, 88, and references therein] including numerical calculations of the acoustic pulse produced by particle cascades. These calculations have been experimentally verified first by Sulak et al. [89] at Brookhaven National Laboratory using a proton beam on a water target, and later by various other groups, using either laser or particle beams to simulate the neutrino-induced cascade in dense media (e.g. [90, 91]). In ice, the thermo-acoustic effect was first demonstrated by [92], using a proton beam. Currently, work is underway to study the quantitative properties

of the thermo-acoustic effect in a $3\,\mathrm{m}^3$ bubble-free ice block with a laser-induced signal [93, 94]. In the following the generation and propagation of acoustic signals in liquids and solids are discussed.

3.4.1.1 Liquids

The equations describing the generation of thermo-acoustic signals in liquids were derived independently by various authors, notably [87, 88]. The volumetric expansion resulting from an increase of temperature is given by the expression

$$\frac{\Delta V}{V} = \alpha_V \, \Delta T = \frac{\alpha_V}{\rho C_p} \, \epsilon \tag{3.22}$$

with the thermal expansion coefficient $\alpha_V = 1/V \cdot (\partial V/\partial T)$, the specific heat C_p, the deposited energy density $\epsilon = E/V$ and the density ρ of the medium. In ideal fluids, the thermal expansion leads to purely compressional (longitudinal) waves, whereas in viscose fluids or in solids also shear (transverse) waves can be generated. The time evolution of the pressure field in an ideal fluid is described by the inhomogeneous wave equation

$$\Delta p(\mathbf{r}, t) - \frac{1}{v_l^2} \frac{\partial^2 p(\mathbf{r}, t)}{\partial t^2} = -\frac{\alpha_V}{C_p} \frac{\partial^2 \epsilon(\mathbf{r}, t)}{\partial t^2}, \tag{3.23}$$

with the sound speed v_l of the longitudinal wave. A general solution of equation 3.23 is given by the Kirchhoff integral over the volume of the energy deposit

$$p(\mathbf{r}, t) = -\frac{\alpha_V}{4\pi \, C_p} \int_V \frac{\mathrm{d}V'}{|\mathbf{r} - \mathbf{r}'|} \frac{\partial^2}{\partial t^2} \, \epsilon(\mathbf{r}', t - \frac{|\mathbf{r} - \mathbf{r}'|}{v_l}). \tag{3.24}$$

For a quasi-instantaneous cascade, see equation 3.21, this expression is reduced to

$$p(\mathbf{r}) = -\frac{\alpha_V}{4\pi \, C_p} v_l^2 \frac{\partial}{\partial R} \int_{\partial V} \frac{\epsilon(\mathbf{r})}{R} \, \mathrm{d}A, \tag{3.25}$$

where the integration is performed over the surface ∂V of a sphere with radius $R = v_l t$ and centered around the observer at $\mathbf{r}$. Hence, for a given medium the pressure field $p(\mathbf{r}, t)$ solely depends on the spatial energy distribution $\epsilon(\mathbf{r})$. For the application to high-energy cascades, various models by different authors exist which use different parametrization and approximations on $\epsilon(\mathbf{r})$.

In [88] Askaryan and Dolgoshein apply the thermo-acoustic model to ocean water. The spatial energy deposition is described as a homogeneous cylinder with length L and diameter d. Although simplistic, this model allows a number of qualitative statements. First, the resulting pressure pulse has a characteristic bi-polar shape with a typical duration of $\tau \sim d/v_l \approx \mathcal{O}(10\,\mu\mathrm{s})$, see figure 3.6(b). Omitting attenuation effects, the pressure amplitude perpendicular to the cylinder axis is calculated as a function of the distance R and frequency f, using equation 3.25. In the near-field ($\lambda \geq R$), the sound pressure is given by

$$|p(f, R)| \propto f \, \frac{\alpha_V}{C_p} \, \frac{E}{\sqrt{R}} \tag{3.26}$$

where E is the total energy deposited in the volume. In the far field ($\lambda \leq R$) the pressure amplitude is

$$|p(f,R)| \propto f \frac{\alpha_V}{C_p} \frac{E}{R} \frac{\sin X}{X} \tag{3.27}$$

where $X = \lambda/2\pi$ with wave length λ. The emission is coherent for frequencies smaller or equal to the critical frequency $f < f_{\text{peak}} = v_l/(2d)$ where the diameter d of the cylinder is one half wavelength. For a cylinder with diameter $d \approx 10\,\text{cm}$, this corresponds to $f_{\text{peak}} \approx 25\,\text{kHz}$.

An analytical solution of equation 3.25 is given by Learned [87] for a radially symmetric Gaussian distribution of the energy deposition. More recent calculations are based on the energy density profiles obtained from dedicated simulations of particle cascades in water or ice, e.g. see [78, 87, 95]. In [87] the energy deposit of a hadronic cascade is modeled as a superposition of a Gaussian radial profile with a decay term along the cascade axis. The various models agree in their predictions on the distance dependence, while the absolute signal strength depends on the radial distribution of the energy deposition.

3.4.1.2 Solids

Solids generally support the propagation of transversal waves, in contrast to ideal fluids where only pure longitudinal waves exist. It can be shown, that for isotropic solids there are two independent wave modes, a longitudinal and a transversal mode. The longitudinal mode is also called pressure or P mode and involves a change of the volume. The transversal mode is also called shear or S mode and describes a shear motion without volume change. In analogy to the thermo-acoustic model in liquids, a wave equation can be derived, see appendix A. The sound speeds for the two modes are

$$v_P = \sqrt{\frac{\lambda + 2\mu}{\rho}} \qquad \text{and} \qquad v_S = \sqrt{\frac{\mu}{\rho}}\,, \tag{3.28}$$

where λ and μ are the Lamé parameters and describe the elastic properties of the medium. In principle, shear waves can be produced either directly at the source or through mode conversion at interfaces between regions with different elastic properties.

For the application to ice it is important to note that the ice-Ih phase is not isotropic but has a six-fold symmetry, which leads to five elastic parameters instead of two [96]. In this case, there are three independent wave modes, one quasi-longitudinal mode and two quasi-transversal modes, each with a different sound speed. In [97] it is discussed that even though all three wave modes are excited by the thermo-acoustic effect, the quasi-longitudinal mode is dominant while only a small fraction of the deposited energy is converted into the two transversal modes. This is mainly because for ice-Ih, the non-isotropic contributions to the elastic moduli are small. Consequently, the equations derived for the isotropic model can be used as an approximation for the application to ice.

3.4.1.3 Grüneisen Coefficients

The temperature-dependent material parameters appearing in the wave equation can be combined in the dimensionless Grüneisen coefficient

$$\Gamma = \frac{v^2 \alpha_V}{C_p}, \tag{3.29}$$

which describes the efficiency of the conversion from heat into elastic energy for a certain medium. The pressure amplitude scales with the Grüneisen coefficient, see equations 3.26 and 3.27. Therefore, it indicates the expected pulse heights of acoustic signals in the different media and characterizes the target materials with respect to acoustic neutrino detection. Table 3.2 gives a comparison for different media that have been considered as detector medium for large scale neutrino detectors. For the same energy deposition, the expected acoustic pulse is ~ 7 times higher in ice than in ocean water, whereas for salt it is even higher.

Table 3.2: *Grüneisen coefficients for ocean water, ice and salt at a characteristic temperature, using typical values of the respective media [98].*

quantity	ocean water	South Pole ice	rock salt
$T\,[°\mathrm{C}]$	15	-51	30
$v\,[\mathrm{ms}^{-1}]$	1530	3920	4560
$\alpha_V\,[\mathrm{K}^{-1}]$	2.555×10^{-4}	1.25×10^{-4}	1.16×10^{-4}
$C_p\,[\mathrm{Jkg}^{-1}\mathrm{K}^{-1}]$	3900	1720	839
Γ	0.15	1.12	2.87

3.4.2 Acoustic Ice Properties

3.4.2.1 Sound Speed and Refraction

As discussed in section 3.4.1 the sound speed depends on the elastic moduli of the medium which also are functions of density and temperature. From top to bottom, the sound speed increases as the glacial ice becomes stiffer due to the increasing density and the increasing pressure causes sintering of the ice crystals. This behavior is confirmed by velocity profiles taken by [59] in seismic measurements up to a depth of 200 m and by recent measurements with the SPATS array for depths down to 500 m (see section 5.2.3). These profiles show a region with a steep sound speed gradient which indicates the transition from firn to bulk ice at about ~ 200 m. Below the firn layer, the sound speed is nearly constant. Following Snell's law of refraction, the gradual change of the sound speed with depth leads to a deflection of an acoustic ray proportional to the velocity gradient

$$\frac{\sin\theta}{\sin\theta_0} = \frac{v}{v_0} \;\rightarrow\; \frac{\mathrm{d}\theta}{\mathrm{d}s} = \frac{\sin\theta_0}{v_0}\frac{\mathrm{d}v}{\mathrm{d}z} = \frac{1}{R}, \tag{3.30}$$

where $\mathrm{d}v/\mathrm{d}z$ is the velocity gradient in z direction, θ the angle with respect to the z-axis and $s = z/\cos\theta$ the coordinate along the ray trajectory, while v_0 and θ_0 represent the initial values.

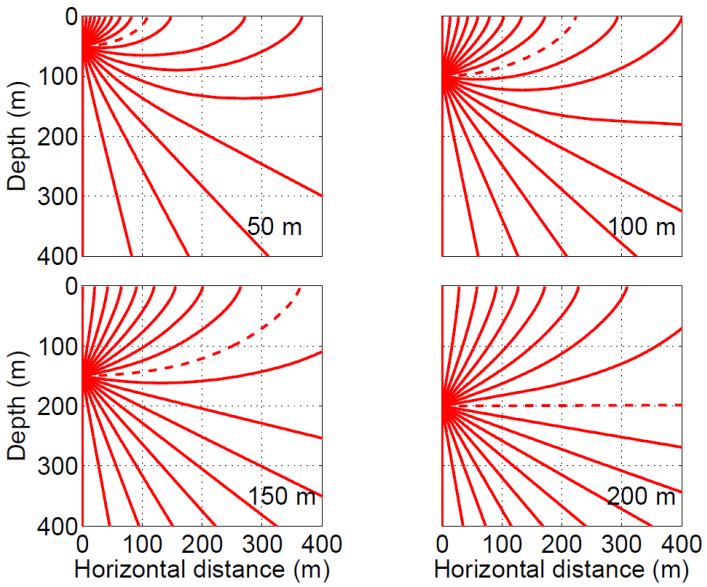

Figure 3.7: *Acoustic wave trajectories for different depths and emission angles, obtained in simulations [99]. The horizontally emitted ray is indicated by the dashed line.*

For a constant gradient, the trajectory describes the arc of a circle with curvature radius R. The trajectories are bent towards the direction of lower sound speed, as illustrated in figure 3.7, which is the result of a ray-tracing simulation by [99]. The figure shows the degree of refraction for individual acoustic rays, emitted by hypothetical point sources in various depths and different emission angles. All trajectories passing the firn layer are bent upwards due to the large sound speed gradient.

This has two implications for acoustic neutrino detection. First, anthropogenic acoustic noise originating at the surface will be refracted back to the surface. Secondly, the reconstruction of the position and time of any acoustic emission evidently benefits from a small curvature radius. Consequently, the optimum location of an acoustic detector is below the firn layer where the curvature radius is small. The in-situ measurement of the sound speed profile at the South Pole is discussed in section 5.2.3.

Finally, it should be noted that in a single ice-Ih mono-crystal, the sound speed depends on the direction relative to the crystal axis. However, naturally grown ice usually has a poly-crystalline composition with randomly distributed orientations of the crystal axes. Hence, this directional dependence vanishes for the glacial ice.

3.4.2.2 Attenuation Length

An acoustic signal propagating through a medium is attenuated by scattering and absorption. This has to be accounted for in order to design an acoustic detector as it is one of the constraints for the spacing of instrumentation. Naturally, a larger attenuation length allows a larger spacing and vice versa. However, the attenuation length has to be considered together with the expected signal strength and the detection threshold which depends on the ambient noise.

On a microscopical scale there is a multitude of contributing effects to both scattering and absorption. The most important ones with respect to the conditions in the polar ice are discussed in the following. On a macroscopic scale, the attenuation is described in terms of an attenuation coefficient α or its inverse, the attenuation length λ, such that for the pressure amplitude in an attenuating medium

$$p(s) = p_0 \, \phi \, \mathrm{e}^{-\alpha \, s} \quad \text{and} \quad \lambda = \alpha^{-1}, \tag{3.31}$$

where s is the length along the traveling path and ϕ the geometrical divergence factor, which is $1/R$ and $1/\sqrt{R}$ for spherical and cylindrical symmetry in the far field, respectively, R being the distance to the source. In section 3.4.1.1 it was shown that for a neutrino-induced thermo-acoustic signal this divergence factor is also $\phi = 1/R$.

It is practical to treat the contributions of absorption α_a and scattering α_s separately as they are caused by different effects and have different values:

$$\alpha = \alpha_a + \alpha_s \tag{3.32}$$

Both terms depend on the frequency. On the other hand, if either the frequency range of interest is sufficiently small or α as function of the frequency is flat, a frequency-averaged attenuation coefficient can be used. In the following sections, the theoretical predictions for the acoustic attenuation length for the polar ice are discussed. Their experimental verification is part of this thesis and subject of chapter 6. It will be shown that there is a strong disagreement between the measurements and the predictions.

Absorption

When a pressure wave propagates through a solid, parts of the wave energy are converted into internal energy of the medium by internal friction. There is a variety of possible interactions which are characterized by their individual mechanical relaxation time τ_m which depends on the temperature T through the so-called Arrhenius relation [98]

$$\tau_m = \tau_0 \mathrm{e}^{U/k_B T}, \tag{3.33}$$

where U is the activation energy for each individual process and k_B the Boltzmann constant.

Table 3.3 summarizes the processes relevant for the conditions met in the South Pole ice at temperatures of $-50\,^{\circ}\mathrm{C}$. For a discussion of the individual processes, see [100]. The two most important mechanisms are proton reorientation and grain boundary sliding. Grain boundary sliding occurs in the plastic deformation of poly-crystals (e.g. from external pressure fields), where neighboring grains of the crystal slide past each other. This process is considered dominant in the relatively warm ice near the bedrock, but less important in shallower depths. Proton reorientation is connected to the rotation of the H_2O dipole moment into favored positions. This is assumed to be the dominant process in the cold ice in the upper ice layers down to a depth of 2000 m and is independent of the grain size.

In [98] the absorption coefficient as function of the frequency f is given by:

$$\alpha_a = \frac{\delta_{\max}}{v_l} \frac{4\pi f^2 \tau_m}{1 + 4\pi f^2 \tau_m^2} \tag{3.34}$$

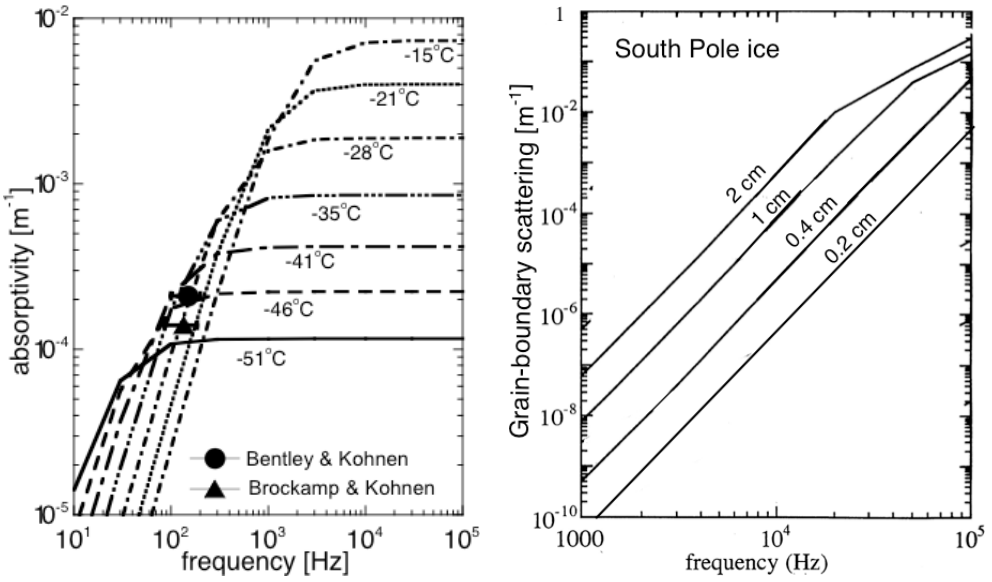

(a) (b)

Figure 3.8: *(a) Theoretical predictions for the absorption coefficient for various temperatures. The two data points show the results from measurements in Greenland and Antarctica. (b) Scattering coefficient from scattering at grain boundaries for various mean grain sizes. Images taken from [98].*

where $\delta_{\max}$ has to be determined experimentally and depends on the wave mode. At frequencies above $1/(2\pi\tau_m)$ the absorption coefficient becomes independent of the frequency, while for lower frequencies $\alpha_a \sim f^2$. The absorption coefficient has been calculated for various temperatures, the results are shown in figure 3.8(a). For these calculations, the parameters U, τ_0 and $\delta_{\max}$ have been obtained from different sets of measurements of laboratory ice samples, see [98] for details. The resulting absorption length ranges between 5.7 km and 11.7 km at a temperature of $-51\,^{\circ}\mathrm{C}$ (similar to the near-surface temperature in winter at the South Pole). In this case, there is also a negligible frequency dependence for the frequency range of $10 - 100\,\mathrm{kHz}$. For larger depths the absorption length is predicted to decrease with temperature, at $-46\,^{\circ}\mathrm{C}$ it is about $3 - 6\,\mathrm{km}$.

Scattering

Scattering occurs when the pressure wave passes inhomogeneities in the medium. The major contributors to scattering in glacial ice are air bubbles and grain boundaries. The mean air bubble diameter is a function of depth, ranging from $\mathcal{O}(1\,\mathrm{mm})$ near the surface to $\mathcal{O}(0.1\,\mathrm{mm})$ in the deep ice, see section 3.1. The wavelengths for the interesting frequencies up to 100 kHz are of the order of $\mathcal{O}(1\,\mathrm{cm})$, which is large compared to the diameters of the bubbles. Therefore, the scattering can be described by the Rayleigh approximation. In [100], the scattering coefficient for the scattering on air bubbles is described by

$$\alpha_{\mathrm{s,bubble}} = 2.68 \cdot 10^{-10} \left(\frac{n_0}{200 cm^{-3}}\right) \left(\frac{d}{0.02\,\mathrm{cm}}\right)^6 \left(\frac{f}{10\,\mathrm{kHz}}\right)^4 [\mathrm{m}^{-1}], \tag{3.35}$$

Table 3.3: *Relaxation times for energy loss by various processes in ice at a temperature of* $-55\,\mathrm{C}^\circ$*, for details see [100].*

Process	$\tau_m[s]$
Grain boundary sliding	10^{-3} to 10^{-4}
Proton reorientation	0.0084
Impurities	$\sim 10^{-4}$
Dislocation dampening	$\sim 10^{-9}$
Thermo-plastic	$\sim 10^{-13}$
Phonon relaxation	$\sim 10^{-12}$

with number density of bubbles n_0, bubble diameter d and frequency f. Even for a rather pessimistic assumptions with $n_0 = 200\,\mathrm{cm}^{-3}$, $d = 0.05\,\mathrm{cm}$ and $f = 30\,\mathrm{kHz}$ the scattering length is about 18 km. This is much larger than the expected value for the absorption length. Consequently, it is expected that the contribution from scattering at air bubbles is not dominant.

In a non-isotropic crystalline solid such as ice, the sound speed depends on direction and scattering occurs at grain boundaries, across which the sound speed changes abruptly. At the same time reflection and mode conversion between P and S waves occurs, as will be discussed in the next section. The mean grain size increases with depth and from extrapolations of previous core samples at the South Pole it is believed that it is less than 0.2 cm in the top 600 m. For frequencies relevant for neutrino-induced wave propagation, again the Rayleigh approximation holds, and the scattering coefficient is calculated in [98] as

$$\alpha_{\mathrm{s,grain}} = 5 \cdot 10^{-4} \left(\frac{d}{0.2\,\mathrm{cm}}\right)^3 \left(\frac{f}{10\,\mathrm{kHz}}\right)^4 [\mathrm{km}^{-1}]. \tag{3.36}$$

Figure 3.8(b) shows the predicted scattering coefficient in dependence on the mean grain diameter and frequency. The contribution of scattering at grain boundaries is extremely low, for a grain size of $d = 0.2\,\mathrm{cm}$ the expected scattering length is 2000 km at 10 kHz and 200 m at 100 kHz.

While scattering at bubbles depends on the sixth power of the mean bubble diameter, the scattering at grain boundaries only depends in third order on the mean grain diameter. In conclusion of these calculations, for the relevant frequencies and in a depth below the firn layer, the attenuation of acoustic waves is dominated by absorption and the effect of scattering is negligible. On the other hand, it has to be noted, that in this simple model, the scattering coefficient is calculated taking into account only the mean grain diameter. Because of the strong dependence on the grain diameter, the above results are not valid for a grain size distribution with a large contribution by grains of much larger diameter than the mean.

3.4.2.3 The Water-Ice Interface

If an acoustic wave passes a medium boundary, the different medium properties on both sides have to be taken into account. For the deployment of acoustical detectors, this has to be taken

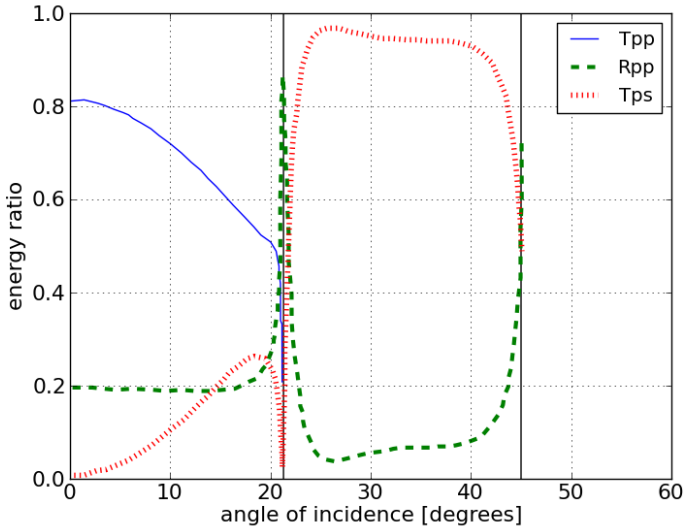

Figure 3.9: *The fraction of energy converted to the various modes with respect to the energy of an incident P wave at a flat interface from water to ice, calculated using the exact solution of the Zoeppritz equations [101]. The vertical lines denote the two critical angles of total reflection. T_{pp} and R_{pp} denote the energy fraction that is converted in the transmission and reflection of the P wave, while T_{ps} denotes the creation and transmission of a S wave. Because of energy conservation, the energy ratios for all waves corresponding to one of the three possible incident wave types sum up to unity.*

into account if either a sensor or a transmitter are operated not in ice but in water. The transmission and reflection coefficients for acoustic waves at medium boundaries including mode conversions are described by a set of non-linear differential equations, the Zoeppritz equations [102]. The coefficients are functions of the angle of incidence and the elastic media properties, namely the density and the sound speeds of the P and S on both sides of the boundary.

As mentioned in section 3.4.1, transversal acoustic modes do not propagate through ideal fluids. Therefore, a water-operated emitter produces a purely longitudinal signal (P wave). However, when the acoustic signal impinges on the water-ice interface at the hole wall, a part of its energy is converted from longitudinal to transverse modes while another part is reflected. The Zoeppritz equations can be used to numerically calculate the transmission and reflection coefficients for this scenario. Figure 3.9 shows the part of energy that is converted to the various wave modes.

For a perpendicular wave (zero incident angle) most of the energy is transmitted while the conversion to S modes is suppressed. For any non-normal incidence, shear waves are produced. There are two critical angles, given by the ratios of sound speeds

$$\theta_1 = \arcsin\left(\frac{v_{\mathrm{p,water}}}{v_{\mathrm{p,ice}}}\right) = 21.3^\circ$$

$$\theta_2 = \arcsin\left(\frac{v_{\mathrm{p,water}}}{v_{\mathrm{s,ice}}}\right) = 45.4^\circ,$$

where v_p and v_s are the sound speed of P and S waves, respectively. The calculations have been performed using the measurements of the sound speed by SPATS, see section 5.2). The critical angles denote total reflection of the P and S modes. Hence for angles larger than θ_1, no energy is transmitted as P wave, most of it is converted to S waves with a small contribution by reflection as P wave. Beyond θ_2, all energy is reflected back as P wave and nothing is transmitted to the ice.

3.4.2.4 Hole Ice

The SPATS array was deployed into deep water-filled holes which have been melted for the installation of the IceCube detector, see chapters 4 and 5. After the deployment, the holes eventually re-freeze, which takes up to several weeks. The acoustical and optical properties of this "hole ice" are poorly known. It is plausible that the hole ice has different properties than the surrounding bulk ice. Unlike the bulk ice it is not produced during thousands of years by accumulated layers of precipitation but over a much shorter time scale. Therefore, it is expected that the hole ice has a higher concentration of air bubbles. These air bubbles will eventually convert to clathrate crystals if the static pressure is sufficiently high. The ice expands and moves inside the bore hole during the refreezing process. It cannot be excluded that this produces cracks and micro-fissures, especially at the hole-bulk interface. As explained in the previous sections, the presence of such inhomogeneities can increase the acoustic attenuation, e.g. by scattering or reflection.

In order to have a better understanding of the time scales of the bubble conversion and the refreezing process in general, an in-ice camera has been installed in one of the IceCube holes during the drill season (2010/11). The data from these measurements is currently under investigation. In laboratory measurements [103], the conditions in the hole ice have been simulated by a fast freezing process. The result was a bubbly ice, pervaded by cracks. As expected, the air bubbles led to an increased signal attenuation by scattering. In addition, a strong anisotropy of the attenuation has been observed, as the cracks appear irregularly in the ice volume.

3.5 Radio Neutrino Detection

As explained in section 3.2.3, the energy deposited by a neutrino-induced cascade is largely contained within a cylindrical volume of $\mathcal{O}(10\,\mathrm{cm} \times 10\,\mathrm{m})$. During the propagation of an electromagnetic cascade in matter an excess of electrons over positrons is created. This is because positrons in the cascade are balanced by electrons in the pair production process, while e.g. Compton scattering transfers additional electrons from the material into the cascade. This leads to an asymmetric charge distribution in the cascade, with an excess of electrons in the cascade core up to $20 - 30\%$.

For wavelengths much larger than the characteristic length of the cascade, the moving particle cascade appears as a single moving charge. Askaryan [104] first described this effect,

noting that inside a dielectric medium such as salt or ice this would lead to a strong coherent radio and microwave Cherenkov emission. For smaller wavelengths, the coherence is lost because of destructive interference.

In ice, the radio-Askaryan effect has been observed first by the ANITA collaboration [105] at the Stanford Linear Accelerator Center (SLAC), using a 7.5 t ice target. The attenuation length of radio signals has been measured in-situ in the ice of the Ross Ice Shelf [106]. The attenuation length was found to vary from 500 m at 75 MHz to 300 m at 1250 MHz. This is considerably larger than the optical attenuation length. Hence, large detector volumes could be achieved with sparser instrumentation. Several experiments have been performed to investigate the feasibility of radio-Cherenkov neutrino detection in ice, a summary is given in the next section.

3.6 High-Energy-Neutrino Detectors

In section 2.2 it was discussed, that the detection of high-energetic neutrinos requires large instrumented detector volumes in order to accumulate sufficient data within a reasonable time scale. For obvious reasons, a detector of the 1 km^3 scale has to use natural media as detection medium, such as ocean or fresh water, ice and rock salt. Each of these media has advantages and disadvantages for the different detection methods. In the following, an overview is given of the various detectors that are currently in operation or in development.

Lake and Ocean Water

Water can be used either for the optical or acoustic detection method, whereas it is not transparent for radio signals. While the optical scattering length in water is large, it has a relatively small absorption length (see table 3.1). Ocean water has a high background of radioactive decays of ^{40}K isotopes as well as bioluminescence while the available fresh water reservoirs in lakes have a limited size and depth. The acoustic attenuation length in water is of the order of several kilometers [107]. On the other hand, there is a large background from transient sources, for instance from ships and waves at the surface and from the maritime fauna.

The DUMAND project (Deep Underwater Muon and Neutrino Detection) was an underwater neutrino telescope to be built from 1976 on near Hawaii [108]. It was focused on the optical detection method but also included acoustic sensors. The project was cancelled in 1995, but many pioneering work was carried out demonstrating the feasibility of underwater arrays. Baikal [109] was the first underwater neutrino detector to be completed. It was built from 1993 to 1998 in the Siberian Lake Baikal at a depth of 1 km. Currently there are plans to extend the Baikal detector to the 1 km^3 scale, named Gigaton Volume Detector (GVD) [110].

There are several Cherenkov detectors located in the Mediterranean Sea: ANTARES [111], NEMO [112] and NESTOR [113]. The first two also have dedicated acoustic extensions, called AMADEUS and ONDE, respectively. Of these detectors, ANTARES is the largest one, consisting of 12 cables with 900 optical modules and 36 hydrophones, deployed in 2.5 km depth.

These three collaborations have joined in a common effort to construct a $\mathcal{O}(1\,\mathrm{km}^3)$ detector in the Mediterranean Sea (KM3NeT), including optical and acoustic detection methods. The construction is expected to start in 2013 and a conceptional design report has been published [114, 115]. SAUND (Study of Acoustic Ultra-high-energy Neutrino Detection) uses an array of military hydrophones near the Bahamas [116]. Since 2006, the experiment is in its second phase and consists of 49 hydrophones. The SAUND project was the first to set an upper limit on the flux of ultra-high-energy neutrinos in sea water using the acoustic detection [50]. ACORNE [51] uses a military hydrophone array in Scotland with eight hydrophones. It is in operation since 2006.

Ice

Compared to water, the Antarctic ice has a larger optical absorption length, but a shorter scattering length. Advantages of ice are the absence of bioluminescence, a low anthropogenic background from the surface and very low levels of radioactive isotopes such as ^{40}K. On the other hand, the instrumented hardware is not recoverable once it has been deployed.

Optical neutrino detection using the Antarctic ice as detector medium was pioneered by the AMANDA project [117]. In its final stage, AMANDA-II consisted of 677 optical modules on 19 strings that had been deployed into the ice at a depth of $1500 - 1900\,\mathrm{m}$. It was the proof-of-principle setup for the larger IceCube detector and was decommissioned in 2009 after 13 years of successful operation. The final data sample of the data taken from 2000 till 2007, contains 6595 neutrino events with a reconstructed energy from 100 GeV to 10 TeV. The data show no indications for a neutrino point source and are consistent with an atmospheric neutrino flux. Limits have been set on the diffuse flux of extraterrestrial neutrinos [42] and for various astrophysical source models with an E^{-2} flux [118].

The IceCube detector was built from 2004-2010 and is about two orders of magnitude larger than its predecessor. Because of its lower energy threshold, AMANDA was used alongside with IceCubeas a low-energy sub-detector until 2009, before the DeepCore sub-detector inherited this task. This is discussed in more detail in chapter 4.

In ice, the radio detection method has been investigated with the Radio Ice Cerenkov Experiment (RICE [119]), the ANtarctic Impulse Transient Array (ANITA [120]) and the FORTE satellite (Fast On-Orbit Recording of Transient Events [46]). RICE is an array of 16 antennas, deployed in 200 m depth into the Antarctic ice approximately 1 km from the South Pole. ANITA is an balloon-borne experiment, and has been launched from Mc Murdo station, Antarctica. It carries an array of 32 antennas, observing the surface of the Antarctic ice for radio emissions with a flight duration of about a month. The FORTE satellite carries two broadband radio-frequency antennas and was launched in 1997 into an orbit with 70 ° inclination towards the equator. From this orbit, Antarctica cannot be observed, to that the observations using large ice deposits are limited to the Greenland ice sheet.

The observational limits on the detection of ultra-high-energy neutrinos set by the various radio detectors are shown in section 2.2.5. Based on the experience gained in these efforts, a new detector is currently in development, the Askaryan Radio Array (ARA) [121]. The proposed design features an array with a fiducial area of $80\,\mathrm{km}^2$, to be built at the South Pole

near the IceCube detector. Because radio waves are also refracted in the firn layer, the ARA antennas will be deployed into the deep ice below 200 m depth.

The feasibility of acoustic neutrino detection at the South Pole is currently being investigated with the South-Pole Acoustic Test Setup (SPATS), an array of 28 hydrophones deployed in four of the IceCube holes. The setup and the recent results of SPATS are described in chapter 5.

Other Materials

Rock salt can occur in large natural underground deposits (salt domes) which can be several cubic kilometers large. Salt domes are currently investigated by the SalSA project as a target material for radio-Cherenkov detection [122]. The Grüneisen coefficient in rock salt is larger than in ice (table 3.2), resulting in an expected acoustic signal amplitude more than a factor 2 larger. Therefore, salt domes have been proposed as a possible medium for acoustic neutrino detection.

Finally, the Moon also provides a huge effective detector volume. The Goldstone Lunar Ultra-high-energy neutrino Experiment (GLUE [47]) used two Deep Space Network antennas to search for radio signals that are possibly produced by neutrino interaction in the surface of the moon. GLUE was able to set an upper limit on the diffuse neutrino flux, see figure 2.7.

Hybrid Detection

On Earth, Antarctic ice is the only material that occurs in amounts that supports a detector with volume $\mathcal{O}(\mathrm{km}^3)$ and allows optical, acoustic and radio neutrino detection simultaneously. Hence, ice allows to combine the three detection methods for a large-scale hybrid detector. In such a detector, the threshold for neutrino detection could be lowered because if an event is detected in coincidence by two or all three methods, the probability for background is reduced. Moreover, this allows a calibration between the different methods.

The largest neutrino detector to date is IceCube with an instrumented volume of $1\,\mathrm{km}^3$, see section 4. For the current IceCube detector, an event rate of $\mathcal{O}(0.1)$ GZK neutrino events per year is expected [32], see table 2.1. Therefore, this volume is not large enough to accumulate the required statistics for the highest energies to allow a study of the energy spectrum and the arrival directions of neutrinos. A larger detector volume is required and this could be achieved by the acoustic or radio method with reasonable cost. The idea to extend the IceCube detector with acoustic and radio detectors was first suggested in [123]. The proposed detector would have a volume of about $100\,\mathrm{km}^3$ where the existing optical IceCube detector would be used as the core of a hybrid array. The predicted large acoustic attenuation length and the measured radio attenuation length allow for a larger spacing of the additional instrumentation and the total volume of the hybrid array could be increased with comparatively small cost, compared to a purely optical detector of the same size.

4 The IceCube Neutrino Observatory

Abstract

The IceCube Neutrino Observatory is a recently completed (December 2010) large-scale neutrino detector built near the Amundsen-Scott South Pole Station. It is the largest neutrino detector which has been constructed to date and contains several thousands of spherical optical sensors deployed into the Antarctic ice. In the first part of this chapter, the design of the detector, data acquisition, processing and the generation of Monte-Carlo data are described. In the second part, the reconstruction of event properties from the measured data is described.

4.1 The Detector

IceCube is a kilometer-scale high-energy neutrino observatory constructed at the South Pole near the Amundsen-Scott Station. It consists of the IceCube in-ice array, including the DeepCore sub-detector, and the IceTop surface array. Figure 4.1 gives a schematic view of the three parts. The primary scientific goal of IceCube as a neutrino telescope is to detect and measure the sources of astrophysical neutrinos as well as the diffuse flux from unresolved sources. Furthermore, there is a large variety of scientific topics, such as the search for dark matter, the observation of supernova explosions, cosmic air showers and the properties of the neutrinos themselves. IceCube is optimized for the neutrino energy range of 100 GeV to 100 PeV [124]. DeepCore lowers the detection threshold to about 10 GeV, which significantly enhances the sensitivity for the indirect search for Dark Matter and the study of neutrino oscillations [125].

The In-Ice Detector

The in-ice array uses the Antarctic ice as detector medium by detecting Cherenkov light emitted by secondary particles produced in high-energy neutrino interactions inside or near the detector volume. It has an instrumented volume of about 1 km^3 and consists of 86 cables (called strings), deployed into a depth of 1450 m to 2450 m. Each of the strings is instrumented with 60 Digital Optical Modules (DOM), resulting in a total number of 5160 modules in the in-ice part. The strings are roughly aligned in a triangular grid pattern, forming a hexagon, see figure 4.2. The average horizontal string spacing is 125 m, while the vertical spacing between neighboring DOMs on the same string is about 17 m. Eight of the 86 strings form the denser DeepCore sub-array, which is built below the dust layer with 62 m string spacing and 7 m vertical DOM spacing respectively.

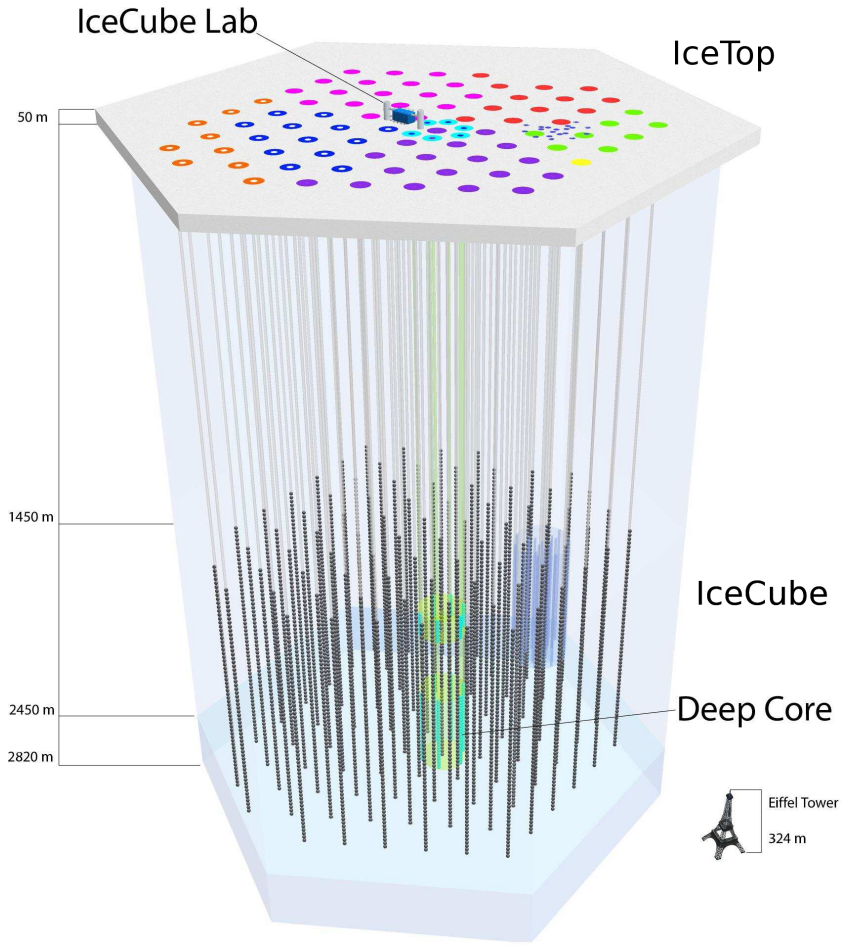

Figure 4.1: *Illustration of the* IceCube *detector. The in-ice instrumentation covers a volume of about* $1\,\mathrm{km}^3$ *ice. The* IceTop *air shower detector is situated at the surface above* IceCube.

Digital Optical Modules (DOMs)

The Digital Optical Module (DOM) is the basic detection unit of the IceCube detector. Each DOM acts autonomously, it receives power, control and calibration signals from the surface and returns digitized waveforms. Figure 4.3 shows a schematic view of a single DOM, it consists of a photomultiplier tube (PMT) inside a 35 cm diameter glass pressure sphere [127], as well as the high voltage power supply and a digitizing system. Because the signal recorded by the PMT is digitized directly in the DOM, the modules are called *Digital* Optical Modules, in contrast to the predecessor AMANDA, where the signals were digitized at the surface. This avoids signal degradation due to attenuation or electronic cross-talk in the cables. Each DOM is also equipped with twelve flasher LEDs, which can be used as an artificial light source for calibration purposes. The flashers have been used to determine the exact position of each individual DOM by flashing the LEDs in one DOM and measuring the arrival times in the other DOMs. The flashers can also been used to study the optical ice properties (section 3.3.2).

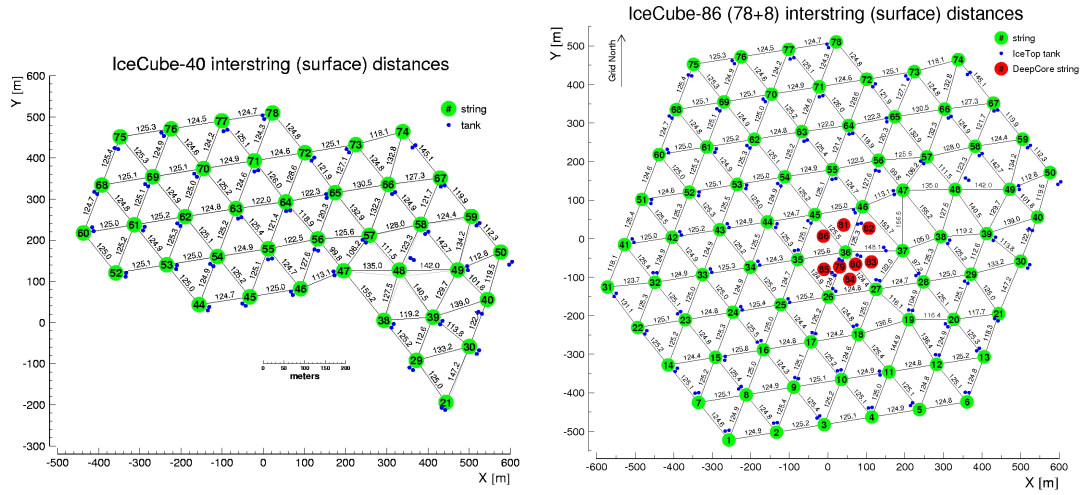

(a) (b)

Figure 4.2: *Horizontal distances between the* IceCube *strings for the IC40 and the IC86 configuration. The strings form a triangular grid that is slightly distorted because individual strings had to be moved during construction.*

A Growing Detector

IceCube was not built in one step, but in multiple construction phases over a duration of six years with only short time windows for construction work during the austral summers. The first string was deployed in December 2004, followed by more strings in the years after, see table 4.1. The individual stages of the are referred to as IC1, IC40, IC86, etc. Measurements and physics analyses have been performed for all these stages.

For the construction of IceCube, 2500 m deep holes were drilled into the Antarctic ice using a hot-water drill which released a high-pressure hot-water stream that melted through the ice. Each hole had a diameter of approximately 50 cm. After retrieving the drill head back out of the hole, a fully instrumented string was lowered into the ice and left to freeze in. Once a DOM has been deployed, it is impossible to retrieve it for maintenance. Hence, the DOMs have been designed to operate reliably for at least 15 years in a cold, high-pressure environment. As of March 2011, about 98% of all deployed DOMs are still in operation.

Table 4.1: *Number of strings after the individual construction stages of the* IceCube *detector.*

year	2005	2006	2007	2008	2009	2010	2011
strings	1	9	22	40	59	79	86

The IceTop Surface Array

At the surface directly above the in-ice array is IceTop, an extensive air shower detector with an area of about 1 km^2. An overview of its design and the physics capabilities is given in

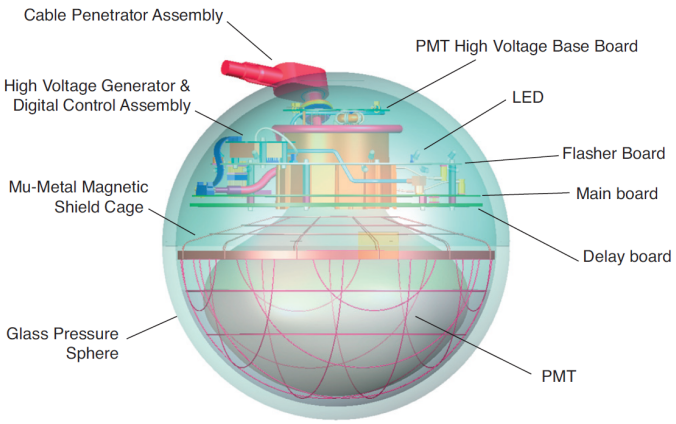

Figure 4.3: *Schematic drawing of a Digital Optical Module (DOM) with a photomultiplier tube (PMT) and associated electronics inside a glass sphere, from [126].*

[128]. IceTop uses largely the same sensor electronics as IceCube and consists of 81 stations each consisting of two ice-filled tanks instrumented with two DOMs. IceTop is used to detect cosmic-ray air showers in the energy range of about 100 TeV to 1 EeV. The combination of the surface array with the in-ice detector gives a three-dimensional air shower array that can measure both the shower size at the surface and the energy deposition by high-energetic muons in the in-ice array. The combined data allows coincident measurements and is sensitive to both the energy and the composition of the primary cosmic rays. In addition, IceTop can also be used for calibration and as a veto for IceCube against high-energy cosmic-ray air showers in neutrino analyses.

4.2 Data Processing

Before any analysis is performed, the data undergo multiple steps of data processing. This also involves several techniques to reject the background of down-going atmospheric muons and to select possible neutrino candidates. In this section, an overview of the IceCube data acquisition and standard data processing is given.

4.2.1 Data Acquisition (DAQ)

The analogue pulses from the photomultiplier in each DOM are digitized directly inside the DOM and marked with a time stamp [129]. Before any data are transferred to the surface, a HLC (Hard Local Coincidence) check is performed. Only if a neighboring or next to neighboring DOM on the same string also has registered a hit within a 1 μs time window, data are transferred. The HLC check reduces noise hits which occur uncorrelated and isolated everywhere in the detector, in contrast to the pattern of hits correlated in time and space expected from particles in IceCube. In IceCube, noise is caused by photons from the decay of radioac-

tive isotopes in the DOMs glass shells in addition to thermal noise. Each DOM has a noise rate of about 650 Hz, therefore without the HLC check the data would be dominated by noise hits.

Even with HLC, it is not possible to continuously read out the full IceCube detector. Instead, small time windows are read out each time one of several trigger conditions is met. There is a variety of different trigger conditions, the most important is the Simple Multiplicity Trigger (SMT) for which a certain number of DOMs has to have a hit within a pre-defined time window. For IC40, this is eight HLC DOMs within 5 μs window. Other triggers are e.g. the String Trigger for which a certain number of hit DOMs has to be on the same string. The data that passed either of the trigger conditions is sent to the IceCube counting house, where the data from the individual DOMs is combined to an event and further processed.

4.2.2 Standard Processing

The data produced by the IceCube DAQ system exceeds the data volume that can be transmitted via satellite from South Pole to the data warehouse located in Madison (USA). The majority of events is caused by atmospheric muons and not associated with neutrinos. Hence, a significant data reduction is performed before the data is transmitted. This is achieved by an online filtering system that runs on a computer cluster at the South Pole and involves several techniques to reject background and to select neutrino candidate events. Only events that pass one of the different filters will be transmitted by satellite, while all data are written to archiving tapes.

In a first step, an initial feature extraction is applied to obtain the arrival times of the individual photons and the deposited total charge from the waveforms recorded by the DOMs [130]. With this data, track reconstructions are performed, including fast and simple first guess algorithms as well as other computationally inexpensive methods. Based on these reconstructions, various software filters select candidate events for any of the physics analyses. These filters are specialized to select certain event classes, for example the Muon, EHE or the Cascade filter [131]. The Muon filter is the primary filter for many analyses and was develop to reject the vast numbers of down-going atmospheric muons and to keep as many candidate muon neutrino events as possible from near or below the horizon. The EHE Filter selects candidates for extremely-high-energy events. For this, the total number of photo-electrons is required to exceed $\log(N_{pe}) = 3.5$. Other filters select events from certain directions e.g. the galactic center or from the Moon or Sun.

The data that has been transmitted to the data warehouse is further processed, called level 2 processing. This includes a reprocessing of the recorded waveforms and an event reconstruction using more computing-time intensive algorithms, such as iterative maximum-likelihood reconstruction methods. This will be discussed in section 4.4. The data is stored in the IceCube data warehouse and is accessible to all members of the IceCube collaboration. The processing is called 'standard data processing', because it provides a common high-quality data sample. In addition, more specialized data processing is done for the individual analyses, for which the data is further processed and different quality selections are applied.

4.3 Simulation

The Monte-Carlo simulation for IceCube includes the neutrino generation, the propagation of lepton and photons through the detector and the subsequent detector response.

- **Neutrino generation:** An event generator creates primary particles based on a given flux model. In IceCube, neutrinos of all flavors are generated by a neutrino generator (NuGen) based on the ANIS software package [132], while the atmospheric muon background is simulated with the CORSIKA package [133]. Neutrinos are generated with a random position on the Earth surface following a given energy spectrum. Typically, the simulations are performed with a hard energy spectrum with $dN_\nu/dE \sim E_\nu^{-1}$. The simulated data is then reweighted to a softer spectrum.

  The generated neutrinos are propagated through the Earth, taking into account absorption due to charged current interactions and energy loss through neutral current interactions. Because of the small the neutrino interaction cross-section, the number of generated neutrinos that would interact close to the detector is also very small. In order to achieve sufficient numbers of triggered neutrinos events, the neutrinos are forced to interact within a predefined volume that fully contains the IceCube detector [134]. The probability of each simulated neutrino to interact inside this volume accounted for with an interaction weight factor, which can be used to calculate the number of neutrino interactions inside IceCube.

- **Muon propagation:** The muon produced in charged current neutrino interactions as well as the atmospheric muons are propagated using the Muon Monte Carlo (MMC) code [69]. MMC includes the various energy loss mechanisms described in section 3.2.2 to propagate the muon through the ice. Depending on the energy loss mechanism, secondary particles are generated.

- **Photon propagation:** The Cherenkov photons produced by the muon and the various secondary particles are propagated from the particle track through the detector. The photon propagation is performed by using one of two methods: numerical tabulation or a direct tracking. The first method is implemented using the Photonics package [81]. Here, the photon propagation is not performed for all photons individually. Instead, the photon distribution as result from dedicated photon propagation simulations is stored in tables, from which the expected number of photons at each DOM can be calculated. These tables are computationally efficient and incorporate the layered structure of the optical ice properties, as described in section 3.3.2.

  The second method is the direct photon tracking provided by PPC (Photon Propagation Code) [135]. Here, the propagation of each photon is calculated individually, taking into account different ice properties along the photon track. This strategy avoids the approximations that are necessary for the tabulated description. However, a direct tracking is

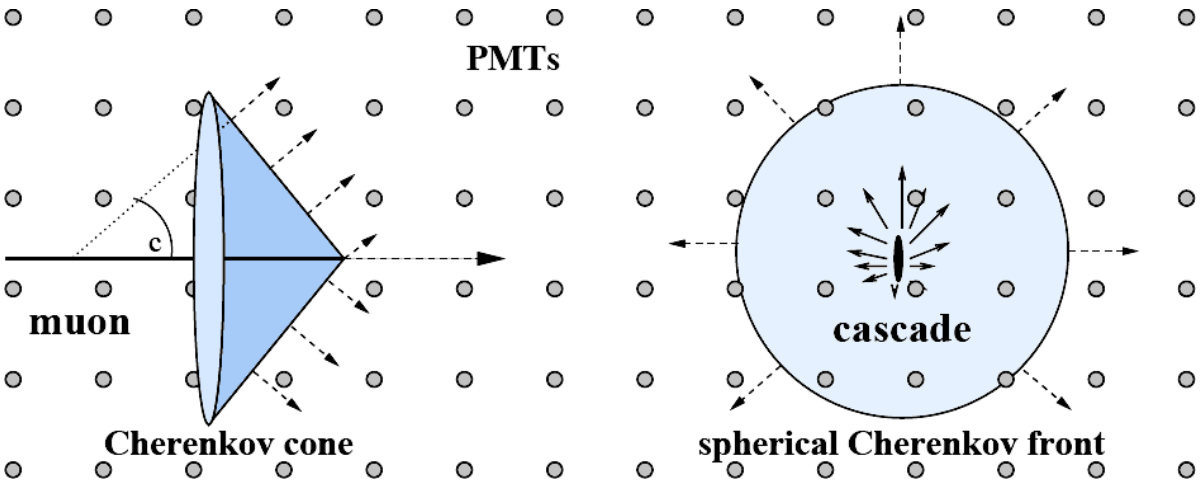

Figure 4.4: *Visualization of a muon track induced by muon-neutrino (left) and a cascade with a spherical signature induced by a electron- or tau neutrino (right), image adapted from [136].*

more computationally intensive and for the current IceCube simulation, the Photonics tables are used.

- **Detector simulation:** The response of the IceCube detector to the Cherenkov photons is simulated in multiple successive steps. In a first step, the output of the photon propagation is used to determine the number of photons that would arrive at the photocathode of the photomultiplier. The next step is to simulate the resulting number of photo-electrons and their arrival times. Then, the response of the DOM electronics is simulated, generating waveforms similar to those recorded by the DOMs at the South Pole. Finally, the same trigger conditions which are used for the measured data at the South Pole are applied. From there, the simulated and measured data undergoes the same data processing, as described in section 4.2.2.

4.4 Event Reconstruction

IceCube can be considered as a large tracking calorimeter, in which the Cherenkov light from charged particles leaves a pattern of hit DOMs. This pattern in principle allows to measure the energy deposition and direction of these particles and also may reveal the flavor of an interacting neutrino.

In section 3.2.2 it was discussed that interactions from different neutrino flavors can be distinguished by their different topologies. Common to all flavors is the initial hadronic cascade at the neutrino interaction vertex. A ν_e produces an electron, which in turn creates an electromagnetic cascade that coincides with the initial hadronic cascade. The Cherenkov light produced in the cascades will lead to an expanding shell of hits, with a larger intensity into the forward direction. The muon from a charged current ν_μ interaction produces a pattern of hits where the timing of the hits follows the traveling direction of the muon. Taus can be identified by their unique topology of two cascades, one at the interaction vertex and another

from the tau decay. The track and cascade shapes are both illustrated in figure 4.4.

The goal of event reconstruction is to determine the properties of the observed particles from the measured hit pattern. From the timing information and the charge deposition in the individual DOMs, the event properties can be reconstructed, namely the arrival direction, the interaction vertex (if inside IceCube) and the energy of the muon. In IceCube the event reconstruction is performed with iterative maximum-likelihood algorithms, this is discussed in the following sections.

4.4.1 Maximum-Likelihood Method

In a generic maximum-likelihood approach, a set of unknown event parameters $\{a\}$ is determined from a set of experimentally measured independent observables $\{x\}$ by maximizing the likelihood

$$\mathcal{L}\left(\{x\} \mid \{a\}\right) = \prod_{i}^{N} p_i(x_i \mid \{a\}), \tag{4.1}$$

where the product is taken over all $i = 1, \ldots, N$ independent observables and p_i is the probability density function to observe a value x_i for the ith observable for given values of the parameters $\{a\}$. Figure 4.5 illustrates the Cherenkov light cone from a muon track which leads to a hit in a DOM. The event parameters describing a single muon are the muon track geometry and the energy

$$\{a\} = \{\mathbf{r}_0, \hat{p} = (\theta, \phi), E_0\}, \tag{4.2}$$

where $\mathbf{r}_0$ is the position on the track at the time t_0, $\hat{p}$ the track direction and E_0 the energy of the muon. Hence, for the full event reconstruction, there are five degrees of freedom for the track geometry and one additional degree of freedom for the energy. Using this description, it is possible to reconstruct all six event parameters together in one step with the same maximum-likelihood algorithm. However, it is often practical to split the energy and track reconstruction and to to develop specialized algorithms. This is because for the track reconstruction, the photon arrival times are the most relevant information, whereas the energy reconstruction requires information on the expected number of photo-electrons as a function of the muon energy.

The maximum of the likelihood with respect to $\{a\}$ (or the minimum of $L = -\log \mathcal{L}$) gives the values of $\{a\}$ with the best agreement to the observed data. Typically, this is done with a minimizer algorithm, which requires an initial track hypothesis, called seed. The seed is obtained using a computationally inexpensive first guess algorithm. However, it is possible that a minimizer algorithm returns a local minimum of the likelihood and not the global minimum. In order to improve the reconstruction performance, multiple iterations of the same algorithm can be performed, each time starting with a different seed. This increases the chance that the global minimum is found and the most accurate track information is returned.

As this is computationally intensive, the iterative reconstruction algorithms are run offline. Simple first guess algorithms and single-iteration likelihood reconstructions are also performed during the online filtering at the South Pole.

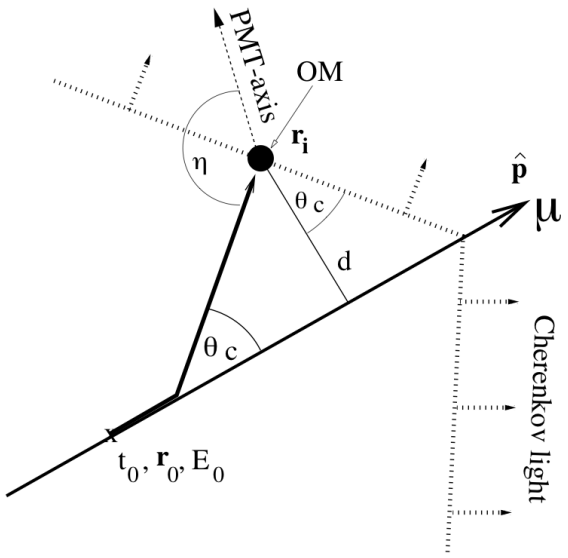

Figure 4.5: *Illustration of the Cherenkov light cone created by a muon track ($\beta = v/c = 1$) and arriving at an optical module [136].*

4.4.2 Muon Track Reconstruction

IceCube uses basically the same track reconstruction which was developed for Amanda. It is described in detail in [136]. For the track reconstruction, the arrival times of the observed photo-electrons are the most relevant information. The corresponding likelihood uses a probability density function (PDF) of the arrival times of single photons at the locations of the DOMs, which can be formulated as a function of the time residuals t_{res}. The time residual is the difference between the measured arrival time t_a and the time t_{geo} the photon would have traveled directly without scattering and is given by (see figure 4.5)

$$\begin{aligned} t_{\text{res}} &= t_a - t_{\text{geo}} \\ t_{\text{geo}} &= t_0 + \frac{\hat{p} \cdot (\mathbf{r_i} - \mathbf{r_0}) + d \tan\theta_c}{c}, \end{aligned} \tag{4.3}$$

where t_{geo} is given by geometrical consideration from the track and the angle θ_c of the Cherenkov light cone. A delay of the arrival time is predominantly caused by scattering of the Cherenkov photons in the ice, but also through electronic jitter and the dark noise in the PMTs.

In a simple model, a likelihood is constructed from the PDF p_1 describing the arrival times of single photons:

$$\log \mathcal{L}_{\text{time}} = \sum_{i=1}^{N_{\text{hit}}} \log p_1(t_{\text{res}} \mid \{a\}), \tag{4.4}$$

where the sum is taken over all registered photons. Equation 4.4 is called the single photo-electron (SPE) likelihood. In case of multiple hits in a DOM, the first photon is usually less scattered than the average single photon. Since all photons travel independently, the arrival

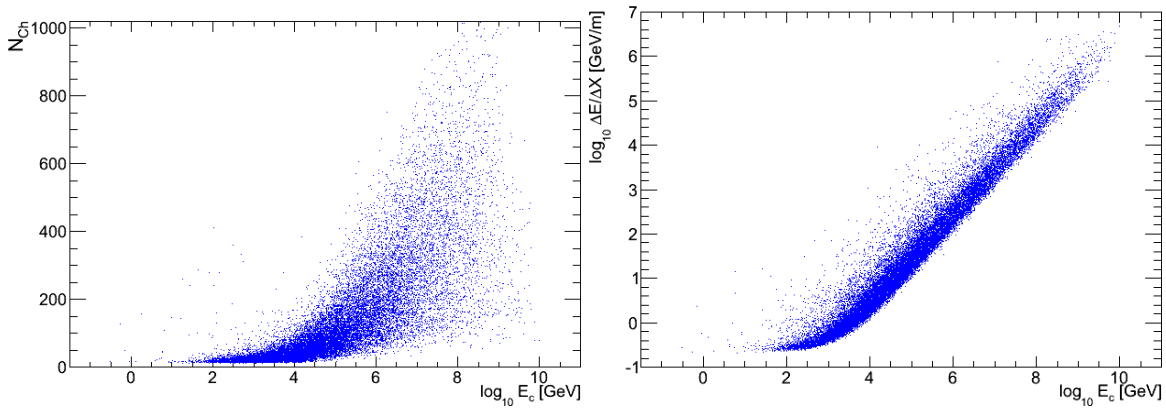

(a) (b)

Figure 4.6: *Correlation between the number of hit channels N_{Ch} (a) or the mean muon energy loss (b) with the muon energy E_c closest to the center of the IC40 detector.*

time distribution of the first out of N photons is given by [136]

$$\begin{aligned} p_N^1(t_{\text{res}}) &= N\, p_1(t_{\text{res}})\, [1 - P_1(t_{\text{res}})]^{N-1} \\ P_1(t_{\text{res}}) &= \int_{-\infty}^{t_{\text{res}}} p_1(t)\text{dt}. \end{aligned} \tag{4.5}$$

This PDF is called the multi-photo-electron (MPE) PDF. Replacing p_1 with p_N^1 in equation 4.4 gives the MPE likelihood. In this analysis, the result of the MPE reconstruction will be used as the geometric seed for the energy reconstruction.

In IceCube, p_1 is often approximated by the so-called Pandel function, which is an analytical expression

$$\begin{aligned} p_1(t_{\text{res}}) &= \frac{\tau^{-d/\lambda}\, t_{\text{res}}^{d/\lambda-1}}{N(d)\,\Gamma(d/\lambda)}\, \mathrm{e}^{-t_{\text{res}}\,(1/\tau + c/\lambda_a) - d/\lambda_a} \\ N(d) &= \mathrm{e}^{-d/\lambda_a} \left(1 + \frac{\tau\, c}{\lambda_a}\right)^{-d/\lambda} \end{aligned} \tag{4.6}$$

with the speed of light c, optical absorption length λ_a and two empirical parameters τ and λ. The Pandel function parametrizes a homogeneous ice with constant absorption length and without dust layers.

4.4.3 Muon Energy Reconstruction

Energy Estimators

For the muon energy reconstruction in IceCube, the following has to be considered. As discussed in section 3.2.1, the muon carries on average 80% of the initial neutrino energy, while the remainder of the energy is transferred to the nuclear target which results in a hadronic cascade at the interaction vertex. In order to determine the neutrino energy, both the energy

of the cascade and the muon have to be measured. Cascades in principle allow a good energy measurement because the energy is contained in a relatively small volume. For muon tracks, the energy is deposited over a larger volume, which is not necessarily contained inside the detector. If the interaction vertex is outside the detector, it is generally unknown how far the muon has traveled and how much energy it has lost before entering the detector. In this case, only a lower bound on the neutrino energy can be calculated.

A simple energy estimator is the number of channels (DOMs) with at least one hit, called NChannel (N_{Ch}). On the other hand, N_{Ch} is strongly affected by the event geometry. Because of attenuation, the probability of a Cherenkov photon to eventually arrive at a DOM depends on its traveling distance and the local ice properties. Tracks passing close to an IceCube string produce more hits than tracks that are farther away while the DOMs inside the dust layer generally have fewer hits than DOMs in the clear ice layers. Figure 4.6(a) shows the correlation between N_{Ch} and the true muon energy for simulated data. With increasing energy, the N_{Ch} estimator becomes less accurate.

With IceCube the muon energy is not measured directly, but through the energy deposited inside the detector volume. From the total deposited energy and the length of the muon track in the detector, the average muon energy loss per unit length $\Delta E/\Delta X$ can be calculated. Figure 4.6(b) shows the correlation between the average muon energy loss and the muon energy for the same simulated data. Compared to N_{Ch}, it has a better correlation with the muon energy, which gives a smaller systematic uncertainty on the energy reconstruction.

Energy Likelihood Description

The muon energy reconstruction is usually performed in two steps. First, the track geometry of the muon is reconstructed without considering the energy. The position and direction obtained in this reconstruction is then used in a separate energy reconstruction.

The IceCube muon energy reconstruction, as it was used e.g. in the IC40 diffuse analysis [38], is based on an expected muon energy loss profile dE/dX, which can either obtained by an analytical parametrization or by means of numerical tables (as discussed below). Using this profile, the expected number of photo-electrons is calculated for each DOM. For a given track, it is a function of dE/dX and depends on the total light yield produced by the muon and the optical ice properties. For the reconstruction, the observed distribution $f(t)$ of photo-electrons in each DOM is compared to an expected distribution function $\mu(t)$. For this, $f(t)$ is binned into K time bins and it is assumed that the probability for each bin is given by Poissonian statistics. Since all DOMs act independently, the likelihood of the full event is given as the product over all DOMs with a hit,

$$\mathcal{L}_{\text{Event}}\left(f(t)\,|\,\mu(t)\right) = \prod_{j=1}^{N_{\text{DOM}}} \mathcal{L}_j, \tag{4.7}$$

where the likelihood for the DOM with index j is given by

$$\mathcal{L}_j = \prod_{i=1}^{K} \frac{\mathrm{e}^{-\mu_{i,j}} \mu_{i,j}^{n_{i,j}}}{n_{i,j}!}. \tag{4.8}$$

Here, $\mu_{i,j}$ is the expected number and $n_{i,j}$ the observed number of entries in the ith time bin of the jth DOM. This equation can be rewritten, using the total number of photo-electrons observed by a DOM $N_j = \sum_{i=1}^{K} n_{i,j}$ and the total number of expected photo-electrons $\mu_{\mathrm{tot},j} = \sum_{i=1}^{K} \mu_{i,j}$ in the same DOM, respectively

$$\mathcal{L}_{\mathrm{Event}} = \prod_{j=1}^{N_{\mathrm{DOM}}} \mu_{\mathrm{tot},j}^{N_j} \, \mathrm{e}^{-\mu_{\mathrm{tot},j}} \prod_{i=1}^{K} \frac{\left(\frac{\mu_{i,j}}{\mu_{\mathrm{tot},j}}\right)^{n_{i,j}}}{n_{i,j}!} \tag{4.9}$$

The term $p_{\mathrm{time,i,j}} = (\mu_{i,j}/\mu_{\mathrm{tot},j})$ corresponds to the probability to observe a given photo-electron in the ith time bin of the jth DOM. Taking the logarithm yields the expression

$$\log \mathcal{L}_{\mathrm{Event}} = \sum_{j=1}^{N_{\mathrm{DOM}}} \left[\sum_{i=1}^{K} (n_{i,j} \ \log p_{\mathrm{time,i,j}}) + N_j \ \log \mu_{\mathrm{tot},j} - \mu_{\mathrm{tot},j} - \sum_{i=1}^{K} \log n_{i,j}! \right]. \tag{4.10}$$

The first term in this equation depends on the normalized arrival time probability $p_{i,j}$ and is independent on the expected brightness (energy) of the track, whereas the second and third term only depend on the total numbers of expected and observed photo-electrons. The last term is a purely combinatorial factor that does not depend on the event parameters.

The expected number of photo-electrons arriving at a DOM can be either obtained from an analytical description or from simulations. Both methods have been implemented for the energy reconstruction in IceCube, as will be described below. $\mu_{\mathrm{tot},j}$ depends on the total light yield produced by the muon and the local optical ice properties. In a simple model, the total number $\mu_{\mathrm{tot,j}}$ of expected photo-electrons is assumed to scale linearly with energy E, e.g. for the jth DOM

$$\mu_{\mathrm{tot},j} = \frac{E}{E_{\mathrm{ref}}} \mu_{0,j} \tag{4.11}$$

where $\mu_{0,j}$ is the number of photo-electrons at a reference energy E_{ref}. In this case, the likelihood can be maximized using an analytical expression:

$$0 = \frac{\mathrm{d}}{\mathrm{d}E} \log \mathcal{L}_{\mathrm{Event}} = \sum_{j=1}^{N_{DOM}} \frac{N_j}{E} - \frac{\mu_{0,j}}{E_{\mathrm{ref}}} \tag{4.12}$$

$$\Rightarrow E = \frac{\sum_{j=1}^{N_{DOM}} N_j}{\sum_{j=1}^{N_{DOM}} \mu_{0,j}} E_{\mathrm{ref}} \tag{4.13}$$

where N_j is the number of photons observed in the jth DOM.

Photorec-llh

For the PHOTOREC-LLH reconstruction [137], the average muon energy loss is modeled as uniform along the track by a chain of mono-energetic cascades that are equally spaced by 1 m. This approximation is called the lightsaber model. The light yield from these cascades is parametrized with the cascade energy, using the parametrization described in section 3.3.1. The layered ice structure of the South Pole ice is incorporated through the PHOTONICS tables (section 4.3). With these tables, the expected number of photons arriving at each DOM is determined. Since the energy loss is modeled as uniform, the energy scaling equation 4.12 can be applied to the chain of cascades to calculate the average energy loss per meter. Finally, the muon energy is then calculated via equation 3.4.

MuE

Another method given by the MUE reconstruction [138]. Different to Photorec-llh, it uses an analytical description of the energy deposition along the muon track and does not include individual ice properties. The energy is reconstructed from the lateral photon density along the track, which is parametrized with the distance between DOM and muon track. This description relies on different approximations for scattering and absorption of the Cherenkov photons from the track, depending on the distance between track and hit DOM.

Both Photorec-llh and MuE reconstruction assume a continuous energy loss profile along the muon track. Due to the stochastic nature of the processes involved, the energy loss actually varies from muon to muon and it is not possible to accurately predict the position or the energy of the secondary cascades. This means that individual stochastic energy losses can produce many Cherenkov photons in large cascades and lead to large deviations from the average energy loss profile. In chapter 7, a complementary energy reconstruction method based on a Top-Down approach is presented. This method employs a direct comparison of individual events without the assumptions and simplifications that are necessary in the above described methods.

5 The South-Pole Acoustic Test Setup (SPATS)

Abstract

For the design of an acoustic detector array at the South Pole, the acoustic properties of the ice have to be known. These properties are the acoustic attenuation length, the ambient noise, sound speed and the rate of transient events. In order to determine these properties, the South-Pole Acoustic Test Setup (SPATS) has been deployed, using the infrastructure provided by the IceCube collaboration. The first part of this chapter gives an overview of the SPATS project, the installed instrumentation and data acquisition, with a focus on the measurement of the acoustic attenuation length using a retrievable pinger. In the second part, the latest results of SPATS are summarized.

5.1 Setup

The South Pole Acoustic Test Setup – SPATS – is an array of acoustic sensors which has been built to evaluate the feasibility of the acoustic neutrino detection at the South Pole [139]. Its primary goal is to measure the characteristics of the South Pole ice in the ultrasonic regime, at frequencies of 10 kHz to 100 kHz, namely the sound speed, the acoustic attenuation length, the ambient noise level and the rate of transient events. Additional measurements have been performed with a retrievable transmitter (pinger). The SPATS array consists of an in-ice component and additional equipment on the surface. Figure 5.1 gives a schematic view of the setup.

5.1.1 In-ice Components

The in-ice part of SPATS consists of four vertically instrumented cables (strings), which are deployed in the upper 500 m of selected IceCube holes to form a trapezoidal array, see figure 5.2. For the measurement of the attenuation length it is important to have a sufficient variation of the distance between transmitter and sensor. Therefore, the strings were positioned in such a way that a set of clearly distinguishable distances was obtained, see table 5.1(a).

SPATS was build in two phases, strings A, B, C were deployed in January 2007 (with IC22) and string D on 24th December 2007 (with IC40). Each of the four SPATS strings was deployed into a water-filled IceCube hole after installation of the respective IceCube string. A SPATS string is instrumented with seven acoustic modules, positioned at different depths. The depths of the modules at the individual strings are listed in table 5.1(b). A schematic view of a single module is shown in figure 5.4. The modules have a total length of 1.5 m and a diameter of 16 cm. Each module is equipped with both, a sensor and a transmitter. Hence, it is possible

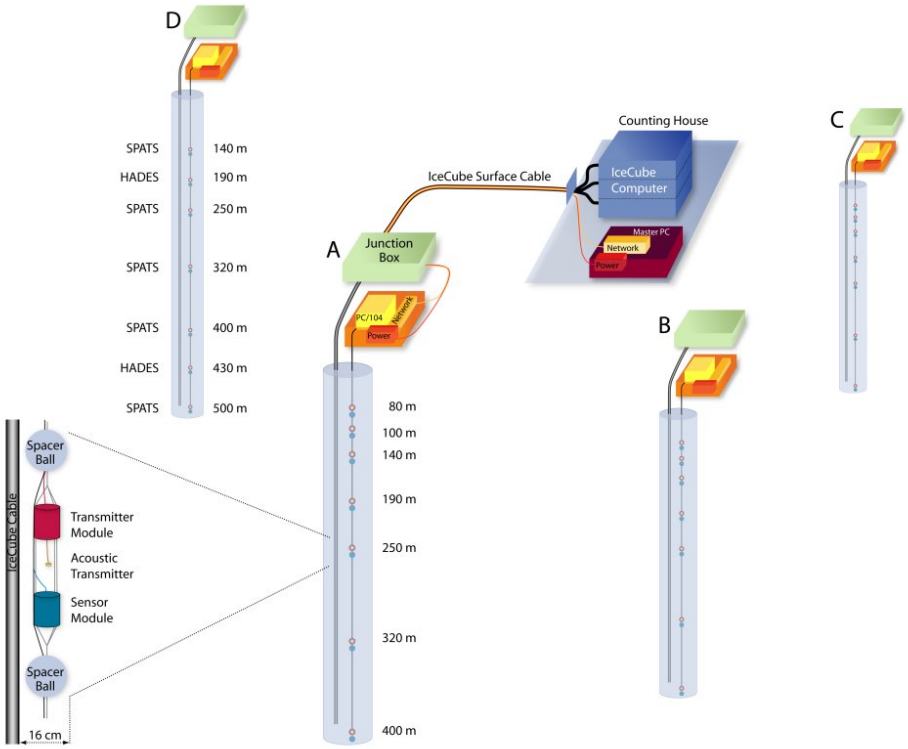

Figure 5.1: *Schematic view of the* SPATS *array with the four strings A-D and the depths of the acoustic modules at each string. The inset graphic to the left shows a single* SPATS *module, consisting of transmitter and sensor as well as two spacer balls.*

to send signals between different modules. In addition, all modules have two spacer balls to protect their sensitive equipment during the installation and to ensure a minimum distance to the IceCube cables. The sensor and transmitter electronics are contained in water-tight steel housings to withstand the high pressure in the ice and to protect the electronics against water during the deployment.

Three types of acoustical sensors have been developed for SPATS, called first and second generation SPATS sensors and HADES sensors. Figure 5.3 shows the three types. Strings A, B and C are deployed with the first generation SPATS sensors. Each of theses sensors has three channels, 120° apart, see figure 5.3(a). A channel consists of a cylindrical piezo-ceramic element that is pressed against the steel housing and is directly connected to an amplifier. It was discovered that the first generation sensors have a notable mechanical coupling between the three channels. String D is equipped with the improved second generation sensors, for which the three channels are mechanically decoupled. The development and testing of the SPATS sensors is described in [97, 139].

Two of the seven modules of string D are equipped with HADES sensors (Hydrophone for Acoustic Detection at the South Pole). The motivation to build these sensors was to develop an alternative to the SPATS sensors. Unlike the SPATS sensors, they are operated outside the pressure housing and therefore have a different coupling to the ice as well as to a different

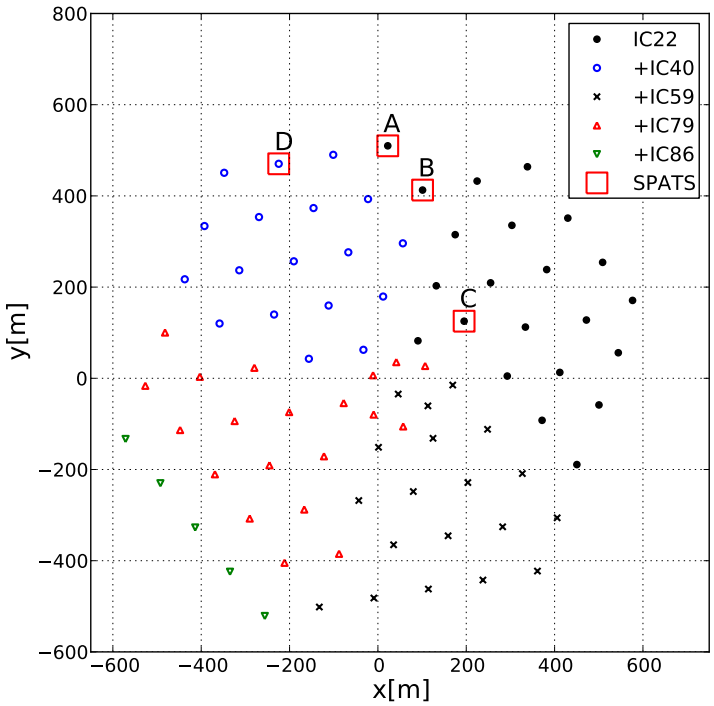

Figure 5.2: *Positions of the* SPATS *array within the* IceCube *detector. The different phases of the growing* IceCube *detector are illustrated.*

dynamic range. A HADES sensor consists of a ring-shaped piezo-ceramic element embedded in polyurethane for protection against water. Their development, optimization and first in-situ results are discussed in [140]. In the following, the individual sensors are referred to by the naming convention

$$(\text{string})\,\text{S}(\text{sensor}) - (\text{channel})$$

for example AS1-0 is the first channel of the first sensor on SPATS string A. The setup has proved to be robust and to work well under extreme environmental conditions. Since their deployment, all four SPATS strings are operational. There are only six malfunctioning channels, all three channels of AS3 and CS1 are either considered dead or have an unpredictable behavior. Overall, 74 of the $21 + 21 + 21 + 17 = 80$ channels are working properly.

Calibration

Prior to the deployment, the sensitivity and self-noise of the SPATS sensors have been measured under laboratory conditions. These measurements were performed in water, using a calibrated commercial hydrophone with a known spectral sensitivity [97]. In addition, a calibration has been performed in the Aachen Acoustic Laboratory (AAL) for sensors that have not been deployed but are similar in construction. The calibration was done in water and ice,

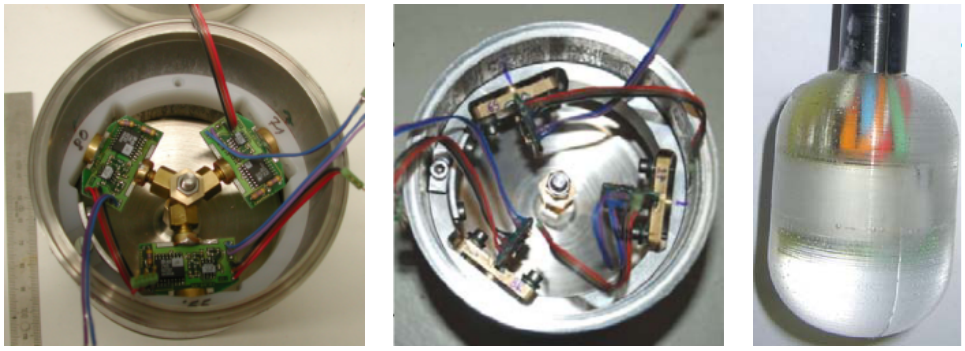

(a) (b) (c)

Figure 5.3: *The three different types of acoustical sensors that have been deployed with* SPATS*, namely the first generation (a) and second generation* SPATS *sensors (b) and the HADES sensors (c), [139, 140]. The* SPATS *sensors consist of three channels, attached to a steel housing – note the different attachment of the three channels.*

Table 5.1: *Horizontal distances between the* SPATS *strings A-D (a) and the depth (b) of the individual acoustic sensor modules at positions 1-7 in meters. String D has a different vertical spacing.*

(a)

strings	AB	AC	AD	BC	BD	CD
distance [m]	125	421	249	302	330	543

(b)

Position	1	2	3	4	5	6	7
A, B, C	80	100	140	190	250	320	400
D	140	190	250	320	400	430	500

using a reciprocity method [141, 142].

However, there is no in-situ calibration of the sensors for the South Pole ice. It is currently being investigated how the calibration results from the laboratory measurements can be applied to the sensors under the conditions at the South Pole, where they are subject to much lower temperatures. In addition, the sensors sensitivity also depends on the acoustic coupling of the sensor to the surrounding ice as well as the angular orientation of the sensor in the hole.

5.1.2 On-ice Components

Each SPATS string is connected to an acoustic junction box (AJB), located at the surface on top of each string. The AJBs are watertight aluminum boxes ($30 \times 50 \times 80\,\mathrm{cm}$), containing an embedded computer, called String PC. The String PCs are used to independently control the seven transmitters and sensors on each string.

Each String PC has three FADCs (fast analog-to-digital converters) with a maximum sampling rate of 1.25 MHz. The String PCs are connected to a Master PC, located in the IceCube Laboratory (ICL). The Master PC provides the central control for power, communication and synchronization of the String PCs and is also equipped with a GPS receiver. The GPS timing signal is distributed over the surface cables to the String PCs where it is used to mark the recorded data with an absolute time stamp.
The analogue signals from the SPATS channels sent to the corresponding String PCs where they are digitized and compressed, before they are sent to the Master PC. The three channels of each sensor are digitized by a different FADC board, which allows to read out all three channels simultaneously.
The data from all strings are stored on the Master PC until it is transferred by satellite to the data servers in the northern hemisphere. SPATS has a limit of 150 MB/day for direct satellite transfer. All data exceeding this quota is automatically queued for tape archiving. For detailed information on the on-ice hardware, see e.g [79, 139, 143, 144].

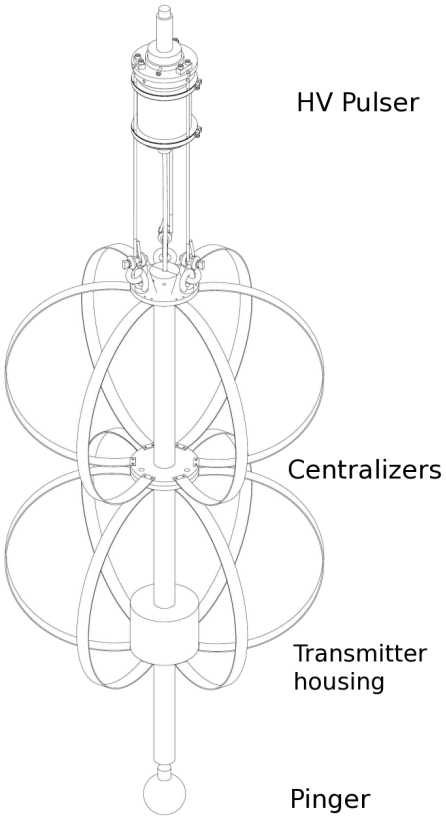

Figure 5.4: *Schematic view of the complete pinger module, consisting of the spherical transmitter, the pressure housing with the board electronics, a high voltage power supply (HV pulser) and centralizers. The pinger module has a length of* 2 m *and a radius of* 50 cm, *image by [145].*

5.1.3 Pinger

In addition to the permanent in-ice array, a retrievable transmitter has been deployed three times during the construction phases of IceCube in the austral summers in seasons 2007/08, 2008/09 and 2009/10. The positions of the frozen-in SPATS strings are fixed, with a maximum horizontal distance of 543 m between two strings (table 5.1(a)). With the pinger it was possible to study the ice properties from different positions and directions and to further increase the baseline between transmitter and sensor.

The pinger was lowered in the water-filled IceCube holes immediately after the drilling and prior to the deployment of the IceCube instrumentation. This allowed for a small time window of a few hours for acoustic measurements. The setup consists of three parts, the

retrievable part with the transmitter, the surface electronics and the cable payout system with a 2700 m long cable spooled over a winch. The retrievable pinger as it was used in 2008/09 and 2009/10 is shown in figure 5.4. It consists of a pressure housing containing the control electronics, a spherical transmitter at the bottom and three pressure sensors (SeaStar) which were used for the depth measurement (see section 6.2.1). The main difference to the first pinger measurements in 2007/08 is that this setup uses brass spring ribs to centralize the pinger in the IceCube hole and therewith suppresses random movement of the pinger. This has greatly improved the quality of the data samples as is discussed in section 6.2.

The transmitter is a spherical piezo-ceramic with a diameter of 10.8 cm which is located 2 m below the pressure housing. The pinger has been thoroughly tested in laboratory measurements (see [144] for details). There, the directivity of the pinger emissions has been confirmed as omni-directional while the frequency spectrum shows a distinct resonance at 16.5 kHz.

The pinger transmitter was driven by a high-voltage pulser with different settings for the various seasons. In 2007/08 and 2008/09 the voltage signal generated by the pinger board was a short sinusoidal half wave which led to the emission of a 100 μs burst, see [144]. In 2009/10 a different setting was used to investigate a possible frequency dependence of the attenuation length. The pinger was operated with 64 cycles sine waves at three different frequencies, 30, 45 and 60 kHz, which were sent in an alternating sequence during the measurements.

5.1.4 Acoustic Data Taking

The SPATS data taking is controlled by automated scripts installed locally on each String PC. There is a variety of specialized data taking modes. In most of these modes, the three channels of each sensor are read out simultaneously, while the sensors on the same string are read out subsequently. The different acoustic data taking modes are:

- **Inter-string:** An acoustic pulse is sent from the transmitter of one SPATS module and is recorded by a sensor of a module on another string.
- **Intra-string:** A sensor records the acoustic signals sent by the transmitter of another module on the same string.
- **Intra-module:** A sensor records acoustic signals originating from the transmitter of the same module. This data has been useful to investigate to freeze-in process after deployment.
- **Pinger runs:** The pinger sends acoustic pulses in a regular interval, for season 2008/09 it was 10 Hz, while the three channels of a sensor simultaneously recorded the pinger signal for 18 s with a sampling rate of 200 kHz. The measurements at the South Pole with the pinger and the determination of the acoustic attenuation length with this data is subject of chapter 6.
- **Untriggered noise:** The ambient noise is recorded for 0.1 s at 200 kHz sampling rate. A histogram of the ADC counts is recorded. This data is used in to investigate the ambient noise.

- **Triggered noise (transients):** If the number of ADC counts on any channel is above a certain threshold, a 5 ms window of data is taken for this channel and marked as a transient event. These runs are used to study the rate and the nature of transient background events, see section 5.2.5.

- **Monitoring:** These runs are performed every day and include a read out of the temperature and pressure sensors inside the modules, the temperature of the FADC boards, the network status, disk space and a list of the transferred files. A summary of this information is sent to the SPATS collaborators, which allows to take immediate action in case of any irregularities.

Currently the SPATS data taking is concentrated on the transient mode, i.e. recording triggered noise. 48 minutes of each hour are dedicated to this mode, while the remaining 12 minutes are reserved for untriggered noise runs and monitoring runs.

5.2 Recent Results of SPATS

5.2.1 Attenuation Length

The acoustic attenuation length is a crucial parameter for the final design of an acoustic neutrino detector in the ice at the South Pole. Within the SPATS project, several approaches to determine the acoustic attenuation length have been applied. These approaches rely on different sets of measurements, namely the pinger measurements, SPATS inter-string runs and the analysis of transient events. The various methods and their results are presented in chapter 6.

5.2.2 Ambient Noise

Figure 5.5(a) shows a typical noise histogram, where the noise data from one month has been combined. This data is taken from the dedicated noise data stream which is used to monitor the performance of SPATS. For most of the channels the noise is well-described by a Gaussian, with a few exceptions of channels that are considered malfunctioning or 'dead'.

Figure 5.5(b) shows the long-term time evolution of the noise for all channels at two different sensors. There are a few notable features seen by all channels. After deployment of a SPATS string, the noise on each channel increased steadily for several weeks until it became stable. This increase is believed to indicate the improved acoustic coupling of the surrounding bulk ice to the sensor during the re-freezing. After the water in the holes is frozen, the noise is stable. The spikes seen in the figure are correlated with the drilling of other IceCube strings nearby the respective SPATS string. Apart from that, there is no evidence for any short-term variation of the noise due to the weather or from anthropogenic sources. In other words, the in-ice sensors seem to be unaffected by the surface noise.

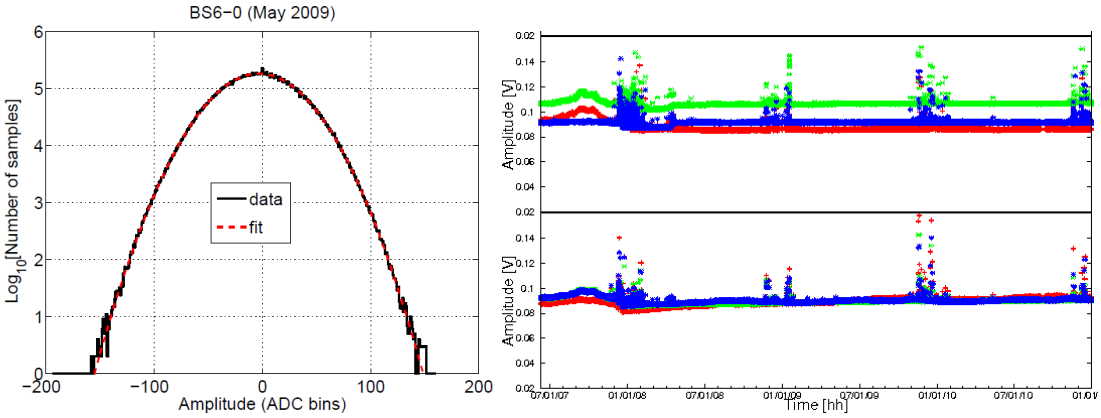

(a) (b)

Figure 5.5: *(a) Histogram of the noise amplitude in ADC counts (from [79]) for an example (channel BS6-0), using all data from May 2009. The noise is very well described by a Gaussian. (b) Long term time evolution of the Gaussian noise amplitude (given by the standard deviation of the noise histograms) for the three channels of two* SPATS *sensors (top: CS3, bottom: CS4), the graph was obtained from the monitoring web page [146].*

5.2.3 Sound Speed

Figure 5.6 shows the results of the measurement of the acoustic sound speed with SPATS , as presented in [99]. The sound speed as a function of depth, called sound speed profiles, was obtained for both pressure (v_P) and shear waves (v_S). The result for the pressure wave is in agreement with earlier measurements in the firn ice by Weihaupt [59]; the transition from the firn to the bulk ice is also clearly visible. The sound speed ratio is $v_P/v_S \sim 2$, which agrees with the expectations (see equation 3.28). Applying a linear fit to the sound speed profiles between 250 m and 500 m depth gives

$$\begin{aligned} v_P(375\,\mathrm{m}) &= (3878 \pm 12)\,\mathrm{m/s} \\ \mathrm{d}v_P/\mathrm{d}z &= (0.087 \pm 0.13)\,\mathrm{s}^{-1} \\ v_S(375\,\mathrm{m}) &= (1975.8 \pm 8.0)\,\mathrm{m/s} \\ \mathrm{d}v_S/\mathrm{d}z &= (0.067 \pm 0.086)\,\mathrm{s}^{-1}. \end{aligned}$$

The sound speed gradient $\mathrm{d}v/\mathrm{d}z$ is consistent with zero for both wave modes, which in principle allows for a good reconstruction of the acoustic sources without the need for ray-tracing algorithms, see section 3.4.2.1. Finally, these measurements confirmed that the preferable position for acoustic detectors is in the bulk ice below 200 m. Complementary to the in-situ measurements, laboratory measurements of both pressure and shear waves has been performed in a $3\,\mathrm{m}^3$ volume of bubble-free ice [147, 148] with temperatures between 0 and $-20\,^\circ$. While there is a similar temperature dependence, the absolute values of the sound speed are about $50\,\mathrm{ms}^{-1}$ above the previous measurements. This deviation is attributed to the absence of air bubbles in the laboratory setup.

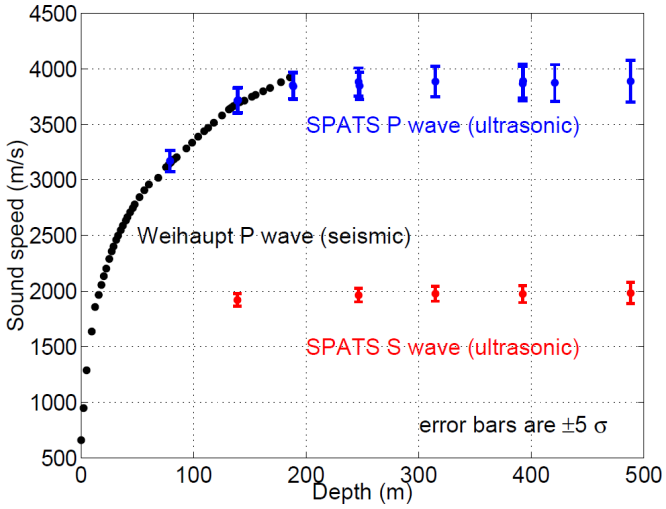

Figure 5.6: *The result of the* SPATS *sound speed measurement [99] for both pressure and shear waves as a function of depth. The seismic measurements by Weihaupt [59] are shown for comparison. Note that the error bars for the* SPATS *measurements are at* $\pm 5\sigma$ *in order to be visible; there is no uncertainty estimate available for the Weihaupt result.*

5.2.4 Shear Waves

The SPATS array has detected shear waves from artificial sources, namely the SPATS transmitters and the pinger, see [149]. From laboratory measurements with frozen-in piezo-electric emitters [148] it is known that the direct coupling of the emitters to the ice can generate shear waves. Therefore it was not surprising to find shear waves originating from the frozen-in SPATS transmitters. The pinger, on the other hand, was operated in water-filled IceCube holes. As shear waves cannot propagate through fluids, in this case they have to be produced by mode conversion either at the water-ice surface (the hole wall) or at grain boundaries. The latter case would occur randomly and lead to incoherent smaller shear waves along the path of the initial pulse and not to a single large-amplitude shear pulse as it is observed. Moreover, for all measurements the arrival time of the shear wave correlates with the arrival time of the primary pressure wave and the distance. A plausible explanation is a mode conversion at the water-ice interface, i.e. the hole wall.

The transmission and reflection coefficients of longitudinal and shear waves as function of the incidence angle and the medium properties on both sides of the interface, are described by the Zoeppritz equations. In section 3.4.2.3 it was described that the mode conversion can happen for any non-zero incident angle, but is suppressed for a normal incidence. Therefore, shear waves are created along diagonal paths, where the pinger and the sensor are in different depths.

5.2.5 Transients

Currently, the SPATS array operates in the transient detection mode (see section 5.1.4). This mode uses a simple threshold trigger requiring that the number of ADC counts at any

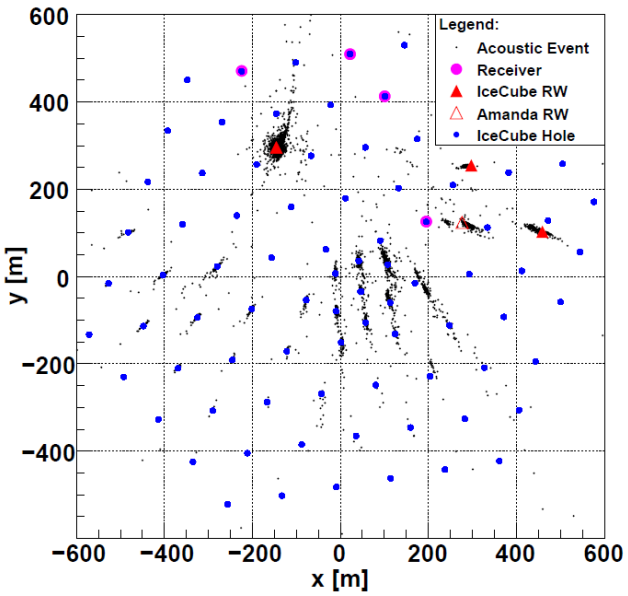

Figure 5.7: *The reconstructed vertexes in the horizontal plane for all transient events detected since August 2008 [40]. Shown are positions of the* SPATS *strings, the* IceCube *holes and the sources of transient noise, which are the Rodriguez Wells (RW) and the refreezing IceCube holes. The smearing effect is an artifact of the vertex reconstruction algorithm.*

predefined channel exceeds a signal to noise ratio of SNR ≥ 5.2. If that trigger condition is met, a small time window of data is recorded for the corresponding channel. The value of SNR was chosen to achieve a data volume of $\sim 100\,\mathrm{MB}$ of transient data per day on all SPATS strings, which is safely within the 150 MB satellite bandwidth quota for SPATS. The rate of the triggered events is relatively stable at about 1 Hz.

While most of these transient events are fluctuations of Gaussian noise, many of them could be identified as genuine non-Gaussian events, for a discussion see [79, chapter 7]. These events are analyzed offline with a time-clustering algorithm by selecting coincident pulses that happen within the same 200 ms time window. This corresponds to the time that is needed for an acoustic pulse to cross the whole SPATS array. A cluster of hits is likely to originate from the same acoustic event and a vertex reconstruction applied to trace its origin.

Figure 5.7 shows the spatial distribution of the reconstructed transient sources between September 2008 and October 2009. For a discussion of these results, see [40]. The data shows a number of hot spots, which are identified with either freshly drilled IceCube holes or the shallow artificial water-filled caverns ("Rodriguez wells") used during the drilling. It is assumed that the majority of transients is produced by cracking of the re-freezing and moving ice at these sources. The absence of any transient signals other than those from known sources allows to calculate a limit on the acoustic detection of high energy neutrinos, see [40] for a discussion and the results of these calculations and section 2.2.5 for the comparison with current limits on neutrino detection.

6
The Acoustic Attenuation Length

Abstract

The acoustic attenuation length is an important parameter for the design of a future acoustic neutrino detector. Within SPATS, there are several independent and complementary approaches to determine the attenuation length using different data samples and different analysis techniques. The subject of this chapter is the determination of the acoustic attenuation length in the South Pole ice from in-situ measurements with the pinger. In the following, the analysis strategy and results are presented and possible systematics are discussed. Finally, the results are compared to other attenuation length analyses of the SPATS *data.*

6.1 Attenuation

The acoustic attenuation length can be determined by comparing the amplitude of an acoustic signal for different traveling distances of the signal. In this analysis, measurements performed with the pinger at different distances to a SPATS channel are compared. Figure 6.1 shows the waveforms of single pinger pulses, as recorded by a single SPATS channel. The waveforms are measured with the same channel, but at different pinger positions and hence with a different traveling distance of the signal. The attenuation of the signal with distance is clearly visible. Also shown are the Fourier spectra of the waveforms after noise was subtracted (this is described in section 6.3).

There are different observables that have been considered to determine the attenuation length from the SPATS waveforms. For the analysis presented here, an "effective amplitude" has been defined as

$$A_{\text{eff}} = \sqrt{E}. \tag{6.1}$$

where E is the total energy of the waveform recorded by a particular channel in response to an incoming acoustic pulse. The energy is calculated from the signal waveform $x(t)$ in frequency or time domain by

$$E = \int_{\Delta T} |x(t)|^2 \,\mathrm{d}t = \int_{\Delta \nu} |X(\nu)|^2 \,\mathrm{d}\nu, \tag{6.2}$$

$$X(\nu) = \frac{1}{\sqrt{2\pi}} \int_{-\infty}^{+\infty} x(t)\, \mathrm{e}^{-i2\pi\nu t} \,\mathrm{d}t \tag{6.3}$$

where $X(\nu)$ is the Fourier transform of the waveform with a time and frequency range ΔT and $\Delta\nu$, respectively. Other possible observables are amplitude of the first peak in the waveform,

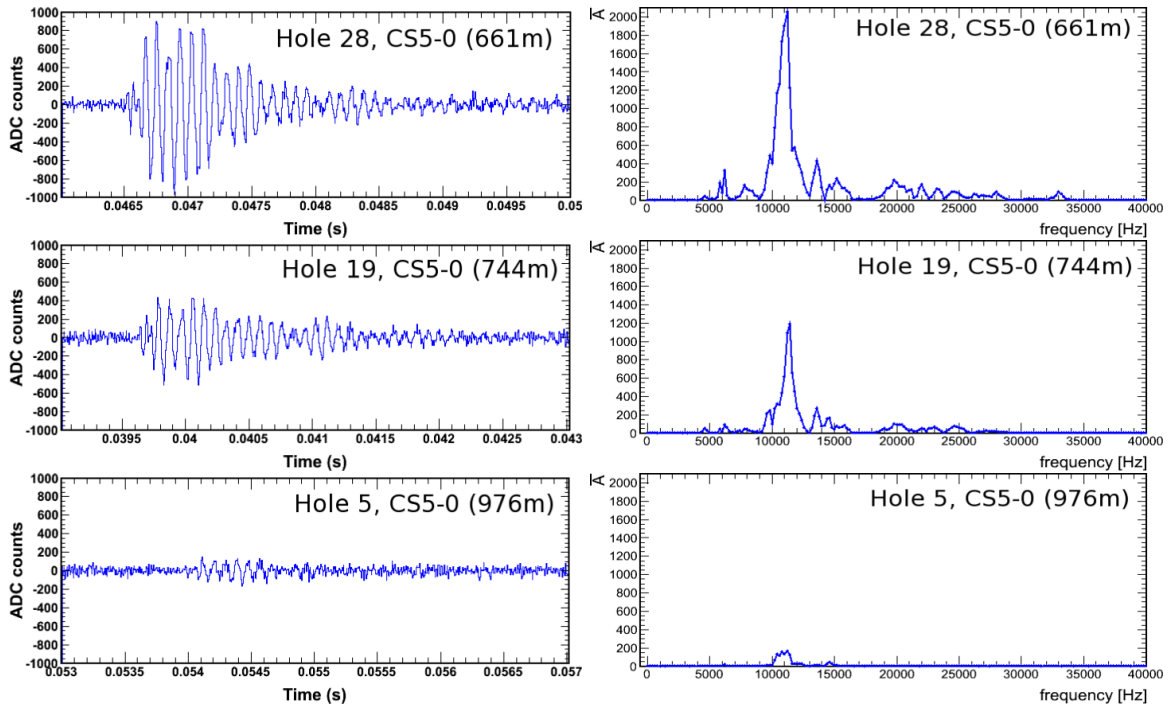

Figure 6.1: *The waveform and its Fourier transform (in arbitrary units) of a single pinger pulse recorded by SPATS channel CS5-0 at three different distances between channel and pinger. The y-axes in all figures are set to the same scale for comparison.*

the peak-to-peak amplitude between the first two peaks or the maximum number of ADC counts of the waveform. Because the shape of the waveform varies from channel to channel, these observables are considered as less reliable than the energy.

Following section 3.4.2.2, the effective amplitude as function of the distance is given by

$$A_{\text{eff}}(d) = \frac{A_0}{d} \cdot \mathrm{e}^{-\alpha\, d} = \frac{A_0}{d} \cdot \mathrm{e}^{-d/\lambda}, \tag{6.4}$$

with the distance d between the pinger and the channel, the attenuation coefficient α and attenuation length λ, respectively. A_0 includes the individual channels sensitivity, the transmittivity of the pinger and the coupling of the pressure pulse from the pinger into the ice. Therefore, A_0 is a function of the direction and it is difficult to disentangle the actual signal attenuation from the angular dependence of sensitivity and transmittivity for arbitrary combinations of channels and pinger positions. In addition, none of the deployed SPATS channels has been calibrated in ice. In order to minimize the effect of the angular dependence of A_0 in the analysis, the following restrictions are applied

- Only data obtained from measurements with the same SPATS channel are compared. Hence, the determination of α via equation 6.4 is independent of variations between different channels. The attenuation coefficient will be determined for each channel separately.

- Ideally, use a fixed angle between pinger and channel. More specifically, perform all measurements in a horizontal plane with respect to the channel. This reduces the angular

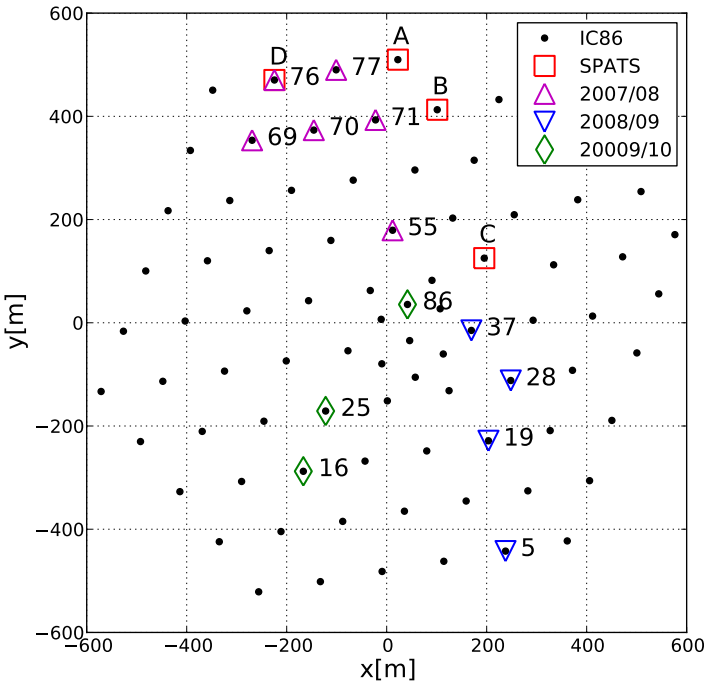

Figure 6.2: *Layout of all pinger measurements from 2007 to 2010, showing the surface coordinates of the IC86 detector, the* SPATS *array and the measurements with the pinger. The measurements in season 2007/08 are very close to the* SPATS *strings, whereas in the following seasons, the measurements were performed at larger distances. In addition, for the last two seasons the pinged holes are roughly in a straight line.*

dependence of the setup. In section 6.2, it will be shown, that the measurements with the pinger in season 2008/09 allowed for a data sample with a small angular variation.

With these restrictions, the dependence of A_0 on the direction is minimal and the attenuation coefficient is obtained by fitting the effective amplitudes as a function of the distance. Equation 6.4 is transformed to a linear equation using the new variable $y = \log(A_{\text{eff}}\, d)$:

$$\log(A_{\text{eff}}\, d) = -\alpha d + \log A_0 \tag{6.5}$$

$$y = -\alpha d + \beta, \tag{6.6}$$

with the attenuation coefficient α as the slope and the intercept β. A linear fit on the data determines the two parameters α and β and their respective errors $\Delta\alpha$ and $\Delta\beta$.

6.2 Pinger Data Sample

Geometry of Pinger Measurements

During the pinger measurements, the pinger is used to send acoustic pulses from different positions in several water-filled IceCube holes which are then recorded by the SPATS array.

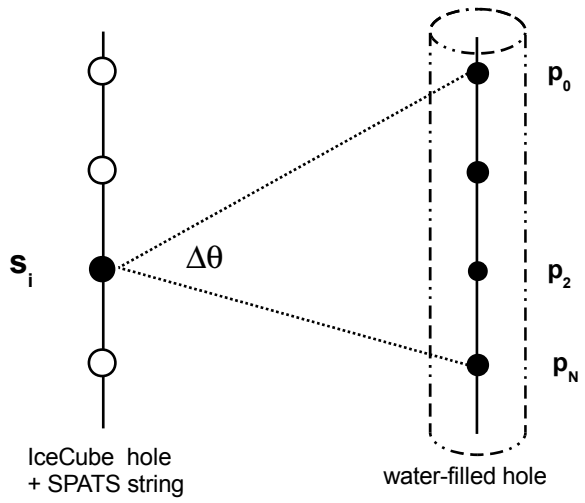

Figure 6.3: *The "vertical" analysis scenario. For a particular sensor s_i all measurements from all pinger stops p_i in the same hole are combined. This setup naturally leads to a large zenith variation $\Delta\theta$.*

It was deployed into newly drilled IceCube holes within the short time span between drilling and deployment of the optical equipment during three austral summers. Figure 6.2 shows the layout of all pinger measurements during the three seasons from 2007 to 2010. The layout is a result of the compromise between optimum geometry for the attenuation analysis and the actual availability of drilled IceCube holes and personnel at the time of deployment.

While the pinger is lowered and pulled back again to the surface, the sensors on all four SPATS strings are read out in a pre-defined sequence, while the pinger continuously sent pulses with a repetition rate of 10 Hz. At each position for which there was a SPATS sensor at the same depth, the pinger was kept stationary for a duration of ≈ 5 minutes, which guaranteed that the pinger was not moving during the measurement and that for every channel at least one complete waveform was recorded. The length of the waveform was 9 s in 2007/08 and 18 s in 2008/09.

For the attenuation length analyses, data from different pinger stop positions are combined. Figures 6.3 and 6.4 shows two different analysis scenarios, distinguished by the relative position between pinger and the respective sensor. Taking a particular sensor as the reference, these scenarios are:

- **vertical:** Data from the measurements at different stopping positions in the same hole are combined, see 6.3. In this case, the pinger and the sensors are at different depths. While there is no azimuthal variation, the zenith-dependence of the sensitivity of the sensors channels have to be taken into account. In addition, the transmission of the pinger pulses from water to ice depends on the incidence angle.

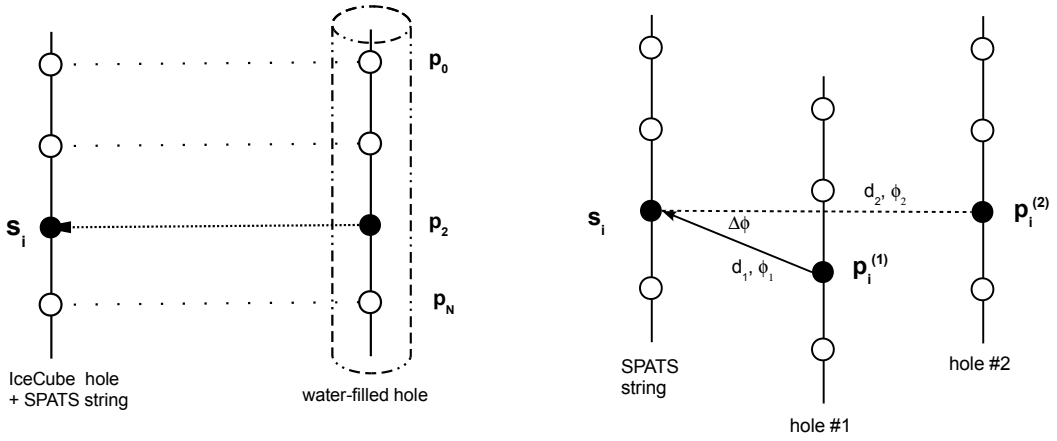

(a) (b)

Figure 6.4: *The "horizontal" analysis scenario, For a particular sensor s_i only the pinger positions p_i with the same depth are used (a). Combining measurements from measurements in different holes leads to an azimuthal variation $\Delta\phi$ (b).*

- **horizontal:** Data from measurements in different holes are combined, while the pinger and the sensors are at the same depth, see figure 6.4. In this case, the zenith variation is minimal, while the azimuthal variation depends on the positions of the pinger holes. The maximum azimuthal spread of the measurements in each season is shown in table 6.1.

Shear Waves and Reflections in the Data

With SPATS, shear waves have been observed during all pinger campaigns, but their occurrence is different for the individual seasons. During the pinger measurements, shear waves are produced for non-zero incidence angles of the pinger pulses with respect to the hole wall. Basically, there are two possible scenarios. First, for every diagonal path where the pinger and the sensor are in different depths and secondly, in the horizontal plane if the pinger is not centralized in the hole. While diagonal shear waves have been observed for all seasons, only the data from season 2007/08 has a notable presence of shear waves in the horizontal configurations.

During this season, the pinger was operated without centralizers, and hence it is believed to have performed irregular pendulum movements inside the hole. The measured amplitudes of both P and S wave varied on short time scales $\mathcal{O}(0.1\,\mathrm{s})$ while their relative heights were anti-correlated [79]. Following the Zoeppritz equations (section 3.4.2.3), this indicates that the total amount of energy was roughly conserved, whereas the partitioning between the wave modes varied as the pinger swung in the hole and the incidence angle changed. This is because the transmission of the pinger pulses from the hole into the ice depends on the incidence angle, see section 3.4.2.3. Depending on the position of the pinger inside the hole, a part of

the energy is converted into shear waves while another part is reflected. The movement of the pinger therefore led to a complicated pattern of shear waves and reflections with varying relative pulse heights.

This assumption is supported by the fact, that horizontal shear waves are greatly suppressed in the data of the following seasons (2008-2010), for which the pinger was centralized.

Pinger 2007/08 Data

In season 2007/08, the measurements were performed in IceCube close to the SPATS array, which had been constructed a year earlier. This leads to two important constraints on the analysis of this data sample. First, the distances between the pinger and the SPATS sensors are rather small. Table 6.2(a) shows the horizontal distances between the pinged holes and the respective SPATS strings, the range is 124.5 m to 543 m. Secondly, the azimuthal spread between the individual measurements is large, as the pinged holes were close or even inside the trapezoidal SPATS volume, see table 6.1 and figure 6.2. Considering the angular-dependent sensitivity of the SPATS channels, a large angular variation naturally complicates the comparison of the measured amplitudes.

The quality of the 2007/08 data sample is further diminished the occurrence of shear waves and reflections. As a consequence, the 2007/08 data are not used for this analysis.

Pinger 2008/09 Data

In season 2008/09, pinger measurements have been performed in four holes with 9 stops in each hole, ranging from 190 m to 500 m, see table 6.5 for a example. The sensors in the firn layer above 190 m were excluded in these measurements. Due to a different geometry of the layout of the measurements, the 2008/09 data is less affected by angular variations, compared to the previous season. The holes where the pinger was deployed, are roughly aligned in a straight line, while all holes are further away from the SPATS array, see figure 6.2. As a result, the maximum azimuthal spread is lower, $\Delta\phi \leq 12\,^\circ$, see table 6.1 and the maximum horizontal distance is considerably larger, about a kilometer, see table 6.2(b).

The uncertainty of the pinger depth measurement of 5 m (section 6.2.1), leads to an uncertainty of the zenith angle. The half opening angles θ for the smallest ($d = 157\,\mathrm{m}$) and largest ($d = 1023\,\mathrm{m}$) distances between pinger and sensor are given by

$$\begin{aligned} \theta &= \arctan\left(5/d[\mathrm{m}]\right) \\ \theta_{157\,\mathrm{m}} &\approx 2\,^\circ, \quad \theta_{1023\,\mathrm{m}} \approx 0.3\,^\circ \end{aligned} \tag{6.7}$$

For this season, the pinger was re-designed and supplemented with brass stabilizers, described in section 5.1.3. Besides the prevention of the undesired pinger movements, this design also centralized the pinger inside the hole. This resulted in a small incidence angle of the pinger pulses on the hole wall and therefore to a suppression of the mode conversion in the horizontal plane. Shear waves were still found on diagonal paths (vertical analysis scenario) but with a

lower intensity than in the previous data sample.

Pinger 2009/10 Data

For the pinger measurements in season 2009/10 the pinger was deployed in three IceCube holes which are roughly in a straight line with SPATS string C. The maximum azimuthal spread is larger compared to 2008/09 (but still smaller than for 2007/08). Four stopping positions were chosen, three at the SPATS levels in 140, 250 and 320 m depth and one additional deep stop below 500 m. For the attenuation analysis, the pinger stops at 250 and 320 m are used, resulting in 2 different depths compared two 5 depths in season 2008/09. In addition, the pinger was modified and operated at three different frequencies, see section 5.1.3.

Table 6.1: *Azimuthal spread $\Delta\phi$ of the pinger measurements of all three seasons, showing the maximum difference of the azimuth between the measurements at the same* SPATS *string.*

season	A	B	C	D
2007/08	79 °	90 °	35 °	120 °
2008/09	7 °	7 °	11 °	12 °
2009/10	9 °	6 °	19 °	20 °

Table 6.2: *Horizontal distances in meter between the pinger and the* SPATS *holes during the measurements in season 2007/08 (a) and in season 2008/09 (b). Note that* SPATS *string D was deployed in hole 76 after the other pinger measurements.*

(a)

pinger hole	A	B	C	D
55	330.5	250.0	190.8	-
70	215.3	249.5	421.6	-
71	124.3	124.5	344.6	-
77	124.7	216.4	469.7	-
76	249.2	330.3	543.0	-
69	329.8	374.5	517.2	124.9

(b)

pinger hole	A	B	C	D
5	976.0	866.1	569.6	1023.4
19	743.5	632.1	335.7	807.5
28	661.2	544.9	243.3	750.0
37	567.2	453.4	156.5	653.3

6.2.1 Pinger Depth Measurement

The analysis of the pinger data requires information on the distance between transmitter and sensor and thus the position of the pinger in the hole. The horizontal position of the pinger is well known and is the same as the position of the corresponding IceCube hole. Its depth however, has to be determined from the measurements. For this, two independent methods have been used [143].

Position	Payout	SeaStar
190	188.0	184.4 +- 2.6
250	250.8	246.1 +- 3.4
320	319.6	316.1 +- 3.8
400	400.3	396.6 +- 4.8
500	499.8	497.1 +- 4.5
400	400.2	397.4 +- 4.5
320	320.0	317.7 +- 4.2
250	249.9	247.2 +- 4.1
190	189.9	188.2 +- 3.8

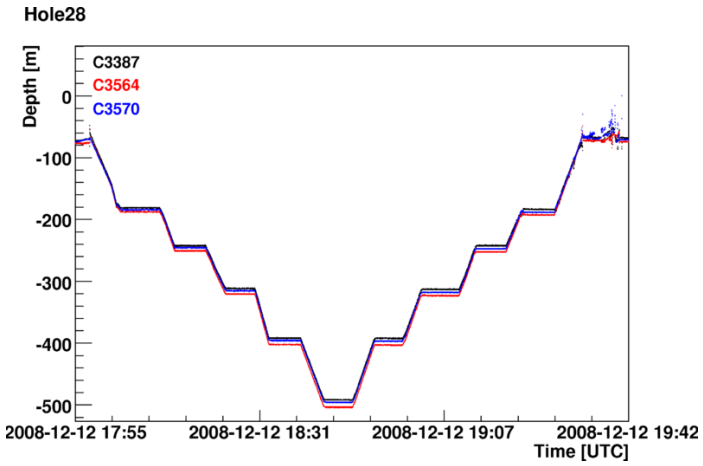

Figure 6.5: *The depth of the pinger versus time during the measurements in hole 28 with clearly visible stops at the individual depths. The depth is calculated from the pressure measured by the SeaStar sensors. Shown in the table are the nominal pinger stopping depth and the results of the independent depth measurements by cable payout system and the SeaStar pressure sensor readout for the pinger measurement in hole 28. The error of the latter is given by the spread of the three SeaStar sensors [143, 150].*

The first method is to use the value given by the cable payout system during the deployment of the pinger, which is basically the length of the cable in the hole.

The second method is to use the pressure measured by the SeaStar sensors, see section 5.1.3. Assuming an incompressible fluid, the conversion of the pressure readout to depth is given by the formula

$$d = w + \frac{1}{\rho g}(P - P_0) + a, \tag{6.8}$$

with the well depth w, density ρ, gravitational acceleration g, the pressure readings at depth P and at surface P_0 and the distance of the SeaStar sensors to the transmitter unit a. The well depth is the distance from surface to the water level in the hole.

Because of the high pressures found deep in the water-filled bore-holes, the compressibility of water has to be considered. In addition, even small levels of aeration produced during the drilling will significantly change the compressibility, see figure 6.6. For the maximum depth of the pinger at 500 m, the deviation due to the water compressibility is ~ 50 cm, and therefore negligible.

Both methods have been applied during the pinger measurements. An example of the results from the pressure methods and the comparison to the payout method is shown in figure 6.5. The movement of the pinger down and up the hole and the stops at various depths are clearly visible in the data. The spread between the three SeaStar sensors is taken as error estimate. Using this error, the two depth measurements are in agreement.

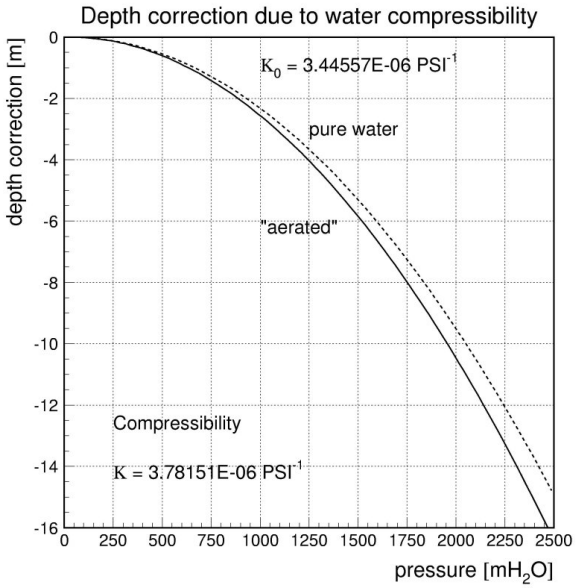

Figure 6.6: *The depth correction due to water compressibility as a function of pressure for pure and aerated water, from [151]. In this figure, the compressibility is given in* PSI^{-1} *(pound per square inch), with* $1\,\mathrm{PSI} \approx 6895\,\mathrm{Pa}$. *At the bottom of IceCube the deviation is* $\sim 15\,\mathrm{m}$.

6.3 Frequency Domain Pinger Analysis

6.3.1 Data Selection

The attenuation length analysis presented in the following is performed on the 2008/09 data sample and therefore benefits from its small angular variation. The 2009/10 data sample is used as a cross check and for a dedicated study of the frequency dependence of the acoustic attenuation length. The following constraints are applied to the data to reduce various systematic effects:

- **Angular variation:** Pinger and channel are required to be at the same depth. As explained in the previous section, constraining the pinger 2008/09 data sample to horizontal measurements conveniently narrows the angular range. As a result, all systematic effects coming from the angular dependence of channels, the pinger transmission or the ice itself are minimal (but not zero).

- **Fixed channel:** The analysis is performed for each channel separately, which means that only the measurements from the same channel but with different pinger positions are compared. This removes all systematic effects that would be introduced by comparing different channels with their individual absolute calibration and corresponding uncertainties.

- **HADES:** The two HADES channels at string D are not considered in this study because they have a different coupling to the ice and dynamic range and hence different systematic effects.

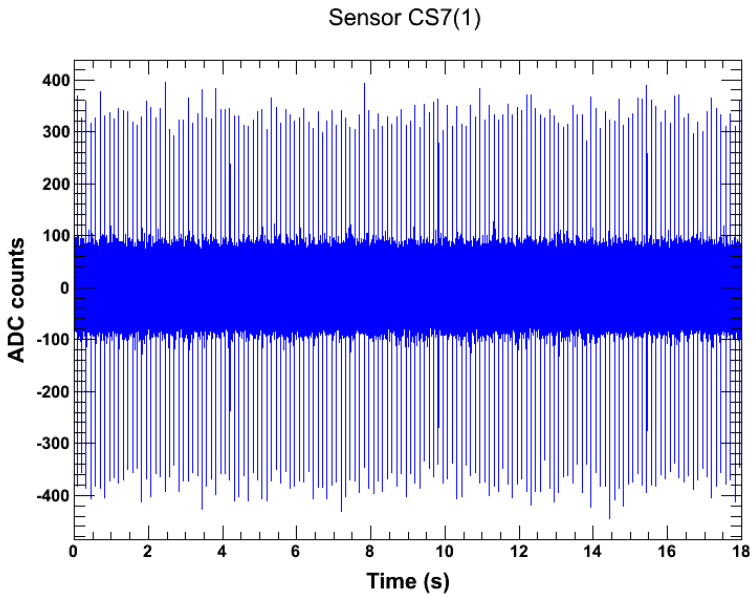

Figure 6.7: *A full* 18 s *waveform recorded by channel CS7-1 while the pinger was in* IceCube *hole 37. The waveform contains 144 pinger pulses because hole 37 was probed with a pinger repetition rate of* 8 Hz *instead of* 10 Hz *as for the other holes.*

6.3.2 Pulse Extraction

Pulse Timing

With the pinger setup in 2008/09, all three channels of the same sensor are read out simultaneously for 18 s and with a sampling frequency of 200 kHz. The pinger sent pulses with a repetition rate of 10 Hz. Therefore, each data file contains a sequence of 180 pinger pulses, where the time difference between two successive pulses is 0.1 s. Figure 6.7 shows an example SPATS waveform with all pinger pulses and figure 6.8 shows the waveform of a single pinger pulse. For all measurements in hole 37, the repetition rate was 8 Hz, resulting in 144 pinger pulses with a time difference of 0.125 s in this case.

The timing of the pulses is obtained by calculating the autocorrelation of each waveform. For the real-valued waveform $x(t)$, it is given by

$$R(\tau) = \frac{1}{\Delta T} \int_{-\Delta T/2}^{\Delta T/2} x(t)\, x(t+\tau)\, \mathrm{d}t,$$

and for discrete data points, where x_n is the value at time t_n

$$R_j = \frac{1}{2N+1} \sum_{n=j-N}^{j+N} x_n\, x_{n-j}, \tag{6.9}$$

where $2N+1$ matches the time interval ΔT. In the calculation of R, a time interval of $\Delta T = 1$ ms is used, corresponding to the typical length of the waveforms of the recorded pinger signals, see figure 6.8(b). While the signal follows a certain periodicity, uncorrelated noise has a

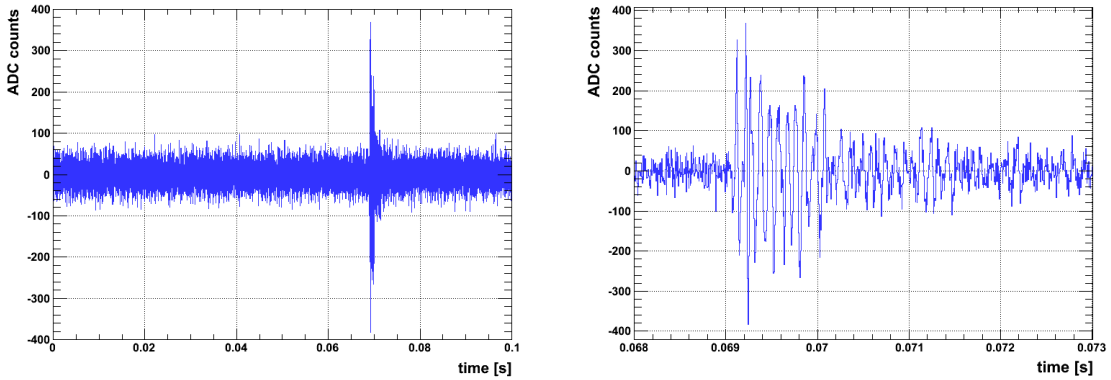

(a) (b)

Figure 6.8: *Example waveform of a single pinger pulse recorded by* SPATS *channel CS7-1. Shown at the right is a zoom of the left image. The waveform of the pinger pulses have a typical length of the order of* 1 ms.

random phase and amplitude. Therefore, applying equation 6.9 suppresses the noise-dominated part of the waveform and the maximum of R indicates the position of the pinger pulse

$$\max_t R(t) \Rightarrow t_{\text{pulse}}. \tag{6.10}$$

Pulse and noise samples

The extracted timing information is now used to select a set of samples, each containing exactly one pinger pulse. For that, a time window of 5 ms is chosen for all samples, and with a sampling frequency of 200 kHz each sample has $N = 1000$ data points. In the same step, a set of noise samples with the same time window is selected from the off-pulse parts of the waveform. To ensure the noise sample is causally independent from the pinger pulse, it is taken from the off-pulse region before the actual pulse, $t < t_{\text{pulse}}$.

The amplitude in the pulse samples is required to exceed a certain pre-defined threshold within its time window. For this, the pulse amplitude within the time window is compared with the noise sample. The signal to noise ratio (SNR) is defined as

$$\text{SNR} = \frac{\max_t |x(t) - \overline{n}|}{\sigma_n}, \tag{6.11}$$

with the waveform $x(t)$, the noise floor $\overline{n}$ and standard deviation of the noise σ_n before the pulse. The noise floor is given by the mean of the waveform in the noise sample and is subtracted to account for a possible offset of the waveform. If the pulse is above the threshold, the waveform is accepted and used in the further analyses, else it is discarded. For this study, $\text{SNR} \geq 5$ was chosen empirically.

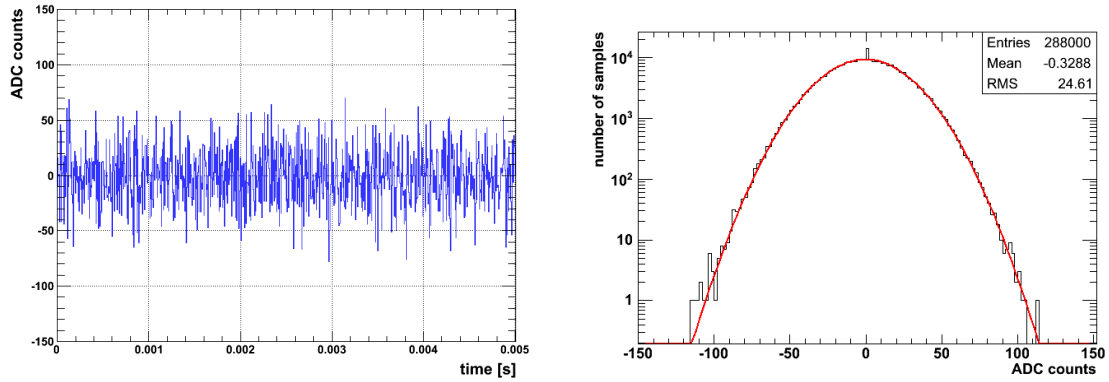

Figure 6.9: *(a) Example for a pure noise sample, taken directly before the pinger pulse shown in figure 6.8(a). (b) Histogram showing the distribution of ADC counts of the noise intervals in between all pinger pulses, taken from the waveform shown in figure 6.7. The noise is well-described by a Gaussian (red line) over 5 orders of magnitude.*

An additional check is performed whether the differential output of the preamplifier of a particular SPATS channel was in saturation. In this case, the recorded waveform was cut at high amplitudes, which would lead to an under-estimation of the energy content.

If t_{pulse} is the time of the first pulse, the time window for the pulse sample with index j is given by

$$t_{\text{start}}^{(j)} = t_{\text{pulse}} + \frac{j}{N_P} T_0 - t_{\text{offset}} \tag{6.12}$$

$$t_{\text{stop}}^{(j)} = t_{\text{start}}^{(j)} + T, \tag{6.13}$$

with the length of the time window $T = 5\,\text{ms}$, the length $T_0 = 18\,\text{s}$ of the full waveform, the number of pulses in the full waveform $N_P = 180\,(144)$ and an offset t_{offset}. The value for t_{offset} is different for each measurement, and is chosen such that the pinger pulse is contained in the time window. Using this description, two disjoint sets of the same size and the same number M of sampling points are obtained, a set of pulse samples and a set of noise samples:

$$\begin{aligned} &\text{pulse samples}: \left\{x^j(t_m)\right\} \qquad j = 1, \ldots, N_P = 180(144) \\ &\text{noise samples}: \left\{y^j(t_m)\right\} \qquad m = 1, \ldots, M = 1000. \end{aligned}$$

Each pulse sample contains exactly one pinger pulse whereas the noise samples are sampled from the waveform before each pulse.

6.3.2.1 Interlude: Clock-drift

The waveforms cannot be averaged in the time domain due to a clock-drift. Each of the four SPATS strings has three FADC boards which are used to digitize the analogue waveforms. Each of the boards has its own clock that drives the ADC operations. The phases of the clocks were discovered to have a time-dependent shift, called clock-drift. As a consequence, the actual

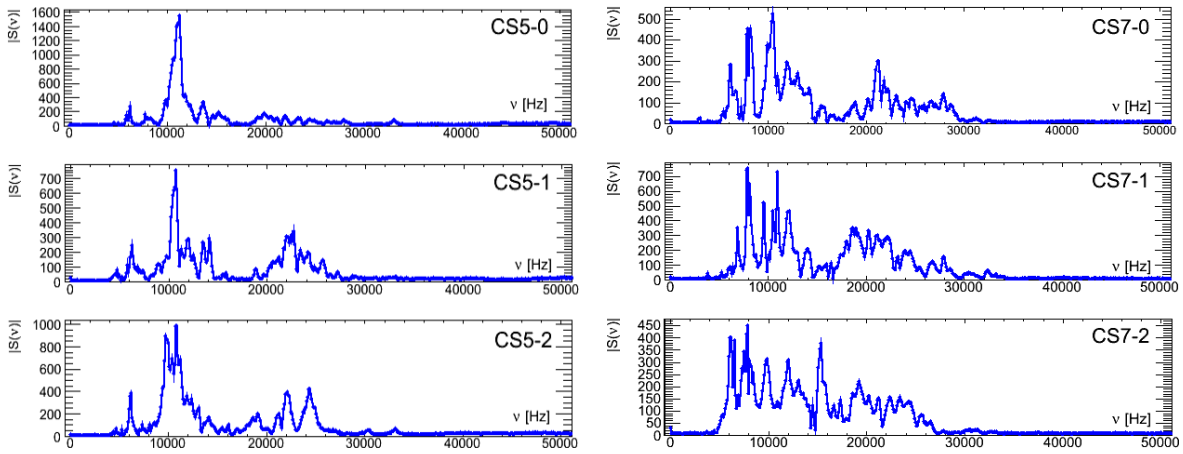

(a) (b)

Figure 6.10: *Noise-subtracted spectra of the three channels of sensor CS5 from the pinger measurements in hole 28 (a) and sensor CS7 from hole 37 (b). The spectra show a number of peaks in the frequency range* $5 - 35\,\mathrm{kHz}$*, while their varies from channel to channel.*

sampling frequency deviates from the nominal sampling frequency. Although the effect is small (typically of the order of a few parts per million), the cumulative effect is a few microseconds per second of absolute time. For the pinger measurements the deviation is therefore on the order of $\mathcal{O}(10\,\mu\mathrm{s})$. If the waveforms are not corrected for the clock drift, their average in time domain will be affected by a destructive de-coherence as the samples are shifted relative to absolute time. However, the clock-drift does not affect the spectral content of the individual pulses. For this analysis, the pulses are first extracted and Fourier transformed and after that averaged in frequency domain.

6.3.3 Fourier Spectra and Noise Subtraction

For each pulse sample x^j, the amplitude at time t_m is the sum of the actual signal s^j plus an irreducible noise contribution n^j:

$$x^j(t_m) = s^j(t_m) + n^j(t_m). \tag{6.14}$$

The discrete Fourier transform yields for each pulse sample

$$\begin{aligned} X^j(\nu_m) &= S^j(\nu_m) + N^j(\nu) \\ j &= 1, \ldots, N_P = 180(144), \quad m = 1, \ldots, M = 1000, \end{aligned}$$

with the frequencies ν_m. X^j, S^j and N^j are complex numbers and are calculated by

$$X^j(\nu_m) = \frac{1}{\sqrt{M}} \sum_{k=0}^{M} x^j(t_k)\, \mathrm{e}^{-i2\pi\nu_m t_k}, \tag{6.15}$$

and similarly for S^j and N^j. The amplitudes of these numbers are called the pulse and noise spectrum, respectively.

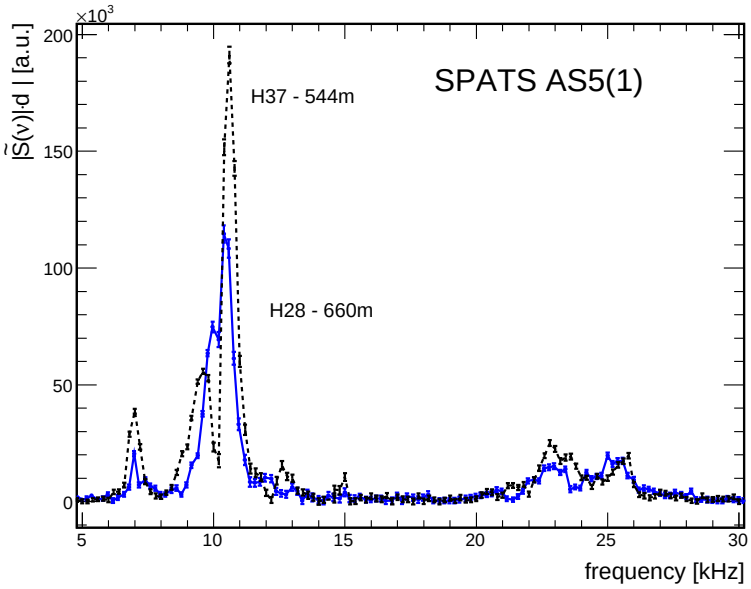

Figure 6.11: *The noise-subtracted spectra recorded by the same channel (AS5-1) for two measurements with the pinger in different holes, resulting in different distances between channel and pinger. The spectra are multiplied with the distance to the pinger to illustrate the effect of the attenuation according to equation 6.4.*

In order to reduce the noise, a spectral noise subtraction is performed by subtracting a noise spectrum from the noise-corrupted spectrum X^j. Since the noise cannot be directly obtained from the signal itself, it has to be estimated from the noise samples taken alongside the pulse samples during the pulse extraction. If Y^j is the Fourier transform of the noise sample y^j, an estimate $\hat{N}$ for the noise spectrum is calculated from the average over all N_P noise spectra

$$\hat{N}(\nu_m) = \frac{1}{N_P} \sum_{j=1}^{N_P} \left| Y^j(\nu_m) \right| . \tag{6.16}$$

Using this noise estimate, an estimate for the noise-subtracted spectrum is obtained [152, 153]

$$\hat{S}^j(\nu_m) = \left[\left| X^j(\nu_m) \right|^2 - \left| \hat{N}(\nu_m) \right|^2 \right]^{1/2} \times \exp(i\phi_{\hat{S}}). \tag{6.17}$$

Since we are only interested in the amplitude information, the phase $\phi_{\hat{S}}$ is arbitrary and is set to the phase of the original signal $X^j(\nu_m)$.

Figure 6.10 shows a few examples of noise-subtracted spectra, and figure 6.12 shows the comparison of a single spectrum before and after the noise subtraction. The Fourier spectra show a number of distinct peaks in the range of $5 - 35\,\mathrm{kHz}$, while the shape of the spectra is different for the various channels. Presumably, these peaks denote the various Eigen modes of the SPATS channels and depend on the mechanical coupling of the piezo-elements to the pressure housing as well as on the orientation of the channels towards the incident pressure

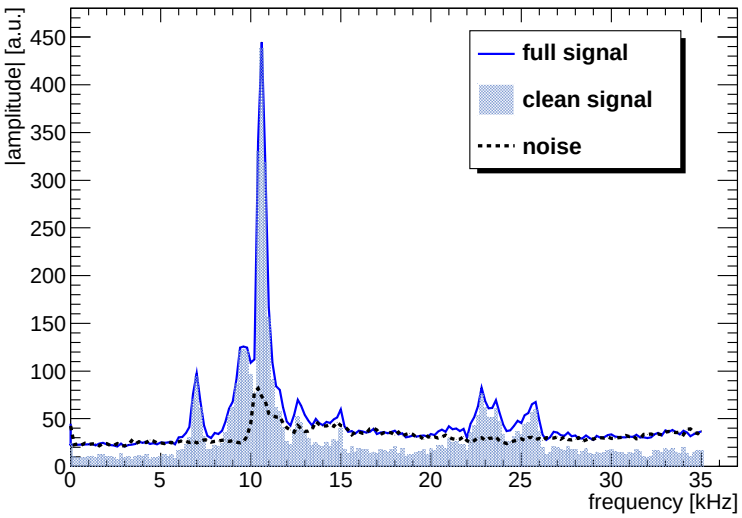

Figure 6.12: *Example illustrating the noise subtraction for a single waveform, recorded by AS4-0. Shown are the full (noise-corrupted) spectrum $|X|$, the noise-subtracted (clean) spectrum $|\hat{S}|$ and the noise spectrum $|\hat{N}|$, respectively.*

pulse. The three channels of the same sensor are 120 ° apart and therefore have a different orientation towards the pinger.

In figure 6.11, the noise-subtracted spectra obtained from measurements with the same channel but with different pinger distances are shown. The shape of the spectra is conserved while the normalization decreases with distance. This decrease, of course, is the effect of the attenuation.

6.3.4 Effective Amplitude

The waveform energy E_S^j of the jth pulse sample is calculated by the sum over the Fourier coefficients

$$\begin{aligned} E_S^j &= \sum_{m=m_{\text{low}}}^{m_{\text{up}}} \left|\hat{S}^j(\nu_m)\right|^2 \\ &= \sum_{m=m_{\text{low}}}^{m_{\text{up}}} \left|\hat{X}^j(\nu_m)\right|^2 - \left|\hat{N}(\nu_m)\right|^2 \\ &= E_{S+N}^j - E_N^j, \end{aligned} \tag{6.18}$$

where the sum is performed over the frequency range denoted by m_{low} and m_{up}. For this analysis, the frequency range is chosen as, see previous section:

$$\nu_{\text{low}} = 5\,\text{kHz}, \quad \nu_{\text{up}} = 35\,\text{kHz}. \tag{6.19}$$

E_{S+N}^j and E_N^j are the energies of the noise-corrupted signal and the noise, respectively. If ignored, the noise leads to a systematic over-estimation of the waveform energy, which

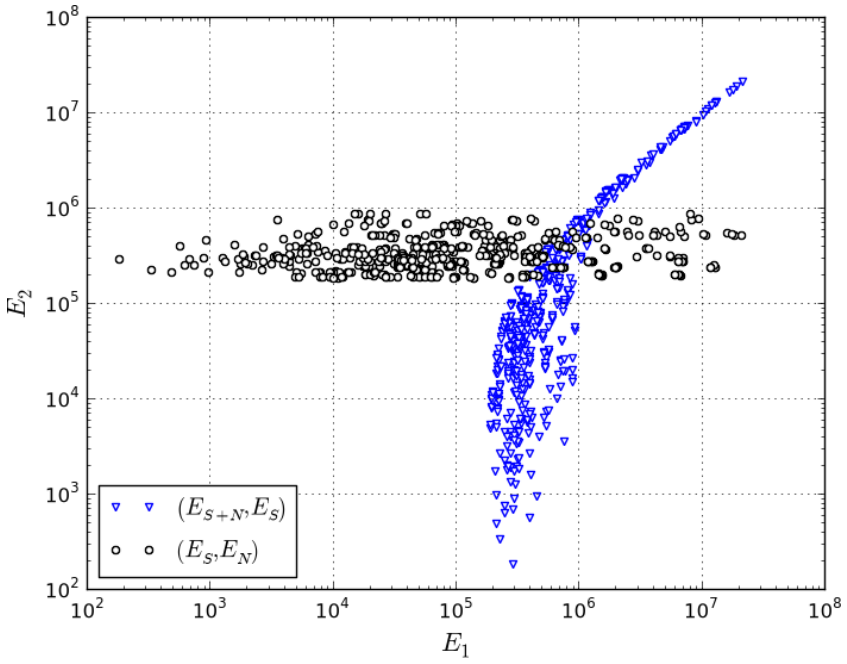

Figure 6.13: *Correlation between the energies of the noise-subtracted signal E_S with both the noise-corrupted signal E_{S+N} and the pure noise E_N, in arbitrary units. Each data point (E_1, E_2) represents a single combination of pinger position and channel. The noise energy is largely independent of the energy of the noise-subtracted signal (black circles) and for large signal energies the noise contribution is less dominant (blue triangles).*

introduces a bias on the calculation of attenuation length. Calculating the average over all N_P pinger pulses in the full waveform, yields the average energy E_S and an error estimate σ_E from standard deviation, as well as the average energies of the noise-corrupted signal E_{S+N} and the noise E_N, respectively.

$$E_S = \frac{1}{N_P}\sum_{j=1}^{N_P} E_S^j = E_{S+N} - E_N \tag{6.20}$$

$$\sigma_E = \text{Stdev}(E_S^j). \tag{6.21}$$

Figure 6.13 shows the correlation of the waveform energy before and after noise subtraction and figure 6.14 shows the individual energies as function of the distance between pinger and channel. The noise energy E_N is independent of the distance and the noise-subtracted energy E_S is independent of E_N.

Finally, the effective amplitude A_{eff} is calculated from the waveform energy

$$A_{\text{eff}} = \sqrt{E_S}. \tag{6.22}$$

The uncertainty on A_{eff} is given by error propagation from σ_E. Figure 6.15 shows the deviation of A_{eff} with respect to its mean value for one example.

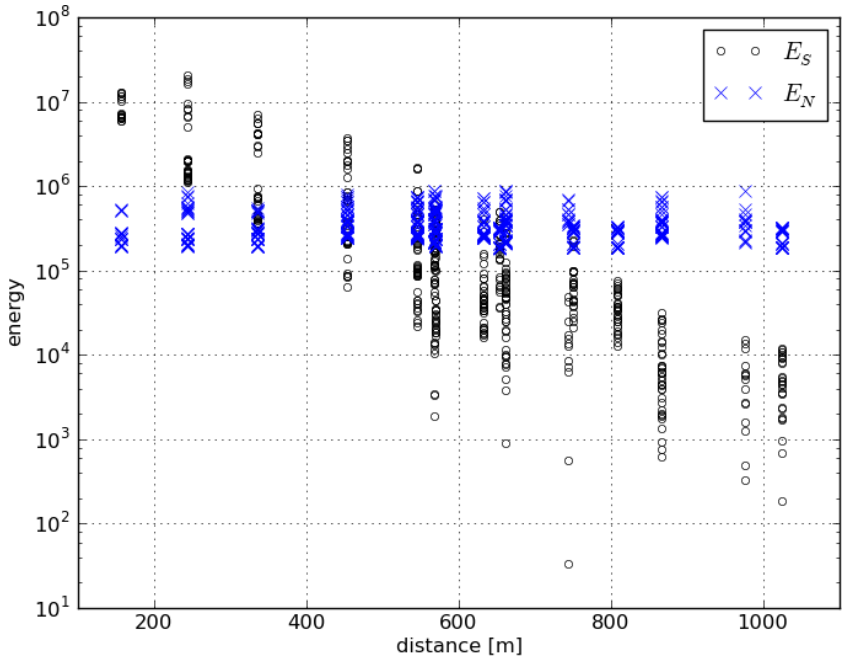

Figure 6.14: *The energies E_S and E_N as function of the distance between pinger and channel. The noise energy is independent on the distance, while E_S is affected by attenuation.*

6.3.5 Attenuation Fit

The attenuation coefficient is calculated for all SPATS channels individually, while a distance variation is achieved by combining measurements with the same channel but different pinger holes. The attenuation length for each channel is obtained by a linear fit on the data, see equation 6.5. Both fitting variables, d and y have an uncertainty, which is discussed in the next section. The parameters obtained from the fit are:

$$y = -\alpha_i d + \beta_i \quad \Rightarrow \quad \{\alpha_i, \Delta\alpha_i, \beta_i, \Delta\beta_i\}\,, \tag{6.23}$$

with the attenuation coefficient α_i, the intercept β_i and their respective errors $\Delta\alpha_i$ and $\Delta\beta_i$, which are obtained from the fit.

If α_i is the result for channel i with an error $\Delta\alpha_i$, and there are in total N_C channels, the weighted mean and the variance over all channels are given by

$$\langle\alpha\rangle = \frac{1}{V_1}\sum_{i=1}^{N_C} w_i\alpha_i\,, \quad \sigma_\alpha^2 = \frac{V_1}{V_1^2 - V_2}\sum_{i=1}^{N_C} w_i \cdot (\alpha_i - \langle\alpha\rangle)^2\,, \quad w_i = \frac{1}{\Delta\alpha_i^2}. \tag{6.24}$$

with

$$V_1 = \sum_{i=1}^{N_C} w_i \quad \text{and} \quad V_2 = \sum_{i=1}^{N_C} w_i^2. \tag{6.25}$$

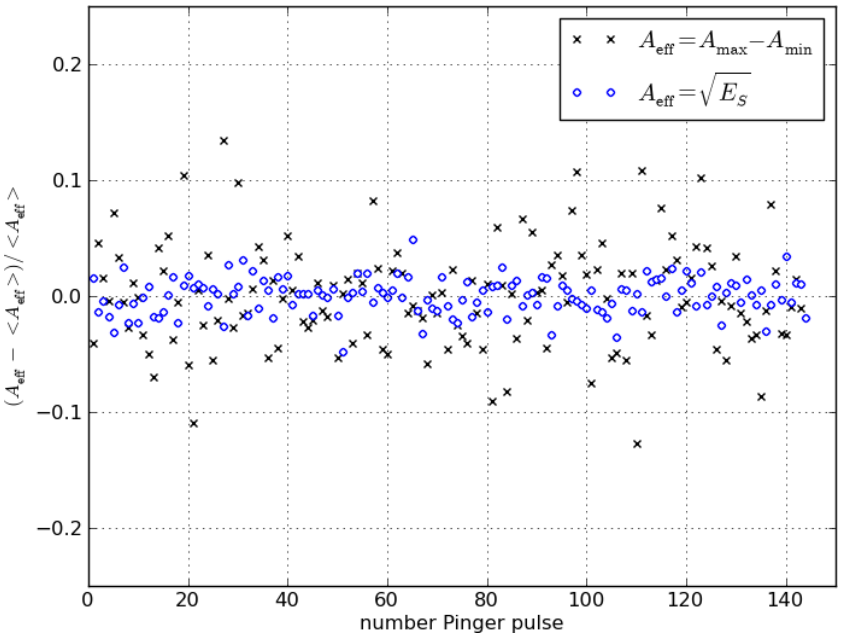

Figure 6.15: *The relative deviation of the effective amplitudes A_{eff} for all pinger pulses in figure 6.7 with respect to their mean value. Shown for comparison are the effective amplitude calculated by either the waveform energy in frequency domain or the difference between minimum and maximum of the ADC counts in time domain.*

6.3.6 Error Estimation

6.3.6.1 Statistical Error on Effective Amplitude

The error σ_A on the effective amplitude A_{eff} is calculated through error propagation from the statistical error on E_S, which is obtained by the standard deviation over all pinger pulses in a waveform, see section 6.3.4. Figure 6.15 shows an example for the variation of A_{eff} for all pinger pulses in the same waveform. Figure 6.16 shows the relative error σ_A/A_{eff} for all measurements as a function of the distance between pinger and SPATS channel. The relative error increases with the distance which is expected as the signal is attenuated, whereas the noise is independent of the distance.

6.3.6.2 Pinger-Sensor Distance

If the pinger and the sensor are exactly on the same level, the error on the distance between them equals the error on the horizontal distance which is estimated from the IceCube hole radius with $\sigma_{d_H} = \sqrt{2} \cdot 50\,\text{cm}$, where the factor 2 is due to the uncertainty in both pinger and sensor hole. On the other hand, if a small deviation Δz from the horizontal position is assumed, the distance between pinger and sensor is

$$d = \sqrt{d_H^2 + \Delta z^2}. \tag{6.26}$$

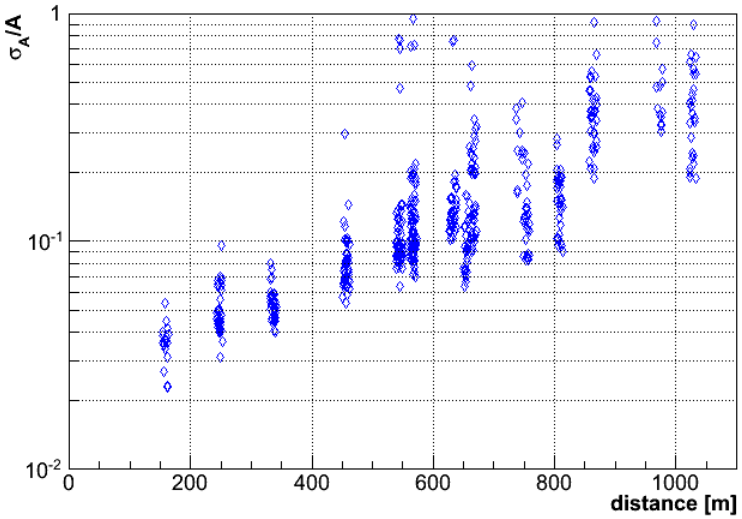

Figure 6.16: *The relative error of the effective amplitude with distance for all data considered in this analysis. The error is calculated from the standard deviation over all pulses in the same waveform.*

The error on the distance is given by error propagation as

$$\sigma_d = \frac{1}{d}\sqrt{(d_H\,\sigma_{d_H})^2 + (\Delta z\,\sigma_z)^2} \tag{6.27}$$

During deployment, the depth of the pinger was determined using different methods, see section 6.2.1. Following the discussion therein, the total uncertainty on the depth was estimated with 5 m. In addition, the maximum vertical difference $\Delta z = |z_{\text{pinger}} - z_{\text{sensor}}|$ is also estimated with 5 m. Applying equation 6.27 for all possible pinger-sensor distances (figure 6.17(a)), shows that the contribution of uncertainty on the distance is $\sigma_d \lesssim 0.5\%$, which is negligible compared to the contribution of the effective amplitude.

6.3.6.3 Systematic Effects

Transmittivity

The transmitter (pinger) was the same during all measurements and from laboratory measurements the pinger emission and pulse timing are known to be reliable [144]. However, the transmission and reflection of the pinger pulses at the water-ice interface depends on the pinger position inside the hole as well as the sound speeds of both sides of the interface, see section 3.4.2.3.

From the uncertainty of both position and sound speed, the uncertainty of the transmission coefficient can be estimated. For a perfectly aligned setup, the pinger is central in the hole and at the same depth as the sensor. In this case, the transmission is maximal, while shear waves are suppressed, as discussed in section 3.4.2.3. For any non-optimal alignment, there is a non-zero incidence angle, leading to mode conversions at the hole wall. A variation on the incidence angle between measurements in different holes therefore leads to an uncertainty on the transmitted energy.

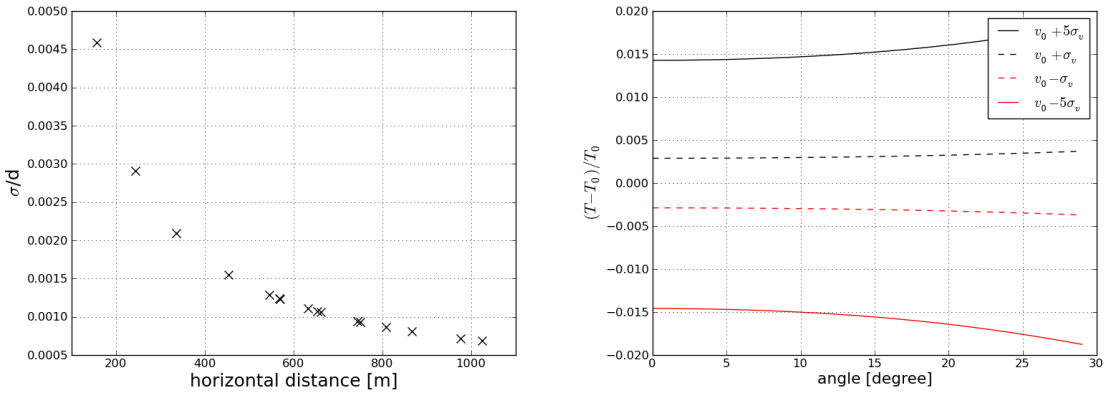

(a) (b)

Figure 6.17: *(a) The relative error on the distance for various horizontal distances between pinger and sensor, see equation 6.27. (b) Ratio of transmission coefficients for the P wave for various sound speeds in ice. The ratios are with respect to the transmission coefficient calculated for the sound speed obtained from the* SPATS *measurements,* $v_0 = (3878 \pm 12)\,\mathrm{m/s}$ *see section 5.2. The lines illustrate the deviation for different levels of uncertainty of the* SPATS *result.*

During the measurements in season 2008/09, the pinger was mechanically fixed and centralized in the hole. Hence, no notable azimuth variation of the incidence angle is expected. In section 6.2, the maximum uncertainty of zenith was estimated with $\Delta\theta \approx 2\,^\circ$. As shown in figure 3.9, the transmission is nearly constant for this angle. However, the variation of the transmission coefficient will be significantly larger if the hole wall has an uneven surface or if the ice close to the pinger contains cracks or other obstacles.

The variation of the transmission coefficient due to an uncertainty of the sound speed can be estimated using the results from the measurements with SPATS, see section 5.2.3. For that, the transmission coefficients are calculated using the Zoeppritz equations for various values of sound speed and various incidence angles, see figure 6.17(b). The resulting relative deviation of the transmission coefficient is 0.3% for an angular uncertainty of $0 - 10\,^\circ$ and a 1σ deviation of the sound speed and 1.5% for a 5σ deviation. Consequently, the transmission and reflection coefficient can be considered as approximately constant for these measurements.

Pinger

The pinger is operated in a water column whose properties are assumed to be basically the same for the different pinger holes. The only known difference is the distance of the water level in the hole to the surface (well depth) at the time the pinger is deployed, see table 6.3. Consequently, the height of the water column above the pinger at a certain nominal depth and in turn the ambient hydrostatic pressure varies from hole to hole. The maximum difference is found between holes 5 and 37 at the 190 m stopping depth

$$\frac{P_{37} - P_5}{P_{37}} = \frac{w_{37}[m] - w_5[m]}{190\,\mathrm{m} - w_{37}[m]} \approx 0.28. \tag{6.28}$$

It is assumed that the pinger emission is independent of the ambient pressure within this range.

Table 6.3: *The final well depth after the deployment of the pinger for the individual pinger holes.*

hole	5	19	28	37
well depth [m]	45	57	67	77

While the pinger is operated in the hole, a part of each emitted pinger pulse is reflected at the hole wall. The signal transmitted in one direction interferes with the signal that is reflected by the opposite side of the hole. The time delay between direct and reflected signal depends on the distance of the pinger to the wall. During the measurements in season 2008/09, the pinger was mechanically fixed and centralized in the hole, resulting in a constant time delay. With a sound speed in water of 1400 m/s the delay is approximately 700 μs, hence both pulses are clearly distinguishable. For season 2007/08, the pinger was allowed to move freely inside the hole, which led to unpredictable interferences of the direct with the reflected pulse.

Hole Ice Properties

Because of the horizontal setup and the small azimuthal ranges of the pinger measurements, no large variation of the ice properties are expected in the analysis.

The only significant change of the ice properties is expected for the so-called hole ice in the re-frozen IceCube holes surrounding the sensors, as described in section 3.4.2.4. Until today, there is no quantitative measurement of the distinctive hole ice properties nor the scale of inhomogeneities near the sensors. Taking the hole ice into account, equation 6.5 is rewritten as

$$y = -\alpha_{\mathrm{I}} d_{\mathrm{I}} - \alpha_{\mathrm{H}} d_{\mathrm{H}} + \beta, \tag{6.29}$$

with the path length d and attenuation coefficients α for South Pole ice (I) and hole ice (H), where $d_H = 50\,\mathrm{cm} << d_I$. Hence, the measurements are affected by two different attenuation effects and their relative contribution depend on the quality of the hole ice. However, for a slowly varying α_H, the second term in this equation will affect all measurements with the same channel equally, leading to a constant offset of the absolute signal seen by the respective sensor. Hence, it is possible to calculate attenuation coefficient as described. If on the other hand, α_H is anisotropic and sufficiently large, the angular window of the measurements will lead to a considerable modulation of the measured signal. Consequently, these effects can be minimized, but not fully excluded in the current setup.

Furthermore, the SPATS equipment shares the holes with the cables of the IceCube detector. These cables shadow the channels for specific directions, also leading to a stationary, azimuth-dependent offset on the measured amplitude.

Saturation

The SPATS channels have a limited dynamic range due to the maximum and minimum output voltage from their amplifiers, which for the settings used during the measurements is $\pm 3.5\,\mathrm{V}$ [154]. Consequently, for a very strong signal, the channel output will saturate and the waveform obtained from this signal will be cut off at high amplitudes. This data cannot be used for an attenuation length analysis as it contains only limited information on the strength of the signal. If a recorded waveform is saturated, the energy calculated from that waveform is under-estimated. As the saturation primarily affects the channels with close distances to the pinger, the attenuation length calculated from this data is over-estimated.

Saturation has been observed in the 2007/08 sample for many of the close distances between the pinger and the SPATS strings. Therefore, a big portion of that data cannot be used for the attenuation length analysis. The pinger 2008/09 data have shown no indications of saturation.

Bad Channels

For the attenuation analysis, it is important that the channels sensitivity does not change during the measurements or between two measurements. Six "bad" channels have been identified by their noise spectra, showing large fluctuations and unpredictable behavior [79, chapter 4]. All three channels of the SPATS modules AS3 and CS1 are considered bad, while all other channels are considered stable. These bad channels are not used for this analysis.

Noise

For any given channel, the noise contribution is independent of the distance between transmitter and channel. Without a noise subtraction, the waveform energy is systematically over-estimated. The relative noise contribution increases with distance, as the signal is attenuated while the noise is not. Hence the attenuation length appears to be larger. For the analysis, the noise has been subtracted.

Channel-to-Channel Variation

The various SPATS channels have very different intrinsic sensitivities, e.g. indicated by the relative amplitude differences in figure 6.20. In this analysis, the variation between different channels is avoided by only comparing measurements with the same channel.

Channel Angular Sensitivity

In addition to the absolute differences between two channels, the sensitivity of each individual SPATS channel is a function of azimuth and zenith. Moreover the rotational orientation of the sensors could not be controlled during deployment and is not known. If data from a large angular range is combined without angular calibration, the resulting attenuation length can be either over- or under-estimated, depending on the channel orientation and the directions at which it is probed.

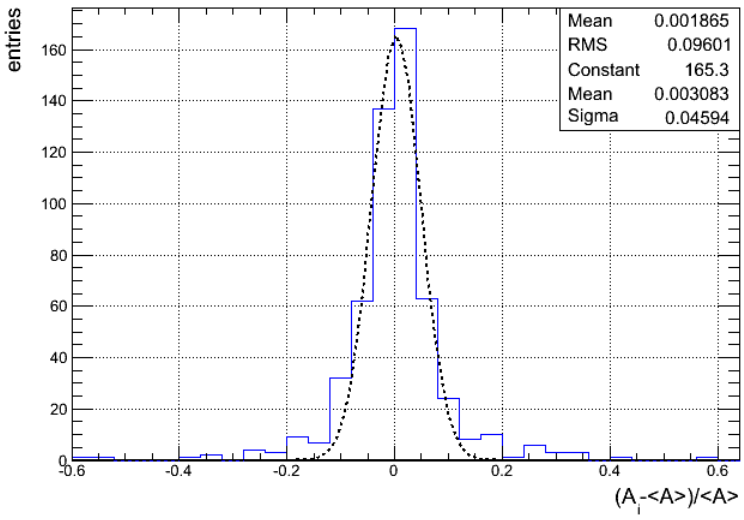

Figure 6.18: *Deviation of the effective amplitude for all measurements obtained for the same channel and pinger stopping position, see equation 6.31. A Gaussian fit yields* $\sigma_{\text{residual}} \approx 5\%$.

As discussed in section 6.2, the maximum spread of the azimuth for the pinger measurements in season 2008/09 is $\Delta\phi = 12\,^\circ$. In addition, for the pinger analysis only data from the same depth is used, with an uncertainty of the zenith with $\Delta\theta = 2\,^\circ$.

From laboratory measurements in water [155], it is known that the SPATS channels have a strong frequency-dependent variation with azimuth. From these measurements, the maximum difference of the channel sensitivity $\mathcal{S}$ over an azimuthal range of $\Delta\phi = 12\,^\circ$ is [155]

$$\sigma_{\mathcal{S}} \approx 30\%. \tag{6.30}$$

However, this value applies to a single frequency and a single channel. Up to now, there are no reliable measurements in ice and there is no information about the angular dependence for all of the SPATS channels. In addition, the relative orientation of the individual channels to the pinger is not known and is assumed to be random.

Residual Zenith Dependence

For each pinger stopping position, there is usually more than one measurement with the same SPATS channel. First, the pinger stops twice at each position, except for the lowest depth. The first stop is done while the pinger is lowered into the hole and another stop is done when it is pulled back to the surface, see section 6.2.1. At each stop, the pinger was stopped for at least 5 min. In many cases the resting time of the pinger in a certain depth was considerably longer and two successive measurements could be completed.

It was observed, that the A_{eff} obtained for different measurements at the same pinger stop can be different. These differences are possibly attributed to small positional differences in the case that the pinger is not exactly at the same depth for the up- and down-going measurements. In order to estimate the effect on these differences on the analysis, the distribution of the

relative deviation of A_{eff} at each depth is calculated for each channel:

$$\Delta_i^{\text{PC}} = \frac{A_i^{\text{PC}} - \langle A^{\text{PC}} \rangle}{\langle A^{\text{PC}} \rangle}, \tag{6.31}$$

where the A_i^{PC} denote the effective amplitudes for all measurements with the same channel and the same pinger stop. $\langle A^{\text{PC}} \rangle$ is the mean value over all measurement for the same combination of pinger stop and channel. A histogram of Δ_i is shown in figure 6.18, a fit with a Gaussian yields a width of

$$\sigma_{\text{residual}} \approx 5\%. \tag{6.32}$$

This value can be used as an estimate of the systematic uncertainties due to a non-perfect horizontal alignment of the pinger stopping positions with the channels. It is sensitive to all residual effects of the zenith dependence, namely the zenith dependence of the channels sensitivity and the transmission of the pinger pulses.

6.3.6.4 Error on Fit Variable

Table 6.4: *Summary of possible systematic effects in the pinger data analysis and their expected effect on the attenuation length λ. The status indicates the impact of each effect on this analysis.*

effect	effect on λ	status
Transmissivity	varying	minimal
Hole Ice	varying	minimal
Saturation	increase	none
Bad channels	varying	none
Noise	increase	minimal
Channel-to-channel	varying	none
Channel sensitivity θ	varying	$\approx 5\%$
Channel sensitivity ϕ	varying	unknown, up to 30%

Table 6.4 summarizes the various systematic effects and their expected effect on the determination of the acoustic attenuation length. The pinger 2008/09 data sample used in this analysis has a small variation for both, azimuth and zenith. While this reduces a number of systematic uncertainties, the presumably strong inherent angular dependence of the SPATS channels sensitivity has to be considered. There is no meaningful estimate for the systematic effects caused by the azimuthal variation, whereas the zenith dependence has been estimated with a residual uncertainty of $\approx 5\%$.

Assuming uncorrelated errors, the error on the fitting variable ($A_{\text{eff}} d$) in equation 6.5 follows from error propagation:

$$\sigma_{Ad} = \sqrt{(\sigma_d A_{\text{eff}})^2 + (\sigma_A d)^2 + \sigma_{\text{residual}}^2}. \tag{6.33}$$

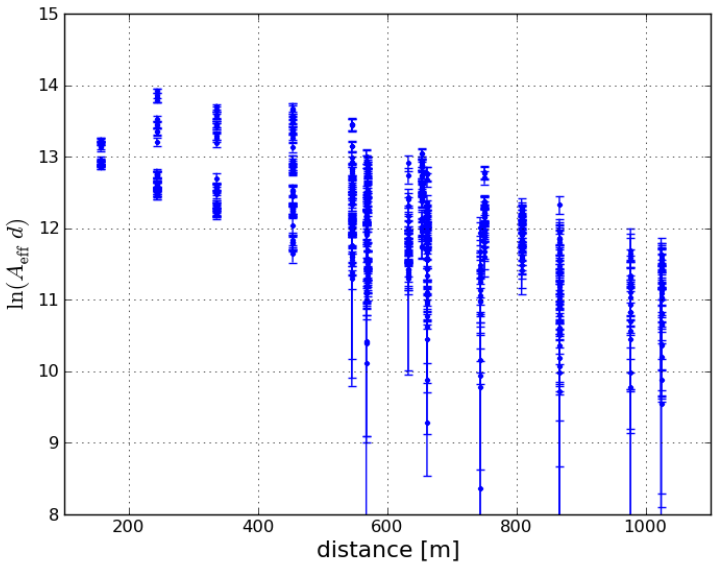

Figure 6.19: *The effective amplitude A_{eff} multiplied with distance d for all selected channels pinger depths with their respective error bars. The data from different channels does not agree due to channel-to-channel variations of the sensitivity.*

σ_A represents the statistical uncertainty of the effective amplitude and σ_d is the uncertainty of the pinger distance. The last term accounts for the systematic error on A_{eff} due to the residual zenith dependence of A_{eff}. The transformation $y = \log(A_{\text{eff}} d)$ leads to asymmetric errors for the fitting variable y.

6.4 Results

6.4.1 Single-Channel Fit

For the single-channel-fits, the attenuation coefficient is calculated for each channel separately and the weighted mean of all results is calculated, as described in section 6.3.5.

In season 2008/09, pinger measurements have been performed in four holes, therefore there is a maximum of four different distances for each SPATS channel. However, for several channels the pinger could not be detected from all four positions. In these cases the signal was buried under the noise and the signal-to-noise ratio was below the required threshold, see section 6.3.2. The number of channels with four, three and two successfully detected distances and the total number N_C of all channels are

$$N_4 : N_3 : N_2 = 34 : 9 : 5, \quad N_C = 48. \tag{6.34}$$

The data has undergone the selection described in section 6.3.1 and figure 6.19 shows the data from all selected combinations of pinger stops and channels. For each of the N_C channels, the fit for the attenuation coefficient is performed In figure 6.21, a selection of single-channel fits is shown, and figure 6.20 shows all performed fits together.

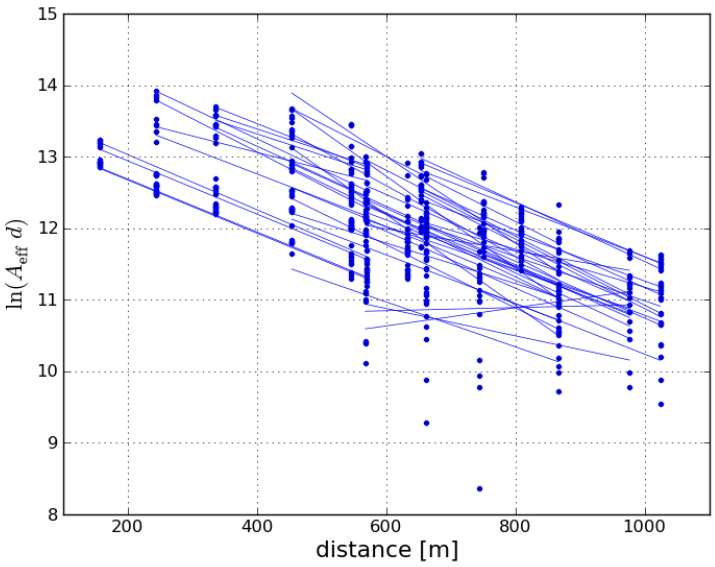

Figure 6.20: *Illustration of the attenuation length fits for all channels, see figure 6.19. Each line represents the fit result for a particular channel. The data points are shown without error bars for better visibility. Note that some data points show large deviation from the corresponding fit.*

For two channels, namely AS4-0 and AS7-0, the fit led to a negative attenuation coefficient. This behavior is expected for channels that are noise-dominated. In these cases, the effective amplitude calculated from the waveform energy is over-estimated and has a relatively small variation with respect to the distance. A fit on the product of effective amplitude and distance therefore leads to a flat or negative attenuation coefficient.

Figure 6.22 shows the attenuation coefficients α_i with their respective errors $\Delta\alpha_i$ for all channels. In most cases the attenuation coefficients for the three channels of the same sensor are consistent with each other, while there are significant differences between the values from different sensors.

A histogram of the attenuation coefficients α_i and the distribution of χ^2-values of the fits for all single-channel fits are shown in figure 6.23. The weighted mean and deviation over all results with $\alpha_i > 0$ is calculated via equations 6.24:

$$\langle\alpha\rangle = (3.79 \pm 0.63)\ \text{km}^{-1}. \tag{6.35}$$

Using $\lambda(\langle\alpha\rangle) = 1/\langle\alpha\rangle$, this result translates into an attenuation length:

$$\lambda(\langle\alpha\rangle) = 264^{+52}_{-37}\,\text{m}, \tag{6.36}$$

where the asymmetric error is obtained from the error of $\langle\alpha\rangle$.

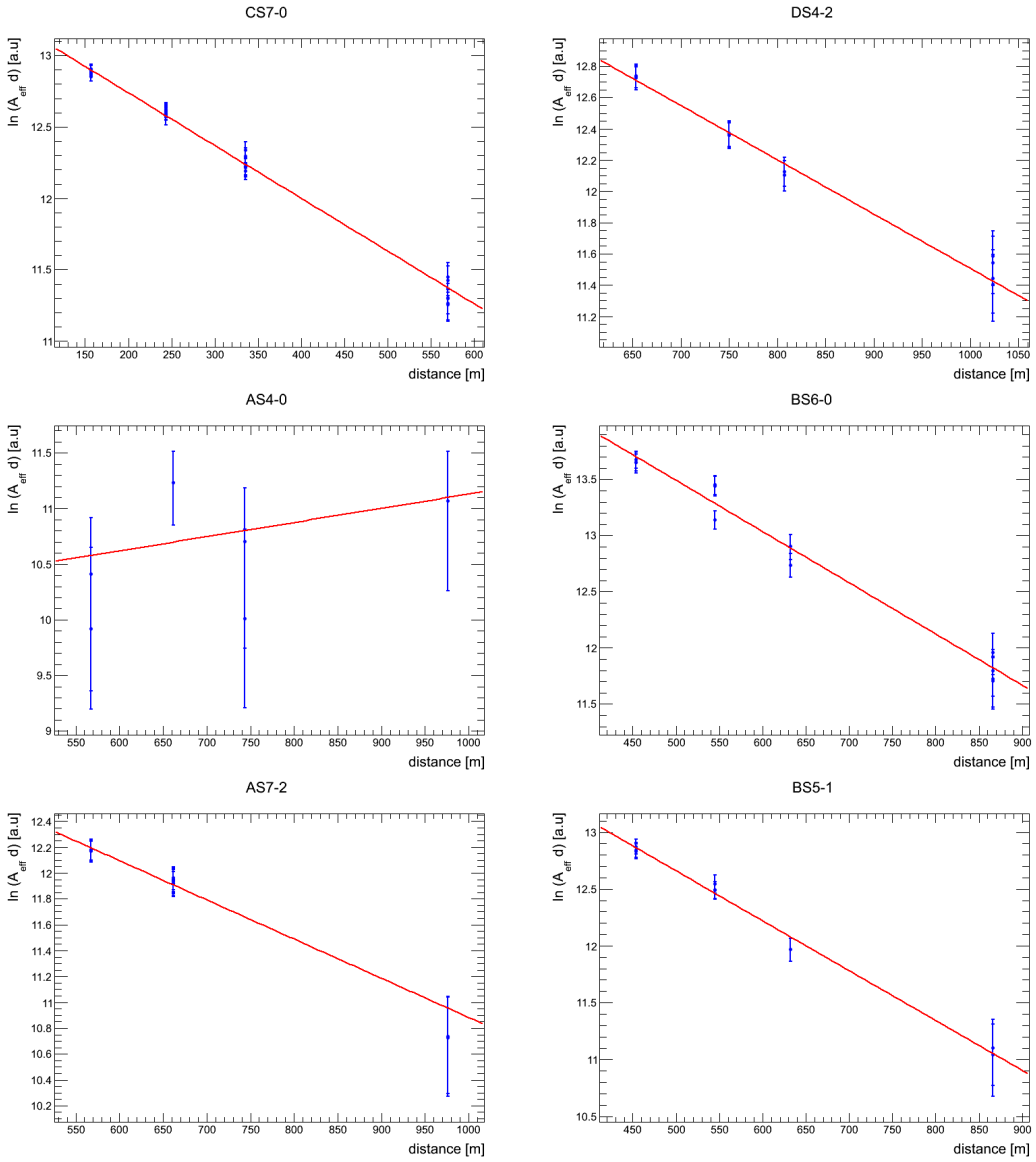

Figure 6.21: *Examples for fit on the data to obtain the attenuation coefficient. The slope of the linear fit yields the attenuation coefficient, whereas the intercept depends on the channels sensitivity. Channel AS4-0 has a noise-dominated* A_{eff}*, resulting in a negative attenuation coefficient.*

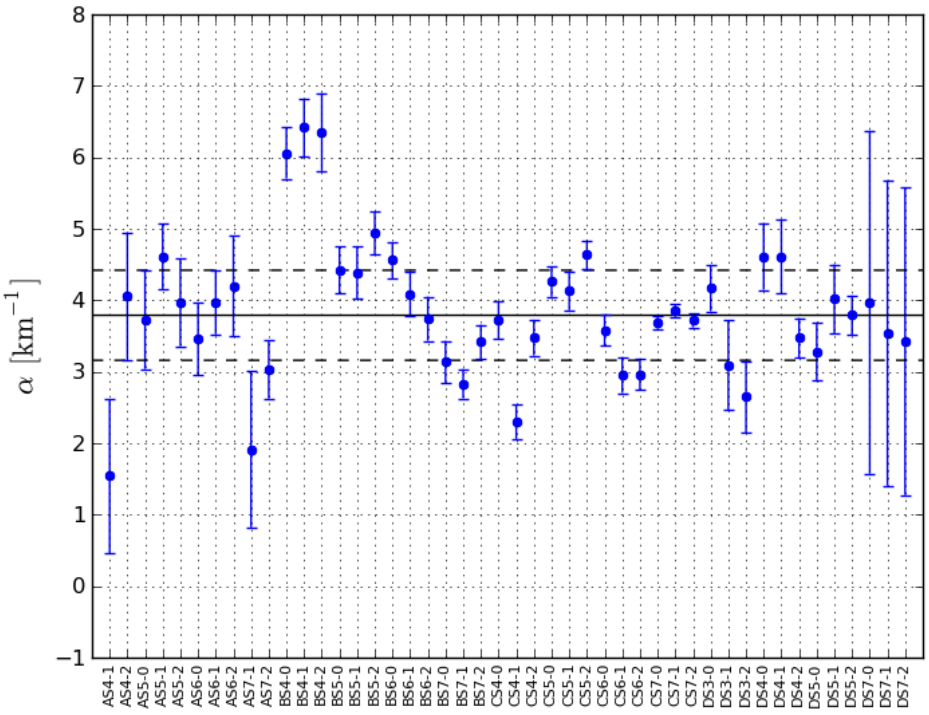

Figure 6.22: *The attenuation coefficients α_i for all 48* SPATS *channels below* 190 m. *The channels are sorted by* SPATS *string and depth. The horizontal lines denote the weighted mean and the standard deviation over all channels.*

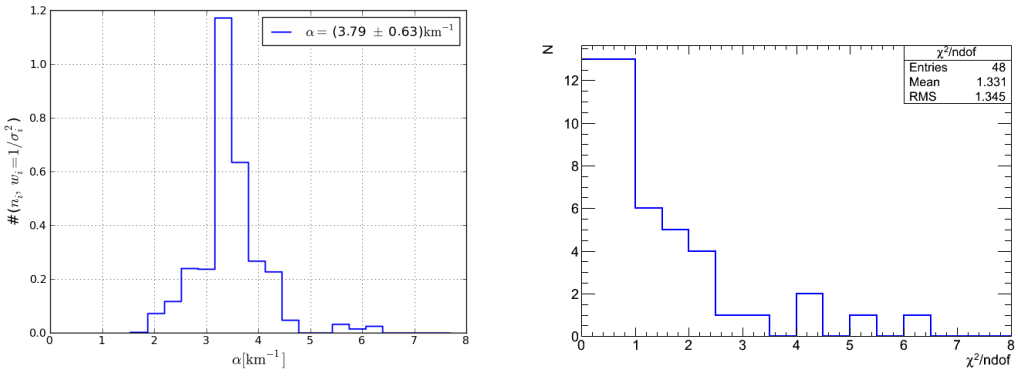

(a) (b)

Figure 6.23: *(a) Histogram of the attenuation coefficients obtained for all channels. The histogram is weighted with the respective errors from the fit. (b) The distribution of χ^2 of all fits (median ≈ 0.85).*

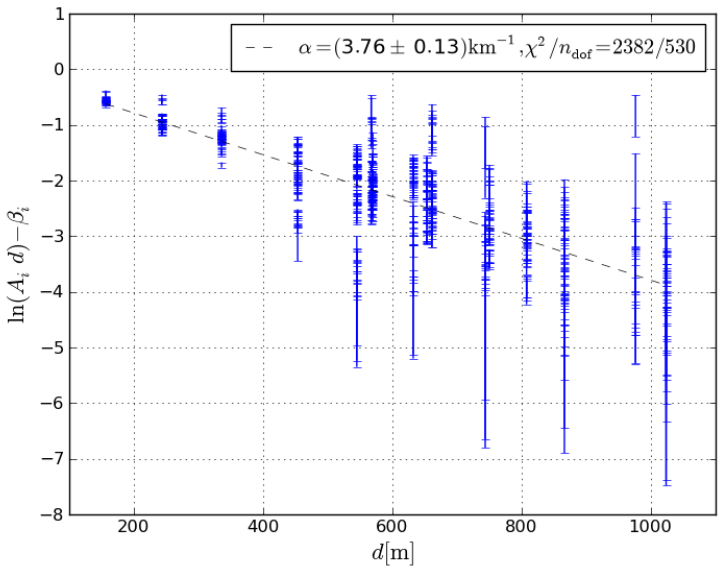

Figure 6.24: *Global fit on the combined data from all channels. The data from the individual channels is calibrated with the results from the previous separate fits. The result is compatible with the mean value over the individual fit with single channels. The systematic uncertainties from the channel-to-channel variations are not included.*

6.4.2 Multi-Channel (Global) Fit

In the previous section, the attenuation coefficient has been calculated separately for each channel to account for the different sensitivities of the individual channels.

Figure 6.20 shows the results from the individual fits. There is a systematic offset by an order of magnitude between different channels, which is related to the different sensitivities for different channels. The intercept β_i obtained from each fit (see equation 6.5) is a simple estimator of the channels sensitivity, allowing a basic relative calibration.

As a cross-check of the single-channel results, a global (or multi-channel) fit on the combined data from all channels is performed, enforcing the attenuation coefficient to be the same for all channels. For that, each data point is corrected using the values of α_i and β_i from the respective single-channel fits. The variable for the global fit is defined as

$$\tilde{y} = y - \beta_i \tag{6.37}$$

The error of $\tilde{y}$ is given by the uncertainty of the previous fitting variable y and the error of the individual β_i obtained in the single-channel fits.

The result of the global fit is shown in figure 6.24 and the attenuation coefficient is determined as

$$\langle \alpha \rangle = (3.76 \pm 0.13)\ \mathrm{km}^{-1}, \tag{6.38}$$

This value is compatible with the weighted mean over the single-channel results, equation 6.35. The error obtained from the global fit is smaller than for the single-channel fits, but it does

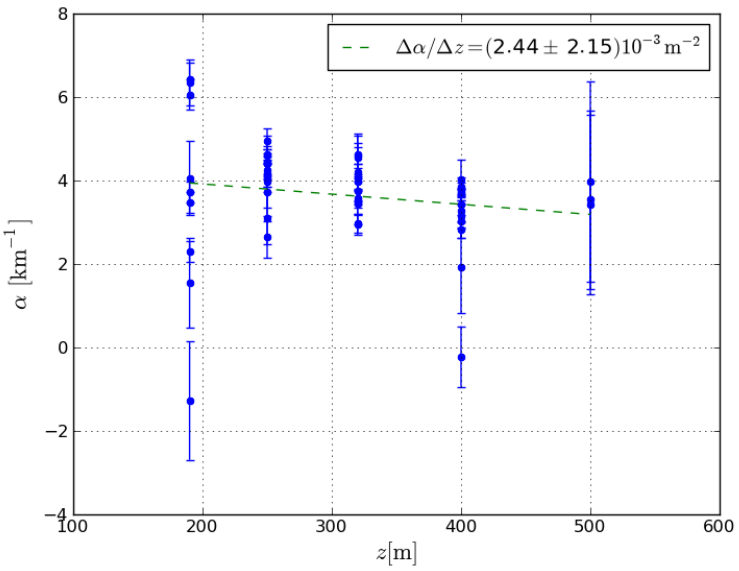

Figure 6.25: *Fit on the depth dependence of the attenuation coefficient. The fit is performed for all strings combined (shown here) and for each string individually, see table 6.5.*

not include the systematic uncertainty on the individual absolute channel calibration. The χ^2 of the fit (figure 6.24) indicates that the error estimate is incorrect.

6.4.3 Depth Dependence

The dependence of the acoustic attenuation coefficient on the depth is investigated for depths below 190 m, i.e. below the firn. The α_i obtained in the single-channel fits (equation 6.23) are sorted by depth, see figure 6.25. The data are fitted with a linear fit, first in a global fit combining all data and secondly for each SPATS string separately. The resulting gradients $\Delta\alpha/\Delta z$ for all fits are listed in table 6.5. The results show no evidence for a global depth dependence. Only for string B a depth dependence with larger values of α at shallow depths is observed. For the other strings, the results are compatible with no depth dependence. The reason for the deviating behavior of string B is not known yet, possible explanations could be related to different (depth-dependent) defects in the local ice.

Table 6.5: *Dependence of the attenuation coefficient on depth for each string individually and for all strings together.*

string	A	B	C	D	combined
$\Delta\alpha/\Delta z\,[10^{-3}\mathrm{m}^{-2}]$	-1 ± 7	-14 ± 2	0.7 ± 2.4	0.4 ± 1.9	2.4 ± 2.2

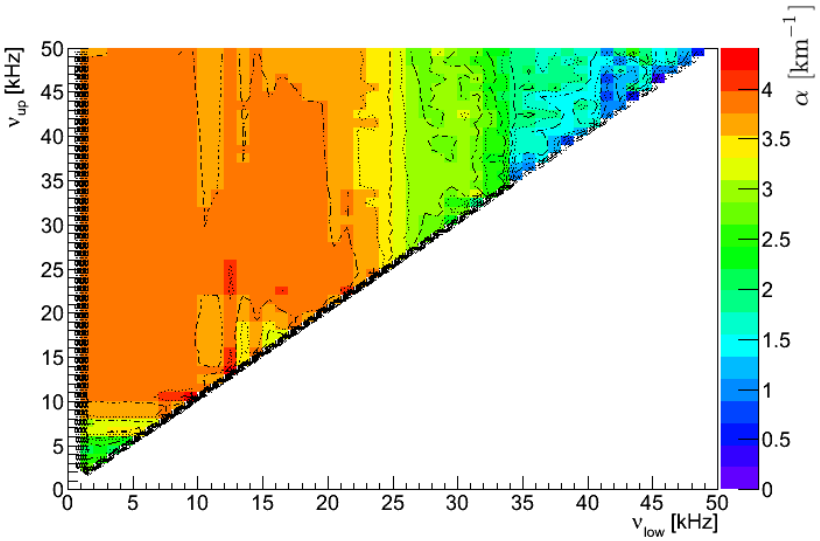

Figure 6.26: *Dependence of the attenuation coefficient on the frequency range* $[\nu_{\text{low}}, \nu_{\text{up}}]$ *in equation 6.18. For noise-dominated frequency ranges, the attenuation coefficient is under-estimated.*

6.4.4 Frequency Dependence

The investigation of the frequency dependence could help to distinguish between different attenuation mechanisms. The scattering coefficient increases with frequency $\sim f^4$, while the absorption coefficient is nearly independent of frequency, see section 3.4.2.2. Hence, a strong frequency dependence of the attenuation coefficient is expected for a scattering-dominated scenario but not for an absorption-dominated scenario.

2008/09 Data

In season 2008/09, the spectra of the pinger pulses, as recorded by the SPATS channels show a number of peaks in the range of $5 - 35\,\text{kHz}$ (figure 6.10). In the attenuation analysis, A_{eff} has been calculated by the sum over the Fourier spectra in this frequency range 6.18. In order to investigate the dependence on the frequency in this analysis, the lower and upper bounds of this sum are varied and the mean attenuation coefficient is calculated for each range, following the method described in the previous sections.

The result is shown in figure 6.26. The attenuation coefficient is independent of the frequency range, as long as the observed peaks in the spectra are contained in this range. If on the other hand the sum is performed over a noise-dominated frequency range, the attenuation coefficient is under-estimated. This is because in these cases, the effective amplitude A_{eff} is over-estimated at large distances due to a distance-independent noise contribution to the signal energy E_S.

2009/10 Data

The pinger data sample of season 2009/10 comprises measurements with three different frequencies, see section 5.1.3. Figure 6.27 shows an example of the Fourier spectrum of a full

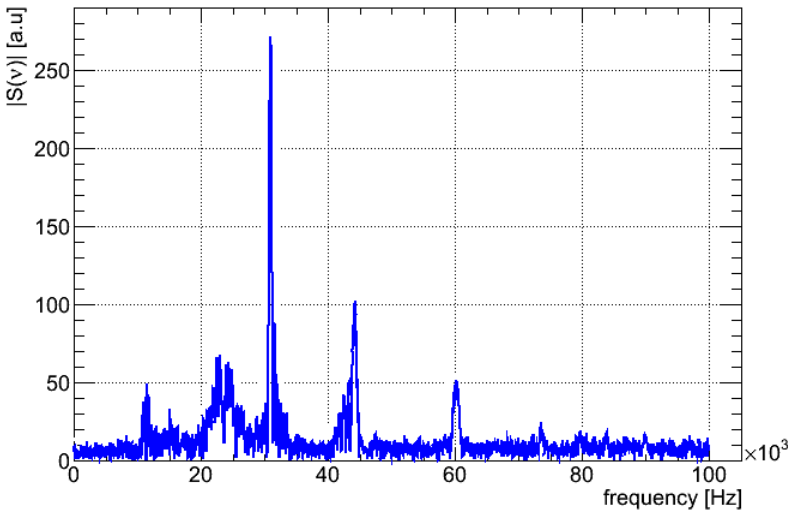

Figure 6.27: *Example Fourier spectrum of the pinger 2009/10 data showing the superposed spectra of the individual pinger pulses with* 30, 45 *and* 60 kHz *arriving from hole 81 at* SPATS *channel CS6-0.*

waveform recorded by a single SPATS channel. The three different frequencies are distinguishable.

The analysis of the 2009/10 data follows the same method as for the 2008/09 data, described in section 6.3. To investigate the frequency dependence, the sum over the Fourier spectra is now performed over a small frequency bands around each frequency, using a bandwidth of ±2 kHz. The attenuation coefficients for the three different pinger frequencies are:

$$\begin{aligned} \langle\alpha\rangle_{30\,\mathrm{kHz}} &= (4.0 \pm 1.7)\ \mathrm{km}^{-1} \\ \langle\alpha\rangle_{45\,\mathrm{kHz}} &= (4.0 \pm 1.6)\ \mathrm{km}^{-1} \\ \langle\alpha\rangle_{60\,\mathrm{kHz}} &= (3.9 \pm 1.7)\ \mathrm{km}^{-1}. \end{aligned}$$

No evidence for a frequency dependence is found, and the results are consistent with the earlier results from 2008/09. For a scattering-dominated attenuation, a dependence on the frequency with $\alpha \sim f^4$ is expected, which would lead to much larger differences as have been observed. A dedicated analysis on the same data sample has recently been performed [156], also showing no indication for a frequency dependence.

The uncertainty on α is larger than in the analysis of the 2008/09 data. This could be due to different reasons, e.g. the larger azimuthal variations between the individual pinger measurements with the same channel, see table 6.1.

6.5 SPATS Attenuation Analysis

There are several attenuation length analyses which have been performed on different SPATS data samples, namely the pinger data, inter-string data and a sample of selected transient events. In the next sections, the results from the different analyses are briefly discussed.

6.5.1 Pinger Time Domain Energy Analysis

Two different analyses have been performed with the pinger 2008/09 data sample. Both analyses use the energy of the waveform, which is either calculated in time or frequency domain. The latter was presented in this thesis, whereas the analysis in time domain is described in [144]. The same data selection was applied, resulting in similar dependence on systematic effects. The differences between the two analyses concern the data processing, the pulse extraction and the averaging over the pulse samples.

In the time domain pinger analysis, an average pinger pulse is obtained by averaging over all pinger pulses in each waveform. This is done in time domain and therefore requires a correction of the time shift caused by the FADC clock-drift, see section 6.3.2.1. The correction algorithm is described in [79]. Using the waveform $\overline{x}$ of the averaged pinger pulse, the energy is calculated by

$$E_{S+N} = \sum_{i=1}^{n} \overline{x}_i^2. \tag{6.39}$$

A noise subtraction is applied and the effective amplitude calculated from the noise-subtracted energy E_S

$$A_{\text{eff}} = \sqrt{E_S} \quad \text{with } E_S = E_{S+N} - E_N. \tag{6.40}$$

The noise energy E_N is estimated using a dedicated noise data run recorded immediately before and after the pinger measurements in each hole. The attenuation coefficient is calculated for each channel separately, using equation 6.23. The weighted mean and error over the distribution of all considered channels is

$$\langle \alpha \rangle = (3.20 \pm 0.57)\ \text{km}^{-1}. \tag{6.41}$$

The dependence of the attenuation coefficient on frequency and depth have been investigated, resulting in no evidence for either depth and frequency dependence.

6.5.2 Inter-String Analysis

Because each of the SPATS modules has a transmitter and a sensor, it is in principle possible to send acoustic pulses between any two modules, allowing many different distances between transmitter and sensor. A distance variation is achieved by combining data from different strings. Two analyses have been performed using inter-string data, a single-level analysis and a ratio analysis, presented in [79, 143]. In both analyses the effective amplitude is calculated from the energy of the noise-subtracted waveforms in time domain. The data processing,

including the waveform averaging and the noise-subtraction is similar to the time domain pinger analysis described in the previous section.

For the single depth analysis, data from a single SPATS transmitter, recorded by all channels at the same depth as the transmitter, are combined. Using a single transmitter removes the systematic effect from the different transmittivities of the transmitters. Using only channels at the same depth mitigates the systematic effects due to the unknown change of transmittivity and sensitivity with the zenith angle. However, due to the geometry of the SPATS array, the dependence on the azimuth still remains. Because data from different channels are compared, a relative calibration is required. This is done similar to the relative calibration presented in section 6.4.2. The channel-to-channel variations of the sensitivity are estimated using the results from the pinger analysis in time domain [143, chapter 5]. Using this calibration, a fit is performed for each transmitter and the final result of the single-level analysis is

$$\langle\alpha\rangle = (3.16 \pm 1.05)\ \mathrm{km}^{-1}. \tag{6.42}$$

The multi-level ratio analysis uses ratios of amplitudes from different combinations of channels and transmitters,

$$\frac{A_{ij}\,A_{kl}}{A_{il}\,A_{kj}}\frac{d_{il}\,d_{kj}}{d_{ij}\,d_{kl}} = \frac{\mathcal{S}_i\mathcal{T}_j\,\mathcal{S}_k\mathcal{T}_l}{\mathcal{S}_i\mathcal{T}_l\,\mathcal{S}_k\mathcal{T}_j}\,\mathrm{e}^{-\alpha\cdot D_x}. \tag{6.43}$$

with the channels sensitivity $\mathcal{S}_\rangle$ and the transmitters transmittivity $\mathcal{T}_\rangle$ and $D_x = (d_{ij} - d_{il}) - (d_{kj} - d_{kl})$. The attenuation coefficient α is obtained from the linear fit

$$\log\left(\mathcal{R}_A\,\mathcal{R}_d\right) = -\alpha D_x + \beta, \tag{6.44}$$

where $\mathcal{R}_A$ and $\mathcal{R}_d$ are the amplitude and distance ratios and β is a free fit parameter. The data is constrained to combinations of neighboring levels to minimize the differences in zenith angle, leading to a maximum variation of zenith of 32 °. In addition, the amplitudes are calculated as the mean value over the three channels of each sensor to account for the unknown sensor orientation. As in the single-level analysis, the uncertainty on the SPATS channels sensitivity is estimated from the pinger measurements whereas the angular variation of the transmitters is estimated from laboratory measurements. Combining the data from all ratios leads to

$$\langle\alpha\rangle = (4.77 \pm 0.67)\ \mathrm{km}^{-1}. \tag{6.45}$$

The single-level and the multi-level ratio analyses use subsets of the same inter-string data but they are sensitive to different systematic effects. The single-level analysis is independent of the zenith but depends on the inherent sensitivity and angular dependence of each channel. The ratio analysis on the other hand is independent of the differences between sensors or transmitters, but suffers from large angular variations.

6.5.3 Transients

In the previous sections the acoustic attenuation coefficient has been determined using the measurements with artificial sound sources. The measurements of acoustic transient events

allow for an independent cross-check of these results. If a transient event is detected by several SPATS channels at different distances, it is possible to reconstruct the position of the source location of the transient from the timing information. Comparing the measurements of the same transient event, measured at different distances from the source, allows to determine the attenuation coefficient.

As described in section 5.2.5, the source for most of these transient events are the refreezing IceCube holes, e.g. the holes which have been used for the pinger measurements. For all transient events that originate close to a previous pinger stopping position, the corresponding calibration constants calculated from that data can be used to perform a relative calibration. For the attenuation analyses, 13 of such transient event have been selected and analyzed individually. The effective amplitude is calculated from the waveform energy in time domain, after taking into account the calibration factors. The resulting average attenuation coefficient and its error are [157]

$$\langle \alpha \rangle = 3.64 \pm 0.29\,\mathrm{km}^{-1}. \tag{6.46}$$

6.6 Comparison of Results

The results of the various attenuation length studies are shown in figure 6.28 and summarized in table 6.6. All results from the other analyses agree with the result presented in this thesis. No evidence on the depth dependence between 190 m and 500 m has been found and there are no indications for a frequency dependence.

The different analyses have different sets of systematic uncertainties, table 6.7 gives an overview of possible systematics and their qualitative attribution to the various analyses. From all data samples, the pinger sample of 2008/09 has the fewest systematic uncertainties and it is assumed to give the most reliable result. The reduction of systematic effects in the pinger data is achieved by the data selection. First, the four IceCube holes where the pinger was deployed are almost in a straight line. Consequently, the SPATS channels were probed with a narrow azimuthal range. Secondly, only data was used were pinger and channel are at the same depth, resulting in a very small zenith dependence. Finally, only data from the same channel is combined in the fits. Therefore, the contribution of all uncertainties connected to the unknown angular dependence of channel sensitivity and transmissivity is small compared to the other data samples. Even though, it cannot be excluded that the SPATS channels have a large sensitivity variation over the angular range of the measurements.

Comparison with Theoretical Predictions

The value of the measured attenuation length is about one order of magnitude smaller than the theoretical predictions, see section 3.4.2.2. In the following, possible explanations for this disagreement are discussed.

- **Scattering:** From the considerations presented in 3.4.2.2, the scattering coefficient was expected to be negligible compared to the absorption coefficient. For the frequency range relevant to acoustic neutrino detection, the scattering is dominated by Rayleigh scattering

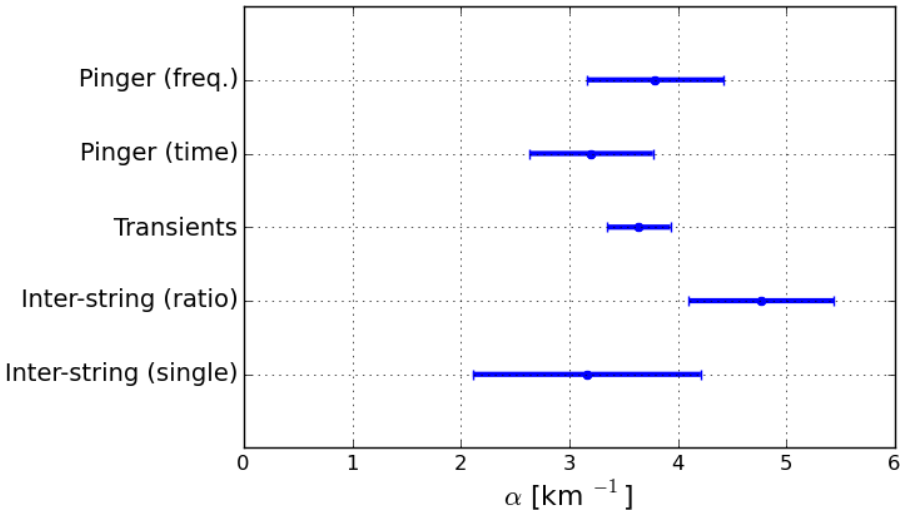

Figure 6.28: *Summary of the results from the various attenuation analyses. Shown are the attenuation coefficients with their respective errors.*

at ice grain boundaries, with a scattering coefficient depending on the diameter of the ice grains d and the frequency f

$$\alpha_{\mathrm{s,grain}} \propto d^3 \, f^4. \tag{6.47}$$

The scattering coefficient will be under-estimated if the grain diameters in the South Pole ice are larger than assumed. In addition, the scattering coefficient was calculated using only the mean grain diameter. Because of the strong dependence on the diameter, the scattering coefficient will be also under-estimated for a grain diameter distribution that has contributions of large diameters. It is possible, that the incorporation of such a grain diameter distribution can account for the measured value of the attenuation coefficient [158] and dedicated calculations have to be performed to investigate this. On the other hand, a scattering-dominated attenuation is disfavored by the current observations, as the scattering depends on the 4th power of frequency whereas no frequency dependence has been observed.

- **Absorption:** The acoustic absorption coefficient depends on a variety on different effects. For the calculations discussed in section 3.4.2.2 the proton reorientation in the ice crystals was considered to be the dominant effect. However, it is possible that the contribution of the other effects, such as the grain boundary sliding has been under-estimated in these calculation. Additional absorption mechanisms, not previously considered, would also lead to an increased absorption. An example is the presence of crystallographic defects or dislocations, which cause a local internal stress field in the ice crystals and therefore influence their elastic properties. Such defects are usually caused by plastic deformations by external forces. An acoustic wave loses energy from the interaction with these dislocations, leading to an increased absorption coefficient.

Table 6.6: *Summary of the results from the various analyses. N_α is the number of fits that have been performed for each analyses. Within their errors, all results are in compatible with the result of the frequency-domain analysis of the pinger data presented in this thesis.*

Analysis	N_α	$\alpha[\mathrm{km}^{-1}]$	λ[m]
Pinger (freq. domain)	48	3.79 ± 0.63	264^{+52}_{-37}
Pinger (time domain)	48	3.20 ± 0.57	312^{+68}_{-47}
Inter-string (single level)	12	3.16 ± 1.05	316^{+157}_{-79}
Inter-string (ratio)	1	4.77 ± 0.67	209^{+34}_{-25}
Transient	13	3.64 ± 0.29	274^{+23}_{-20}

Table 6.7: *Summary of the systematic effects in the various analyses. $\mathcal{S}$ and $\mathcal{T}$ denote the sensitivity of the* SPATS *channels and the transmittivity of the transmitters in dependence of azimuth ϕ and zenith θ, respectively.*

Systematic effect	Pinger	inter-string (single level)	inter-string (ratio method)	transients
Channel-to-channel	no	yes	no	minimal
Channel $\mathcal{S}(\phi)$	minimal	yes	yes	minimal
Channel $\mathcal{S}(\theta)$	minimal	no	yes	minimal
Transmittivity $\mathcal{T}(\phi)$	no	yes	yes	no
Transmittivity $\mathcal{T}(\theta)$	no	minimal	yes	no

7

Top-Down Reconstruction of Muon Energies

Abstract

In this chapter, we present a new method for the reconstruction of the energy of muons in IceCube*, following a "Top-Down" approach. The method is based on the direct comparison of a measured event with a large sample of simulated events. The Top-Down principle is motivated and the implementation for the muon energy reconstruction* IceCube *is described. The performance of the reconstruction is tested with Monte-Carlo data and results are presented for the IC40 detector.*

7.1 The Top-Down Concept

The concept of a "Top-Down" event reconstruction can be motivated when seen in contrast to the conventional "Bottom-Up" approach. In a Bottom-Up approach, the properties of a measured event are determined step by step, using different kinds of approximations in each step. For instance, the IceCube muon energy reconstruction as described in section 4.4.3, follows such a Bottom-Up approach. In a first step, the track geometry is reconstructed. Then, the muon energy loss is approximated as a continuous process, omitting individual stochastic energy losses along the track. Finally, the muon energy is obtained from equation 3.4, relating the muon energy to the average energy loss.

The Top-Down approach is conceptually complementary to the Bottom-Up approach. It is based on the direct comparison of a measured event with single simulated Monte-Carlo events by means of statistical tests, applied to detector-level observables. The event comparison is formulated as a maximum-likelihood method, and performed over a large sample of Monte-Carlo events. The event from this sample with the maximum value of the likelihood is considered as the event with the best agreement. As all event properties of the simulated events are naturally known, the event with the best agreement yields an estimate for the properties of the measured event. Different to the Bottom-Up approach, no approximations other than included in the Monte-Carlo simulations are applied during the reconstruction.

In principle, the Top-Down method can be used to reconstruct all event parameters in one step. In this work, it is applied to the one-dimensional case of the muon energy reconstruction. Because the Top-Down method requires large numbers of Monte-Carlo events for the comparison, it is generally more computationally intensive than the Bottom-Up methods. Therefore, we intent to apply the Top-Down method to a sample of interesting muon-neutrino events with a well-reconstructed track geometry.

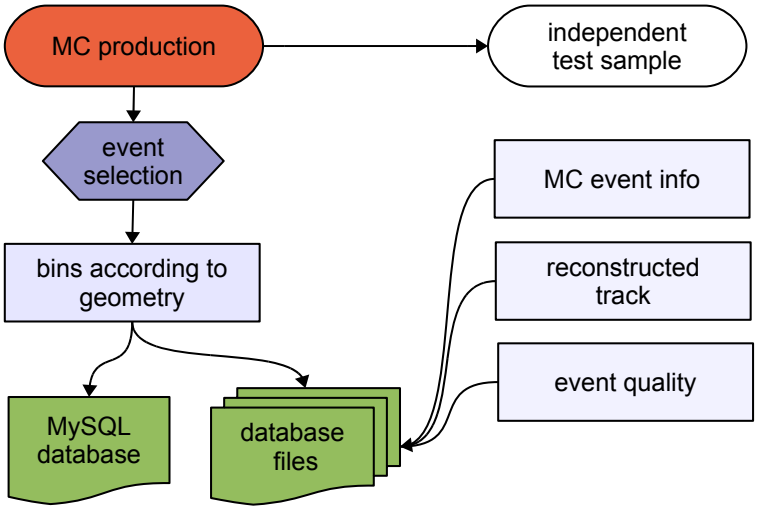

Figure 7.1: *Illustration of the creation of a database of events. The simulated Monte-Carlo events (MC) are produced with sufficient statistics and sorted into separate files, according to their track geometry. The files contain the simulated event information as well as all available information of the event quality. The content of the files is organized by a MySQL database.*

A first concept of the application of the Top-Down method to IceCube data was elaborated in [159]. As part of this thesis, a first implementation within the IceCube software framework has been developed and tested. The implementation of the method is described in the following section. The results of a performance study using Monte-Carlo data are presented in section 7.3.

7.2 Implementation

In this section, the implementation of the Top-Down method for muon energy reconstruction is described. The Top-Down method requires a sample of Monte-Carlo events, a set of event observables and a comparison algorithm that quantifies the agreement of a measured event with the Monte-Carlo events based on these observables.

7.2.1 Monte-Carlo Database

For the Top-Down muon energy reconstruction, a measured event is compared with a sample of simulated events with a similar geometry. Prior to the energy reconstruction, a muon track reconstruction is performed with IceCube reconstruction methods. The obtained directional information is used to create a specific sample of Monte-Carlo events for this event. In principle, this can be done in two different ways, as will be discussed below.

The first method is to create a new sample of simulated events for each measured event.

This is done by taking the reconstructed track geometry as an input for a dedicated simulation to produce Monte-Carlo events with a similar track geometry. This approach has the advantage that for very large number of events the reconstructed energy should converge to the true value. On the other hand, this approach is limited by CPU resources and introduces a considerable overhead for repeatedly creating simulated events for each reconstructed event.

The second method avoids this overhead. Here, the simulated data are created with large statistics and permanently stored in a database. This is illustrated in figure 7.1. Starting from a suitable sample of Monte-Carlo data, the individual events are sorted into event classes according to their track geometry, after an event selection has been performed. All event classes are then written to separate database files on disk while the information of the file location and the class content is managed by a *MySQL* database. The database files contain all information on the properties of the simulated event, as well as the track reconstruction and the event quality. The contents of the database used in this study is described in the next section.

It is also practical to keep an independent test sample which is not filled into the database. In this work, the test sample will be used to investigate the reconstruction performance of the Top-Down algorithm.

A database is naturally finite, because it contains a finite number of events. It is neither technically feasible nor desirable to fill infinite numbers of events into the database. On the other hand, the database events have to be representative for the reconstructed events. In particular, for any reconstructed event, there has to be a sufficient number of Monte-Carlo events with a similar track geometry, in order to allow for a meaningful event comparison. Moreover, for the energy reconstruction it is required that the distribution of the muon energy of all events in the database covers the full possible energy range of the reconstructed events. Hence, in order to obtain a representative database, the events for the database are simulated with an E^{-1} neutrino energy spectrum, providing sufficient statistics over the full energy range (see section 4.3). In addition, the same selection criteria on the database events and the reconstructed events are applied.

Finally, the granularity of the database (number of event classes or files, respectively) has to be optimized against the computational effort. For a large number of files, the overhead of file access operations is significant, because for every event a large number of files has to be read and processed.

7.2.1.1 Database Contents

The following information of the Monte-Carlo events is stored in the database files:

- **Reconstructed geometry:** A muon track reconstruction is performed on the Monte-Carlo events. For the IC40 configuration, the MPE reconstruction is used (see section 4.4.2). The obtained track geometry is stored in the database, together with all available information on the reconstruction quality. The track position used for the database is the point on the reconstructed track with the closest distance to the center of the IceCube

detector, called C_{app}. The track geometry is parametrized by

$$\text{geometry} = \{C_{\text{app}}X,\, C_{\text{app}}Y,\, C_{\text{app}}Z,\, \theta,\, \phi\}\,, \tag{7.1}$$

with the reconstructed direction θ, ϕ of the track and the X, Y, Z components of the C_{app} position. This description has the advantage that it is independent of the reconstruction of the neutrino interaction vertex, which is not known for measured events.

Table 7.1 summarizes the database parameters and their respective range. It is furthermore convenient to define the impact parameter in the horizontal plane

$$C_{\text{app}}R = \sqrt{C_{\text{app}}X^2 + C_{\text{app}}Y^2}. \tag{7.2}$$

- **Pulse map:** The complete information of the event (pulse maps) which has been obtained from the feature extraction, including the timing, position and charge information of all hit DOMs is stored for each event. From this information the various observables are obtained that are used in the likelihood-based event comparison (section 7.2.3). Storing the full pulse maps instead of these observables allows to later include other observables using the same database.

- **Monte-Carlo parameters:** By design, the information on the Monte-Carlo simulation is necessary for the Top-Down method. The muon energy at the interaction vertex and inside the detector, the muon energy loss, the length of the track and the neutrino energy are stored in the database. For this study, the muon energy inside IceCube is defined as follows. If the neutrino interacts inside the detector, the energy $E_{\mu,0}$ of the simulated muon at the interaction vertex is taken. For an interaction far outside the detector, the muon has already lost part of its energy on its path through the ice before entering the detector. In this case, the energy $E_{\text{MMC,entry}}$ of the muon at the entry point into the MMC volume is taken as reference. The MMC volume is the volume in which the muon was propagated by the muon propagator (MMC) during the simulation (see section 4.3).

$$E_{\text{IC}} = E_{\text{MMC,entry}} \quad \text{or} \quad E_{\mu,0} \tag{7.3}$$

The average muon energy loss inside the detector is defined as

$$\frac{\Delta E}{\Delta X} = \frac{E_{\text{lost}}}{L}, \tag{7.4}$$

where E_{lost} is the total energy deposited by the simulated muon during propagation and L is the track length of the muon inside the propagation volume. The Top-Down reconstruction returns the values of these parameters from the Monte-Carlo event with the best match as reconstructed values.

- **Event quality:** All available quality information from the standard data processing are written to the database, e.g. the likelihood values from the track reconstruction or the filters the event has passed. This information allows to perform a quality selection on the database contents before the Top-Down reconstruction or after the reconstruction to further adjust the quality of the reconstructed events. The quality selections considered in this study are described in section 7.3.2.

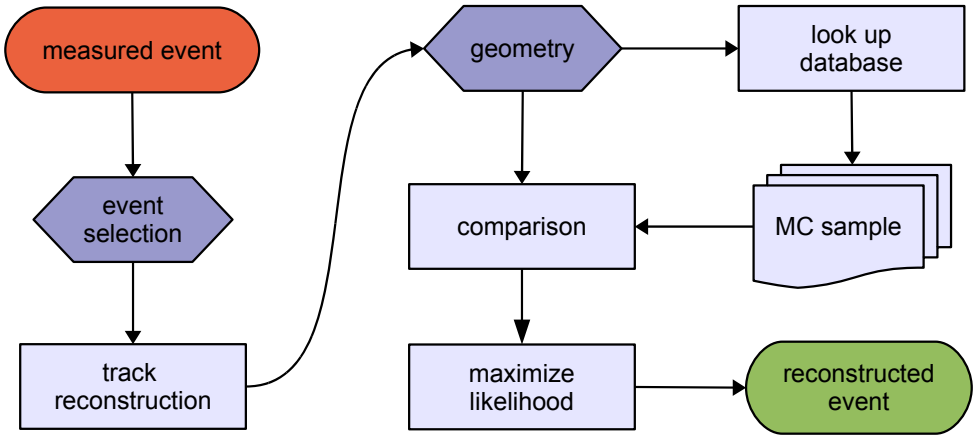

Figure 7.2: *Reconstruction of a (measured) event using the Monte-Carlo database. After an event selection, a sample of events is selected from the database and compared with the measured event. The properties of the Monte-Carlo events with the maximum likelihood give an estimate for the values of the reconstructed event.*

- **Energy reconstruction:** The results from the Top-Down energy reconstruction will be compared with the current IceCube energy reconstruction, namely the MuE and the Photorec-llh reconstruction (section 4.4.3). Therefore, the results from both energy reconstructions are also written to the database.

Table 7.1: *The muon event parameters and their ranges, as used in the database.*

parameter	E_ν [GeV]	ϕ	$\cos\theta$	$C_{\text{app}}X, Y, Z$ [m]
range	$10 - 10^{10}$	$(0, 2\pi)$	$(-1, 1)$	$(-1000, 1000)$

7.2.2 Event Comparison

The comparison of a measured event with Monte-Carlo events is formulated using a likelihood function. The unknown event parameters of the measured event are determined by finding the Monte-Carlo event (or class of events) which give the maximum of this likelihood. More specifically, the unknown event parameters $\{a\}$ are obtained from the comparison of the measured event observables $\{x\}$ with the same observables $\{\xi\}$ of simulated events. If there are K observables, the likelihood for the comparison is written as a product:

$$\mathcal{L}\left(\{x\} \mid \{\xi\}, \{a\}\right) = \prod_{i=1}^{K} l_i(x_i \,|\, \xi_i, \{\alpha\}), \tag{7.5}$$

where l_i is the likelihood of the ith observable. Hence, the likelihood is the product of various different statistical tests, each comparing a single experimental observable. The observables

and likelihoods used in this study are discussed in the next section.

Figure 7.2 illustrates the reconstruction using a database of Monte-Carlo events. In the most general case, the likelihood (equation 7.5) depends not only on the muon energy, but also on the track geometry. Therefore, the measured event is compared with a sample of Monte-Carlo events that have a similar track geometry, but different muon energies. For this, a successful muon track reconstruction is required and the information obtained from this reconstruction is used to select a sample of Monte-Carlo events with a similar track geometry from the database. The geometrical constraints to describe this similarity are discussed below.

Using the selected Monte-Carlo sample, the likelihood is calculated for each event of the sample individually in an event-by-event comparison. As discussed in section 7.2.1.1, the database contains several energy-related event parameters,

$$\{\alpha\} = \{E_{\mu,0},\, E_{\mathrm{IC}},\, \Delta E/\Delta X, ...\}\,.$$

The Monte-Carlo event from the selected sample, that maximizes the likelihood, defines the reconstructed values of either event parameter:

$$\max \mathcal{L} \;\Rightarrow\; E_{\mathrm{IC,reco}},\; \Delta E/\Delta X_{\mathrm{reco}}, \ldots\,. \tag{7.6}$$

In this work, the track geometry is described by the direction (θ, ϕ) and the C_{app} position of the track. The sample of similar events is selected by requiring a maximal positional and angular difference between measured and database event:

$$\Delta C_{\mathrm{app}} \leq a_C, \quad \Delta\psi \leq a_\psi, \tag{7.7}$$

where a_C and a_ψ are the maximal differences of these parameters and ΔC_{app} is the distance between the positions of both events. The performance of the Top-Down reconstruction depends on quality of the preceding track reconstruction as well as the constraints when selecting geometrically similar events. The dependence of the reconstruction on the constraints is investigated in section 7.3.3.4.

7.2.3 Observables

At detector level, an event in IceCube is described by the timing and spatial distribution of the hit DOMs. The timing and the charge are obtained from the waveforms recorded by the DOMs during the feature extraction (section 4.2). With this information, an event is described as a set of observables

$$\{\overrightarrow{x_i}, q_i, \{t_a\}_i\}\,, \quad i = 1, \ldots, N_{Ch} \tag{7.8}$$

with the position $\overrightarrow{x_i}$ of the DOM, the arrival times t_a and the total charge q_i deposited in this DOM. N_{Ch} is the total number of DOMs (i.e. channels) that had at least one hit. In this work, the following observables are considered:

- **Nch:** The total number of hit DOMs of the event. As discussed in section 4.4.3, N_{Ch} is a simple energy estimator. It is strongly affected by the track geometry. However, in the context of the Top-Down reconstruction, the energy is not reconstructed directly from the measured N_{Ch} value, but from the agreement between two events based on their individual N_{Ch} values.

- **Hit distances:** The distribution of the hit distances d_i, where d_i is calculated as the perpendicular distance of each hit DOM to the reconstructed muon track (see figure 4.5). This observable is sensitive the the spatial energy deposition of the muon in the detector.

$$R = \{d_i\}\,, \quad i = 1, \ldots, N_{Ch} \tag{7.9}$$

- **Timing:** The distribution of arrival times $t_{a,i}$ and time residuals $t_{i,\mathrm{res}}$ (see equation 4.3) of the hits in each DOM. For this study, only the timing of the first photon arriving in each DOM is used.

$$T = \{t_{a,i}\}\,, \quad T_{\mathrm{res}} = \{t_{i,\mathrm{res}}\}\,, \quad i = 1, \ldots, N_{Ch} \tag{7.10}$$

- **Charge:** The distribution $Q = \{q_i\}$ of the charge over all DOMs is also tested. For this, a histogram of the charge per DOM is created from all hit DOMs of the event.

7.2.4 Likelihood Definition

Nch Test

It is assumed that the number of hit DOMs in an event N_{Ch}, is given by a Poissonian distribution. Hence, the probability of observing n hit DOMs is given by

$$p(n \,|\, \mu) = \frac{\mu^n \mathrm{e}^{-\mu}}{n!}, \tag{7.11}$$

where μ is the unknown expectation value. μ depends on the energy as wells as of the geometry of the track, such as the direction and the position relative to the detector center

$$\mu = \mu\,(\mathbf{X}, \theta, \phi, \mathbf{E})\,. \tag{7.12}$$

For two events with different N_{Ch} values, e.g. a measured event with $n = N_1$ and a simulated event with $n = N_2$, the agreement is tested with the hypothesis that the two N_{Ch} values are drawn from the same Poisson distribution, i.e. that the expectation values of both are the same, $\mu = \mu_1 = \mu_2$. However, this expectation value is not known. Integrating over the joint probability function over all possible expectation values yields

$$\begin{aligned} \mathcal{L}_N &= \int_0^\infty p(N_1 \,|\, \mu)\, p(N_2 \,|\, \mu)\, \mathrm{d}\mu \\ &= \binom{N_1 + N_2}{N_2} \cdot 2^{-(N_1+N_2+1)}. \end{aligned} \tag{7.13}$$

This expression does not depend on the unknown expectation value μ, but only on the observed N_{Ch} values N_1 and N_2 of both events. It is used to quantify the agreement between two events with similar geometry but different value of N_{Ch}.

An alternative derivation is given in [160]. A Bayesian approach used to derive the probability, taking the sum $N = N_1 + N_2$ as a nuisance parameter.

$$\begin{aligned} p(N_2 \,|\, N = N_1 + N_2) &= \frac{p(N \,|\, N_2) \cdot p(N_2)}{p(N)} \\ &= \frac{\mu_1^{N-N_2}\, \mathrm{e}^{-\mu_1}}{(N-N_2)!} \cdot \frac{\mu_2^{N_2}\, \mathrm{e}^{-\mu_2}}{N_2!} \Big/ \frac{(\mu_1+\mu_2)^N\, \mathrm{e}^{-(\mu_1+\mu_2)}}{N!} \\ &= \binom{N}{N_2} \left(\frac{\mu_2}{\mu_1+\mu_2}\right)^{N_2} \left(\frac{\mu_1}{\mu_1+\mu_2}\right)^{N-N_2} \end{aligned} \tag{7.14}$$

For $\mu_1 = \mu_2$, this expression reduces to

$$\tilde{\mathcal{L}}_N = \binom{N_1+N_2}{N_2} \cdot 2^{-(N_1+N_2)}, \tag{7.15}$$

which is equivalent to equation 7.13 except for the factor $1/2$ due to normalization.

Shape Test - Kolmogorov-Smirnov

While N_{Ch} is a discrete quantity, the other above considered observables are one-dimensional distributions. In order to compare two events, the shape of these distributions is tested. A shape test is a test of the hypothesis that two distributions are drawn from the same parent distribution. Although this test does not specify what that common distribution is, it describes the level of agreement between the shapes of the two distributions. Here, two shape tests have been implemented and tested, the Kolmogorov-Smirnov test and a binned likelihood value shape test. These tests are independent of the absolute normalization of the considered distributions, e.g. the total number of hits for the test of the hit distances.

With the two-sample Kolmogorov-Smirnov (KS) test, the cumulative $C(x)$ of the distribution of an observable x for two events are compared by their maximum absolute difference D as test statistics

$$D = \max_x |C_1(x) - C_2(x)|. \tag{7.16}$$

The number of data points in these distributions is the number of hit channels of both events, N_1 and N_2 respectively. The probability, that for an observed value D both distributions are the same, is given by [161]

$$\mathcal{L}_{\mathrm{KS}} = 1 - P_{KS}\left(D\,\sqrt{\frac{N_1 N_2}{N_1+N_2}}\right) \tag{7.17}$$

with the Kolmogorov-Smirnov distribution

$$P_{KS}(x) = 1 - 2\sum_{j=1}^{\infty} (-1)^{j-1}\, \mathrm{e}^{-2j^2x^2}. \tag{7.18}$$

Small values of $\mathcal{L}_{\mathrm{KS}}$ indicate that both distributions are significantly different from each other. An advantage of the KS test is that it does not depend on the parametrization of the observable and can also be applied to unbinned data.

Shape Test - Likelihood Value Test

An alternative distribution shape test is the binned likelihood value test. Here, the shapes of two histograms are compared using a similar approach as it was used for the N_{Ch} test, only that in this case a separate Poissonian distribution is associated to each bin. Given two events, each with a histogram $u = \{u_i\}$ and $v = \{v_i\}$ of an observable, the joint probability distribution is given by

$$p(u,v) = \prod_{i=1}^{N_{\mathrm{bins}}} \frac{\mu_i^{u_i}\ \mathrm{e}^{-\mu_i}}{u_i!} \cdot \frac{\nu_i^{v_i}\ \mathrm{e}^{-\nu_i}}{v_i!} \tag{7.19}$$

where the product is performed over all N_{bins} bins. The expectation values for the number of entries in each bin for the two histograms are denoted by μ_i and ν_i, respectively. Using the same reasoning as in equations 7.14, the probability is written as

$$\mathcal{L}_{\mathrm{V}} = \prod_{i=1}^{N_{\mathrm{bins}}} \binom{t_i}{v_i} \left(\frac{\nu_i}{\mu_i+\nu_i}\right)^{v_i} \left(\frac{\mu_i}{\mu_i+\nu_i}\right)^{t_i-v_i}, \tag{7.20}$$

with $t_i = u_i + v_i$. This is similar to equation 7.14, only that in this case a product is performed over all bins. If both histograms are sampled from the same parent distribution, the entries in each bin for the two histograms are assumed to scale with a constant (unknown) factor

$$\nu_i = a\ \mu_i, \quad a = \mathrm{const.} \tag{7.21}$$

This means that the shapes of the two histograms are the same, although their absolute normalizations are different. Using the estimator $\hat{a} = N_v/N_u$, with $N_u = \sum_i u_i$ and $N_v = \sum_i v_i$, gives the test statistics

$$-\log \mathcal{L}_V = -\sum_{i=1}^{N_{\mathrm{bins}}} \left[\log \binom{t_i}{v_i} + t_i\ \log \frac{N_u}{N_u+N_v} + v_i\ \log \frac{N_v}{N_u}\right]. \tag{7.22}$$

Different to the KS test, the likelihood test depends on the binning of the observable. As a consequence for the Top-Down method, the binning as well as the range have to be optimized for each binned observable.

Table 7.2 summarizes the likelihoods considered in this study. The reconstruction performance of the individual likelihoods and the products of likelihoods will be tested.

Table 7.2: *Overview of the likelihoods considered in this study, with the N_{Ch} test (equation. 7.13), the Kolmogorov-Smirnov test L_{KS}, (equation 7.17) and the binned likelihood value test L_V (equation 7.22).*

symbol	observable	likelihood
L_N	N_{Ch}	N_{Ch} test
$L_{\mathrm{KS,Q}}$	charge per DOM	KS. test
$L_{\mathrm{KS,R}}$	hit distances	KS. test
$L_{\mathrm{V,R}}$	hit distances	binned test
$L_{\mathrm{KS,TRes}}$	time residuals	KS test
$L_{\mathrm{V,TRes}}$	time residuals	binned test
$L_{\mathrm{KS,T}}$	arrival times	KS. test

7.3 Monte-Carlo Data Study

7.3.1 Data Sample

For this work, the official IceCube simulation production dataset 3311 is used, which can be retrieved from the IceCube data warehouse[1]. The 3311 dataset is a neutrino signal dataset, simulated for the IC40 detector configuration. The data were simulated with a hard neutrino energy spectrum, $\mathrm{d}N/\mathrm{d}E_\nu \sim E_\nu^{-1}$, over an energy range of $10 - 10^{10}\,\mathrm{GeV}$.

The simulated data have undergone the the same standard level 2 processing that is applied to the experimental data, including the online filtering and all standard IceCube event reconstructions, see section 4.2.2. For the muon track reconstruction, the MPE likelihood was used, see section 4.4. An event selection is performed on this data:

- The event has to have passed either the Muon or the EHE filter. The Muon filter was developed to reject down-going, atmospheric muons and to keep candidate muon-neutrino events from near or below the horizon. The EHE filter selects high energetic events from all directions, based on the deposited charge in all DOMs.

- A successful track reconstruction is required. During the standard IceCube track reconstruction, all events are marked with a fit status, indicating whether the reconstruction has failed or has successfully converged. Only events for which the MPE likelihood fit has converged, are considered.

The reconstructed track direction, described by (θ, ϕ) and the C_{app} position, are used to select events from the database, see section 7.2.1.1. The distribution of these track parameters in the data sample is shown in figure 7.3. The angular distribution of the track direction is a result of the applied filters.

Figure 7.4 shows the center of gravity (COG) of the events. The COG is calculated from

[1] `http://internal.icecube.wisc.edu/simulation/dataset/3311`

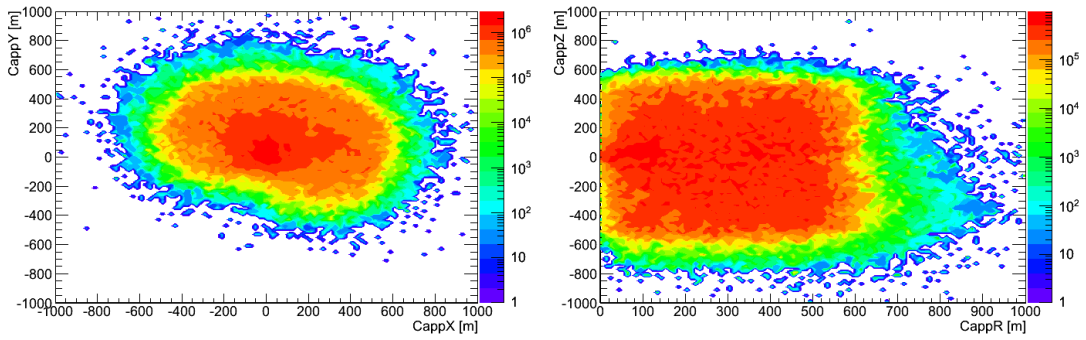

(a) (b)

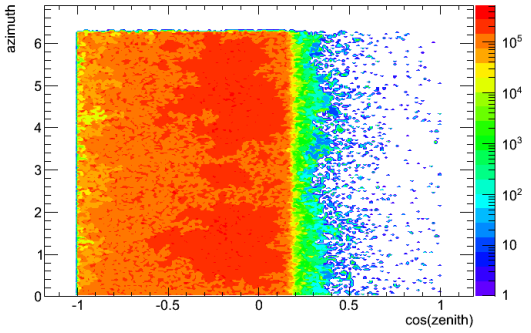

(c)

Figure 7.3: *Distribution of the track parameters of the reconstructed muon tracks in the data sample , weighted to an E^{-2} spectrum. (a) and (b) show the Capp position, with $CappR = \sqrt{CappX^2 + CappY^2}$. (c) shows the reconstructed muon track direction.*

the sum over the positions $\overrightarrow{x_i} = (x, y, z)_i$ of all channels in an event with a hit, with charge q_i

$$\overrightarrow{x}_{\mathrm{COG}} = \sum_{i=1}^{N_{Ch}} q_i \overrightarrow{x_i} / \sum_{i=1}^{N_{Ch}} q_i. \tag{7.23}$$

In these figures, the shape of the IC40 detector as well as the horizontal dust layer just below the detector center are visible.

Database

The Monte-Carlo database is created from dataset 3311, following the description in section 7.2.1. Table 7.3 lists the total number of events in the database in comparison with the number of generated neutrinos, triggered and filtered events after the IceCube standard level 2 processing. Using the above-mentioned selection criteria, about 60% of the level 2 data are kept and filled into the database.

For the creation of the database, it was decided to only use a basic event selection as described above, while also storing all available information on the event quality in the database, see section 7.2.1.1. The quality information can be used during the Top-Down reconstruction

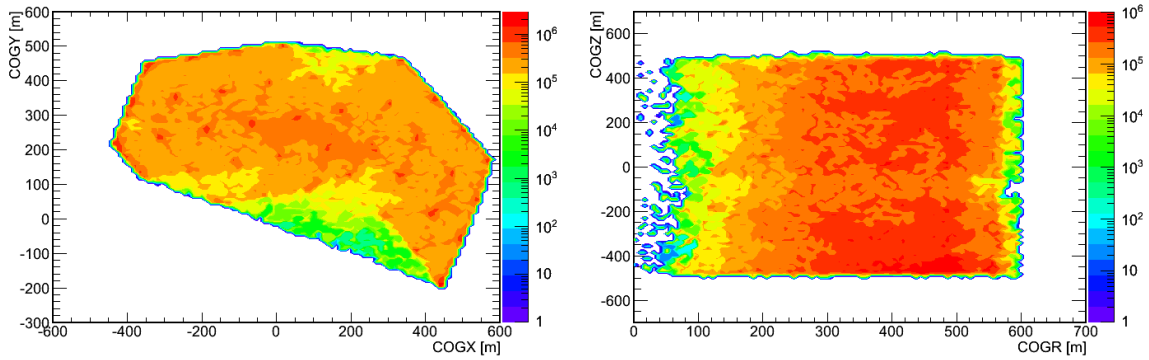

(a) (b)

Figure 7.4: *The center of gravity (COG, see equation 7.23) for the events in the data sample, weighted to an E^{-2} spectrum. The shape of the IC40 detector and the positions of individual strings are visible.*

to provide samples with different event quality. This strategy allows to use the same database for different event selections. Depending on the analysis, different samples of database events can be selected.

Table 7.3: *Number of events on neutrino generation level, standard IC40 processing levels and in the database.*

level	generated ν	triggered	level 1+2	database
events	10^7	1195000	272500	166494

7.3.2 Quality Selection

Because the energy reconstruction uses the result of a preceding track reconstruction as input, a good track reconstruction is desirable. In order to test the reconstruction performance, event selections similar to the IC40 point source analysis [162] and the IC40 diffuse flux analysis [38] have been applied. The selections used in the Top-Down performance study are a sub-set of these selection schemes[2]. In this study, the following quality variables are considered.

- **Reduced log-likelihood (rlogL and plogL):** The track has been reconstructed using a maximum-likelihood algorithm (MPE), section 4.4.2. The likelihood values of the found maximum can be used to estimate the quality of the reconstruction. For this, the so-called reduced log-likelihood value, $\mathrm{rlogl} = -\log\mathcal{L}/(N_{Ch} - 5)$ is used. The number of degrees of freedom during the likelihood fit is the number of hit channels minus the number of free parameters. For the track reconstruction there are five free parameters (position x,y,z and direction θ, ϕ). The so-called *re-defined* reduced log-likelihood

[2]The full set of selections in these studies include additional parameters that have not been written to the current event database and therefore cannot be applied here.

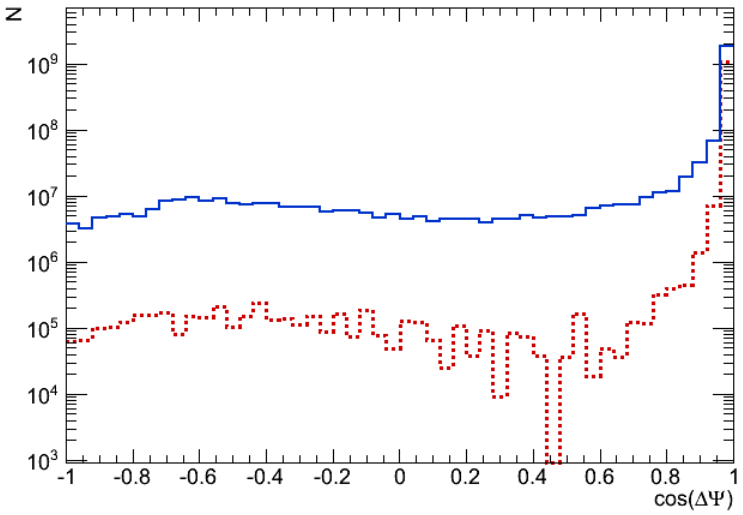

Figure 7.5: *Distribution of the angular difference between the reconstructed muon track (MPE likelihood) and the initial neutrino direction, before (solid line) and after (dotted line) the quality selection, for an E^{-2} neutrino spectrum. The quality selection greatly reduces the number of badly reconstructed muon tracks, indicated by their large angular deviation. For well-reconstructed tracks* $\cos\Delta\Psi \approx 1$.

plogl $= -\log\mathcal{L}/(N_{Ch} - 2.5)$ has been introduced to improve the separation performance of the reduced log-likelihood at small N_{Ch} values. Both parameters can be used as quality parameters with small values corresponding to a higher quality.

- **Error estimate of the track direction ($\sigma_{\text{Paraboloid}}$):** An error estimate for the directional reconstruction is obtained by varying the direction of the reconstructed muon track and calculating the likelihood for each point. The contour of the error ellipse defines an uncertainty on the muon track direction. An error estimate is obtained from the mean over the two semi-axes of this ellipse [163]. A large value indicates a lower reconstruction quality.

- **Bayesian log-likelihood ratio ($LLHR_{\text{Bay}}$):** In order to reject tracks that have been falsely reconstructed as up-going events, the hypothesis of an up-going muon track is tested against the alternative hypothesis of a down-going muon track [136]. The likelihood values for both hypothesis are calculated (by restricting the zenith to above or below the horizon) and compared using a log-likelihood ratio. An event is rejected if the value of the up-going reconstruction is not significantly better than the down-going reconstruction.

- **Direct hits and direct length ($Ndir$, $Ldir$):** $Ndir$ is the number of DOMs that have a direct hit. A hit is considered a direct hit if it arrives within a time window characteristic for Cherenkov emission without scattering. Direct hits provide the best information for the track reconstruction, a large number allows for a good reconstruction. The direct length $Ldir$ is the maximum length between the positions of DOMs with direct hits,

projected along the reconstructed muon track. It can be interpreted as the lever arm of the track reconstruction, a large value corresponds to a more robust result.

Table 7.4 lists the values of the quality variables. The angular resolution before and after the event selection is shown in figure 7.5. The event selection reduces the number of badly reconstructed tracks with large angular deviations between the reconstructed and the true direction of the muon track. The event passing rate with respect to the level 2 filtering is $\approx 40\%$ for a E_ν^{-2} spectrum.

Table 7.4: *The quality event selections applied in this study. There are different subsets of cuts for up- and down-going tracks.*

Selection criterion
up-going:
$rlogL_{\mathrm{MPE}} < 8$ OR $plogL_{\mathrm{MPE}} < 7.1$
$rlogL_{\mathrm{MPE}} < 8.3$
$\sigma_{\mathrm{paraboloid}} < 3\,^\circ$
$LLHR_{\mathrm{Bay}} > 30$
$NDir > 5$
$LDir > 200\,\mathrm{m}$
down-going:
$\sigma_{\mathrm{paraboloid}} < 1.5\,^\circ$
$rlogL_{\mathrm{MPE}} < 7.5$

7.3.3 Results

The performance of the Top-Down reconstruction algorithm is tested on a sample with approximately 20000 simulated neutrino events. The test sample and the database events are independent sub-samples of the same Monte-Carlo dataset, where the quality selection described in the previous section has been applied. For this study, the following geometrical constraints on the track geometry are chosen, see section 7.1

$$\Delta\psi \leq 20\,^\circ, \quad \Delta C_{\mathrm{app}} \leq 200\,\mathrm{m} \tag{7.24}$$

with the angular distance $\Delta\psi$ between the tracks and the distance between the C_{app} positions. Typically, these constraints result in a few hundred selected database events for each comparison. The optimum values for the constraints depend on the database, this is discussed in section 7.3.3.4.

7.3.3.1 Likelihood Landscapes

Figure 7.6 exemplary shows the Top-Down reconstruction for selected events with different average muon energy losses $\Delta E/\Delta X$. Each point in these figures corresponds to the likelihood

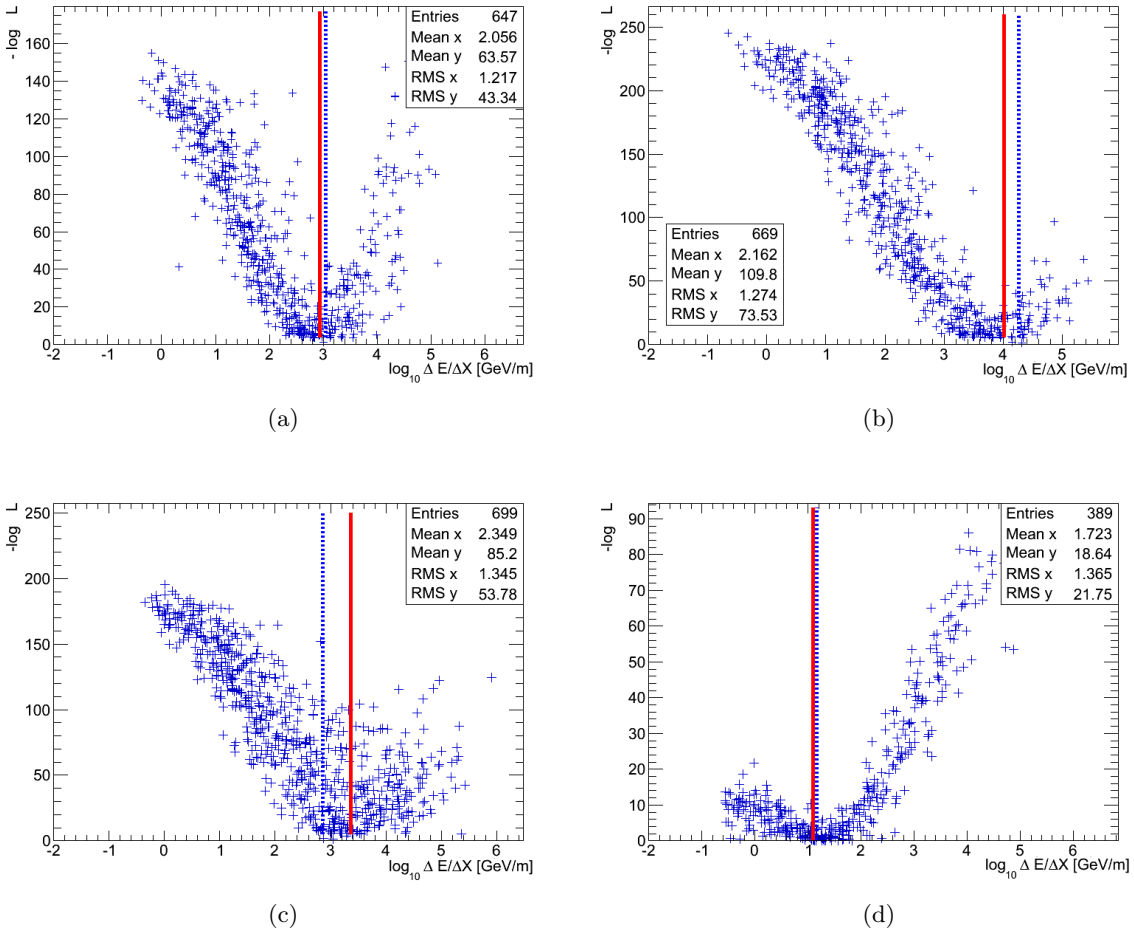

Figure 7.6: *Examples for the likelihood landscape for various simulated events and the $\mathcal{L}_{KS,R}$ likelihood. The reconstructed $\Delta E/\Delta X_{\text{reco}}$ (broken blue line) and the simulated (solid red line) value $\Delta E/\Delta X_{\text{MC}}$ are shown. The reconstructed value is obtained from the event with the maximum likelihood, i.e. the minimum of $-\log \mathcal{L}_{KS,R}$.*

value from the comparison of the reconstructed event with a single event from the database. The calculated likelihood value quantifies the agreement between these events. A minimum of $-\log \mathcal{L}$ is formed around the true Monte-Carlo value $\Delta E/\Delta X_{\text{MC}}$ of the reconstructed event. The reconstructed value $\Delta E/\Delta X_{\text{reco}}$ is obtained as described in section 7.2.2.

7.3.3.2 Reconstruction Resolution

The Top-Down reconstruction is now applied to all events of the test sample. The correlation between the reconstructed and the simulated $\Delta E/\Delta X$ of all reconstructed events is shown in figure 7.7. The correlation is linear over the considered range, indicating that there is no substantial over- or underestimation of the reconstructed value.

In order to evaluate the reconstruction performance, the following definitions and abbrevi-

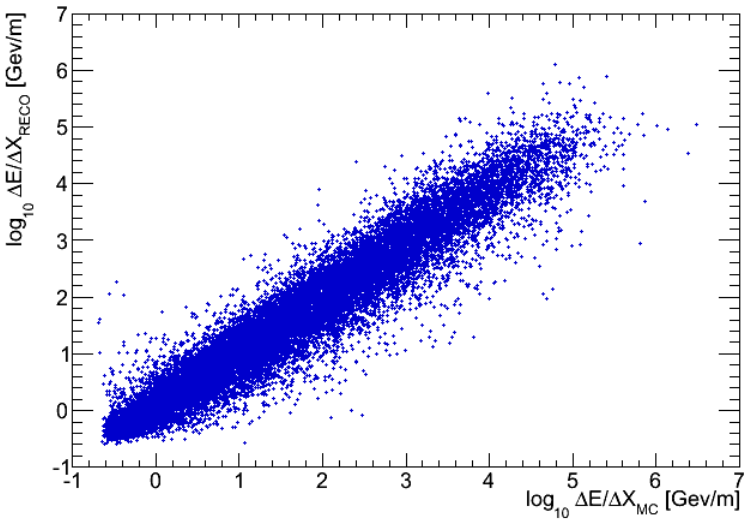

Figure 7.7: *Correlation between the reconstructed muon energy loss $\Delta E/\Delta X_{\text{reco}}$ and the true Monte-Carlo value $\Delta E/\Delta X_{\text{MC}}$. The reconstruction was performed with the $\mathcal{L}_{KS,R}$ likelihood.*

ations are used:

$$\begin{aligned} \Delta \log_{10} E &= \log_{10} \left(E_{\text{reco}} / E_{\text{IC}} \right) \\ \Delta \log_{10} \frac{\Delta E}{\Delta X} &= \log_{10} \left(\frac{\Delta E/\Delta X_{\text{reco}}}{\Delta E/\Delta X_{\text{MC}}} \right) \end{aligned} \tag{7.25}$$

with the reconstructed and simulated values of either energy or energy loss, defined by 7.3 and 7.4 respectively. $\Delta \log_{10}$ and $\Delta \log_{10} \frac{\Delta E}{\Delta X}$ are calculated for each reconstructed event and the mean values and the standard deviations over their distributions are determined:

$$\begin{aligned} \mu_E &= \text{Mean} \left(\Delta \log_{10} E \right), \quad \mu_\Delta = \text{Mean} \left(\Delta \log_{10} \Delta E/\Delta X \right) \\ \sigma_E &= \text{Stdev} \left(\Delta \log_{10} E \right), \quad \sigma_\Delta = \text{Stdev} \left(\Delta \log_{10} \Delta E/\Delta X \right). \end{aligned}$$

The mean value indicates a bias of the reconstructed values to larger or smaller values, i.e. it is a measure for a systematic over- or underestimation of the reconstructed value with respect to the true Monte-Carlo value. The standard deviation of distributions are taken as a measure of the reconstruction resolution.

Single Likelihoods

The Top-Down reconstruction is now performed for all the likelihoods defined in table 7.2. In a first step, the reconstruction is investigated for each of the considered likelihoods separately. This allows to evaluate their performance unaffected by the other observables. The product over multiple likelihoods is investigated in the next section. Figure 7.8 shows the results for various likelihoods and table 7.5 summarizes the results for all considered likelihoods.

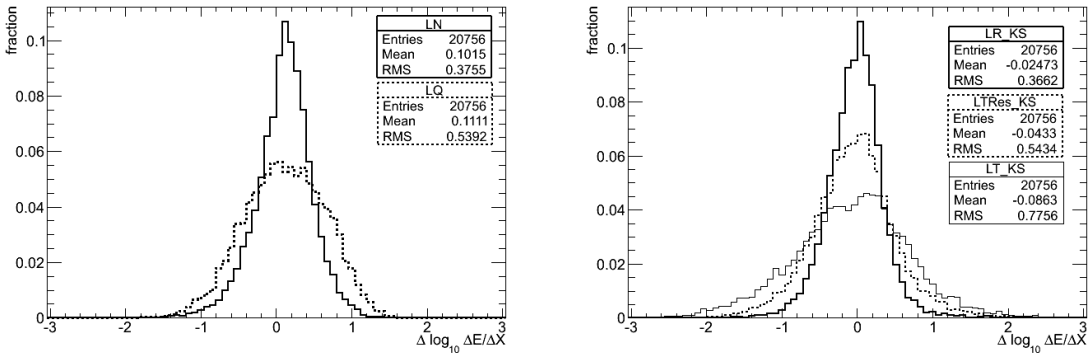

(a) (b)

Figure 7.8: *The reconstruction resolution of single likelihoods, each testing a particular observable, see table 7.2.*

The Kolmogorov-Smirnov (KS) test on the perpendicular hit distances $\mathcal{L}_{\mathrm{KS,R}}$ and the N_{Ch} test $\mathcal{L}_{\mathrm{N}}$ provide the best results for the single likelihood reconstruction. For both the distribution of hit distances and for the time residuals, two different likelihoods have been tested, namely the KS test and the binned likelihood shape test (equation 7.22). In both cases, the KS test performs better than the binned likelihood test for the same observable. The binned likelihood test depends on the binning, whereas the KS test is performed on the un-binned distributions. It is possible, that an optimized binning could improve the result. However, for the further study, only the KS test is considered.

Table 7.5: *Results of the reconstruction from the various likelihood using the same MC data sample, see table 7.2. The distributions* $\Delta \log_{10}$ *and* $\Delta \log_{10} \frac{\Delta E}{\Delta X}$ *are weighted to an* E^{-2} *neutrino energy spectrum.*

likelihood	μ_E	σ_E	μ_Δ	σ_Δ
$\mathcal{L}_{\mathrm{N}}$	0.09	0.41	0.10	0.37
$\mathcal{L}_{\mathrm{KS,Q}}$	0.09	0.59	0.11	0.54
$\mathcal{L}_{\mathrm{KS,R}}$	-0.05	0.42	-0.02	0.37
$\mathcal{L}_{\mathrm{V,R}}$	-0.14	0.49	-0.23	0.43
$\mathcal{L}_{\mathrm{KS,TRes}}$	-0.07	0.59	-0.04	0.54
$\mathcal{L}_{\mathrm{V,TRes}}$	-1.2	1.01	-1.01	0.81
$\mathcal{L}_{\mathrm{KS,T}}$	-0.12	0.82	-0.09	0.78

Products of Likelihoods

So far, the performance of single likelihoods has been investigated. It was seen that the individual likelihoods performed differently. In this section it is investigated, whether the product of multiple likelihoods provides an improvement. For this, in a first step the individual

likelihoods are multiplied pair-wise and applied to the same test sample as before.

$$\mathcal{L}^{(2)} = \mathcal{L}_i \times \mathcal{L}_j, \qquad i,j = \text{likelihoods} \tag{7.26}$$

The combination with the best performance is kept and more likelihoods are added to this product iteratively,

$$\mathcal{L}^{(n+1)} = \mathcal{L}^{(n)} \times \mathcal{L}_n. \tag{7.27}$$

In each step, the combination of likelihoods with the best performance is taken as $\mathcal{L}^{(n)}$ for the next iteration.

As before, μ_Δ and σ_Δ are used to evaluate the performance of the reconstruction. The results for the product of two likelihoods $\mathcal{L}^{(2)}$ are shown in tables 7.6 and 7.7. For most combinations the resolution improves or gives comparable results with respect to the values of the single likelihood. The only exception is the test on the arrival times $\mathcal{L}_{KS,T}$, which leads to generally worse results. The combination of the N_{Ch} test $\mathcal{L}_N$ with the KS test on the hit distance distribution $\mathcal{L}_{KS,R}$ provides the best result. Therefore, this combination is used for the next steps of the iteration. The results of all steps are shown in table 7.8. The reconstruction performance does not further improve after the first iteration. On the contrary, the product of all likelihoods together except for the arrival times

$$\mathcal{L}^{(4)} = \mathcal{L}_N \times \mathcal{L}_{\text{KS,R}} \times \mathcal{L}_Q \times \mathcal{L}_{\text{KS,TRes}}, \tag{7.28}$$

has a large bias μ_Δ while σ_Δ has also increased. This behavior might be attributed to fluctuations introduced by the individual likelihoods. For the further investigations, the combination with the best performance, namely

$$\mathcal{L}_{\text{TopDown}} = \mathcal{L}_N \times \mathcal{L}_{KS,R} \tag{7.29}$$

is used as the final Top-Down likelihood in this study.

Table 7.6: *The values of μ_Δ for various products of likelihoods for a simulated E_ν^{-2} neutrino spectrum. The diagonal shows the result for the single likelihood without product.*

μ_Δ	L_N	$L_{\text{KS,R}}$	$L_{\text{KS,TRes}}$	$L_{\text{KS,T}}$	$L_{\text{KS,Q}}$
L_N	0.10	0.02	0.04	0.07	0.12
$L_{\text{KS,R}}$	–	-0.02	-0.03	-0.03	0.0
$L_{\text{KS,TRes}}$	–	–	-0.04	-0.14	-0.01
$L_{\text{KS,T}}$	–	–	–	-0.09	-0.03
$L_{\text{KS,Q}}$	–	–	–	–	0.11

Table 7.7: *The values of σ_Δ for various products of likelihoods for a simulated E_ν^{-2} neutrino spectrum. The diagonal shows the result for the single likelihood without product. The Nch likelihood and the Kolmogorov-Smirnov test on the hit distances provide the best results.*

σ_Δ	L_N	$L_{\mathrm{KS,R}}$	$L_{\mathrm{KS,TRes}}$	$L_{\mathrm{KS,T}}$	$L_{\mathrm{KS,Q}}$
L_N	0.37	0.36	0.38	0.45	0.39
$L_{\mathrm{KS,R}}$	–	0.37	0.39	0.42	0.38
$L_{\mathrm{KS,TRes}}$	–	–	0.54	0.59	0.44
$L_{\mathrm{KS,T}}$	–	–	–	0.78	0.57
$L_{\mathrm{KS,Q}}$	–	–	–	–	0.54

Table 7.8: *Iterative product of likelihoods, see table 7.2. Shown are the mean and the standard deviation over the distributions weighted to an E^{-2} neutrino spectrum. In each step the product is expanded by an additional likelihood while the reconstruction is performed for each step individually.*

$\mathcal{L}^{(n)}$	μ_Δ	σ_Δ
$\mathcal{L}_N$	0.1	0.37
$\mathcal{L}_{\mathrm{KS,R}}$	-0.02	0.37
$\mathcal{L}_N \times \mathcal{L}_{\mathrm{KS,R}}$	0.02	0.36
$\mathcal{L}_N \times \mathcal{L}_{\mathrm{KS,R}} \times \mathcal{L}_Q$	0.02	0.38
$\mathcal{L}_N \times \mathcal{L}_{\mathrm{KS,R}} \times \mathcal{L}_Q \times \mathcal{L}_{\mathrm{KS,TRes}}$	0.35	0.41

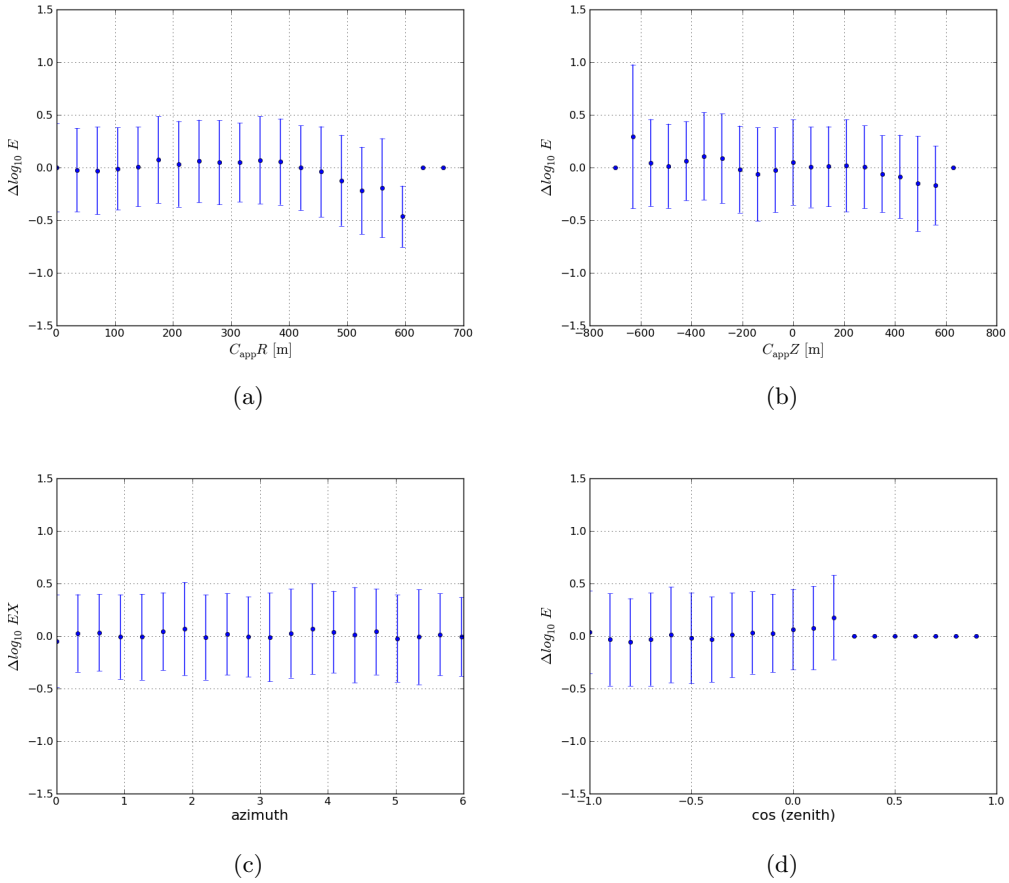

Figure 7.9: *Reconstruction resolution of the reconstructed muon energy as a function of the track parameters of the database. Each data point in these figures shows the mean with the corresponding standard deviation of the distribution over* $\Delta \log_{10} E$ *for a given parameter range.*

7.3.3.3 Dependence on Track Parameters

The dependence of the Top-Down reconstruction on the geometry of the measured event (or the Monte-Carlo event of the test sample, respectively) is investigated. The distribution of the geometrical track parameters C_{app}, θ and ϕ in the used data sample was discussed in section 7.3.1. In order to investigate the dependence on the track geometry, μ_E and σ_E are shown as function of these parameters, see figure 7.9. The study was performed with the final Top-Down likelihood, equation 7.29.

The result is nearly independent of the impact parameter C_{app}, except for large values $C_{\text{app}}R \gtrsim 500\,\text{m}$ and $|C_{\text{app}}Z| \gtrsim 500\,\text{m}$, where the position is outside the detector. There is no strong dependence on the direction (θ, ϕ), except for zenith angles $\cos\theta \gtrsim 0.1$, for which the statistics in the data sample is low.

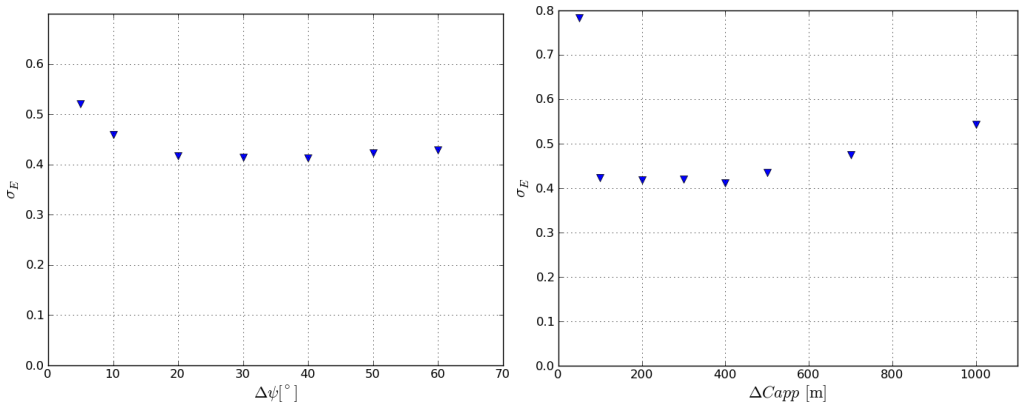

(a) (b)

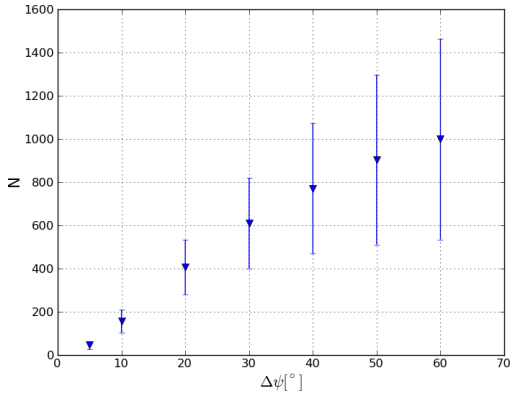

(c)

Figure 7.10: *Energy reconstruction resolution in dependence of the geometrical constraints. (a) shows the dependence on the maximum angular distance $\Delta\psi$ for a fixed maximum track distance $\Delta Capp < 200\,\mathrm{m}$ and (b) shows the dependence on $\Delta Capp$ for a fixed maximum angular distance $\Delta\psi < 20\,^\circ$. (c) The mean and standard deviation of the number of Monte-Carlo events selected from the database as a function of $\Delta\psi$. The number of selected database events decreases with narrower constraints on the track geometry.*

7.3.3.4 Dependence on Geometrical Constraints

The Top-Down reconstruction depends on the geometrical constraints (section 7.2.2) used to retrieve database samples for each reconstructed event. Two opposing effects have to be considered. First, the reconstruction resolution depends on the similarity of the track geometry between the reconstructed event and the events in the selected sample. The resolution is expected to improve with more stringent geometrical constraints.

On the other hand, the number of events in the database sample has to be sufficiently large to be representative. If the geometrical constraints are too strict, only a few matching events are retrieved from the database. In this case, no meaningful comparison is possible. The impact of both effects on the reconstruction depends on the contents of the database, in particular the absolute number of database events. A large database naturally allows to apply

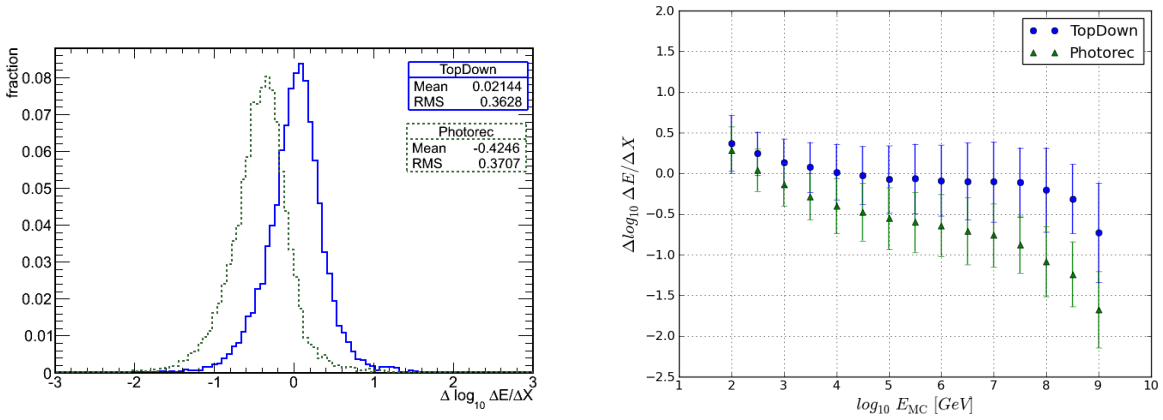

(a) (b)

Figure 7.11: *Histogram of the distribution* $\Delta \log_{10} \Delta E/\Delta X$ *(a) and the reconstruction resolution* σ_Δ *and* μ_Δ *as function of the muon energy for the Top-Down and the Photorec-llh reconstruction (b). The histograms are weighted to an* E^{-2} *neutrino spectrum.*

stricter constraints, without the number in the selected sample becoming to small.

The constraints used in this study were determined by varying the maximum allowed angular difference $\Delta\psi$ and the distance $\Delta Capp$ between the positions of reconstructed track and the tracks of the database events. Each parameter was varied while the other constraint was fixed. Figure 7.10 shows the dependence of σ_E on both constraints. The deviation σ_E increases for very narrow constraints. In these cases, the number of selected events is too small, see figure 7.10(c).

For larger values of $\Delta Capp$, i.e. for less rigorous constraints, σ_E also increases.

The dependence on the angular distance has only been tested for $\Delta\psi \leq 60\,^\circ$. This is because the absolute number of events is also a limiting factor for the general computing performance of the reconstruction algorithm. Because each event is compared individually, the algorithm becomes naturally slower with larger numbers of events in the selected database samples. From the above investigations, the optimum values for the geometrical constraints were determined as $\Delta\psi \leq 20\,^\circ$ and $\Delta Capp \leq 200\,\mathrm{m}$. These values are used as final constraints for all following investigations with the same database.

7.3.3.5 Comparison of Energy Reconstructions

The results of the Top-Down reconstruction are compared to the results from the Photorec-llh and the MuE energy reconstruction, which have been described in section 4.4.3. The three energy reconstruction methods are applied to the same Monte-Carlo test sample and the same quality selection is applied.

Average Muon Energy Loss $\Delta E/\Delta X$

Figure 7.11(a) shows the distribution of $\Delta \log_{10} \Delta E/\Delta X$ as defined by equation 7.25, weighted to an E^{-2} neutrino energy spectrum. Note, that in the current implementation the MuE

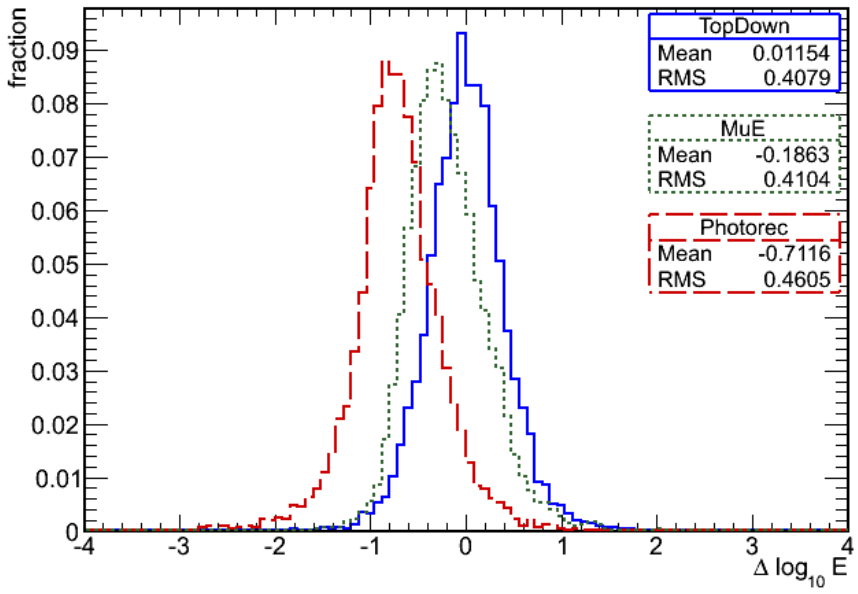

Figure 7.12: *Histograms of the distribution* $\Delta \log_{10} E$*. Shown are the Top-Down, MuE and Photorec-llh reconstruction for comparison. The histograms are weighted to an* E^{-2} *neutrino spectrum.*

reconstruction does not return the value of $\Delta E/\Delta X$ from the calculation. Hence, in this study $\Delta E/\Delta X$ is only compared for the Top-Down and Photorec-llh reconstructions. The resolution σ_Δ is comparable for both reconstruction methods, while the Top-Down energy has a smaller bias, indicated by μ_Δ:

$$\begin{aligned} \text{TopDown}: &\qquad \mu_\Delta = 0.02, \quad \sigma_\Delta = 0.36 \\ \text{Photorec} - \text{llh}: &\qquad \mu_\Delta = -0.42, \quad \sigma_\Delta = 0.37. \end{aligned}$$

Figure 7.11(b) shows μ_Δ and σ_Δ as a function of the muon energy. The Top-Down reconstruction gives a smaller bias over the considered range.

Muon Energy

Figure 7.12 shows the distribution $\Delta \log_{10} E$ for the Top-Down, the MuE and the Photorec-llh muon energy reconstruction for comparison. Similar to the results for $\Delta E/\Delta X$, the Top-Down reconstruction has a smaller bias, while the reconstruction resolution, denoted by σ_E is comparable for all three energy reconstructions.

$$\begin{aligned} \text{TopDown}: &\qquad \mu_\Delta = 0.01, \quad \sigma_\Delta = 0.41 \\ \text{MuE}: &\qquad \mu_\Delta = 0.17, \quad \sigma_\Delta = 0.41 \\ \text{Photorec} - \text{llh}: &\qquad \mu_\Delta = -0.71, \quad \sigma_\Delta = 0.46. \end{aligned}$$

Note, that with the Top-Down reconstruction, the muon energy and $\Delta E/\Delta X$ are independently determined from the database event with the best agreement.

In figures 7.13 and 7.14 the results are shown as function of the muon energy and the neutrino energy respectively. The Top-Down reconstruction has a small bias over the considered energy range, while the other two methods show a systematic under-estimation of the muon energy at larger energies.

At smaller energies, below about 1 TeV, the energy loss is nearly independent of the muon energy. Because IceCube measures the energy deposited in its volume, the energy reconstruction is less reliable at these energies. For very large muon energies ($> 10^8$ GeV), there are fluctuations in the results due to a low event statistics.

Reconstructed Energy Spectra

The reconstructed values from the different reconstruction methods are filled into a histogram, see 7.15 and 7.16 for the muon energy loss and the muon energy, respectively. In the current implementation of the Top-Down method, no error estimate on the reconstruction result has been included yet. A possible error estimate is described in the next section.

Unlike the Top-Down method, both the MuE and the Photorec-llh reconstruction show a systematic under-estimation of the reconstructed energies at high energies.

Because the predicted astrophysical fluxes have a harder energy spectrum than the dominant atmospheric neutrino background, they would be visible as a small excess above this background at the high-energy tail of the measured neutrino energy distribution. The outcome of the search for this excess is affected by the performance of the energy reconstruction and its capability to deliver an un-biased result. For an unbiased energy reconstruction, this excess should be more distinguishable from the background, compared to a reconstruction with a systematic under-estimation. If the reconstructed energy is systematically under-estimated, a possible astrophysical neutrino signal may not be found because it is shifted towards lower energies where it remains hidden in the background. If on the other hand, the reconstructed energy is systematically over-estimated, a fake signal excess may be produced from background events.

The application of the Top-Down energy reconstruction as an neutrino energy estimator for the upcoming search for a diffuse astrophysical neutrino flux with the IC79 data is currently being discussed. The impact of the various energy reconstruction methods on the result of the diffuse analysis will be investigated [164].

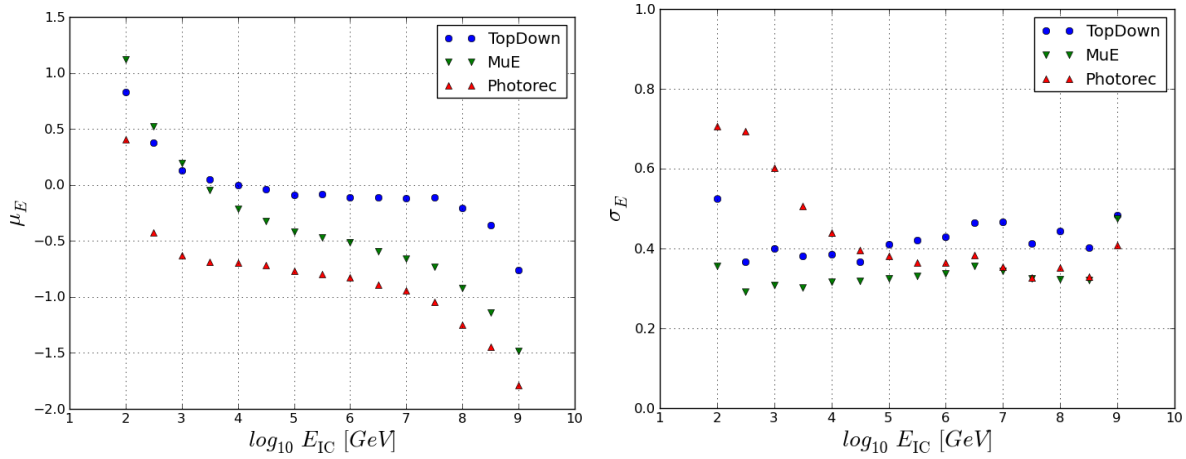

(a) (b)

Figure 7.13: *The mean μ_E and the standard deviation σ_E from the results in figure 7.12 as function of the muon energy E_{IC}.*

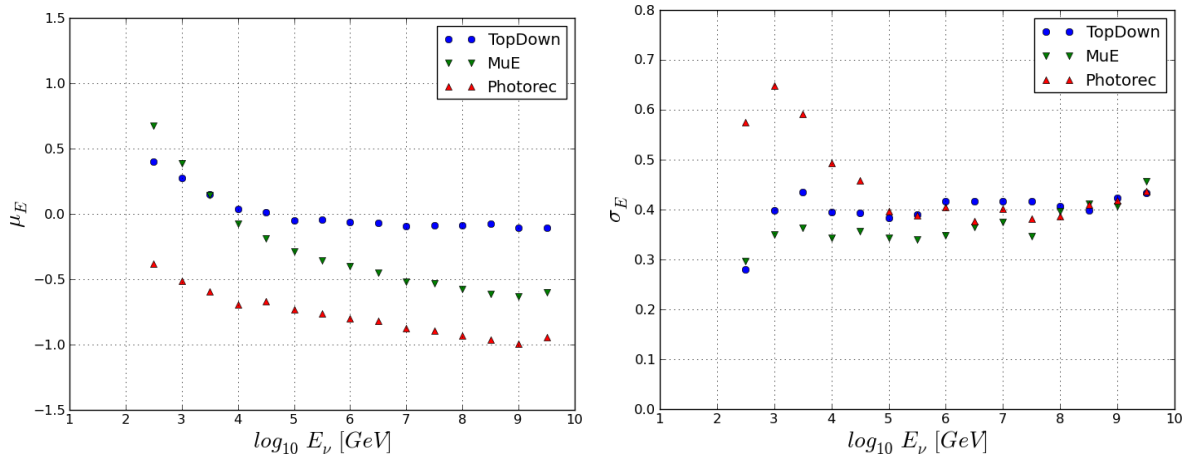

(a) (b)

Figure 7.14: *The mean μ_E and the standard deviation σ_E from the results in figure 7.12 as function of the neutrino energy E_{ν}.*

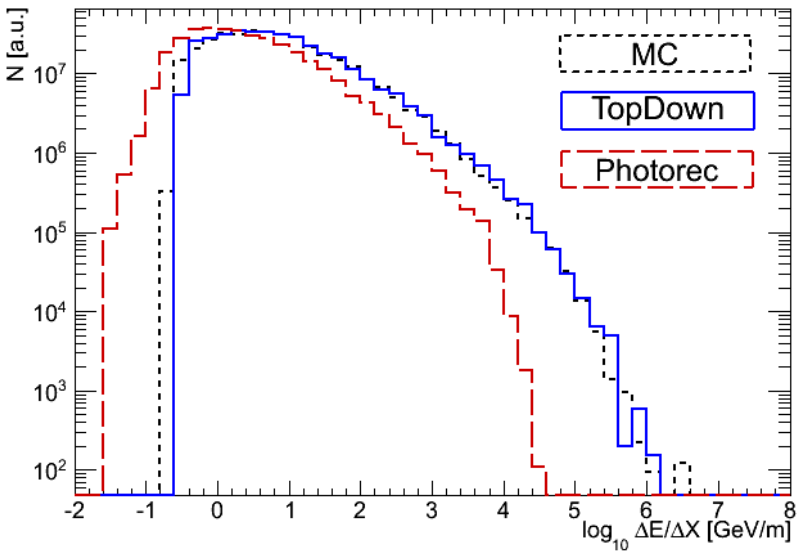

Figure 7.15: *The spectrum of the reconstructed average muon energy loss $\Delta E/\Delta X$ for the Top-Down and the Photorec-llh reconstruction in comparison with the true Monte-Carlo value (MC). The spectra are weighted to an E^{-2} neutrino energy spectrum.*

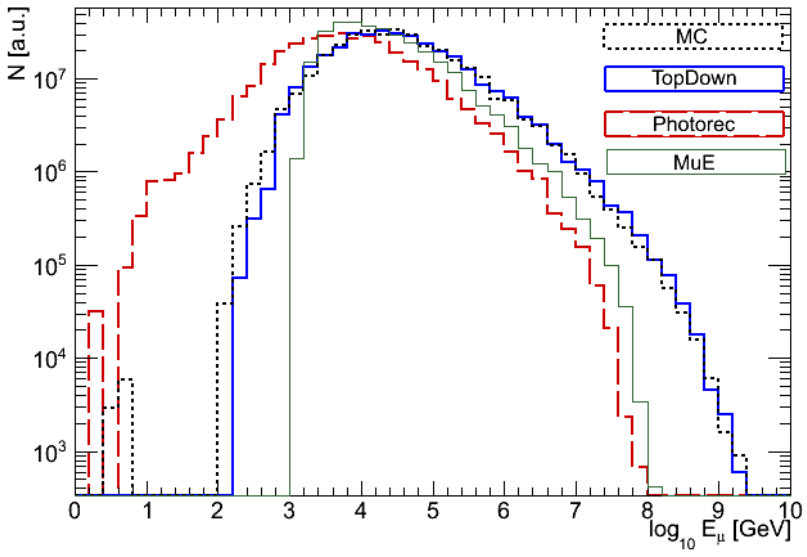

Figure 7.16: *The spectrum of the reconstructed muon energy for the Top-Down and the Photorec-llh reconstruction in comparison with the true Monte-Carlo value (MC). The spectra are weighted to an E^{-2} neutrino energy spectrum.*

7.4 Future Developments

The Top-Down reconstruction method has been implemented into the IceCube software framework and a proof-of-concept study has been performed for the muon energy reconstruction. The results have been shown in the previous sections. There are on-going studies to further improve the performance of the current implementation for future application.

Likelihood Description

In the current implementation of the Top-Down algorithm, a small number of simple detector-level observables is used for the event comparison. From the Monte-Carlo study it was seen that the best results were provided by the product of $\mathcal{L}_R$ and $\mathcal{L}_N$, for the spatial hit distribution and the number of hit channels, respectively. In order to improve the reconstruction resolution, different observables could be used and other statistical tests could be developed. These additional likelihoods can be added to the product in equation 7.5.

So far, the reconstructed energy is taken from the event with the best agreement, i.e. the event with the maximum likelihood value. Alternatively, the reconstructed energy could be obtained from a fit on the likelihood landscape or by an adequate mean value over a sample of many database events.

Error Estimate

In order to evaluate the application of the Top-Down reconstruction to future analyses, an error estimate for the reconstructed energy is desirable. For instance, such an error estimate can be developed by using the log-likelihood values from the event comparison. For each reconstructed event, there is a set of N_{db} likelihood values and energies (or any other reconstructed event parameter)

$$\{L, E\}_i\,, \quad i = 1, \ldots, N_{\mathrm{db}}. \tag{7.30}$$

L is the likelihood value from the comparison of the reconstructed event with a single Monte-Carlo event from the database and N_{db} is the number of the database events the event was compared to and E is the energy of each database event. The likelihood values of the comparison of individual events allow for an event-based error estimate. A log-likelihood difference to the minimum likelihood value

$$\Delta L_i = L_i - L_{\mathrm{min}} = \frac{1}{2}\,{\xi_i}^2 \tag{7.31}$$

corresponds to a deviation of ξ_i standard deviations σ_i. This can be used to assign a weight for each event, using the p-value corresponding to $\xi_i \sigma_i$

$$w_i = \mathrm{Erfc}\left(\frac{\xi_i}{\sqrt{2}}\right), \tag{7.32}$$

where Erfc is the complementary error function. Using this weight, a weighted mean of the reconstructed energy can be calculated over all N_{db} database events

$$\bar{E} = \frac{\sum_{i=1}^{N_{\mathrm{db}}} w_i\, E_i}{\sum_{i=1}^{N_{\mathrm{db}}} w_i} \tag{7.33}$$

and a two-sided error is given by the weighted standard deviation

$$\sigma_{\pm} = \sqrt{\frac{\sum_{\pm} w_i \left(E_i - E_{\mathrm{minL}}\right)^2}{\sum_{\pm} w_i}} \tag{7.34}$$

where E_{minL} is the energy from the database event with minimum log-likelihood and the sum is performed for all events with either larger or smaller energy. The implementation of an error estimate based on the above considerations is currently under development [165].

Database

The Top-Down reconstruction depends on the database that provides the Monte-Carlo events for the comparison. The database can be optimized with regard to its size and its contents to improve the reconstruction performance and to reduce the computational effort.

In section 7.3.3.4, it was seen that the reconstruction resolution is limited by the size of the database, i.e. the total number of database events. The database has to be large enough to provide sufficient numbers of events for each measured event and given constraints on the geometrical similarity between measured event and database events. If the number of database events is too small, no meaningful comparison is possible.

So far, a basic event selection has been applied to the events that were filled into the database. This has been done in order to investigate the reconstruction performance for different event selections. In principle, a more rigorous selection could be applied, leading to a higher initial quality of the database events. On the other hand, using less rigorous selections allows to use the same database for different analyses with different selection schemes.

Computational Issues

By design, the Top-Down method is more computationally intensive than the conventional Bottom-Up reconstruction methods, because each reconstructed event is compared with large numbers of Monte-Carlo events, while the likelihood is calculated for each Monte-Carlo event separately. The database events are stored in separate files on a disk server. The files contain the full event information, i.e. extracted pulses, track reconstruction and quality parameters. During the reconstruction, a varying number of these files is read, leading to many file access operations. Therefore, the algorithm is computationally intensive, in particular if many events are reconstructed in parallel. The performance can be improved by re-organizing the database and optimizing the content of the database files.

8

Summary & Outlook

Neutrino astronomy is a field of astroparticle physics that uses neutrino detectors as telescopes to observe astrophysical objects. Over the last few decades, several dedicated neutrino telescopes have been built and several other are planned for the near future. The currently largest setup is the recently completed IceCube neutrino telescope, which has been deployed into the Antarctic ice at South Pole and uses the ice as a detector medium to detect charged particles, produced in neutrino interactions, by their Cherenkov light.

IceCube is optimized for the detection of high-energetic neutrinos in the range of 10 GeV to 100 PeV. Such neutrinos are predicted from a large variety of astrophysical objects while their production is closely connected to the acceleration of cosmic rays. At even higher energies, cosmogenic neutrinos are expected to be generated through the GZK effect, where the expected GZK neutrino flux is sensitive to the composition of cosmic rays.

Therefore, the observation of high-energetic astrophysical neutrinos may help to answer a variety of interesting questions about the nature of the highest-energy phenomena in the universe, such as the origin and acceleration mechanism of cosmic rays and their propagation in the universe. So far, there is no evidence for astrophysical neutrinos in this energy range, though with the current neutrino telescopes it was already possible to constrain a number of theoretical predictions.

Altogether, the detection of high-energetic astrophysical neutrinos remains challenging and in this thesis two of these challenges have been addressed. In the first part of this thesis, the determination of the acoustic attenuation length in South Pole ice is presented. This is part of a feasibility study to explore the acoustic neutrino detection as a possibility to enhance the detection of the highest-energy neutrinos, called SPATS. In the second part of the thesis, an new energy reconstruction method following a Top-Down approach has been developed and tested for the IceCube collaboration.

Determination of the Acoustic Attenuation Length

The predicted astrophysical neutrino flux is extremely low and decreasing with energy, while at the same time the neutrino interaction cross sections are also very small. At the highest energies, as for the detection of GZK neutrinos, less than one detected neutrino per cubic kilometer and year are expected. Consequently, in order to accumulate sufficient numbers of detected neutrinos within reasonable time, detector volumes of the order of 100 km^3 are

desired. A detector of this scale has to rely on natural media as a detector medium, such as the Antarctic ice. Nevertheless, this volume is two orders of magnitude larger than IceCube as the largest existing detector. Therefore, new detection methods, such as the radio and the acoustic method, have been investigated in order to achieve a $100\,\mathrm{km}^3$ detector volume at comparably small cost.

The feasibility of the radio method in ice has been proven successfully and a new detector based on this method is currently under development, called the Askaryan Radio Array (ARA). The feasibility of the acoustic neutrino detection at the South Pole is currently being investigated. For this, the South Pole Acoustic Test Setup (SPATS) has been built to determine the acoustic ice properties from in-situ measurements, namely the acoustic attenuation length, the sound speed, the ambient noise level as well as the rate of transient noise events.

In this thesis, the acoustic attenuation length is determined using data from in-situ measurements with SPATS and an additional retrievable transmitter (pinger), which was deployed into a depth between 190 and 500 m using the water-filled drilling holes during the construction of the IceCube detector. The setup of these measurements allowed for a data sample with few systematic effects. Even though, the unknown angular-dependent sensitivities of the SPATS sensor channels cannot be avoided and are considered as the dominant systematic effect for these measurements.

The acoustic attenuation length is measured by comparing the energy contents of the pinger pulses recorded by the various SPATS sensor channels for different distances between the pinger and the respective channel. The energy was calculated from the Fourier spectra of the pinger pulses for a frequency range between 5 and 35 kHz. The attenuation coefficient is calculated for each channel individually and the weighted mean over the distribution of all considered channels leads to an attenuation coefficient α and an attenuation length λ of

$$\alpha \;=\; 3.79 \pm 0.63\,\mathrm{km}^{-1}, \qquad \lambda = 264^{+52}_{-37}\,\mathrm{m}.$$

This result is consistent with complementary analyses, using either different data samples or different analyses techniques. The measured value of the attenuation length is an order of magnitude smaller than the theoretical prediction. This leads to the following implications for the acoustic neutrino detection at the South Pole.

First, it is important to understand the mechanism of the acoustic attenuation in order to decide whether acoustic neutrino detection is feasible at South Pole. The disagreement between the measurements and the theoretical prediction indicate that some of the assumptions leading to the predicted value have to be revised. In the current model the acoustic attenuation below the firn layer is assumed to be absorption-dominated, whereby an acoustic signal loses energy predominantly through dipole re-orientation in the ice grains. On the other hand, if the attenuation is instead dominated by scattering, an acoustic signal will rather lose its directional information. In this case, the pattern of a neutrino-induced acoustic signal will change from a flat "acoustic pancake" to a more spherical shape, while it is in principle possible to recover part of the scattered energy for detection.

Studying the dependence of the attenuation length on the depth and the frequency allows to understand the attenuation mechanism and to distinguish scattering- and absorption-dominated models. As show in this thesis, with the current data there are no indications for either depth or frequency dependence, which suggests an absorption-dominated attenuation mechanism.

Secondly, the attenuation length affects the possible spacing for the instrumentation of a future acoustic detector at South Pole. Using the new information, a much denser spacing is required to achieve the same detection threshold as compared to the initial assumptions. Consequently, the acoustic method is not as cost-efficient as previously thought and an acoustic detector of the $100\,\mathrm{km}^3$ has become unlikely under this premises. The current effort of the SPATS collaborators is to evaluate the feasibility of a combined radio-acoustic hybrid detector. In such a detector, an acoustic sub-array could possibly be used to decrease the detection threshold and the identification of high-energetic neutrino events.

Top-Down Reconstruction of Muon Energy

In the second part if this thesis, an event reconstruction method based on a Top-Down approach is presented. The method has been implemented into the IceCube software framework and has been applied to the reconstruction of the muon energy for the IC40 detector.

The Top-Down method is based on the direct comparison of single measured events with a large sample of simulated (Monte-Carlo) events. Using a maximum-likelihood description, the Monte-Carlo event from this sample which has the largest likelihood value, gives an estimate for the properties of the measured event. The Monte-Carlo events required for the comparison are stored in a database, containing the full event information from the simulations. For each measured event, a sample of Monte-Carlo events with a similar track geometry is selected from this database and compared with the measured event.

An advantage of the Top-Down method is that it follows a forward-folding concept, incorporating all properties of the IceCube detector, such as its finite resolution and the ice properties, through the Monte-Carlo simulations. On the other hand, the choice of observables and the likelihoods used for their comparison are not a-priori given. For the purpose of this study, a set of simple detector-level observables has been defined and tested, such as the spatial distribution of hit DOMs or the total number of DOMs with a hit. This likelihood description can be easily extended or replaced to include additional observables.

A disadvantage of the Top-Down method is that it relies on large numbers of Monte-Carlo events and that it is more computationally intensive than conventional reconstruction methods. Consequently, it is intended for the reconstruction of samples of interesting events, rather than as a standard reconstruction procedure for all events.

In this thesis, a proof of concept study using Monte-Carlo data has been performed to investigate the applicability of the Top-Down method to the muon energy reconstruction in IceCube. The Top-Down method has been demonstrated to work well and the results from this

study can be used to further develop the concept and to improve the reconstruction resolution as well as the general performance of the algorithm. The resulting energy reconstruction resolution is comparable to the existing energy reconstruction methods in IceCube, while the Top-Down method generally has a smaller bias. A reconstruction bias corresponds to a systematic over- or underestimation of the reconstructed energy, therefore a minimal bias is desirable.

Currently, the application of the Top-Down energy reconstruction as an alternative energy estimator for upcoming analyses is being investigated. In addition, an event-based error estimate for the reconstructed energy can be obtained from the likelihood description. The performance of this error estimate is also currently being investigated and will be included in a future implementation of the Top-Down reconstruction.

Appendix A

Thermo-acoustic effect in solids

In a continuous solid body, deformations are described in terms of a relative displacement field, called the strain. In case of infinitesimal displacements, the strain tensor is given by

$$\mathbf{S} = \frac{1}{2}\left(\nabla\mathbf{u} + (\nabla\mathbf{u})^T\right) \quad \text{or} \quad S_{ij} = \frac{1}{2}\left(\partial_i u_j + \partial_j u_i\right) \tag{A.1}$$

where $\mathbf{u}(\mathbf{r}, t) = \mathbf{x}' - \mathbf{x}$ is the displacement vector denoting the positional change of an infinitesimal volume before and after displacement.

A deformation is usually caused by either external forces, body forces such as gravity or electromagnetic forces, or a temperature change inside the body. The reaction to these external causes are described by the stress field $\mathbf{T}$, which is a measure of the average force per unit area of an infinitesimal surface within the body

$$T_{ij} = \lim_{\Delta s_j \to 0}\left(\frac{\Delta F_i}{\Delta s_j}\right), \tag{A.2}$$

such that the elements T_{ij} describe the ith component of the force acting per unit area on a surface perpendicular to the direction x_j. The diagonal elements T_{ii} describe a force perpendicular to the surface and hence correspond to a compressional stress, whereas the elements $T_{ij}, i \neq j$ describe forces parallel to the surface and correspond to shear stress. In the most general case the diagonal elements are not identical and the non-diagonal elements are all non-zero so that the resulting force is not parallel to the displacement. Therefore, instead of a scalar pressure (as in ideal fluids) the reaction of a solid to an external stress field is described by a tensor equation.

In analogy to Newton's second law, the elastodynamic equation of motion is given by

$$\nabla \cdot \mathbf{T} + \mathbf{\Phi} = \rho\, \partial_{tt}\mathbf{u}, \tag{A.3}$$

where ρ is the mass density and Φ the sum of all body forces.

The elastic regime is characterized by a linear relationship between stress and strain and reversible deformations. This is only valid for small displacements and scenarios below the elastic limit, beyond which the material starts to deform plastically. In generalization of Hooke's law and using the common summation convention:

$$T_{ij} = C_{ijkl}\, S_{kl} \;=\; C_{ijkl}\partial_k u_l \tag{A.4}$$

where $\mathbf{C}$ is the rank four stiffness tensor. In the most general case $\mathbf{C}$ has 36 independent components [1]. For isotropic media the physical properties do not depend on the orientation of

[1] As T and S are symmetric, only 36 from the $3^4 = 81$ components C_{ijkl} are independent.

the solid. An applied force will result in the same relative displacements, independent of the direction in which the force is applied. In this case the stiffness tensor has only two independent parameters (the so-called elastic moduli) and can be written as

$$C_{ijkl} = K\,\delta_{ij}\,\delta_{kl} + G\,(\delta_{ik}\delta_{jl} + \delta_{il}\delta_{jk} - \tfrac{2}{3}\,\delta_{ij}\,\delta_{kl}) \tag{A.5}$$

with the bulk modulus or incompressibility K, the shear modulus G and the Kronecker symbol δ_{ij}. In addition, if the material is homogeneous, the elastic moduli are not a function of position. Putting together equations A.4 and A.5, Hooke's law for isotropic materials is now:

$$T_{ij} = K\delta_{ij}S_{kk} + 2G(S_{ij} - \tfrac{1}{3}\delta_{ij}S_{kk}). \tag{A.6}$$

The first term on the right side is associated with a scalar pressure whereas the traceless second term is responsible for shear forces. A common representation of equation A.6 uses the Lamé constants $\lambda = K - 2G/3$ and $\mu = G$:

$$T_{ij} = \lambda\delta_{ij}S_{kk} + 2\mu S_{ij} \quad \text{or} \quad \mathbf{T} = \lambda\,\mathrm{tr}(S)\,\mathbf{I} + 2\mu S. \tag{A.7}$$

External stresses caused by particle-induced cascades can be accounted for by replacing $\mathbf{T} \rightarrow \mathbf{T}+\mathbf{T}^{ext}$, where $\mathbf{T}^{ext}$ is given by the following ansatz. The thermal expansion of a small volume is given by

$$\Delta V = \frac{\alpha}{\rho\, C_p} E, \tag{A.8}$$

similar to equation 3.22. The volume expansion also follows from the displacement over the surface ∂V of the volume

$$\Delta V = \int_{\partial V} \mathbf{u}\cdot\mathbf{dS} = \int_V \nabla\cdot\mathbf{u}\,\mathrm{d}V \tag{A.9}$$

where Gauss' theorem was used. Assuming that this equation is true for any volume, $\Delta V \rightarrow 0$ leads to

$$\nabla\cdot\mathbf{u} = \frac{\alpha}{\rho\, C_p}\epsilon, \tag{A.10}$$

and the comparison with equation A.4 gives

$$T^{ext}_{ij} = C_{ijkk}\frac{\alpha}{\rho C_p}\,\epsilon(\mathbf{r},t) = (\lambda+2\mu)\delta_{ij}\,\frac{\alpha}{\rho C_p}\,\epsilon(\mathbf{r},t). \tag{A.11}$$

Inserting equation A.1 and A.7 into the elastodynamic equation A.3, using $\mathrm{tr}(S) = \nabla\cdot\mathbf{u}$ and neglecting body forces $\mathbf{\Phi}$ yields:

$$\begin{aligned} \rho\,\partial_{tt}\mathbf{u} &= \nabla\left(\lambda\,\mathrm{tr}(S)\,\mathbf{I} + 2\mu S + \mathbf{T}^{ext}\right) \\ &= \lambda\nabla(\nabla\cdot\mathbf{u}) + \mu\,\nabla\cdot\left((\nabla\mathbf{u})^T + \nabla\mathbf{u}\right) + \nabla\mathbf{T}^{ext} \\ &= (\lambda+\mu)\nabla(\nabla\cdot\mathbf{u}) + \mu\Delta\mathbf{u}. + (\lambda+2\mu)\,\frac{\alpha}{\rho C_p}\,\nabla\epsilon(\mathbf{r},t). \end{aligned} \tag{A.12}$$

It is now useful to introduce a scalar potential ϕ and a vector potential ψ so that $\mathbf{u} = \nabla\phi + \nabla\times\psi$. Inserting this decouples the above differential equation into a scalar and vector component

$$\begin{aligned} 0 &= \nabla\cdot\left((\lambda+2\mu)\,\left(\Delta\phi + \frac{\alpha}{\rho C_p}\,\epsilon(\mathbf{r},t)\right) - \rho\,\partial_{tt}\phi\right) \\ &+ \nabla\times(\mu\,\Delta\psi - \rho\,\partial_{tt}\psi) \end{aligned} \tag{A.13}$$

and yields two independent wave equations for the scalar and the vector potential

$$\Delta\phi - \frac{1}{v_P^2}\partial_{tt}\phi = -\frac{\alpha}{\rho C_p}\,\epsilon(\mathbf{r},t) \tag{A.14}$$

$$\Delta\psi - \frac{1}{v_S^2}\partial_{tt}\psi = 0 \tag{A.15}$$

The sound speed for both cases follows from the comparison of equations A.13 and A.14

$$v_P = \sqrt{\frac{\lambda+2\mu}{\rho}} \qquad \text{and} \qquad v_S = \sqrt{\frac{\mu}{\rho}}. \tag{A.16}$$

Equation A.14 describes the propagation of a curl-free wave, $\nabla\times\nabla\phi = 0$ and therefore corresponds to a longitudinal wave also referred to as either 'compressional' or P wave. On the other hand, equation A.15 represents a purely rotational field, $\nabla\cdot(\nabla\times\psi) = 0$ and thus describes a 'transversal' or 'shear' wave (S wave). For an ideal fluid $\mu = 0$, therefore shear waves will not propagate.

From equation A.13, only the longitudinal component is affected by the volume expansion term. Hence, in isotropic solids only longitudinal waves are created by the thermo-acoustic effect. In this case the displacement vector $\mathbf{u} = \nabla\phi$ is parallel to the normal vector of the wave front $\mathbf{n}$ at any point. In analogy to the thermo-acoustic model in liquids, a wave equation can be constructed for the longitudinal mode, using the normal traction T_i^n which describes the force exerted in direction of $\mathbf{n}$. From equation A.2 and A.3 follows

$$T_i^n = T_{ij}n_j = \rho\partial_{tt}\phi. \tag{A.17}$$

Using this expression and the second time derivative of equation A.13, the longitudinal wave equation is rewritten as

$$\Delta T_i^n - \frac{1}{v_l^2}\,\frac{\partial^2 T_i^n}{\partial t^2} = -\frac{\alpha}{C_p}\,\frac{\partial^2\epsilon(\mathbf{r},t)}{\partial t^2}, \tag{A.18}$$

which is identical to the wave equation 3.23 in liquids. Consequently the same behavior of the pressure amplitude in near and far field is found for liquids and isotropic solids.

References

[1] Particle Data Group. Astrophysics and Cosmology. *Physics Letters B*, 667:212–260, September 2008.

[2] John Linsley. Evidence for a primary cosmic-ray particle with energy 10^{20} eV. *Phys. Rev. Lett.*, 10(4):146–148, Feb 1963.

[3] J. R. Hoerandel. On the knee in the energy spectrum of cosmic rays. *Astroparticle Physics*, 19:193–220, May 2003.

[4] The Pierre AUGER Collaboration. Update on the correlation of the highest energy cosmic rays with nearby extragalactic matter. *Astroparticle Physics*, 34:314–326, December 2010.

[5] Kseniya V. Ptitsyna and Sergei V. Troitsky. Physical conditions in potential accelerators of ultra-high-energy cosmic rays: updated Hillas plot and radiation-loss constraints. *Physics-Uspekhi*, 53(7):691, 2010.

[6] A. M. Hillas. The Origin of Ultra-High-Energy Cosmic Rays. ARA&A, 22:425–444, 1984.

[7] E. Fermi. On the origin of the cosmic radiation. *Phys. Rev.*, 75(8):1169–1174, Apr 1949.

[8] W. I. Axford, E. Leer, and J. F. McKenzie. The structure of cosmic ray shocks. A&A, 111:317–325, July 1982.

[9] W. I. Axford, E. Leer, and G. Skadron. The acceleration of cosmic rays by shock waves. In *International Cosmic Ray Conference*, volume 11 of *International Cosmic Ray Conference*, pages 132–137, 1977.

[10] T.K. Gaisser. *Cosmic Rays and Particle Physics*. Cambridge University Press, 1990.

[11] S. Bhattacharyya and P. Pal. Simple leaky box model for cosmic-ray propagation, models for production of antiprotons at ultrahigh energies and the estimations of the p(-)/p ratios. *Nuovo Cimento C Geophysics Space Physics C*, 9:961–983, October 1986.

[12] F. A. Aharonian and et al. Constraints on the extremely high-energy cosmic ray accelerators from classical electrodynamics. *Phys. Rev. D*, 66(2):023005, Jul 2002.

[13] R. Antonucci. Unified models for active galactic nuclei and quasars. ARA&A, 31:473–521, 1993.

[14] R. V. E. Lovelace. Dynamo model of double radio sources. Nature, 262:649–652, August 1976.

[15] A. Dar. The GRB/XRF-SN Association. *ArXiv Astrophysics e-prints arXiv:astro-ph/0405386*, May 2004.

[16] E. Nakar. Short-hard gamma-ray bursts. Phys. Rep., 442:166–236, April 2007.

[17] P. Mészáros. Gamma-ray bursts. *Reports on Progress in Physics*, 69:2259–2321, August 2006.

[18] S. Dado and A. Dar. The Cannonball Model Of Long GRBs-Overview. In *American Institute of Physics Conference Series*, volume 1111 of *American Institute of Physics Conference Series*, pages 333–343, May 2009.

[19] A. Dar. The origin of cosmic rays —A 92-year-old puzzle solved? *Nuovo Cimento B Serie*, 120:767–+, June 2005.

[20] The Pierre AUGER Collaboration. Measurement of the energy spectrum of cosmic rays above 10^{18} eV using the Pierre AUGER Observatory. *Physics Letters B*, 685:239–246, March 2010.

[21] R. Aloisio, V. Berezinsky, and A. Gazizov. Ultra high energy cosmic rays: The disappointing model. *Astroparticle Physics*, 34:620–626, March 2011.

[22] K. Greisen. End to the cosmic-ray spectrum. *Phys. Rev. Lett.*, 16(17):748–750, Apr 1966.

[23] G. T. Zatsepin and V. A. Kuz'min. Upper Limit of the Spectrum of Cosmic Rays. *ZhETF Pis ma Redaktsiiu*, 4:114–+, August 1966.

[24] G. B. Thomson for the HiRes Collaboration. Observation of the GZK Cutoff by the HiRes Experiment. *ArXiv Astrophysics e-prints, arXiv:astro-ph/0609403*, September 2006.

[25] E. Waxman and J. Bahcall. High energy neutrinos from astrophysical sources: An upper bound. *Phys. Rev. D*, 59(2):023002, Dec 1998.

[26] J. Bahcall and E. Waxman. High energy astrophysical neutrinos: The upper bound is robust. Phys. Rev. D, 64(2):023002–+, July 2001.

[27] J. K. Becker, P. L. Biermann, and W. Rhode. The diffuse neutrino flux from FR-II radio galaxies and blazars: A source property based estimate. *Astroparticle Physics*, 23:355–368, May 2005.

[28] A. Mücke and et al. BL Lac objects in the synchrotron proton blazar model. *Astroparticle Physics*, 18:593–613, March 2003.

[29] S. Razzaque, P. Mészáros, and E. Waxman. Neutrino tomography of gamma ray bursts and massive stellar collapses. Phys. Rev. D, 68(8):083001–+, October 2003.

[30] Karl Mannheim. High-energy neutrinos from extragalactic jets. *Astroparticle Physics*, 3(3):295 – 302, 1995.

[31] F. W. Stecker. Note on high-energy neutrinos from active galactic nuclei cores. Phys. Rev. D, 72(10):107301–+, November 2005.

[32] D. Hooper, A. Taylor, and S. Sarkar. The impact of heavy nuclei on the cosmogenic neutrino flux. *Astroparticle Physics*, 23:11–17, February 2005.

[33] V. S. Beresinsky and G. T. Zatsepin. Cosmic rays at ultra high energies (neutrino?). *Physics Letters B*, 28:423–424, January 1969.

[34] Ralph Engel, David Seckel, and Todor Stanev. Neutrinos from propagation of ultrahigh energy protons. *Phys. Rev. D*, 64(9):093010, Oct 2001.

[35] G. Sigl and et al. Probing grand unified theories with cosmic-ray, gamma-ray, and neutrino astrophysics. Phys. Rev. D, 59(4):043504–+, February 1999.

[36] Z. Fodor, S. D. Katz, and A. Ringwald. Z-Burst Scenario for the Highest Energy Cosmic Rays. *ArXiv High Energy Physics - Phenomenology e-prints, arXiv:hep-ph/0210123*, October 2002.

[37] S. Yoshida, G. Sigl, and S. Lee. Extremely high energy neutrinos, neutrino hot dark matter, and the highest energy cosmic rays. *Phys. Rev. Lett.*, 81(25):5505–5508, Dec 1998.

[38] IceCube Collaboration. A Search for a Diffuse Flux of Astrophysical Muon Neutrinos with the IceCube 40-String Detector. *Paper submitted, preprint available: astro-ph.HE:1104.5187*, April 2011.

[39] The IceCube Collaboration. Constraints on the extremely-high energy cosmic neutrino flux with the icecube 2008-2009 data. *Phys. Rev. D*, 83(9):092003, May 2011.

[40] The IceCube Collaboration. Background studies for acoustic neutrino detection at the South Pole. *Paper submitted, preprint available: astro-ph.IM:1103.1216*, March 2011.

[41] The ANTARES Collaboration. Upper limit on the diffuse flux of cosmic ν_μ with the ANTARES neutrino telescope. *arXiv astro-ph.HE:1101.3670*, January 2011.

[42] The IceCube Collaboration. Multiyear search for a diffuse flux of muon neutrinos with AMANDA-II. *Phys. Rev. D*, 76(4):042008, Aug 2007.

[43] The IceCube Collaboration. First search for extremely high energy cosmogenic neutrinos with the IceCube Neutrino Observatory. Phys. Rev. D, 82(7):072003–+, October 2010.

[44] The RICE Collaboration. Rice limits on the diffuse ultrahigh energy neutrino flux. *Phys. Rev. D*, 73(8):082002, Apr 2006.

[45] The ANITA Collaboration. Observational constraints on the ultrahigh energy cosmic neutrino flux from the second flight of the ANITA experiment. Phys. Rev. D, 82(2):022004–+, July 2010.

[46] N. G. Lehtinen and et al. The FORTE VHF instrument as a high-energy cosmic ray detector. In P. W. Gorham, editor, *Society of Photo-Optical Instrumentation Engineers (SPIE) Conference Series*, volume 4858 of *Society of Photo-Optical Instrumentation Engineers (SPIE) Conference Series*, pages 296–304, February 2003.

[47] P. W. Gorham, K. M. Liewer, C. J. Naudet, D. P. Saltzberg, and D. R. Williams. "radio limits on an isotropic flux of ¿100 EeV cosmic neutrinos". *ArXiv Astrophysics e-prints arXiv:astro-ph/0102435*, February 2001.

[48] The Pierre AUGER Collaboration. Limit on the diffuse flux of ultrahigh energy tau neutrinos with the surface detector of the Pierre AUGER Observatory. Phys. Rev. D, 79(10):102001–+, May 2009.

[49] The HiRes Collaboration. An Upper Limit on the Electron-Neutrino Flux from the HiRes Detector. ApJ, 684:790–793, September 2008.

[50] N. Kurahashi, J. Vandenbroucke, and G. Gratta. Search for acoustic signals from ultrahigh energy neutrinos in 1500 km^3 of sea water. *Phys. Rev. D*, 82(7):073006, Oct 2010.

[51] The ACORNE Collaboration. Acoustic detection of UHE neutrinos - the ACORNE project. *Journal of Physics Conference Series*, 136(4):042070–+, November 2008.

[52] M. Honda and et al. New calculation of the atmospheric neutrino flux in a three-dimensional scheme. 70(4):043008, Aug 2004.

[53] G. D. Barr and et al. Three-dimensional calculation of atmospheric neutrinos. *Phys. Rev. D*, 70(2):023006, Jul 2004.

[54] A. A. Kochanov, T. S. Sinegovskaya, and S. I. Sinegovsky. High-energy cosmic-ray fluxes in the Earth atmosphere: Calculations vs experiments. *Astroparticle Physics*, 30:219–233, December 2008.

[55] The IceCube Collaboration. Direct Measurement of the Atmospheric Muon Energy Spectrum with IceCube. *ArXiv e-prints astro-ph.HE:0909.0679*, September 2009.

[56] C. Lobban, J. L. Finney, and W. F. Kuhs. The structure of a new phase of ice. *Nature*, 391:268–270, January 1998.

[57] D. G. Albert. Theoretical modeling of seismic noise propagation in firn at the South Pole, Antarctica. Geophys. Res. Lett., 25:4257–4260, 1998.

[58] A. J. Gow. Results of measurements in the 309 meter bore hole at Byrd Station, Antarctica. *Journal of Glaciology*, 4:771–784, October 1963.

[59] J. Weihaupt. Seismic and gravity studies at the south pole. *Geophysics*, 28(4):582–592, 1963.

[60] P. B. Price and et al. Temperature profile for glacial ice at the South Pole: Implications for life in a nearby subglacial lake. *Proceedings of the National Academy of Science*, 99:7844–7847, June 2002.

[61] The IceCube Collaboration. Icecube internal wiki: Temperature profile. `http://wiki.icecube.wisc.edu/index.php/Temperature_profile`.

[62] M. Choukroun and O. Grasset. Thermodynamic model for water and high-pressure ices up to 2.2 GPa and down to the metastable domain. J. Chem. Phys., 127(12):124506–+, September 2007.

[63] N. Maeno and T. Ebinuma. Pressure sintering of ice and its implication to the densification of snow at polar glaciers and ice sheets. *J. Phys. Chem.*, 87:4103–4110, 1983.

[64] P. B. Price. Kinetics of Conversion of Air Bubbles to Air Hydrate Crystals in Antarctic Ice. *Science*, 267:1802–1804, March 1995.

[65] A. J. Gow. Preliminary Results of Studies of Ice Cores from the 2164 m-Deep Drill Hole, Byrd Station, Antarctica. *Assoc. Internat. d'Hydrologie Scientifique*, 86:76–90, 1970.

[66] S. L. Miller. Clathrate Hydrates of Air in Antarctic Ice. *Science*, 165:489–490, August 1969.

[67] R. Gandhi and et al. Ultrahigh-energy neutrino interactions. *Astroparticle Physics*, 5:81–110, August 1996.

[68] J. G. Learned and K. Mannheim. High-Energy Neutrino Astrophysics. *Annual Review of Nuclear and Particle Science*, 50:679–749, 2000.

[69] D. Chirkin and W. Rhode. Propagating leptons through matter with Muon Monte Carlo (MMC). *ArXiv High Energy Physics - Phenomenology e-prints arXiv:hep-ph/0407075*, July 2004.

[70] Particle Data Group. Review of particle physics. *Journal of Physics G: Nuclear and Particle Physics*, 37(7A):075021, 2010.

[71] Yung-Su Tsai. Pair production and bremsstrahlung of charged leptons. *Rev. Mod. Phys.*, 46(4):815–851, Oct 1974.

[72] K. Kamata and J. Nishimura. The Lateral and the Angular Structure Functions of Electron Showers. *Progress of Theoretical Physics Supplement*, 6:93–155, 1958.

[73] S. Klein. Suppression of bremsstrahlung and pair production due to environmental factors. *Rev. Mod. Phys.*, 71(5):1501–1538, Oct 1999.

[74] C.H. Wiebusch. *The Detection of Faint Light in Deep Underwater Neutrino Telescopes.* PhD thesis, RWTH Aachen, 1995.

[75] J. Alvarez-Muñiz and E. Zas. Cherenkov radio pulses from EeV neutrino interactions: the LPM effect. *Physics Letters B*, 411:218–224, September 1997.

[76] J. Alvarez-Muñiz and E. Zas. The LPM effect for EeV hadronic showers in ice: implications for radio detection of neutrinos. *Physics Letters B*, 434:396–406, August 1998.

[77] V. Niess and V. Bertin. Underwater acoustic detection of ultra high energy neutrinos. *Astroparticle Physics*, 26:243–256, November 2006.

[78] The Acorne Collaboration. Simulation of ultra high energy neutrino induced showers in ice and water. *Astroparticle Physics*, 28:366–379, November 2007.

[79] J. Vandenbroucke. *Acoustic Detection of astrophysical neutrinos in South Pole ice.* PhD thesis, University of California, Berkeley, 2009.

[80] The AMANDA Collaboration. Optical properties of deep glacial ice at the South Pole. *Journal of Geophysical Research (Atmospheres)*, 111:D13203, July 2006.

[81] J. Lundberg and et al. Light tracking through ice and water–scattering and absorption in heterogeneous media with photonics. *Nuclear Instruments and Methods A*, 581(3):619 – 631, 2007.

[82] The ANTARES Collaboration. Transmission of light in deep sea water at the site of the ANTARES neutrino telescope. *Astroparticle Physics*, 23:131–155, February 2005.

[83] I.A. Belolaptikov and et al. The baikal underwater neutrino telescope: Design, performance, and first results. *Astroparticle Physics*, 7(3):263 – 282, 1997.

[84] Anthony J. Gow and Terrence Williamson. Volcanic ash in the antarctic ice sheet and its possible climatic implications. *Earth and Planetary Science Letters*, 13(1):210 – 218, 1971.

[85] E.G. Anassontzis and et al. Light transmissivity in the nestor site. *Nuclear Instruments and Methods A*, 349(1):242 – 246, 1994.

[86] C. Richardt and et al. Reconstruction methods for acoustic particle detection in the deep sea using clusters of hydrophones. *Astroparticle Physics*, 31:19–23, February 2009.

[87] J.G. Learned. Acoustic radiation by charged atomic particles in liquids: An analysis. *Phys. Rev. D*, 19(11):3293–3307, Jun 1979.

[88] G.A. Askariyan and et al. Acoustic detection of high energy particle showers in water. *Nuclear Instruments and Methods*, 164(2):267 – 278, 1979.

[89] L. Sulak and et al. Experimental studies of the acoustic signature of proton beams traversing fluid media. *Nuclear Instruments and Methods*, 161(2):203 – 217, 1979.

[90] P. I.and et al. Golubnichy. Utilization of Lasers for Modeling Acoustic Effects Arising in the Interactions of Particles with Liquids. In *International Cosmic Ray Conference*, volume 11 of *International Cosmic Ray Conference*, pages 202–+, 1979.

[91] V. Bychkov and et al. Study of the acoustic field produced by a 50-mev electron beam in water. *Moscow University Physics Bulletin*, 62:155–159, 2007. 10.3103/S0027134907030071.

[92] S. Böser and et al. Acoustic Sensor and Transmitter Development for a Large Volume Neutrino Detection Array in Ice. In *International Cosmic Ray Conference*, volume 5 of *International Cosmic Ray Conference*, pages 29–+, 2005.

[93] The IceCube Collaboration. Sensor development and calibration for acoustic neutrino detection in ice. In *Proceedings of the 31st International Cosmic Ray Conference*, International Cosmic Ray Conference, July 2009.

[94] D. Heinen. Laboratory measurements of the thermo-acoustic effect in bubble-free ice: private communication. 2010.

[95] The ACORNE Collaboration. Study of the acoustic signature of UHE neutrino interactions in water and ice. *Nuclear Instruments and Methods A*, 607:398–411, August 2009.

[96] S. Nanthikesan and S. Shyam Sunder. Anisotropic elasticity of polycrystalline ice ih. *Cold Regions Science and Technology*, 22(2):149 – 169, 1994.

[97] Böser. *Acoustic Detection of Ultra-High Energy Cascades in Ice*. PhD thesis, Humboldt Universität zu Berlin, 2006.

[98] P. B. Price. Attenuation of acoustic waves in glacial ice and salt domes. *Journal of Geophysical Research (Solid Earth)*, 111:2201–+, February 2006.

[99] The Icecube Collaboration. Measurement of sound speed vs. depth in South Pole ice for neutrino astronomy. *Astroparticle Physics*, 33:277–286, June 2010.

[100] P.B. Price. Mechanisms of attenuation of acoustic waves in antarctic ice. *Nuclear Instruments and Methods A*, 325(1-2):346 – 356, 1993.

[101] CREWES. Zoeppritz explorer browser applet. `http://www.crewes.org/`.

[102] K. Aki and P. Richards. *Quantitative seismology*. University Science Books, 2002.

[103] M. Bothe. Influence of hole-cie properties on measurements of the South Pole Acoustic Test Setup. Diplomarbeit, Technische Universität Berlin, 2007.

[104] G.A. Askariyan. Excess negative charge of an electron-photon shower and its coherent radio emission. *Sov. JETP*, 14:441443, 1962.

[105] P. W. Gorham and et al. Observations of the askaryan effect in ice. *Phys. Rev. Lett.*, 99(17):171101, Oct 2007.

[106] T. Barrella, S. Barwick, and D. Saltzberg. Ross Ice Shelf (Antarctica) in situ radio-frequency attenuation. *Journal of Glaciology*, 57:61–66, March 2011.

[107] The ANTARES Collaboration. AMADEUS - The Acoustic Neutrino Detection Test System of the ANTARES Deep-Sea Neutrino Telescope. *Nuclear Instruments and Methods A*, 626-627:128 – 143, 2011.

[108] P. C. Bosetti. DUMAND Status Report. *Nuclear Physics B Proceedings Supplements*, 48:466–468, May 1996.

[109] V. Aynutdinov and et al. The BAIKAL neutrino experiment - Physics results and perspectives. *Nuclear Instruments and Methods A*, 602:14–20, April 2009.

[110] The Baikal Collaboration. The gigaton volume detector in lake baikal. *Nuclear Instruments and Methods A*, 639(1):30 – 32, 2011. Proceedings of the Seventh International Workshop on Ring Imaging Cherenkov Detectors.

[111] The ANTARES Collaboration. A Deep Sea Telescope for High Energy Neutrinos. *ArXiv Astrophysics e-prints arXiv:astro-ph/9907432*, July 1999.

[112] P. Sapienza and the NEMO Collaboration. The NEMO project: achievements and perspectives. *Journal of Physics Conference Series*, 120(6):062010–+, July 2008.

[113] The Nestor Collaboration. The NESTOR underwater neutrino telescope project. *Nuclear Instruments and Methods A*, 602:54–57, April 2009.

[114] The Km3NeT Consortium. KM3NeT: A cubic-kilometre scale deep sea neutrino telescope in the Mediterranean Sea. *Journal of Physics Conference Series*, 203(1):012124–+, January 2010.

[115] The KM3NeT Consortium. Conceptual design for a deepsea research infrastructure incorporating a very large volume neutrino telescope in the mediterranean sea. `http://www.km3net.org/CDR/CDR-KM3NeT.pdf`, 2008.

[116] N. Kurahashi. Updates from the Study of Acoustic Ultra-high energy Neutrino Detection phase II. In *Proceedings of the 3rd International Workshop on the Acoustic and Radio EeV Neutrino Detection Activities*. Nuclear Instruments and Methods A, 2009.

[117] R. Wischnewski. The AMANDA-II neutrino telescope. *Nuclear Physics B Proceedings Supplements*, 110:510–512, July 2002.

[118] The AMANDA Collaboration. Search for point sources of high energy neutrinos with final data from AMANDA-II. Phys. Rev. D, 79(6):062001–+, March 2009.

[119] I. Kravchenko et al. Updated limits on the ultra-high energy (UHE) neutrino flux from the RICE experiment. *Int. J. Mod. Phys.*, A21S1:153–157, 2006.

[120] P. W. Gorham and et al. New Limits on the Ultrahigh Energy Cosmic Neutrino Flux from the ANITA Experiment. *Physical Review Letters*, 103(5):051103–+, July 2009.

[121] The ARA Collaboration. Askaryan Radio Array - MRI Proposal, 2010, unpublished. `http://ara.physics.wisc.edu/resources/project_description.pdf`.

[122] P.and et al. Gorham. Measurements of the Suitability of Large Rock Salt Formations for Radio Detection of High Energy Neutrinos. *ArXiv High Energy Physics - Experiment e-prints arXiv:hep-ex/0108027*, August 2001.

[123] J. A. Vandenbroucke and et al. Simulation of a hybrid optical/radio/acoustic extension to icecube for EHE neutrino detection. *International Journal of Modern Physics A*, 21:259–264, 2006.

[124] The IceCube Collaboration. IceCube - Preliminary Design Document, unpublished. `http://www.icecube.wisc.edu/science/publications/pdd/`.

[125] The IceCube Collaboration. Physics Capabilities of the IceCube DeepCore Detector. *ArXiv e-prints, astro-ph.IM:0907.2263*, July 2009.

[126] Francis Halzen and Spencer R. Klein. Invited review article: Icecube: An instrument for neutrino astronomy. *Review of Scientific Instruments*, 81(8):081101, 2010.

[127] The IceCube Collaboration. Calibration and characterization of the IceCube photomultiplier tube. *Nuclear Instruments and Methods A*, 618:139–152, June 2010.

[128] The IceCube Collaborationa. Status, performance, and first results of the IceTop array. *Nuclear Physics B Proceedings Supplements*, 196:159–164, December 2009.

[129] The Icecube Collaboration. The IceCube data acquisition system: Signal capture, digitization, and timestamping. *Nuclear Instruments and Methods A*, 601:294–316, April 2009.

[130] M. Wallraff. Design, implementation and test of a new feature extractor for the icecube neutrino observatory. Diplomarbeit, RWTH Aachen, 2010.

[131] The IceCube Collaboration. Internal icecube wiki: Trigger filter transmission board. `http://wiki.icecube.wisc.edu/index.php/Trigger_Filter_Transmission_Board`.

[132] A. Gazizov and M. Kowalski. ANIS: High energy neutrino generator for neutrino telescopes. *Computer Physics Communications*, 172:203–213, November 2005.

[133] D. Heck and et al. *CORSIKA: a Monte Carlo code to simulate extensive air showers.* Forschungszentrum Karlsruhe GmbH, Karlsruhe (Germany), February 1998.

[134] The Icecube Collaboration. Internal report icecube/200608001: Note on neutrino-generator and JULIeT: Effective area and event rate using the event weighting technique, 2006.

[135] The IceCube Collaboration. Photon propagation code. `http://www.icecube.wisc.edu/~dima/work/WISC/ppc/`.

[136] The AMANDA Collaboration. Muon track reconstruction and data selection techniques in AMANDA. *Nuclear Instruments and Methods A*, 524:169–194, May 2004.

[137] S. Grullon, D. Boersma, and G. Hill. Internal report icecube/200807001-v3: Photonics-based Log-Likelihood Reconstruction in IceCube. 2008.

[138] D. Chirkin. Internal report icecube/200807006: Neutrino search with IceCube. 2008.

[139] The IceCube Collaboration. Design and performance of the South Pole Acoustic Test Setup. *Preprint available: astro-ph.IM:1105.4339*, May 2011.

[140] The Icecube Collaboration. Hades-hydrophone for acoustic detection at south pole. *Nuclear Instruments and Methods A*, 604:215–+, June 2009.

[141] T. Meures. Reciprocity calibration of hydrophones in the Aachen Acoustic Laboratory. Diplomarbeit, RWTH Aachen, 2010.

[142] L. Paul. Characterization and calibration of acoustic devices for the South Pole Acoustic Test Setup. Diplomarbeit, RWTH Aachen, 2010.

[143] F. Descamps. *Feasibility of acoustic neutrino detection in ice with the South Pole Acoustic Test Setup*. PhD thesis, University of Gent, 2010.

[144] D. Tosi. *Measurement of Acoustic Attenuation in South Pole Ice with a Retrievable Transmitter*. PhD thesis, Humboldt Universität zu Berlin, 2009.

[145] R. Heller. Pinger schematics, DESY Zeuthen. 2010.

[146] The IceCube Collaboration. SPATS Monitoring Web Page. `http://inwfsun1.ugent.be/~freija/Moni-SPATS/`.

[147] C. Vogt, K. Laihem, and C. Wiebusch. Speed of sound in bubble-free ice. *Acoustical Society of America Journal*, 124:3613–+, 2008.

[148] C. Vogt. Aufbau eines Messplatzes zum Test akustischer Sensoren für den Nachweis ultrahochenergetischer Neutrinowechselwirkungen. Diplomarbeit, RWTH Aachen, 2007.

[149] The Icecube Collaboration. Measurement of acoustic properties of South Pole ice for neutrino astronomy. *Nuclear Instruments and Methods A*, 604:164–+, June 2009.

[150] The IceCube Collaboration. Icecube internal wiki: Seastar plots and summary. `http://wiki.icecube.wisc.edu/index.php/Seastar_plots_and_summary`.

[151] The IceCube Collaboration. Icecube internal wiki: Compressibility. `http://wiki.icecube.wisc.edu/index.php/Compressibility`.

[152] N.W.D. Evans and et al. An assessment on the fundamental limitations of spectral subtraction. *Acoustics, Speech and Signal Processing, 2006. ICASSP 2006 Proceedings. 2006 IEEE*, May 2006.

[153] S. F. Boll. Suppression of acoustic noise in speech using spectral subtraction. *IEEE Transactions on Acoustics, Speech, and Signal Processing*, 27(2):113–120, April 1979.

[154] The Icecube Collaboration. Internal report: South Pole Acoustic Test Setup (SPATS) DAQ.

[155] J.H. Fischer. Acoustic transducers for the south pole acoustic test setup. Diplomarbeit, Humboldt Universität zu Berlin, 2006.

[156] Y. Abdou. Private communication: Frequency dependence of the acoustic attenuation length. 2011.

[157] The Icecube Collaboration. Measurement of acoustic attenuation in South Pole ice. *Astroparticle Physics*, 34:382–393, January 2011.

[158] J. Vandenbroucke. private communication. 2010.

[159] Hülß, J.-P. Private communication: Idea for a top-down reconstruction for icecube. 2009.

[160] F. C. Porter. Testing Consistency of Two Histograms. *ArXiv e-prints*, April 2008.

[161] W.H. Press, B. P. Flannery, S.A. Teukolsky, and W.T. Vetterling. *Numerical Recipes in C book*. Cambridge University Press, 1992.

[162] The IceCube Collaboration. Time-integrated searches for point-like sources of neutrinos with the 40-string icecube detector. *The Astrophysical Journal*, 732(1):18, 2011.

[163] T. Neunhoeffer. Estimating the angular resolution of tracks in neutrino telescopes based on a likelihood analysis. *Astroparticle Physics*, 25(3):220 – 225, 2006.

[164] A. Schukraft. Private communication: Search for a diffuse flux of astrophysical neutrinos with icecube. 2010.

[165] J. Blumenthal. Private communication: Development of an error estimate for the top-down reconstruction. 2010.

Danksagung

Hiermit möchte ich allen Personen danken, die am Zustandekommen dieser Arbeit beteiligt waren.

Zunächst gilt mein Dank Prof. Christopher Wiebusch, zum einem für die äußerst interessante Aufgabenstellung, die weit genug gefasst war und mir damit zahlreiche Freiheiten bei der Ausgestaltung der Arbeit erlaubte, sowie für seine langjährige Unterstützung.

Mein besonderer Dank gilt außerdem Prof. Thomas Hebbeker für seine Bereitschaft das Zweitgutachten zu dieser Arbeit zu übernehmen.

Ich möchte mich weiterhin bedanken bei der gesamten Aachener IceCube - Gruppe, einschließlich aller Kollegen die die Gruppe mittlerweile verlassen haben, für die zahlreichen Anregungen, Diskussionen und Hilfestellungen.

Meinen Bürokollegen, Martin Bissok, Karim Laihem und Larissa Paul gilt mein besonderer Dank für die freundschaftliche und inspirierende Arbeitsatmosphäre.

Weiterhin gilt mein Dank allen Kollegen, die diese Arbeit zur Korrektur gelesen haben und mit konstruktiver Kritik und vielen Hinweisen beigetragen haben, darunter Jan Blumenthal, David Boersma, Anne Schukraft und Marius Wallraff.

Und nicht zuletzt möchte ich meiner Familie und meinen Freunden danken, die mich in meiner Entscheidung zu dieser Promotion unterstützt haben und mir während der gesamten Zeit mit gutem Rat zur Seite standen.